UNIVERSIDADE FEDERAL DO MARANHÃO
CENTRO DE CIÊNCIAS EXATAS E TECNOLOGIA
PROGRAMA DE PÓS-GRADUAÇÃO DOUTORADO EM QUÍMICA

ELAINE SÁ MENEZES CUTRIM

NANOPLATAFORMAS HÍBRIDAS A BASE DE PONTOS QUÂNTICOS DE CARBONO E SUPORTES INORGÂNICOS NATURAIS E SINTÉTICOS

SÃO LUÍS
2026

ELAINE SÁ MENEZES CUTRIM

NANOPLATAFORMAS HÍBRIDAS A BASE DE PONTOS QUÂNTICOS DE CARBONO E SUPORTES INORGÂNICOS NATURAIS E SINTÉTICOS

Defesa apresentada como requisito parcial para a obtenção do grau de Doutor em Química com área de concentração em Química Inorgânica pelo Programa de Pós-graduação Doutorado em Química da Universidade Federal do Maranhão

Orientadora: Prof.ª. Dr. Ana Clécia Santos de Alcântara

SÃO LUÍS
2026

Ficha gerada por meio do SIGAA/Biblioteca com dados fornecidos pelo(a) autor(a).
Diretoria Integrada de Bibliotecas/UFMA

Cutrim, Elaine Sá Menezes.
Nanoplataformas híbridas a base de pontos quânticos de carbono e suportes inorgânicos naturais e sintéticos / Elaine Sá Menezes Cutrim. - 2026.
186 f.

Orientador(a): Ana Clécia Santos de Alcântara.
Tese (Doutorado) - Programa de Pós-graduação Doutorado em Química/ccet, Universidade Federal do Maranhão, São Luís, 2026.

1. Argilominerais. 2. Pontos Quânticos de Carbono. 3. Redes Metalorgânicas. 4. Sepiolita. 5. Montmorilonita. I. Alcântara, Ana Clécia Santos de. II. Título.

ELAINE SÁ MENEZES CUTRIM

NANOPLATAFORMAS HÍBRIDAS A BASE DE PONTOS QUÂNTICOS DE CARBONO E SUPORTES INORGÂNICOS NATURAIS E SINTÉTICOS

Tese apresentada como requisito parcial para a obtenção do grau de Doutor em Química com área de concentração em Química Inorgânica pelo Programa de Pós-graduação Doutorado em Química da Universidade Federal do Maranhão

São Luís, 06 de março de 2026

BANCA EXAMINADORA

Prof.ª Dr. Ana Clécia Santos de Alcântara (Orientadora)
Universidade Federal do Maranhão - UFMA

Prof. Dr. Cícero Wellington Brito Bezerra
Universidade Federal do Maranhão – UFMA

Prof. Dr. Marcelo Moizinho Oliveira
Instituto Federal do Maranhão -IFMA

Prof. Dr. Marco Aurelio Suller Garcia
Universidade Federal do Rio de Janeiro - UFRJ

Prof.ª Dr. Renato Sonchini Gonçalves
Universidade Federal do Paraná -UFPR

À minha mãe pelo apoio e amor incondicionais

AGRADECIMENTOS

À Prof.ª Dr. Ana Alcântara por sua orientação e sugestões valiosas ao longo de todo o período de elaboração desta tese de doutorado.

À Prof.ª Dr. Vanesa Fernandez-Moreira e Maria Concepción Gimeno (UNIZAR) por terem me recebido em seu grupo de pesquisa. O período sanduíche foi de muito aprendizado e amadurecimento pessoal.

Ao Prof.º Dr. Hernane Barud que me recebeu no mestrado e no doutorado no seu grupo de pesquisa BioPolMat, esse auxílio foi essencial para realização do meu trabalho. Em especial, agradeço a Marina Fontes pela realização dos ensaios de bioimagem celular.

Ao Laboratório de Patologia e Imunoparasitologia (LPI), em especial à professora Lucilene Silva e Alina Figueiredo pelos ensaios de hemólise realizados para esta tese.

Ao Centro de Ciência Exatas e Tecnologia – UFMA pela infraestrutura oferecida que proporcionou o desenvolvimento desta pesquisa. Em especial, a Central Analítica e a Central de Materiais.

À Universidade Federal do Maranhão pela minha formação e por me receber novamente, me proporcionando mais uma oportunidade de aprendizado e crescimento profissional e pessoal.

Ao Programa de Pós-graduação Doutorado em Química.

À FAPEMA pela bolsa concedida.

À CAPES pela bolsa de doutorado sanduíche concedida.

Aos colegas e amigos do Bionanos, Fernanda, Ismael Rodrigues, Jaynne Martins, Josefa Santos, Lucas, Marília Melo, Mayara Teixeira, Rayssa Cândido, Rebecca Jemima, Socorro Silva, Vanessa Campos, Wallyson Leandro, além dos agregados André Frazão e Jhnonathan Menezes. Vocês com certeza tornaram esse caminho mais leve. Obrigada pelas memórias e muito sucesso a todos!

À Emerson Silva por toda a ajuda ao longo do caminho. Agradeço pelo cafezinho da tarde, pelas pausas, pela paciência e pela ajuda com algumas imagens também!

À minha mãe por todo auxílio ao longo dessa longa jornada acadêmica (rs). Seu apoio foi essencial para que eu chegasse até aqui!

A todos que de forma direta ou indireta contribuíram para execução desse trabalho, muito obrigada!

ABSTRACT

Clays are widely combined with other nanomaterials to improve their properties and to obtain multifunctional hybrid systems. These materials offer advantages such as enhanced mechanical and rheological performance, reduced toxicity, and compatibility with green chemistry principles, making them suitable platforms for incorporating functional nanostructured materials. In this work, hybrid nanomaterials based on carbon quantum dots (CQDs) and inorganic supports with different morphologies were developed, including fibrous sepiolite (SEP), layered montmorillonite (MMT), and ZIF-8. CQDs were synthesized by a solvothermal route using citric acid and urea in dimethylformamide and subsequently associated with the supports either using preformed CQDs or through *in situ* synthesis. Spectroscopic analyses indicate that CQDs interact with SEP mainly through surface silanol groups and hydroxyl groups associated with zeolitic water, as evidenced by FT-IR spectroscopy. Photoluminescence (PL) spectroscopy demonstrates that the association between CQDs and clay minerals does not compromise the PL properties of the CQDs. The hybrid nanomaterials exhibit shifts in the maximum emission wavelength, indicating modification of the emissive states induced by the clay environment. In addition, most hybrid systems display dual-emission behavior. Raman analysis shows an increase in the sp^2 carbon network for sepiolite–CQD hybrids synthesized *in situ*, accompanied by a decrease in the I_D/I_G ratio, indicating higher structural ordering as a function of synthesis time. For the MMT-based hybrid nanomaterials, X-ray diffraction (XRD) analysis reveals both the presence of diffraction features associated with CQDs and an increase in the basal spacing of MMT. Drug intercalation studies demonstrate that 5-fluorouracil is incorporated into MMT as a monolayer with planar orientation, producing an increase in basal spacing from approximately 1.21 nm to values close to 1.27 nm, depending on drug loading. The resulting clay–CQD–drug systems exhibit stable structural organization without collapse of the layered framework. The ZIF-8/CQD hybrid nanomaterial preserves the crystalline structure and porosity of ZIF-8, as confirmed by XRD and nitrogen adsorption–desorption analyses, although a reduction in specific surface area is observed due to the incorporation of CQDs. Hemolysis assays performed over a concentration range from 5000 to 36 μg mL^{-1} show hemolysis percentages below 5%, indicating good hemocompatibility. Overall, the results demonstrate that the association of CQDs with clays and metal–organic frameworks leads to structurally stable hybrid nanoplatforms with tunable optical properties, preserved porosity, and low toxicity.

RESUMO

Argilominerais são amplamente combinados com outros nanomateriais para melhorar suas propriedades e obter sistemas híbridos multifuncionais. Esses materiais oferecem vantagens como melhoria das propriedades mecânicas e reológicas, redução da toxicidade e compatibilidade com os princípios da química verde, tornando-os plataformas adequadas para a incorporação de nanomateriais funcionais. Neste trabalho, foram desenvolvidos nanomateriais híbridos baseados em *carbon quantum dots* (CQDs) e suportes inorgânicos com diferentes morfologias, incluindo sepiolita fibrosa (SEP), montmorilonita lamelar (MMT) e ZIF-8. Os CQDs foram sintetizados por uma rota solvotérmica utilizando ácido cítrico e ureia em dimetilformamida e posteriormente associados aos suportes utilizando CQDs previamente formados ou por síntese *in situ*. Análises espectroscópicas indicam que os CQDs interagem com a SEP principalmente por meio de grupos silanol superficiais e grupos hidroxila associados à água zeolítica, como evidenciado por espectroscopia FT-IR. A espectroscopia de fotoluminescência (PL) demonstra que a associação entre CQDs e argilominerais não compromete as propriedades de PL dos CQDs. Os nanomateriais híbridos apresentam deslocamentos no comprimento de onda máximo de emissão, indicando modificação dos estados emissivos induzida pelo ambiente da argila. Além disso, a maioria dos sistemas híbridos apresenta comportamento de dupla emissão. A análise por Raman mostra um aumento da rede de carbono sp^2 para os híbridos sepiolita–CQD sintetizados *in situ*, acompanhado por uma diminuição na razão ID/IG, indicando maior ordenamento estrutural em função do tempo de síntese. Para os nanomateriais híbridos baseados em MMT, a análise por difração de raios X (XRD) revela tanto a presença de características de difração associadas aos CQDs quanto um aumento no espaçamento basal da MMT. Estudos de intercalação de fármacos demonstram que o 5-fluorouracil é incorporado na MMT como uma monocamada com orientação planar, produzindo um aumento no espaçamento basal de aproximadamente 1,21 nm para valores próximos de 1,27 nm, dependendo da carga do fármaco. Os sistemas resultantes argila–CQD–fármaco apresentam organização estrutural estável sem colapso da estrutura lamelar. O nanomaterial híbrido ZIF-8/CQD preserva a estrutura cristalina e a porosidade do ZIF-8, conforme confirmado por análises de XRD e adsorção–dessorção de nitrogênio, embora seja observada uma redução na área superficial específica devido à incorporação dos CQDs. Ensaios de hemólise realizados em uma faixa de concentração de 5000 a 36 $\mu g\ mL^{-1}$ apresentam porcentagens de hemólise inferiores a 5%, indicando boa hemocompatibilidade. De modo geral, os resultados demonstram que a associação de CQDs com argilominerais e estruturas metalorgânicas leva à formação de nanoplataformas híbridas estruturalmente estáveis, com propriedades ópticas moduláveis, porosidade preservada e baixa toxicidade.

LIST OF ILLUSTRATIONS

LIST OF TABLES

LIST OF ABBREVIATIONS AND ACRONYMS

5-FU	5-Fluorouracil
BET	Brunauer-Emmett-Teller
CD	Carbon Dots
CND	Carbon Nanodots
CQD	Carbon Quantum Dots
CPD	Carbonized Polymer Dots
CEC	Cation Exchange Capacity
DLE	Drug Loading Efficiency
DMF	Dimetilformamide
DTG	Derivative Thermogravimetry
EE	Entrapment Efficiency
FT-IR	Fourier-transform infrared
GQD	Graphene Quantum Dots
HKUST	Hong Kong University of Science and Technology
HNT	Halloysite Nanotubes
IRMOF	Isoreticular metal-organic frameworks
MIL	Materials Institute Lavoisier
MMT	Montmorillonite
MOF	Metal-Organic Framework
PAL	Palygorskite
PBS	Phosphate Buffered Saline
PL	Photoluminescence
QCE	Quantum Confinement Effect
QY	Quantum Yield
SBU	Secondary building units
SEM	Scanning Electron Microscopy
SEP	Sepiolite
TG	Thermogravimetric Analyses
TEM	Transmission Electron Microscopy
UiO	University of Oslo
UV-Vis	Ultraviolet-Visible
XRD	X-ray Diffraction

ZIF-8	Zeolitic Imidazolate Framework-8
XPS	X-ray Photoelectron Spectroscopy

CONTENTS

1 RESEARCH MOTIVATION AND THESIS OUTLINE

Contents

Chapter I Abstract

This chapter provides the background for developing this thesis and its main objectives. Additionally, a summary of each chapter is included.

1.1 THESIS MOTIVATION AND RESEARCH AIM

The Maya blue pigment used in wall paintings in Mexico from the 7th to the 16th century is often cited as the first example of a hybrid material in which indigo, a natural dye from *Indigofera tinctoria*, was occluded into the structural tunnels of palygorskite (PAL), a fibrous clay (Doménech et al., 2009; Gettens, 1962). In this case, PAL guarantees protection against external agents, giving rise to stable blue pigments that resist heating at temperatures close to 250 °C, treatments with organic solvents, acid, and basic media, and exposure to the action of microorganisms (Arnold et al., 2008; Ruiz; Ruiz-García; Ruiz-Hitzky, 2023). Since its beginning from nowadays, the field of hybrid materials has become a broad scientific and technological area, including important fields such as sol-gel chemistry, polymer nanocomposites, and hybrid nanomaterials.

By definition, hybrid nanomaterials are a combination of two or more components at the nanoscale, integrating the physical and chemical properties of the constituent nanomaterials. This approach has the potential to improve the properties and functionalities of the nanomaterials, overcoming or reducing the limitations associated with single-component systems (Li et al., 2023a; Ma, 2019). In fact, this occurs as a result of the synergistic effects of the counterparts at the nanoscale, surpassing the original features of the precursors. In addition, hybrid nanomaterials offer the possibility to monitor and alter their properties by modifying their composition and morphology, providing hybrid nanomaterials with superior properties, leading to a wide range of applications in biology and health (Park et al., 2020; Shuai et al., 2021) to photonic devices (Prete et al., 2024), catalysis and environment (Wang et al., 2023a), smart coatings (Dashuai et al., 2022), and energy (Hsu et al., 2022).

In this thesis, materials from different classes were chosen to form hybrid nanomaterials. Carbon quantum dots (CQD) are a smart choice due to their attractive properties, such as tunable photoluminescence properties, high water solubility, chemical stability, low toxicity, and easy surface modification (Gao et al., 2020; Ghosh et al., 2023). Moreover, they are zero-dimensional carbon-based nanomaterials (diameter <10 nm) with spherical or quasi-spherical morphology, and the presence of functional groups (*i.e.*, hydroxyl, carboxyl, amino, amide, carbonyl) at the surface provides sites of interactions with other nanomaterials (Barhoum et al., 2023). Despite these advantages, the nanoparticle aggregation of pure CQD may result in photoluminescence quenching and loss of stability (Carbonaro et al., 2020). In this regard, the association of CQD and porous materials could efficiently reduce these drawbacks and also can endow the final nanomaterials with new characteristics and functionality. Benefiting from, but

not limited to, the high surface area and high porosity, clay minerals and metal-organic frameworks (MOF) are ideal host matrices for the incorporation of CQD.

Clay minerals are historically one of the most used materials in a wide range of applications. The interest in this class of materials is constantly renewed by their outstanding properties, such as high surface area, layer charge density, cation exchange, swelling capacity, chemical stability, and rheological behavior. They are also abundant and low-cost materials (Tipa et al., 2022; Xie; Chen; Yang, 2023) . In addition, clay minerals have the ability to interact with other entities such as molecules, particles, and ions, through different mechanisms according to the type of clay used (lamellar, fibrous or tubular), being of great importance to understand how the variation in composition, structure and morphology of the silicate used can influence the final properties of the system(Ruiz; Ruiz-García; Ruiz-Hitzky, 2023). As a result, the association of clay minerals and carbon nanomaterials, including graphene (Alamier et al., 2025), graphene oxide (Vengatesan et al., 2017), and carbon nanotubes (Hsu et al., 2022) results in hybrid nanomaterials with application in environmental remediation, energy storage, and biomedical applications.

MOFs are crystalline materials formed by the assembly of metal ions/clusters with organic linkers, resulting in structures with diverse chemical compositions (Nakatani et al., 2025). Their exceptionally large surface areas, adjustable porosity, uniform pores and fully exposed active sites have positioned them as versatile platforms for innovative hybrid nanomaterials (Hou et al., 2022; Zhou et al., 2023). In pioneering work, Yaghi and co-workers reported a series of host-guest materials by the incorporation of fullerenes and organic dyes into MOF-177 (Chae et al., 2004). Since then, extensive research has explored MOFs as unique host matrices for the integration of secondary components. To date, a wide range of guest species, including metals (Jin et al., 2022), metal oxides (Huang et al., 2021), carbon nanotubes (Zhang et al., 2024), quantum dots (Fan et al., 2024), and polymers (Siva et al., 2023) have been successfully embedded within MOFs, leading to hybrid systems with enhanced functionalities.

Despite the increasing interest in hybrid materials based on CQDs and porous inorganic hosts, a systematic understanding of how the morphology and structure of the host matrix influence the properties of these systems remain limited. In particular, comparative studies involving different porous supports, such as MMT, SEP, and MOFs, and their role in modulating the structural and optical behavior of CQD-based hybrids has not been thoroughly investigated. In addition, the development of ternary systems combining clay minerals, CQDs, and therapeutic molecules is a growing research area.

Therefore, the focus of this thesis is on developing hybrid nanomaterials based on carbon quantum dots and mesoporous materials and studying the structure-property relationships of clay-CQD and MOF-CQD. It is expected that the association of clays or MOFs with carbon quantum dots to enable the development of nanomaterials with multiple properties, such as thermal stability, photoluminescence, and low toxicity. These properties expand the potential applications of such materials in various fields, ranging from electronics to pharmaceuticals, thereby opening new opportunities for technological innovation with potential impacts across scientific, technological, and societal domains. The key objectives are:

1. To prepare hybrid nanomaterials based on clay with different morphologies and CQD, investigating the effect of different synthetic routes on the properties of the resultant materials;
2. To associate a drug with clay-CQD hybrid nanomaterials as a potential drug delivery system;
3. To synthesize ZIF-8 in the presence of CQD and characterize the hybrid nanomaterial ZIF-8/CQD;
4. To evaluate the toxicity of the hybrid nanomaterials using the hemolysis assay.

1.2 OUTLINE OF THE THESIS

Chapter II is a literature review that describes the chemistry and structure of carbon dots and clay minerals, besides the association of this class of materials into hybrid and their application in different areas.

Chapter III describes the starting materials and methods for obtaining hybrid nanomaterials. In addition, characterization techniques used to obtain information about morphologies, structure, and optical properties, and assay procedures are described.

Chapter IV and V discuss the association of carbon quantum dots with sepiolite and montmorillonite, respectively, the structural, thermal, and optical properties of these hybrid nanomaterials. Additionally, the effects of different routes to obtain are discussed. The toxicity of the materials was assessed through a hemolysis test.

Chapter VI approaches the association of clay-CQD with a drug, 5-Fluorouracil, as a potential nanoplatform in a drug delivery system.

Chapter VII aims to provide an overview of MOF, addressing its concept and main characteristics, highlighting the subclass of ZIF and one of its members, ZIF-8. Additionally, the methods of association with CQDs are also reviewed. This chapter is also intended to

discuss the results obtained from the hybrid nanomaterial CQD@ZIF-8 concerning its morphology, structure, and optical properties.

2 LITERATURE REVIEW

Contents

Chapter 2 Abstract

This chapter presents a literature review on the structure, properties, and classification of carbon dots and clay minerals. It also discusses the association between these materials into hybrid nanomaterials and their applications.

2.1 THE COUNTERPARTS: AN OVERVIEW OF CLAY MINERALS AND CARBON DOTS CHEMISTRY

2.1.1 Carbon dots

Carbon plays an essential role in nanomaterials development due to its remarkable ability to form stable structures with distinct dimensionalities and properties. Carbon-based nanomaterials, ranging from three-dimensional (3D) graphite to two-dimensional (2D) graphene and graphene oxide, as well as one-dimensional (1D) carbon nanotubes, have attracted considerable attention because of their outstanding physicochemical properties and great potential applications (Xue et al., 2023). More recently, carbon dots (CDs) have emerged as a novel class of fluorescent carbon nanomaterials. CDs were discovered accidentally when Xu et al. (2004) prepared single-walled carbon nanotubes by electric arc discharge. During purification of the product by electrophoresis, they identified an unknown carbonaceous material that exhibited bright fluorescence. After that, Sun et al. (2006) officially introduced the term “carbon dots” when they demonstrated that surface passivation could significantly enhance the photoluminescence of these nanoparticles.

Further studies focused on the development of multicolor-emitting and surface-functionalized CDs (Liu et al., 2007; Liu et al., 2009), and the development of CQDs for biosensing and protein detection (Li et al., 2010; Xu et al., 2012). According to Tavan et al. (2025), the evolution of CDs research can be divided into three main stages: (i) the discovery and early development phase (2004–2011), characterized by the initial reports of CDs predominantly synthesized through top-down approaches; (ii) the advanced development phase (since 2011), marked by the increasing adoption of bottom-up synthesis strategies; and (iii) the recent sustainability and scalability phase, which emphasizes the use of biomass-derived precursors and environmentally benign solvents to enable large-scale and industrially viable production. More recent studies have focused on scalable and cost-effective synthesis routes, further enhancing the accessibility of CDs (Huang; Ren, 2025; Supajaruwong et al., 2023).

CDs are commonly described as quasi-spherical or spherical nanoparticles with diameters typically below 10 nm (Sen; Bose, 2025; Shabbir; Csapó; Wojnicki, 2023). They usually exhibit a core–shell structure, in which the core consists predominantly of sp^2-hybridized carbon atoms arranged in graphitic or amorphous domains, while the shell is rich in surface functional groups such as carboxyl, hydroxyl, and amino moieties. These surface functionalities play a key role in determining the aqueous solubility, surface charge, and

biocompatibility of CDs (Barhoum et al., 2023). In particular, carboxyl groups generally confer a negative surface charge, whereas amino groups confer a positive charge, directly influencing colloidal stability and electrostatic interactions with other entities (Tavan et al., 2025; Xia et al., 2019). Moreover, surface functionalization with small organic molecules or polymers, as well as heteroatom doping (e.g., B, N, P, and S), are widely employed strategies to enhance the quantum yield, photoluminescence, and other physicochemical properties of CDs, while also improving water solubility and introducing new functionalities (Huang; Ren, 2025).

The optical properties of CDs are one of their most relevant characteristics, particularly their excitation-dependent emission behavior. Advances in synthetic strategies have enabled the development of CDs with high QY and unique features, including near-infrared (NIR) emission, chirality, and thermally activated delayed fluorescence (TADF) (Alafeef et al., 2024). Despite extensive investigation, the PL mechanism of CDs is not yet fully understood, which can contribute to the diversity of synthesis strategies and the inconsistent PL behaviors reported in the literature (Peng et al., 2017). Nevertheless, three main mechanisms have been proposed to explain the PL of CDs: (i) an intrinsic bandgap associated with quantum confinment effect (QCE) or conjugated π-domains, governed by the carbon core of the CDs; (ii) the formation of trap states, such as surface defects, within the bandgap induced by surface functionalization or heteroatom doping; and (iii) the presence of individual fluorescent molecular species (fluorophores) on the surface or embedded within the CDs (Jiang et al., 2019; Li et al., 2023b; Yi et al., 2022). According to these explanations, the broad and tunable emission of CDs is generally attributed to their wide size distribution, heterogeneous surface chemistry, and the lack of precise control during synthesis (Tavan et al., 2025).

A wide range of approaches has been developed to fabricate CDs with tailored properties, which are generally classified into top-down and bottom-up strategies. Top-down methods are based on the exfoliation and cutting of macroscopic carbon structures under relatively severe conditions, including techniques such as laser ablation, arc discharge, electrochemical exfoliation, and chemical oxidation (Banger et al., 2023; Mansuriya; Altintas, 2021). Top-down approaches generally require long processing times, harsh reaction conditions and expensive materials and equipment (Cui et al., 2021). In contrast, bottom-up approaches involve the formation of CDs through the carbonization of molecular precursors, enabling precise control over the composition and structure of the resulting CDs (Kar et al., 2024; Wang et al., 2025a) . Bottom-up synthesis techniques include hydrothermal or microwave treatment, ultrasonic assistance, pyrolysis, and acid-assisted reactions. This synthetic route also facilitates the production of CDs from renewable raw materials, including natural resources (Ge et al.,

2022), agricultural residues (Liang et al., 2022), and by-products of the food industry (Kim et al., 2021), which represent attractive carbon sources due to their wide availability, low cost, and consistency with the principles of green and sustainable development.

Figure 1 - (A) The absorption and PL emission spectra with increase longer excitation wavelengths of PPEI-EI CDs in aqueous solution (normalized spectra are shown in the inset); B) Aqueous solution of the PEG1500N-attached CDs (a) excited at 400 nm and photographed through band-pass filters of different wavelengths as indicated, and (b) excited at the indicated wavelengths and photographed directly

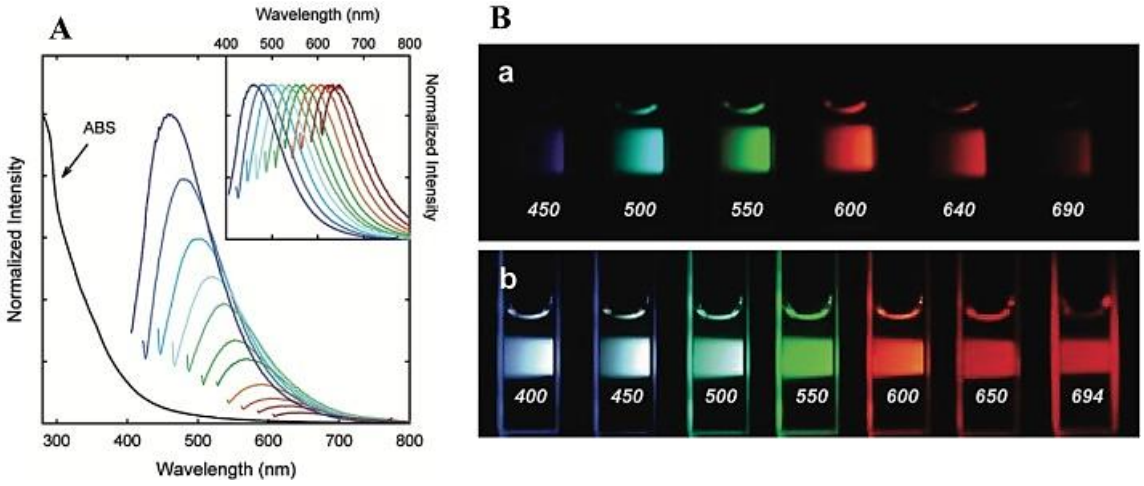

Source: Peng et al. (2017)

Owing to their unique optical properties and intrinsic biocompatibility, CDs have emerged as competitive alternatives to conventional quantum dots (QDs), which are often associated with toxicity and environmental concerns (Behi et al., 2022). In addition to their low toxicity, CDs exhibit excellent water solubility and high chemical and optical stability, particularly resistance to photobleaching, and can be synthesized through cost effective and environmentally friendly routes. The synergistic combination of these features makes CDs highly attractive for a wide range of applications, including bioimaging (Choppadandi et al., 2021; Khan et al., 2022; Kundu et al., 2018), photocatalysis (Mas et al., 2020; Morbiato et al., 2025; Peng et al., 2020), sensing (Siripothula et al., 2025; Yang et al., 2018; Zhang et al., 2019b), and optoelectronic devices (Li et al., 2025; Yan et al., 2021; Yuan et al., 2023).

2.1.1.1 Classification of CD

The family of nanomaterials referred to as CDs refers to a wide variety of carbon-based 0D nanostructures exhibiting intense photoluminescence. Establishing a clear definition for CDs remains challenging due to the structural diversity within this class of nanomaterials. Nevertheless, classification of CDs has been proposed in the literature, primarily based on

differences in core structure and surface composition. In addition, the origin of photoluminescence is considered a key criterion in distinguishing between different types of CDs (Innocenzi; Stagi, 2023). Accordingly, CDs are commonly classified into carbon nanodots (CNDs), carbon quantum dots (CQDs), carbonized polymer dots (CPDs), and graphene quantum dots (GQDs).

GQDs are small graphene fragments composed of single or a few layers of graphene, typically synthesized via top-down approaches from precursors, such as graphite powder, carbon rods, carbon fibers, carbon black or graphene oxide, among others (Innocenzi; Stagi, 2023; Liu; Li; Yang, 2020). They exhibit well-defined graphene lattices and abundant edge functional groups, which give rise to pronounced quantum confinement and edge effects. Morphologically, GQDs display disk-like or quasi-discoidal shapes with predominantly sp^2-hybridized carbon atoms and high crystallinity derived from the graphene lattice (Đorđević et al., 2022). Their thickness is generally governed by the number of graphene layers, typically not exceeding five layers (≈2.5 nm), while the lateral dimensions are usually below 20 nm (Xia et al., 2019). The photoluminescence of GQDs originates from a combination of quantum confinement effects and surface- or edge-related states associated with functional groups located at the graphene edges (Tian et al., 2018).

CQDs are typically described as quasi-spherical or spherical carbon nanomaterials composed of a graphitic crystalline core predominantly formed by sp^2-hybridized carbon atoms, surrounded by a carbonaceous surface rich in sp^3-hybridized domains containing oxygen- and nitrogen-containing functional groups (Rasal et al., 2025; Zhang et al., 2022b). The graphitic core exhibits crystallinity associated with both graphene-like lattice ordering and interlayer stacking, while the surface functional groups contribute to surface-state-related emission. QCE within the graphitic domains play a central role in governing the photoluminescence of CQDs, consequently, modulation of CQD dimensions provides a direct strategy for regulating emission wavelength (Đorđević et al., 2022; Xia et al., 2019). In contrast to graphene quantum dots (GQDs), which consist of single or a few graphene layers with lateral dimensions exceeding their thickness, the degree of exfoliation during synthesis is a critical factor in determining whether the resulting nanomaterial is classified as CQDs or GQDs (Liu; Li; Yang, 2020).

CNDs exhibit a high degree of carbonization and typically lack a well-defined crystalline lattice or distinct polymeric features. Their photoluminescence mainly arises from defect and surface-related states, as well as subdomain states within the graphitic core without size-dependent QCE (Xia et al., 2019). They usually display quasi-spherical morphology and

contain abundant surface functional groups such as hydroxyl, carboxyl, and amino that influence their optical behavior (Rasal et al., 2025).

CPDs are typically spherical or quasi-spherical nanoparticles with a well-defined core–shell structure. Their core consists of a partially carbonized and cross-linked polymer network, while the shell is constituted of abundant functional groups or polymer chains (Bartkowski et al., 2024; Tao et al., 2022). This structure endows CPDs with enhanced stability, improved compatibility, and easy surface modification and functionalization, thus improving their range of applications (Liu; Li; Yang, 2020). Unlike the photoluminescence mechanisms observed in GQDs and CQDs, the optical properties of CPDs mainly originate from molecular states associated with the chemical crosslinking or physical immobilization of polymer chains. This phenomenon, known as the crosslink-enhanced emission (CEE) effect, allows for a more controllable relationship between CPD structure and performance (Tao et al., 2020; Xia et al., 2019; Zheng et al., 2024).

The characteristics and the main differences between the members of CDs group are observed in Figure 2 and summarized in Table 1.

Figure 2 - Schematic illustration of differences between GQDs, CQDs, CNDs, and CPDs regarding their morphology, structure and quantum confinement effect

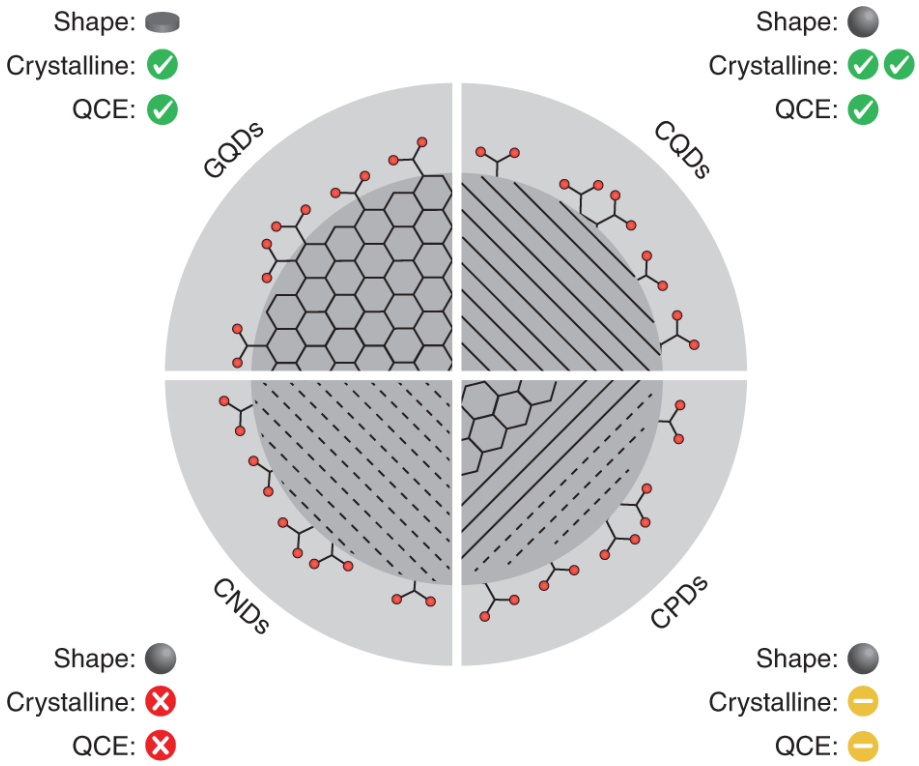

Source: Đorđević et al. (2022)

Table 1 – Classification of carbon dots based on their structure, hybridization, and PL mechanism

Type	Morphology	Hybridization	PL mechanism
GQDs	Discoidal-shaped graphene sheets	sp^2	QCE or conjugated π domains
CQDs	Quasi-spherical or spherical	sp^2	QCE or conjugated π domains
CNDs	Quasi-spherical or spherical	sp^2 or sp^3	Defect states
CPDs	Quasi-spherical or spherical	sp^3	Molecular states and crosslink-enhanced emission

Source: Adapted from Rasal et al. (2025)

2.1.2 Clay minerals

The term clay refers to sedimentary particles with diameters smaller than 2 μm and thicknesses below 10 nm. From a mineralogical perspective, clay minerals are hydrated aluminum phyllosilicates that may contain varying amounts of Fe, Mg, K (Dehmani et al., 2026). Chemically, clay particles consist of different types of hydrated aluminosilicates, exhibiting diverse compositions and crystalline arrangements. One defining property of clay minerals is their plastic behavior in the presence of water, which enables them to retain shape after the removal of applied stress, distinguishing them from other mineral materials (Balkanloo et al., 2022). Nevertheless, their most attractive attributes arise from their high specific surface area, low cost, natural abundance, favorable rheological behavior, and high ion-exchange capacity (Alcântara; Darder, 2018; Diab et al., 2026; Wang et al., 2024b).

Clay minerals are characterized by two main structural components: tetrahedral (T) and octahedral (O) sheets (Figure 3). Each tetrahedron has a central cation in the clay mineral structure, usually silicon (Si^{4+}), coordinated with four oxide anions (O^{2-}) at the vertices. Consequently, every tetrahedron possesses three basal O^{2-} groups and one apical O^{2-}group. The three-shared basal O^{2-} groups can interact with each other, leading to the polymerization of tetrahedra to form a tetrahedral sheet with variable dimensions (Mousa et al., 2018; Murray, 2006). The apical O^{2-} remains unshared and acts as the main point of connection with the octahedral sheet. Each octahedron has a central metal cation (M^{n+}), commonly the aluminum cation (Al^{3+}) or magnesium (Mg^{2+}), coordinated with six O^{2-} groups located at the vertices. Adjacent octahedra interact by sharing their edges (two O^{2-} or OH groups), forming an

octahedral sheet. If M^{n+} is a divalent cation, a trioctahedral or brucite-like sheet is produced, if it is a trivalent cation, such as Al^{3+}, two in every three octahedral sites are occupied, leaving a vacant site and the generation of a dioctahedral or gibbsite-like sheet. Moreover, the Si^{4+} of the tetrahedra and the Al^{3+} of the octahedra can be replaced by cations of lower valence and similar atomic radius. For example, Si^{4+} can be exchanged by Al^{3+}, and Al^{3+} can be replaced by Mg^{2+}, or ferrous cation (Fe^{2+}) (Peixoto et al., 2021).

Figure 3 - Structural units of phyllosilicates. Single tetrahedral with a central cation in yellow, usually Si^{4+}. Single octahedral with a central cation in red, usually Al^{3+}

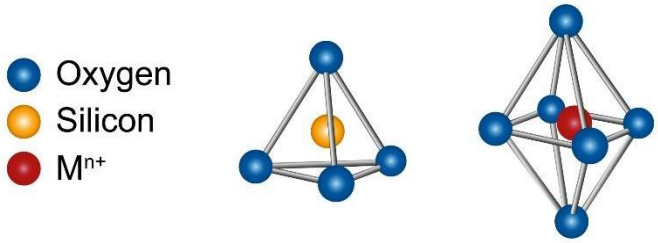

Source: The author (2025)

The tetrahedra and octahedra sheets can connect through electrostatic interactions, Van der Waals forces, interlayer cations, or through hydrogen bonding, forming crystalline structures with varied morphology. These layered structures can be classified into different categories, 1:1, 2:1, or 2:1:1, based on the arrangement of the sheets (Diab et al., 2026). The 1:1 (T:O) phyllosilicates group consists of a tetrahedral sheet stacked directly on an octahedral sheet. This arrangement creates a highly stable structure, due to the hydrogen bonds formed between the sheets. These clay minerals are electrically neutral, which means there are no counterbalancing cations present in the interlayer space. Consequently, these types of clay minerals are not hydrated and are considered nonswelling in nature. They possess a basal interlayer distance of 7 Å, and they represent the serpentine-kaolin group (Belghazdis; Hachem, 2022; Nomicisio et al., 2023).

In 2:1 (T:O:T) phyllosilicates, each structural layer is composed of an octahedral sheet sandwiched between two tetrahedral sheets. In opposition to 1:1 clay minerals, weaker interactions occur between the tetrahedral sheets of adjacent layers, and the interlayer space may contain counterbalancing cations if the structure has a negative charge or may not contain any counterbalancing cations if the structure is neutral. As a result, negatively charged structures can become hydrated, and therefore have the capability to swell. These layers present a thickness of approximately 10 Å, whereas the basal spacing can vary from 9 Å to 15 Å depending on the nature of the interlayer species (Figure 4) (Nomicisio et al., 2023).

Pyrophyllite and talc, representative members of this group, are characterized by the absence of isomorphous substitutions, which results in electrically neutral layers with low surface reactivity. In contrast, smectites and vermiculites exhibit partial isomorphous cation substitutions within the tetrahedral and/or octahedral sheets, generating permanent layer charges that strongly influence surface reactivity, cation exchange capacity, and swelling behavior (Tipa et al., 2022). The smectite group is mainly known for MMT and laponite (a synthetic hectorite), which are the most investigated among phyllosilicate regarding bioapplications. Vermiculites display relatively high layer charges (0.6–0.9 per unit structure), which restrict water penetration into the interlayer space, thereby limiting swelling, exfoliation, and overall reactivity. Nevertheless, these materials still present high specific surface areas (up to ~750 $m^2.g^{-1}$) and cation exchange capacities in the range of 120–200 meq/100 g (Diab et al., 2026).

Figure 4 - The structure of different groups of clay minerals

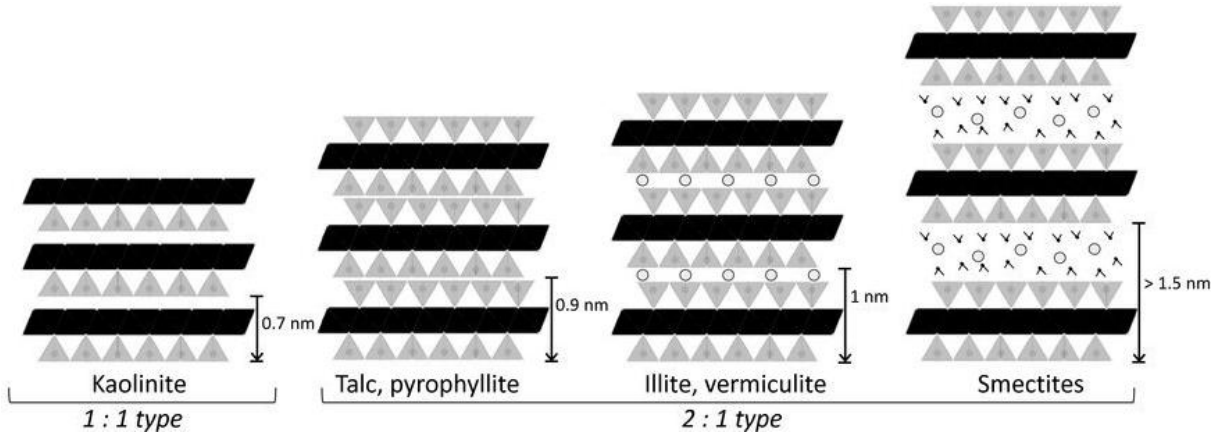

Source: *Dawson & Oreffo (2013)*

Similarly, illites exhibit even higher layer charges (0.8–1.0 per unit formula), which further suppress interlayer expansion, resulting in low swelling ability, reduced specific surface area (~30 $m^2.g^{-1}$), and low cation exchange capacity (10–40 meq/100 g) (Mousa et al., 2018; Wypych; De Freitas, 2022). Sepiolite and palygorskite are distinct members of this group due to their inverted 2:1 ribbons, which endow these clay minerals with fibrous morphology and high SSA. The 2:1:1 phyllosilicate group has an octahedral sheet continuous to a 2:1 layer, or this can also be referred to as an octahedral layer occupying the interlayer space, creating a basal space of around 14 Å. Chlorites are included in this group (Nomicisio et al., 2023). In addition to crystalline clay minerals discussed above, it is also possible to find non-crystalline

clay minerals, including allophane, imogolite and hisingerite (Lazorenko; Kasprzhitskii, 2025; Tipa et al., 2022).

2.1.2.1 Kaolin group

The kaolin group is characterized by a 1:1 layer structure, which inhibits interlayer expansion and, consequently, swelling behavior. Kaolinite is the most abundant mineral in this group and typically occurs as hexagonal platelets with particle sizes smaller than 2 μm (Awad et al., 2017). Each platelet consists of two sheets, an aluminum octahedral sheet (aluminol surface) and a silicon tetrahedral sheet (siloxane surface), stacked on top of one another (Figure 5). The siloxane surface exhibits a permanent negative charge, whereas the aluminol surface is positively charged, giving rise to a pronounced dipolar character (Peixoto et al., 2021). Kaolinite platelets are strongly held together through hydrogen bonding, leading to a rigid and non-expandable structure. In addition, the platelet edges exhibit pH-dependent surface charges due to the protonation and deprotonation of surface hydroxyl groups (Mousa et al., 2018). Considering that no isomorphous substitution takes place in the 1:1 layer kaolinite displays a low cation exchange capacity, typically in the range of 3–5 meq/100 g (Moraes et al., 2017). Its limited adsorption capacity is therefore attributed to both the low layer charge and the relatively small specific surface area, which was found to be 25 $m^2.g^{-1}$ (Zhang et al., 2017).

Figure 5 – (A) Schematic representation of kaolinite structure showing the tetrahedral and the octahedral sheet and (B) their SEM image (field of view 20 μm) made available by Mineralogical Society of the UK and Ireland[1]

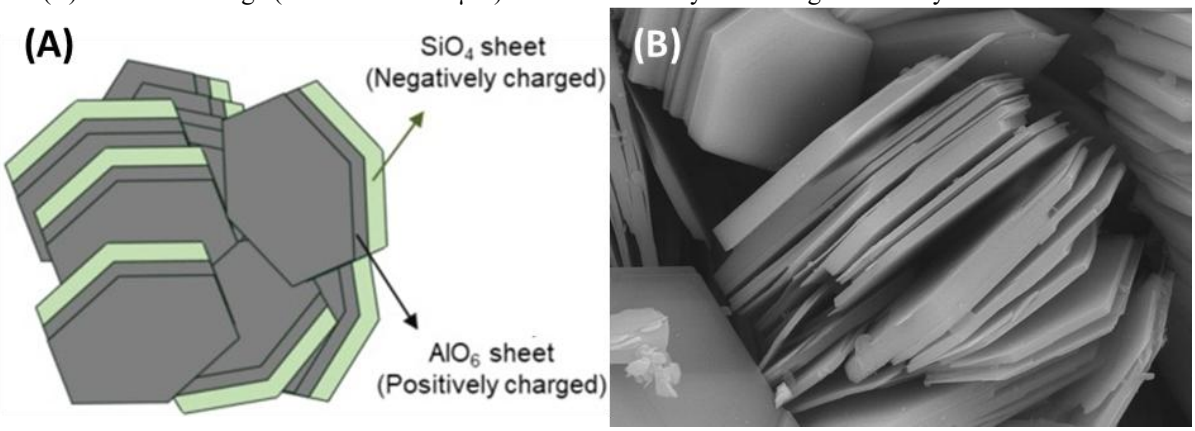

Source: Islam et al. (2025)

Another representative member of the kaolin group is halloysite, whose 1:1 sheet rolls up several times into nanotubes, that in opposition to kaolin give rise to high SSA (20 – 150

[1] Available in <https://www.minersoc.org/images-of-clay.html/nggallery/page/6>

$m^2.g^{-1}$) and total pore volume (0.063–0.869 cm^3g^{-1}) (Lazorenko; Kasprzhitskii, 2025). HNTs are typically 0.2 to 1.5 µm in length, while their outer and inner diameters are 40 to 70 nm and 10 to 30 nm, respectively. The wall is made up of 10-15 bilayers with a gap of approximately 0.72 nm (Goda et al., 2019; Yendluri et al., 2017). Another interesting feature is the presence of two different OH groups: those that are located between the layers and lumen surfaces, inner OH groups (aluminols), and those that are located on the surface, outer OH groups (silanols) (Peixoto et al., 2021). This provides different charges on the surfaces of the nanoparticles over a pH range of 2.5–8.5, which are positive on the inner surface thanks to the octahedral ($Al(OH)_3$) sheet and negative on the outer one for the presence of SiO_2 groups. However, in severely acidic circumstances, the outer surface of the halloysite becomes positively charged (Nomicisio et al., 2023).

Figure 6 - (A) HNTs morphology and chemical structure and (B, C) SEM images of HNTs[2]

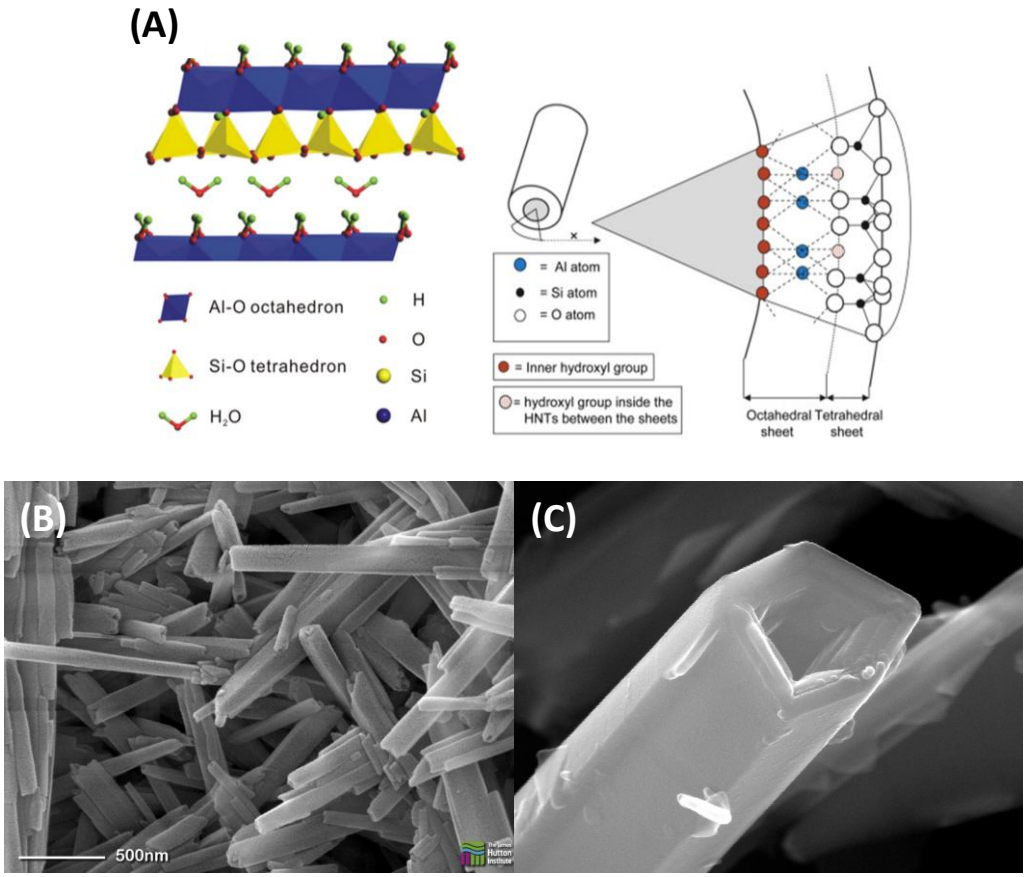

Source: Adapted fromMassaro et al. (2020)

The distinctive tubular morphology and surface chemistry of HNTs enable selective functionalization, allowing the encapsulation of a wide range of molecules, including both

[2] Available in <https://www.minersoc.org/images-of-clay.html/nggallery/page/4>

anionic and cationic compounds, as well as hydrophilic and hydrophobic molecules (Nath et al., 2022). Owing to the presence of negatively charged surface and a positively charged lumen in the HNTs structure, multiple interaction mechanisms can be established, encompassing electrostatic interactions, non-covalent forces, and covalent bonding (Nomicisio et al., 2023).

2.1.2.2 Smectite group

Smectites are a group of expandable 2:1 phyllosilicate composed of an octahedral sheet, (Al, Mg, or Fe), sandwiched between two tetrahedral silica sheets (TOT), which interact with each other by weak Van der Waals forces (Uddin et al., 2024). Permanent negative charges on the layer surfaces arise primarily from isomorphic substitutions within the tetrahedral and/or octahedral sheets and are compensated by exchangeable interlayer cations such as Na^{+}, K^{+}, Ca^{2+}, and Mg^{2+}, a feature that results in the high CEC characteristic of this clay family (Moraes et al., 2017a). The weak electrostatic bonding of interlayer cations enables the incorporation of water molecules and other polar species into the interlayer space, promoting swelling behavior and facilitating ion exchange. Consequently, smectites exhibit high adsorption capacities, which are closely related to their thin platelet morphology (Nawaz et al., 2022). At the nanoscale, smectite platelets present thicknesses of approximately 1 nm (single layer) and lateral dimensions typically ranging from tens to hundreds of nanometers, resulting in high aspect ratios and large surface areas. Morphologically, these minerals generally occur as flakes or spheroidal aggregates (Diab et al., 2026).

This group includes both dioctahedral and trioctahedral varieties, depending on the occupancy of the octahedral sites. Dioctahedral smectites, such as montmorillonite, beidellite, and nontronite, are more abundant in nature, whereas trioctahedral varieties include hectorite, saponite, and sauconite (Nawaz et al., 2022). Among these minerals, MMT remains the most extensively studied. In its structure, isomorphic substitution of Al^{3+} by Mg^{2+} in the octahedral sheet and of Si^{4+} by Al^{3+} in the tetrahedral sheet generates a permanent negative layer charge (-0.2 to -0.6 per celula unit), which is balanced by exchangeable cations, including Na^{+} and Ca^{2+}, located in the interlayer space (Hossain et al., 2023; Xie; Chen; Yang, 2023). MMT platelets typically exhibit a thickness of approximately 1 nm and much larger lateral dimensions, commonly ranging from 300 to 500 nm (Figure 7A-B), resulting in a high SSA (up to ~756 $m^2 g^{-1}$) (Kohay et al., 2017; Peixoto et al., 2021). These structural features provide a large number of interaction sites for guest species, particularly within the interlayer space, which can expand upon intercalation. The hydrophilic nature of the interlayer region confers excellent swelling

behavior in aqueous media (Chen; Grabowski; Goel, 2022). In addition, MMT exhibits favorable mechanical and thermal properties, including high thermal stability, elevated Young's modulus, and high mechanical strength (Nomicisio et al., 2023).

Figure 7 – (A) Structure of Na-MMT. The green sheet indicates a tetrahedral silica layer (T), the yellow sheet indicates an octahedral alumina layer (O), and the blue spheres represent sodium cations. (B) SEM images of MMT[3] (dioctahedral) and (C) saponite[4] (trioctahedral)

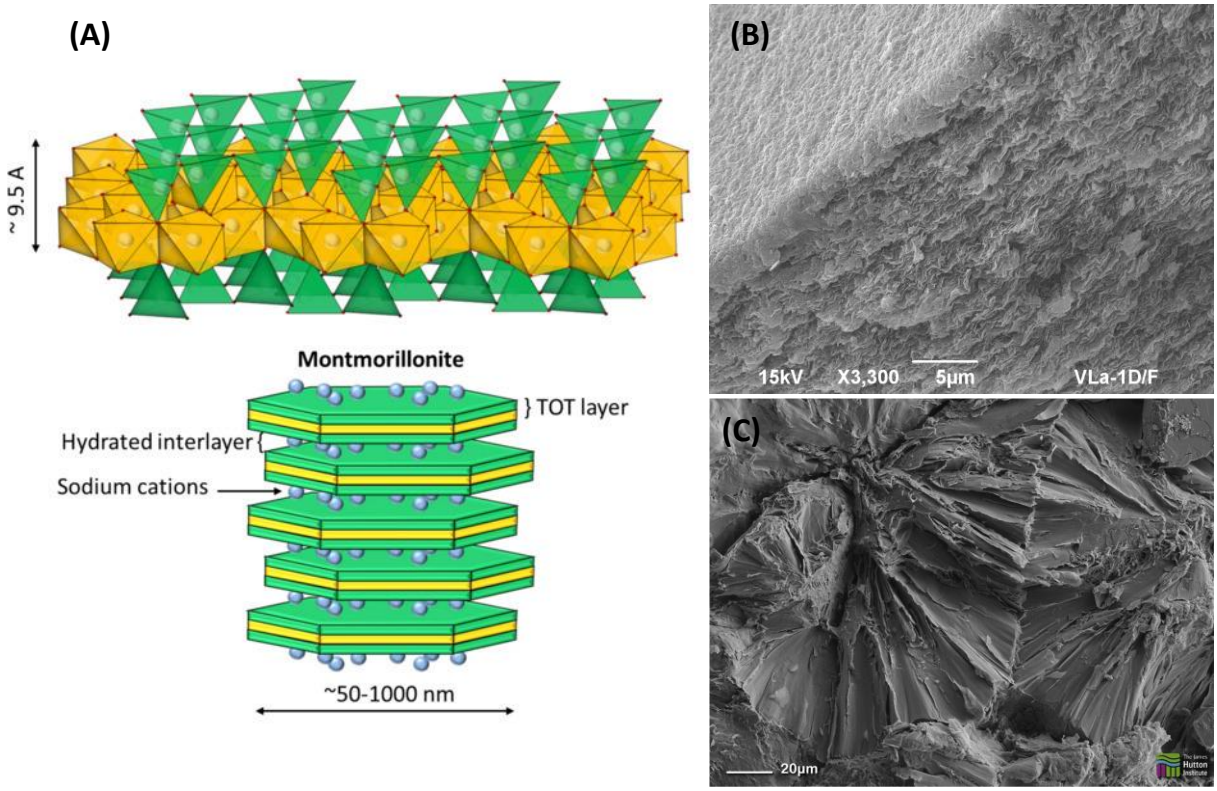

Source: Adapted from Nieto et al. (2022)

Bentonite is a commercial term referring to clay materials composed predominantly of MMT, with physicochemical properties mainly determined by the content and CEC of this clay mineral (Nones et al., 2015). Bentonite is commonly classified into sodium and calcium types, which differ mainly in their hydration and swelling characteristics (Moraes et al., 2017a). Structurally, it consists of irregularly stacked lamellar particles with small dimensions, resulting in a high specific surface area, while these fine platelets tend to aggregate into larger and thicker agglomerates due to interparticle interactions (Peixoto et al., 2021).

Beidellite also possesses a dioctahedral structure containing Al^{3+} as the central cation of the octahedral sheet, nevertheless, unlike MMT the layer charge distribution in beidellite originates primarily from isomorphic substitution of Si^{4+} for Al^{3+} in the tetrahedral sheet. Due

[3] Available at: <https://www.minersoc.org/images-of-clay.html/nggallery/page/10>
[4] Available at: <https://www.minersoc.org/wp-content/gallery/shimages/138-1359898_06.jpg>

to this substitution, beidellite often exhibits strong surface interactions, which can also affect its swelling properties (Dai et al., 2024). On the other hand, nontronite is a Fe-rich dioctahedral smectite endowed with redox-activity, where Fe(III) can be reduced to Fe(II) and subsequently oxidized back to Fe(III). This cycling of iron allows it to function as a significant electron acceptor and donor in environmental systems, mediating the degradation or transformation of various contaminants (Zhang; Tong; Yuan, 2021; Zhao et al., 2015).

In addition, saponite, sauconite, and hectorite are classified as trioctahedral smectites, in which the octahedral sheet is mainly occupied by divalent cations. In saponite (Figure 7C), Mg^{2+} is the dominant octahedral cation, and the layer charge primarily arises from Al^{3+} for Si^{4+} substitutions in the tetrahedral sheets (Franco et al., 2024; Madejová; Gates; Petit, 2017). In contrast, sauconite is characterized by the predominance of Zn^{2+} in the octahedral sheet. Hectorite exhibits partial substitution of Li^{+} for Mg^{2+} within the octahedral layer. This structural feature contributes to its high swelling and delamination capacity in aqueous media, leading to exceptional rheological properties (Dai et al., 2024; Zhang et al., 2019a).

2.2.2.1 Sepiolite and palygorskite group

Sepiolite (ideal formula: $Mg_4Si_6O_{15}(OH)_2{\cdot}6H_2O$ and palygorskite (ideal formula: $Si_8Mg_5O_{20}(OH)_2(OH_2)_4.4H_2O$) are natural non-planar phyllosilicates with a 1D nanofibrous morphology (Nomicisio et al., 2023). They exhibit a typical 2:1 ribbon structure in which the apical O^{2-} groups of the tetrahedral sheets are inverted, leading to discontinuities in the octahedral sheet. This inversion occurs every six atoms of Si for SEP and every four atoms of Si for PAL, enabling the formation of parallel structural tunnels, along the fiber axis (Rebitski et al., 2018). Additionally, the discontinuous octahedral sheet results in regularly distributed silanol groups (Si–OH) on the external surface of the fibers. Owing to this unique structural arrangement, SEP and PAL occurs in the shape of flexible elongated needles, with a high surface area, generally with values of 150 m^2/g and 300 m^2/g, respectively (Zhuang et al., 2024). This confers outstanding adsorption capacity; however, when compared to smectite clays, SEP and PAL exhibit a lower cation exchange capacity (CEC) (Moraes et al., 2017b; Peixoto et al., 2021).

Palygorskyte, also known as attapulgite, and sepiolite share a similar crystal architecture, differing mainly in channel dimensions. The channels in sepiolite are slightly wider (10.6 Å ×3.7 Å) than those in palygorskyte (6.4 Å × 3.7 Å) (Álvarez et al., 2011). Although both minerals display fibrous morphology, samples from different geological deposits

may show significant variations in fiber length, width, thickness, and aggregation state. Typically, SEP and PAL fibers present lengths ranging from 0.2 to 2 μm, widths of 10–30 nm, and thicknesses of 5–10 nm (Álvarez et al., 2011; Zhuang et al., 2024). The high density of surface silanol groups (–SiOH), mainly located at the edges of the structural blocks, explains the pronounced hydrophilicity of these fibrous clays. Combined with their natural channel structure, high surface area, and rich surface silanol group, these features endow SEP and PAL with a strong ability to adsorb a wide variety of compounds, making them highly effective in numerous applications (Alcântara et al., 2023; Cao et al., 2022).

Figure 8 -The schematic illustration of (A) fibrous clay and (B) SEM images of palygorskite[5]

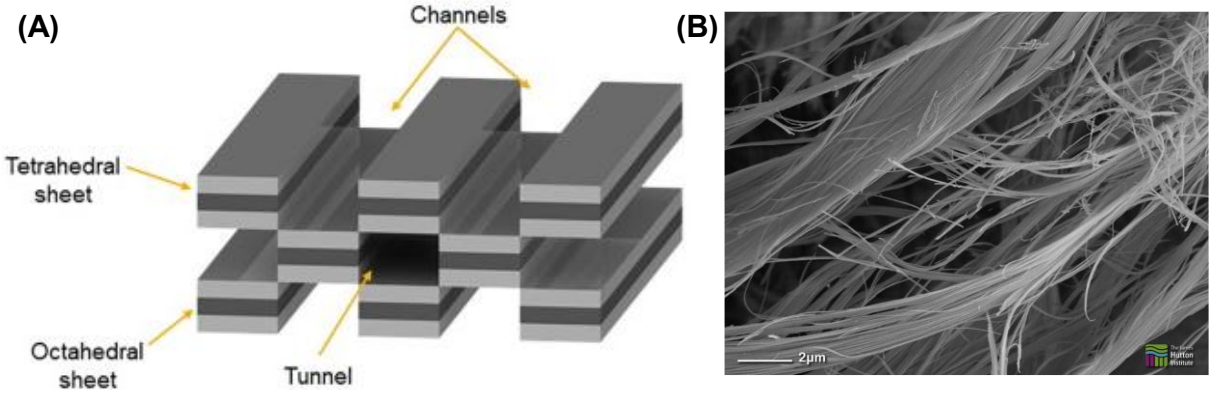

Source: Adapted from Peixoto et al. (2021)

2.2 FABRICATION OF CLAY-CARBON DOTS HYBRID NANOMATERIALS

This section reviews the main strategies reported for the fabrication of hybrid nanomaterials based on natural clay minerals and CDs, including both the incorporation of pre-synthesized CDs and their *in situ* generation on clay surfaces, with emphasis on the distinct characteristics and interaction mechanisms governing the assembly of these components.

2.2.1 Previously prepared CD

The fabrication of clay–CD hybrid nanomaterials using pre-synthesized CDs is a simple strategy that can be achieved through self-assembly in aqueous dispersions of clay minerals and CDs or by employing solid-state methods without the use of solvents. Zhai et al. (2019)reported the preparation of g-CDs@MMT materials in which g-CDs synthesized from citric acid (CA)

[5] Available in: <https://www.minersoc.org/images-of-clay.html>

and urea (U) were first dispersed in water and subsequently added to an aqueous suspension of MMT under continuous stirring for 30 min. XRD analysis showed no significant shift in the basal (001) reflection of MMT after material formation, indicating that the g-CDs are predominantly adsorbed on external surfaces and edge sites rather than intercalated in the interlayer space of MMT. Electrostatic attraction between g-CDs and MMT was inferred from the opposite zeta potentials of the counterparts, although the value for the final g-CDs@MMT material was not reported. In addition, XPS measurements revealed a shift of the Al 2p peak toward lower binding energy in the material compared to pristine MMT, indicating coordination interactions between surface g-CDs and the clay structure. In detail, the authors assume that the carboxyl/hydroxyl groups in g-CDs could provide Al with electrons, which increase the electron cloud density of Al, resulting in a decreased Al binding energy. The resulting g-CDs@MMT material also exhibited excellent photostability, retaining approximately 98% of its emission intensity after 60 min of UV irradiation. (Yu; Yan, 2017) also obtained a material based on montmorillonite (PGV) and carbon dots, named as C-dots@PGV, using a similar strategy by adding 1.0 mL of a C-dots solution to 0.25 g of PGV powder. The authors suggest that the C-dots are adsorbed onto the external surface of the PGV and intercalated in its interlayer space. However, this interpretation is not supported by the XRD data that does not indicate a basal spacing shift.

In the work developed by Mehdi et al. (2018), multifunctional halloysite nanotubes (HNTs-g-PEG-CDs) were prepared through a multistep surface modification process. Initially, the nanotubes were functionalized with aminopropyl groups and converted into carboxyl groups using succinic anhydride, which enabled the covalent grafting of six-arm poly(ethylene glycol)-amine (PEG-NH_2) through EDC/NHS chemistry. Separately, nitrogen-doped CDs were synthesized hydrothermally from citric acid and ethylenediamine (EDA), producing highly fluorescent nanoparticles with excitation and emission maxima at 340 and 440 nm, respectively. These pre-formed CDs were then covalently linked to the free amine terminals of the PEG branches on the nanotubes through carbodiimide-mediated coupling. In this reaction, EDC and NHS activated the carboxyl groups of the CDs, allowing the formation of stable amide bonds with PEG-NH_2.

Massaro et al. (2024) also used a previous step in which HNTs were functionalized with 3-aminopropyltriethoxysilane (APTES) to obtain HNTs-NH_2 and with 3-methacryloxypropyltrimethoxysilane followed by itaconic acid grafting to obtain HNTs-COOH. In parallel, N-doped CDs were synthesized by reacting itaconic acid with EDA using microwave irradiation and purified by gel filtration chromatography. Covalent attachment of

CDs to the functionalized HNTs was achieved using EDC to promote amide bond formation, yielding HNTs-NCDs1 and HNTs-NCDs2. TGA analysis indicated organic loadings of 5.8 wt% for HNTs-NCDs1 and 3.2 wt% for HNTs-NCDs2. Dynamic light scattering revealed hydrodynamic diameters of 380 ± 37 nm for HNTs-NCDs1 and 422 ± 46 nm for HNTs-NCDs2. In contrast, pristine N-doped CDs dispersed in water exhibited a hydrodynamic diameter of 749 ± 39 nm, attributed to aggregation of CDs. The smaller diameters of the hybrid materials compared to free CDs indicate that anchoring onto HNTs reduces CDs aggregation. However, TEM images showed the formation of large nanotube aggregates, possible due to the formation of links between HNTs through CDs during amide bond formation. Fluorescence QY decreased to 3% for both HNTs-NCDs1 and HNTs-NCDs2, compared to 26% for N-doped CDs. This reduction indicates that the covalent coupling process affected the emissive surface states of the carbon dots. Potentiometric titration showed the loss of free carboxylic and amine groups after condensation, suggesting that functional groups involved in radiative recombination were consumed during amide bond formation. These results indicate that the CDs coupling affected surface functionality and emission efficiency.

2.2.2 *In situ* carbon dots formation

In this approach, carbon precursors are carbonized in the presence of the clay mineral support, promoting the formation of surface-anchored CDs. This strategy avoids post-synthetic mixing steps and enhances surface contact between components. Uchida et al. (2022) reported one-step solvent-free synthesis of CD-based layered composites with tunable photoluminescence. The materials were obtained by heating mixtures of phloroglucinol and saponite, with or without an additional precursor, at 200 °C for 3 hours under nitrogen flow. Phloroglucinol alone produced CDs with greenish-blue emission around 525 nm, while the introduction of resorcinol (P-CD) led to a blue-shifted emission near 500 nm, boric acid (PB-CD) induced a yellow-green emission at about 535 nm, and phosphorus pentoxide (PP-CD) produced orange emission centered at 585 nm, confirming the strong effect of precursor chemistry on photoluminescence properties. In addition, the XRD analysis revealed an expansion of the basal spacing of saponite from ~10.5 Å to ~14.6 Å after thermal treatment, indicating that the CDs were formed in the interlayer space of saponite. X-ray photoelectron spectroscopy (XPS) results indicate that condensation of phloroglucinol for the formation of P-CD was affected by saponite to give more C-C bonds in the chemical structures, confirming

that the confinement of the precursor in the interlayer space of saponite may result in the formation of larger π-conjugated structures.

Halloysite–carbon dot hybrid nanomaterials were prepared through a bottom-up approach based on the *in situ* formation of N-doped CDs (NCDs) using different amine passivation agents. The synthesis involved three main steps: first, HNTs were functionalized with 3-methacryloxypropyltrimethoxysilane, reaching a functionalization degree of 3.5 wt%; second, itaconic acid was covalently linked via an AIBN-catalyzed reaction, yielding a carboxylated precursor with a loading of 4.8 wt%; finally, microwave-assisted pyrolysis at 240 °C for 3 min in water promoted the formation of NCDs directly anchored to the HNTs surface (HNTs-NCDs). EDA, spermine, and hexamethylenediamine acted as passivating agents, producing HNTs-NCDsa, HNTs-NCDsb, and HNTs-NCDsc, respectively. Microscopy images (HAADF-STEM) confirmed that the tubular morphology of HNTs was preserved after pyrolysis and EDX mapping confirmed that NCDs were homogeneously distributed on the HNTs surface. The synthetic route preserved the surface functionality of the NCDs, as indicated by the fluorescence QY of HNTs-NCDsa (24%), which is comparable to that of pristine NCDs (26%), and by the coexistence of carboxylic and amine groups detected by potentiometric titration. The optical band gap decreased to 3.9 eV for HNTs-NCDsa, compared to 5.8 eV in pure NCDs, which could indicate the presence of richer surface-related electronic states, contribution for the application of the work in Fe^{3+} sensing (Massaro et al., 2024).

Figure 9 - Schematic representation of the synthesis of HNTs-NCDs$_{a-c}$ nanomaterials. The inset shows the organic portion loaded onto the HNTs' surface after each synthetic step, estimated by TGA

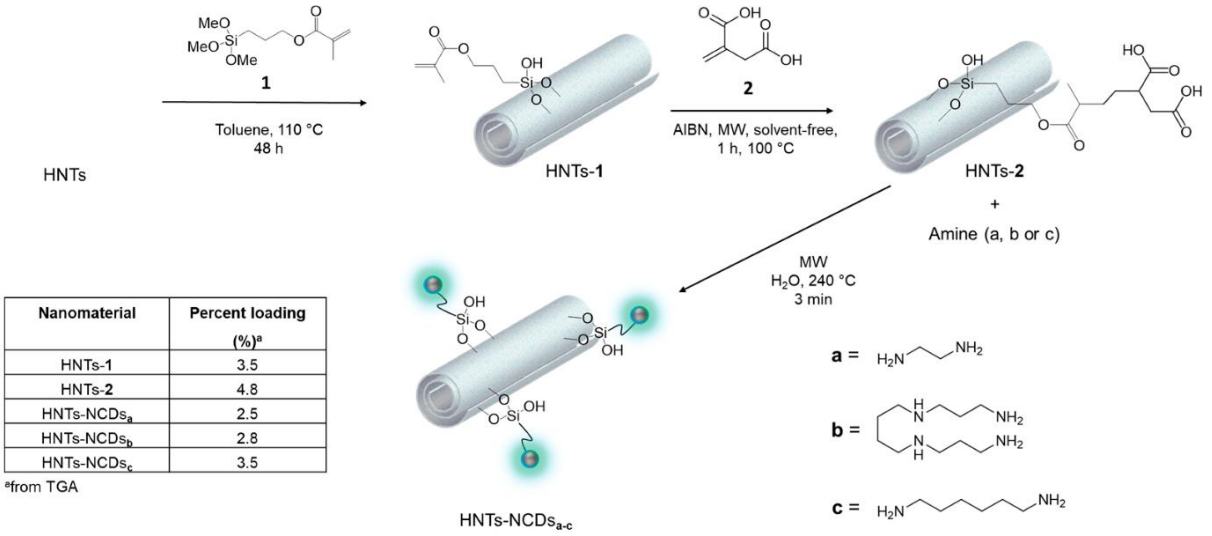

Nanomaterial	Percent loading (%)[a]
HNTs-**1**	3.5
HNTs-**2**	4.8
HNTs-NCDs$_a$	2.5
HNTs-NCDs$_b$	2.8
HNTs-NCDs$_c$	3.5

[a]from TGA

Source: Massaro et al. (2024)

The study developed by Jia et al. (2021) describes the preparation of a material based on attapulgite (Atta), CDs, and Eu^{3+}, obtained through a multistep strategy, involving silane grafting, polymer anchoring, and hydrothermal carbonization. Atta is first acid-activated and functionalized with 3-chloropropyltrimethoxysilane (CPTEOS), enabling the covalent grafting of polyethyleneimine (PEI) in the clay surface. PEI provides amine-rich sites that act both as anchoring points and as nitrogen source for the following CDs formation. CDs are then generated by *in situ* hydrothermal carbonization of CA in the presence of PEI-modified Atta at 160 °C for 12 h, resulting in uniformly dispersed nanoparticles with an average size of approximately 3 nm, as revealed by TEM images. In the final step, Eu^{3+} ions are coordinated to carboxyl groups on the CDs, forming the Atta-CDs-Eu material. FT-IR spectra show the appearance of C=O and C–O stretching bands at 1650 cm^{-1} and 1410 cm^{-1} after hydrothermal treatment, confirming the formation of carboxyl-rich CDs on the Atta surface. XRD patterns indicate that the characteristic reflections of the clay remain unchanged after modification, while a broad plane reflection at $2\theta = 21°$ is assigned to amorphous carbon, evidencing CD formation without structural disruption of the Atta. In addition, the authors affirm that CDs contribute to the optical stability of the material as both CD and Eu^{3+} emissions are preserved.

2.3 APPLICATION OF CLAY MINERALS-CARBON DOTS HYBRID NANOMATERIALS

2.3.1 Adsorption

Jlassi et al. (2023) study bentonite-carbon dots (B-CDs) nanohybrid for removing Pb^{2+} ions from aqueous solution under dark and light conditions. The B-CDs showed outstanding performance for Pb^{2+} removal from aqueous solution. At pH 8 and room temperature, the hybrid reached 95% removal within 10 min under light irradiation, while only 70% was achieved in the dark. In comparison, pure bentonite removed about 81% under the same light conditions. The improvement is attributed to the nitrogen and sulfur doped CDs, which introduce functional groups such as –COOH, –OH, and –NH, enabling strong complexation with Pb(II) ions. These groups also enhance light absorption and charge separation, increasing the number of active sites available for adsorption. The process followed a pseudo-second-order kinetic model and fitted the Langmuir isotherm, indicating monolayer chemisorption. Moreover, the (Na + K)/(Si + Al) atomic ratios using XPS data were 0.075, 0.048, and 0.038 for bentonite, B-CDs and B-CD-Pb, respectively, indicating partial substitution of Na^+ and K^+ by CDs and Pb(II) in the bentonite layer.

A magnetic nanomaterial based on HNTs, nickel ferrite, and GQDs ($NiFe_2O_4$/HNTs/GQDs) was also employed for the removal of Pb^{2+} ions from aqueous solutions. GQDs were covalently immobilized onto the APTES-modified $NiFe_2O_4$/HNTs surface through amide bond formation. The carboxylic groups present on the GQDs readily react with the $–NH_2$ groups of APTES, resulting in the attachment of GQDs to the external surface of the $NiFe_2O_4$/HNTs. Adsorption experiments demonstrated a high Pb^{2+} removal efficiency, reaching up to 97.14% under optimized conditions (pH ≈ 5.96, contact time of 54 min, adsorbent dose of 0.36 g, and initial Pb^{2+} concentration of ≈ 91 $mg \cdot L^{-1}$). According to the Langmuir model, the maximum adsorption capacity was 42.02 $mg \cdot g^{-1}$ at 298 K, indicating monolayer adsorption on homogeneous sites. Kinetic data followed a pseudo-second-order model (R^2 = 0.999), and thermodynamic analysis revealed that the adsorption process was spontaneous and endothermic, with an activation energy of 48.23 $kJ \cdot mol^{-1}$, characteristic of chemisorption. The authors propose that Pb^{2+} adsorption occurs through the formation of mono- and bidentate surface complexes (Figure 10) involving carboxylate ($–COO^-$) and hydroxyl groups (-OH) on the external surface of the $NiFe_2O_4$/HNTs/GQDs. In addition, the magnetic core allows straightforward recovery of the adsorbent from aqueous media (Pirhaji et al., 2020).

Figure 10 - Proposed adsorption mechanism of Pb(II) ions onto $NiFe_2O_4$/HNTs/GQDs

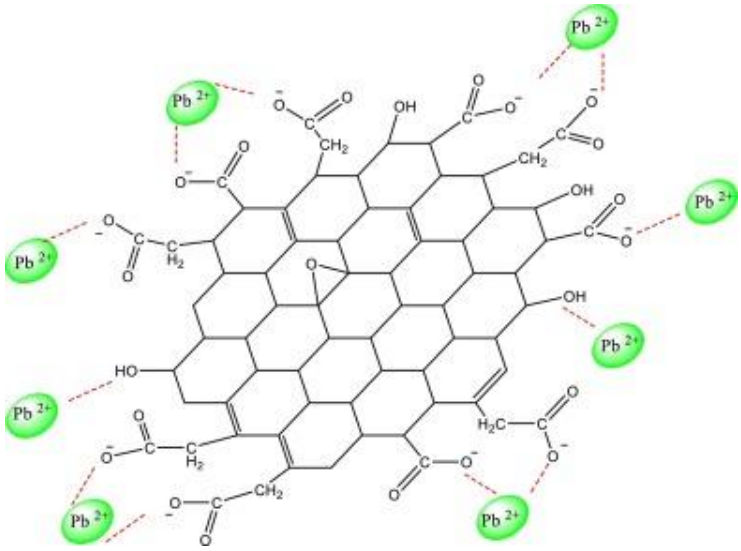

Source: Pirhaji et al. (2020)

2.3.2 Drug delivery

Hybrid nanocarriers based on clay minerals and CDs have emerged as versatile platforms for drug delivery, as they combine the structural stability and adsorption capacity of

clays with the surface functionality introduced by carbon-based nanomaterials. The study developed by Rahmani et al. (2022) presents a pH-responsive chitosan-montmorillonite-nitrogen-doped carbon quantum dots (CS-MMT-NCQDs) nanocomposite for doxorubicin (DOX) delivery (Figure 11), addressing the limitations of DOX, such as its low solubility and short circulation time. The CS-MMT-NCQDs nanocomposite demonstrated enhanced loading and entrapment efficiencies, achieving a sustained release of DOX over 96 hours, particularly at pH 5.4, simulating tumor conditions. The release kinetics were analyzed using Korsmeyer-Peppas and other models, indicating controlled release at acidic pH. Cytotoxicity assays on MCF-7 breast cancer cells revealed that CS-MMT-NCQDs-DOX exhibited superior cytotoxic effects compared to free DOX and CS-MMT-DOX, with significant reductions in cell viability. Incorporating NCQDs improved drug release and cellular uptake, highlighting the potential of CS-MMT-NCQDs as an effective drug delivery system for cancer therapy.

Figure 11 - Schematic representation of cross-linked CS-MMT-NCQDs-DOX hydrogel nanocomposite

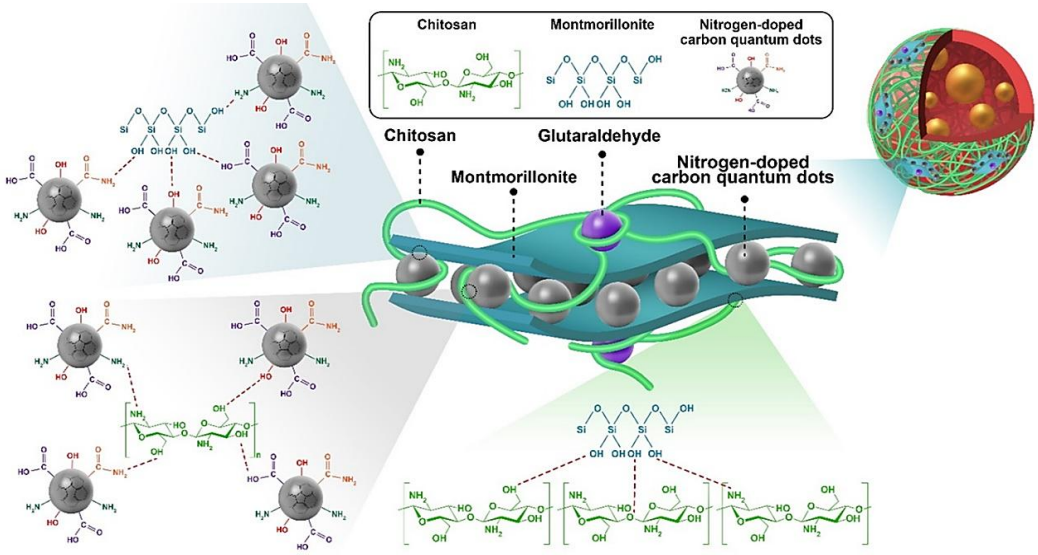

Source: Rahmani et al. (2022)

The HNTs-g-PEG-CDs nanoparticles reported previously (section 2.2) were decorated with biotin for quercetin loading and controlled release. Biotin was chosen to active targeting of tumor cells, while quercetin, a natural flavonoid with recognized antioxidant and anticancer activity, was used as the model drug. The modified HNTs showed a quercetin loading capacity of 278.36 mg g^{-1}, much higher than pristine HNTs, due to the strong π–π and hydrogen bonding interactions between quercetin and PEG chains. Drug release was sustained and pH-dependent: only 44.2% of quercetin was released at pH 7.4 after seven days, while 67.9% and 75.4% were released at pH 6.8 and 5.0, respectively. This pH sensitivity is related to the dissociation of

hydrogen bonds in acidic conditions, which favors faster release inside tumor environments. Cytotoxicity assays demonstrated low toxicity of the HNTs-g-PEG-Biotin nanocarrier toward HeLa cell line (>80% cell viability). Free quercetin exhibited at higher concentration (100 $\mu g.mL^{-1}$) cell viability of 34.52%, while HNT-g-PEG-CDs-Biotin-Que showed a viability of approximately 17%, confirming enhanced therapeutic potential for targeted cancer treatment. Despite the improved cytotoxicity, the effect of CDs was not clear, once the capability of HNT-g-PEG-CDs-Biotin to induce death of cancer cells was not evaluated (Mehdi et al., 2018).

Beyond the drug delivery scope, Massaro et al. (2019) developed a multifunctional HNT–CDs hybrid system designed as a non-viral nanocarrier for oral gene delivery. The association with DNA is driven by electrostatic interactions between the negatively charged phosphate backbone of DNA and the positively charged amino groups introduced on the surface of the carbon dots. As a result, the HNT–CDs system achieved a DNA loading capacity of approximately 6 wt%, while circular dichroism analysis confirmed that the DNA secondary structure was preserved upon adsorption. Release studies revealed a pH-dependent behavior, with strong DNA retention under acidic conditions (pH 1.0) and a more sustained release at physiological pH (7.4), highlighting the ability of the hybrid carrier to protect genetic material during gastrointestinal transit. Overall, these results demonstrate that the HNT–CDs hybrid enables controlled, environment-responsive DNA release, reinforcing its potential as a clay-based non-viral carrier for gene delivery applications.

2.3.3 Active packaging

Active food packaging aims to extend shelf life in order to preserve food quality and meet the increasing food demand (Sul; Ezati; Rhim, 2023). Biopolymers such as alginate, chitosan, and hydroxypropyl cellulose can be used as polymeric matrices, into which clay-CDs materials are incorporated for food packaging applications. These hybrid materials are attractive for this purpose because they combine the barrier effect and loading capacity of clays with the optical properties and antioxidant properties of CDs (Saadat; Rawtani; Rao, 2022). In this context, physical protection can be associated with functions such as UV shielding, moisture control, and antioxidant or antimicrobial activity.

Cinà et al. (2024) produced HNTs-CDs hybrids by covalently anchoring CDs precursors on the external surface of HNT and converting them by microwave assisted synthesis. Pure alginate films showed a UV transmittance at 300 nm of 68%, while this value decrease to 41%

with HNT and to 28% with HNTs-CDs, indicating that UV shielding is mainly associated with the presence of CDs. This effect is also observed in the mechanical behavior after UV exposure, since pure Alg and Alg/HNT show reductions in stress at break of about 28% and 21%, respectively, whereas alginate containing HNTs-CDs maintains unchanged mechanical strength. Water vapor permeability followed the same trend, where the values decreased from $.53 \times 10^{-8}$ g $m^{-1}s^{-1}Pa^{-1}$ for alginate to 0.95×10^{-8} for the HNT-CDs film, which can be related with to the formation of tortuous diffusion pathways due to the tubular structure of HNT. The lumen of the HNTs-CDs was used to load a natural extract, which was then incorporated into alginate films. In addition, only the HNT-CDs containing films show antioxidant activity, with about 25% DPPH inhibition after 96 hours, confirming that the hybrid filler transforms alginate from a passive barrier into an active functional material. Apple and banana slices coated with the resulting film were stored for 7 days at room temperature and 60% of relative humidity. Uncoated fruits showed marked browning, and uncoated apples also exhibited visible microbial degradation after storage. In contrast, coated fruits retained their visual appearance over the same period, with no evident browning or microbial growth.

Gao et al. (2024) presented a chitosan-based composite film developed for active food packaging by incorporating attapulgite clay and honeysuckle extract containing natural CDs (HEAC). Pure chitosan exhibits limited antibacterial performance, whereas HEAC films reach antibacterial inhibit of 99.27 ± 0.18% against *E. coli* and 98.85 ± 0.65% against *S. aureus*. This enhancement is attributed to the combined effect of CDs and bioactive compounds immobilized on the clay surface, together with the physical interaction between attapulgite and bacterial cell walls. Regarding antioxidant properties, pure chitosan films present a hydroxyl radical scavenging efficiency of 40.96%, while HEAC films reach up to 95.46%, indicating a stronger ability to retard oxidative process in food. In addition, mechanical properties benefit from the hybrid filler as well. The tensile strength of pure chitosan films is 13.0 ± 0.79 MPa and the elongation at break is 38.6%, whereas HEAC films containing 4.76 wt% filler reach 24.9 ± 2.35 MPa and 64.8 ± 2.11%, respectively. HEAC films also reduce UV transmittance below 400 nm compared with chitosan, while remaining transparent in the visible region. Strawberry preservation tests were carried out at 25 °C using both dip-coated fruits and free-standing films. Uncoated strawberries and those coated with pure chitosan showed visible decay after 2 days of storage. In contrast, strawberries coated with HEAC films remained visually fresh for up to 3 days, with no evident mold growth or severe shrinkage at higher HEAC contents. Similar behavior was observed for strawberries packaged with HEAC films, confirming that the hybrid system effectively delays microbial and oxidative degradation.

2.3.4 Other applications

Chuaicham et al. (2022) obtained a material based on BiOBr, carbon quantum dots, and saponite (CQDs/Clay@BiOBr) for the photocatalytic degradation of ciprofloxacin (CIP) under visible light. The selection of saponite in this work was due to its high purity, which had no effect on the optical properties of CQD. CQDs/Clay materials were prepared using different methodologies: one was prepared through in situ pyrolysis, and the other through a physical mixing process. The results indicated that the material CQDs/Clay@BiOBr exhibited higher photocatalytic performance compared to pure BiOBr, probably caused by a reduction in the recombination of photogenerated charges, facilitated by electron transfer from BiOBr to clay. This fact is supported by the observed decrease in electron accumulation density in the Energy-resolved distribution of electron (ERDT) trap patterns for Clay@BiOBr. In addition, the authors show that the samples containing CQD significantly enhanced their photocatalytic performance, achieving approximately 95% efficiency with CQDs/Clay (IS)@BiOBr-50 within 5 minutes of the reaction. However, the excess amount of the CQDs in CQDs/Clay (IS)@BiOBr-100 decreases the CIP degradation efficiency. This indicates that the excessive loading of CQDs on the BiOBr surface inhibits light adsorption and acts as a recombination center for electrons, which results in reduced production of photogenerated charge carriers for the degradation reaction.

Massaro et al. (2019) obtained a hybrid nanomaterial based on halloysite and carbon dots (HNT-CDs) using a one-step microwave-assisted pyrolysis of tartaric acid and ethylene diamine as a synthetic route. The HNT-CDs hybrid was explored as a non-viral vector for oral gene therapy and cellular imaging due to the photoluminescence properties of the HNT-CDs. The fluorescence microscopy analysis was carried out using the HeLa cell line, where HNT-CDs primarily accumulate in the perinuclear and cytoplasmic regions of the cells, with weak fluorescence in the nuclei. In comparison, CDs can also be localized mainly in cytoplasm and nuclei (Figure 12). Moreover, flow cytometry results revealed that HNT-CDs entered HeLa cells significantly after just 30 minutes, showing positive events of 77% and 78% in the FL1-H and FL2-H channels, respectively. This contrasts with previous findings on HNT uptake, which typically required 24 hours. The improved uptake is likely due to primary amino groups on the HNT-CDs surface enhancing interaction with the cell membrane. After 24 hours, fluorescence intensity slightly increased, confirming that most HNT-CDs penetrate the cellular membrane within the first 30 minutes. These results indicated that the association of halloysite

nanotubes with carbon dots enhances cellular uptake, which could be attributed to the presence of primary amino groups on the HNT-CDs surface, endowing the nanomaterial with uptake by improving the interaction with the cell membrane.

Figure 12 - Fluorescence microscopy images of (a) HeLa cells; (b) HeLa cells treated with HNT-CDs (10 μg mL^{-1}) and (c,d) HeLa cells treated with CDs (50 μg mL^{-1}) at 20x (c) and 40x (d) of magnification, respectively

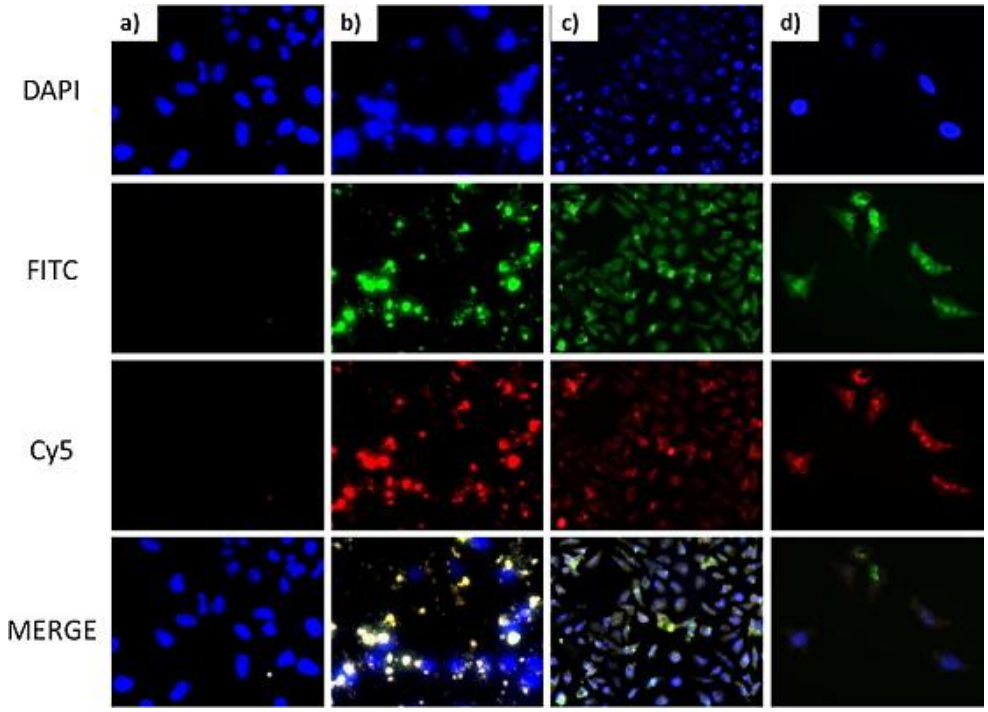

Source: Massaro et al. (2019)

In the study developed by Ma et al. (2023), MMT was decorated with modified GQD to improve fire retardancy of polystyrene (PS). The incorporation of GQDs produced nanohybrids (CG@MMT) that showed not only better distribution in the polymer matrix but also strong interfacial interactions. SEM and TEM images revealed that neat MMT tends to form agglomerates in the PS matrix. However, CG@MMT appears to be more separated as a flake like-platelets dispersed in the PS phase. Thermogravimetric analyses up to 700 °C revealed that PS/CG@MMT nanomaterial exhibited a residue of 3.3 wt%, while neat PS exhibit a residue of 0.7%, representing a significant enhancement in the nanocomposite thermal stability. To evaluate pyrolysis and flammability performances, a microscale combustion calorimeter (MCC) was used. When 5% of MMT was introduced into the PS matrix it was observed a reduced of 20% in the peak heat release rate (pHRR). After the incorporation of nanohybrids, the resulting PS/CG@MMT exhibits a much greater reduction in pHRR (36%) and delayed the maximum heat release temperature by approximately 25 ºC. This improvement was mainly

attributed to the synergistic barrier effect of exfoliated MMT layers and the thermally stable, graphitic structure of GQDs, which promoted the formation of a continuous, compact carbonaceous layer during combustion, effectively reducing heat and gas diffusion (Figure 13).

Figure 13 - SEM images of the fractured surface of (a) neat PS, (b) PS/MMT, and (c) PS/CG@MMT-3. (d) Proposed mechanism of improving fire retardancy

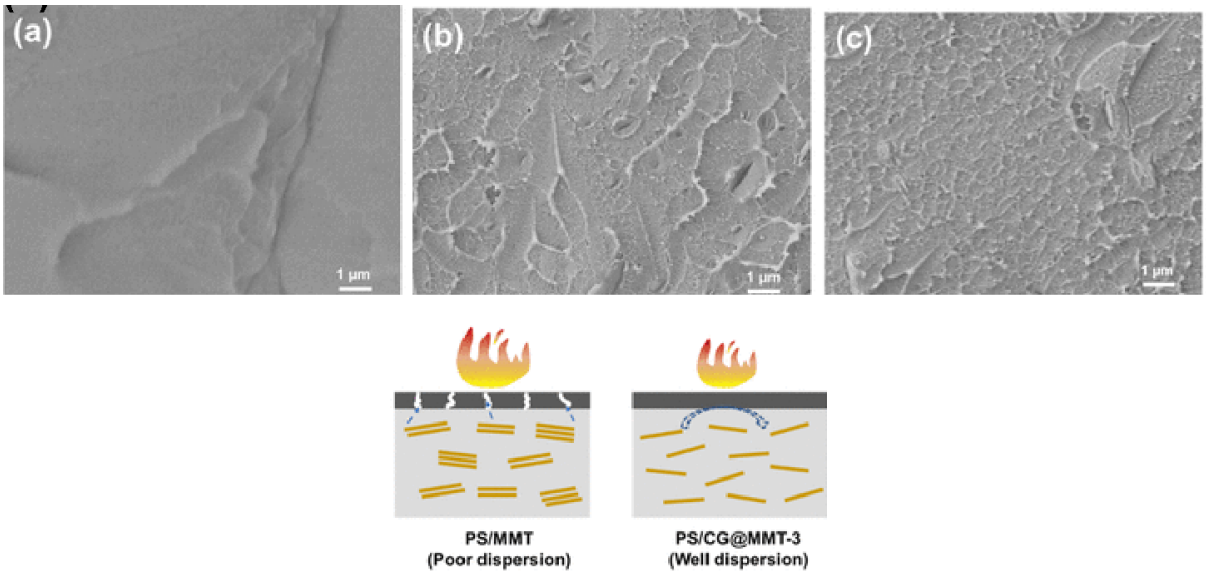

Source: Ma et al. (2023)

3 MATERIALS AND METHODS

Contents

Chapter 3 Abstract

This chapter describes the starting materials used in this thesis, the reagents employed in the synthesis of the materials, the characterization techniques applied to elucidate the relationship between structure and properties, as well as the methodology adopted for the biological assays.

3.1 STARTING MATERIALS

Different clays were employed to prepare the hybrid nanomaterials described in this section. A natural Wyoming montmorillonite (MMT) clay with Na^+ interlayer cation with a Cation Exchange Capacity (CEC) of 93 mEq per 100 g was purchased from Southern Clay Products (USA) and corresponds to the commercial product Cloisite®Na^+. Microfibrous sepiolite (SEP) from Vallecas-Vicálvaro, Spain, with >95% purity and CEC value of approximately 15 mEq/100g, was commercialized as Pangel S9® by Tolsa S.A. (Spain) and kindly provided by Prof. Dr. Eduardo Ruiz-Hitzky from *Instituto de Ciencia de Materiales de Madrid*, Spain. Clays were stored at room temperature and used without further modification.

Table 2 provides information about the reagents used in this Thesis, including their formula, provenance, and purity. Deionized water (resistivity >18.2 MΩ.cm) was obtained from a Millipore® Ultrapure water system.

Table 2 - List of reagents used and their respective formula, supplier, and purity

Reagent	Formula	Supplier	Purity (%)
2-methylimidazole	$C_4H_6N_2$	Sigma-Aldrich	99
Fluorouracil	$C_4H_3N_2FO_2$	Sigma-Aldrich	> 98.0
Citric acid	$C_6H_8O_7$	Êxodo	> 99.5
Dimetylformamide	C_3H_7NO	Êxodo	> 99.8
Hydrochloric acid P.A.	HCl	Êxodo	37%
Methanol	CH_4O	Êxodo	> 99.0
Sodium hydroxide	NaOH	Synth	> 98.0
Urea	CH_4N_2O	Dinâmica	> 99.0
Zinc nitrate	$Zn(NO_3)_2{\cdot}6H2O$	Dinâmica	>96.0

3.2 SYNTHESIS OF CARBON QUANTUM DOTS

Nitrogen-doped CQD was obtained following a procedure reported by Qu et al. (2016) (Figure 14). In a typical synthesis, citric acid (1 g) and urea (2 g) were added to 10 mL of DMF and sonicated until the precursors were completely dissolved. The solution was transferred to a 15 mL Teflon-lined stainless-steel autoclave and then heated to 160 °C for 6 h. The obtained dark brown solution was cooled to room temperature naturally before being mixed with 20 mL of NaOH aqueous solution (50 $mg{\cdot}mL^{-1}$) and centrifuged at 15,000 rpm for 30 min. The

precipitate was collected, suspended in deionized water, centrifuged twice under the same conditions described above, and then freeze-dried at −35 °C for 72 h to obtain the powder product. The addition of sodium hydroxide during the purification step neutralizes carboxyl groups and other acidic by-products, favoring the formation of surface functional groups.

Figure 14 - Schematic illustration of the synthesis procedure for CQD

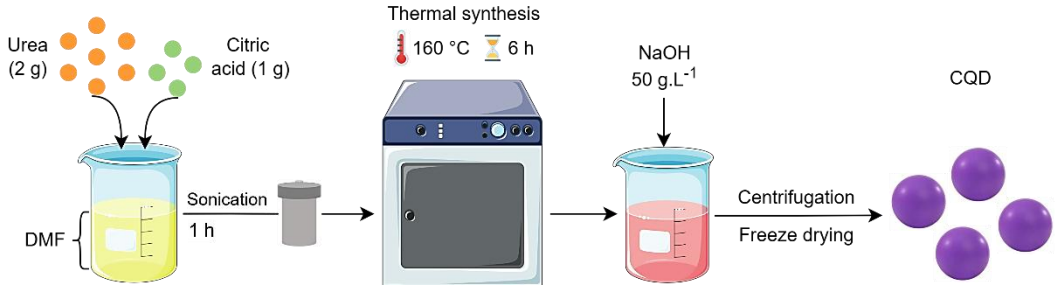

Source: Author (2025)

3.3 SYNTHESIS OF ZIF-8

ZIF-8 was synthesized following the procedure previously described by Schejn et al. (2014). Briefly, solution A was prepared by dissolving 0.595 g of $Zn(NO_3)_2 \cdot 6H_2O$ in 20 mL of methanol, while solution B was obtained by dissolving 1.642 g of 2-methylimidazole in 20 mL of methanol. Solution A was then poured into solution B, and the resulting mixture was allowed to react for 24 h at room temperature. The formed ZIF-8 was collected by centrifugation at 4,000 RPM for 15 min, washed twice with methanol under the same conditions, and finally dried at 70 °C for 24 h (Figure 15). Each synthesis yielded approximately 200 mg of ZIF-8.

Figure 15 – Schematic illustration of the synthesis procedure for ZIF-8

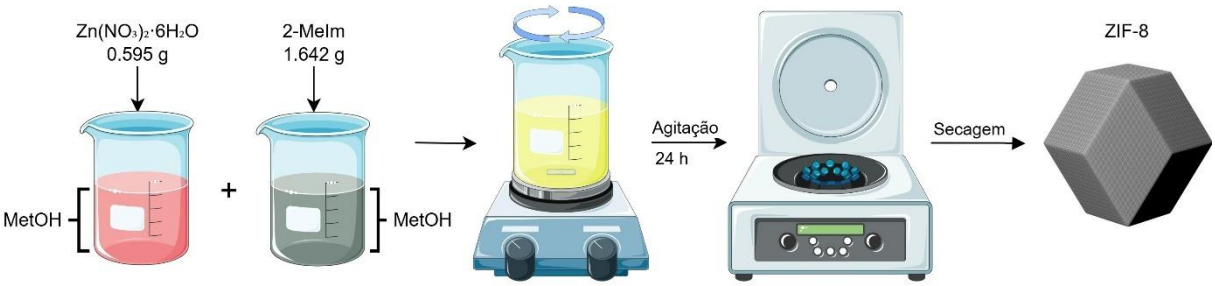

Source: Author (2026)

3.4 PREPARATION OF CLAY-CARBON QUANTUM DOTS HYBRID MATERIALS

Two synthetic routes were explored to obtain different clay–carbon quantum dot hybrid nanomaterials. In the first route, 10 mg of previously prepared CQDs and 50 mg of either

montmorillonite or sepiolite were individually dispersed in 25 mL of deionized water and stirred for 1 h (Figure 16). The CQD suspension was then poured into the clay dispersion and continuously stirred for 24 h. After the reaction period, the resulting mixture was centrifuged at 8,000 rpm for 10 min, washed twice with deionized water, and dried at 50 °C for subsequent experiments. The obtained nanohybrids were denoted as MCQD-R1 and SCQD-R1, corresponding to the MMT and SEP hybrids, respectively.

Figure 16 - Schematic illustration of the synthetic routes employed to fabricate the sepiolite-carbon quantum dots hybrid nanomaterials

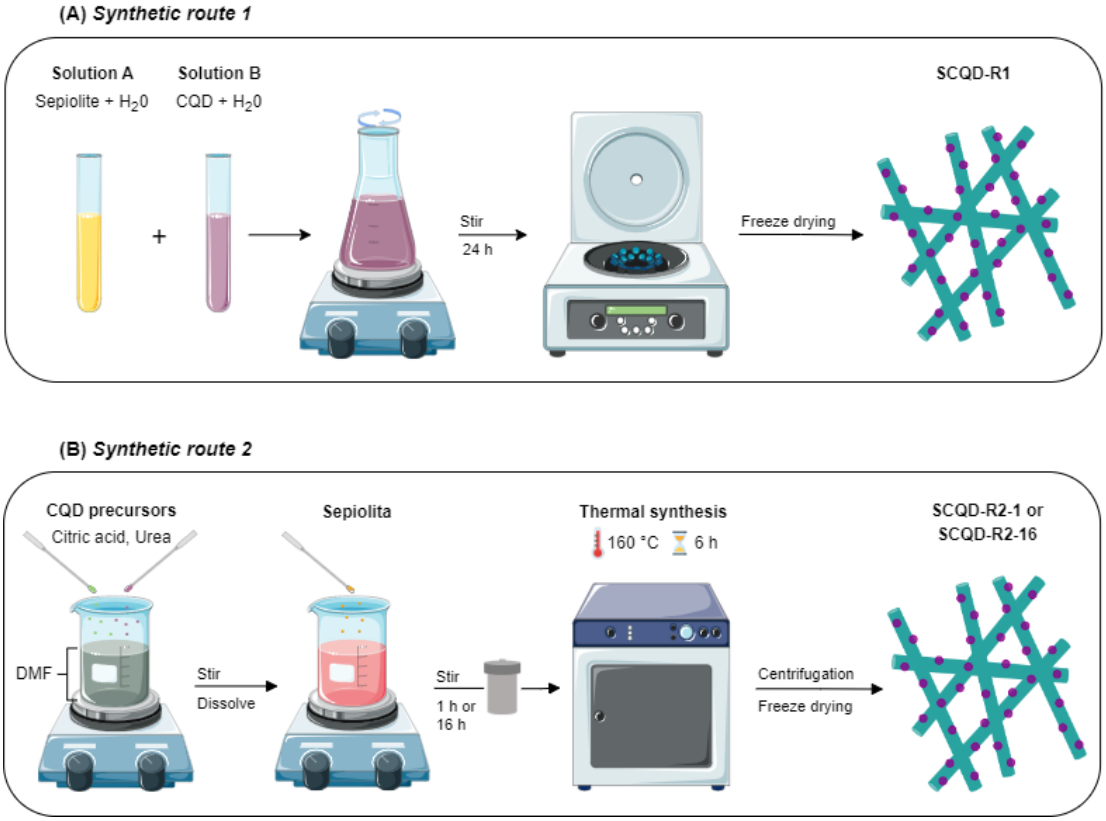

Source: Author (2026)

In the second route, the CQD was prepared *in situ, i.e.*, in the presence of the clay minerals (Figure 16). For this, citric acid (1 g) and urea (2 g) were added to 10 mL DMF, and the mixture was sonicated until complete solubilization of the precursors. After that, 50 mg of MMT or SEP was added to the mixture, which was stirred for 1 h or 16 h, and then the dispersion was transferred to a 15 mL Teflon-lined stainless-steel autoclave and heated to 160 °C for 6 h. The subsequent steps of this route followed the procedure described for the synthesis of pure CQD (section 3.2). After reaction time, the obtained dark product was mixed with 20 mL of NaOH aqueous solution (50 $mg.mL^{-1}$) and centrifuged at 15,000 RPM for 30 min. The precipitate was collected, suspended in deionized water, and centrifuged twice under the same

conditions as described above. The isolated solids were freeze-dried at -35 °C for 72 h and denoted as MCQD-R2-1 and MCQD-R2-16 for hybrids based on montmorillonite and SCQD-R2-1 or SCQD-R2-16 for sepiolite-based hybrids prepared with 1 h and 16 h, respectively.

3.5 PREPARATION OF THE CLAY-DRUG HYBRID NANOMATERIALS

For the preparation of the clay-drug hybrid nanomaterials, drug solutions with different concentrations (250-2000 mgL^{-1}) were prepared in deionized water and homogenized using an ultrasonic bath until complete solubilization of the drug. Simultaneously, 0.10 g of MMT or SEP was dispersed in 50 mL of water and kept under stirring during 1 h to properly disperse the clay. Then, each drug solution was slowly added to a clay suspension, forming a single bath which was kept under magnetic stirring and dark conditions for 72 h at room temperature. After the reaction time, the mixtures were centrifuged at 8000 RPM for 10 min. The solid products were suspended in deionized water, and centrifuged twice at the same conditions as described above to remove excessive drug, and then dried at 50 °C. The resulting hybrid nanomaterials were denoted as MMT-5FU followed by the initial amount of the drug.

3.6 DETERMINATION OF DRUG ENCAPSULATION EFFICIENCY AND DRUG LOADING CAPACITY

The drug entrapment efficiency (EE) and drug loading content (DLC) of the prepared materials were evaluated by Elemental Analysis (CHN). In this case, the amount of drug was calculated considering the composition of pure 5-FU as parameter. The EE and the DLC of 5-Fluorouracil in the hybrid nanomaterials were calculated according to the following equations:

$$EE\ (\%) = \frac{drug\ loaded\ in\ hybrid\ nanomaterials(g)}{initial\ drug\ amount\ (g)}\ x\ 100 \qquad \textbf{Equation 1}$$

$$DLC\ (\%)\ = \frac{drug\ loaded\ in\ hybrid\ nanomaterials\ (g)}{hybrid\ material\ amount\ (g)} x\ 100 \qquad \textbf{Equation 2}$$

3.7 PREPARATION OF ZIF-8/CQD HYBRID NANOMATERIALS

The synthesis of ZIF-8/CQD hybrid nanomaterials followed the same initial step adopted for pure ZIF-8, as described in Section 3.3. Briefly, solution A was prepared by

dissolving 1.642 g of 2-methylimidazole in 20 mL of methanol, while solution B was obtained by dissolving 0.595 g of $Zn(NO_3)_2 \cdot 6H_2O$ in 20 mL of methanol. Both solutions were stirred for 30 min to guarantee complete homogenization of the MOF precursors. After that, 400 mg or 200 mg of CQDs were added to solution A and the mixture was stirred for an additional 30 min to completely disperse CQDs in methanol (Xu et al., 2016) . Solution B was then slowly poured into the CQD-containing solution A to form a single reaction mixture, which was allowed to react at room temperature for 24 h (Figure 17). The resulting ZIF-8/CQD hybrid materials were recovered by centrifugation at 4000 rpm for 15 min, washed twice with methanol under the same conditions, and dried at 70 °C for 24 h. The obtained hybrids were denoted as ZIF-8/CQD 400 and ZIF-8/CQD 200, according to the initial CQD content used during synthesis.

Figure 17 – Schematic illustration of the synthetic route employed to fabricate ZIF8/CQD hybrid nanomaterial

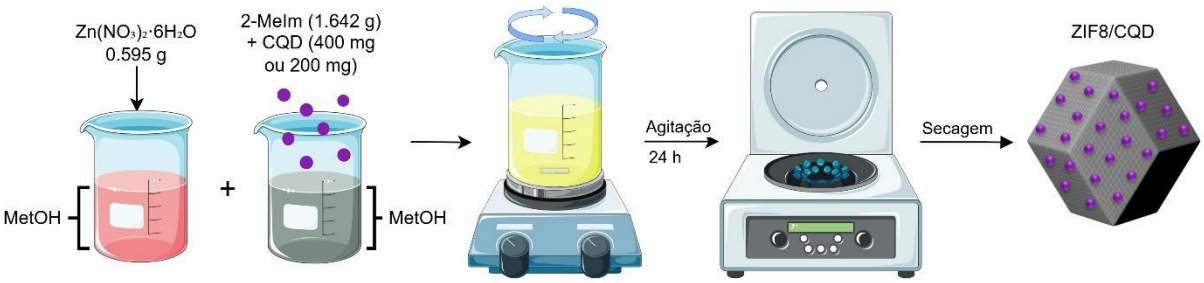

Source: Author (2026)

3.8 PREPARATION OF THE CLAY-CQD-5FU HYBRID NANOMATERIALS

For the preparation of the clay–CQD-R2-5FU samples, 120 mg of the respective hybrid nanomaterials (SCQD-R2-16) and 50 mg of 5-FU were weighed and dispersed separately in 50 mL of deionized water. Both dispersions were stirred for 30 min to promote complete homogenization, then combined and kept under agitation for 72 h. The final materials were collected by centrifugation, washed twice with deionized water, and dried in an oven at 60 °C.

3.9 CHARACTERIZATION TECHNIQUES

3.9.1 Transmission Electron Microscopy (TEM)

For visualization of the carbon dots and their respective hybrids on a very fine scale, TEM images were recorded on a FEI Tecnai G2 F2 TEM operating at 200 kV accelerating

voltage. The materials were dispersed in isopropyl alcohol, and 4 μL of each dispersion was dripped on a copper grid and allowed to air-dry before measurement.

3.9.2 X-ray Diffraction (XRD)

X-ray diffraction is a versatile and non-destructive technique that is used for the identification of the crystalline phases in solid materials and for analyzing their structural properties (Azhar; Olad, 2014). Powder X-ray diffraction data were collected on a Bruker D8-Advance X-ray diffractometer using Cu Kα (λ = 0.1542 nm) as the radiation source, with a voltage and current source of 30 kV and 10 mA, respectively. The diffraction patterns were recorded between 4° and 70° (2θ) angles with a speed of 2º/min. In the case of samples containing MMT clay, the basal space was calculated from Bragg's law (Equation 3).

$$n\lambda = 2dsin\theta, \qquad \textbf{Equation 3}$$

where, it is assumed n = 1 for the first order reflection, λ is the wavelength of the X-ray beam, d is the distance between the lattice planes, and θ is the diffraction angle.

3.9.3 Fourier Transform Infrared Spectroscopy (FT-IR)

The Fourier-transform infrared (FT-IR) spectroscopy is an analytical technique that allows obtaining infrared spectra to identify the chemical substances and functional groups present in materials. The vibrational spectra for all samples were obtained using a Bruker TENSOR 27 FTIR spectrometer in ATR (Attenuated Total Reflectance) mode using ZnSe crystal. The spectra were recorded in the 400-4000 cm^{-1} range, at a spectral resolution of 2 cm^{-1} over 64 scans. A background of the clean cell was performed for each analysis undertaken.

3.9.4 Raman spectroscopy

Raman spectroscopy is a technique used to determine the vibrational modes of molecules for the identification and quantification of chemical structure, crystalline and polymorphic phases, and molecular interaction. In this thesis, Raman spectroscopy was employed to investigate the structural features of CQDs, particularly the relative contribution of sp^2- and sp^3-hybridized carbon domains, and to assess the influence of the clay minerals on

the structural organization of the CQDs. The Raman spectra of the powdered samples were recorded on a Micro Raman Labram HR Horiba Jobin Yvon (Unesp, Araraquara) with a He-Ne 632.8 nm laser line. Spectral data were recorded between 800 to 1800 cm^{-1} with an accumulation time of 5 seconds. The LabSpec software was executed for the acquisition of spectral data. The Raman spectra were deconvoluted by Lorentzian fitting to obtain the ratio I_D/I_G.

3.9.5 Thermal analysis

Thermogravimetric analysis (TG) along with Derivative Thermogravimetric Analysis (DTG) provides information about the thermal stability, and the differences of material properties with the change of temperature over time. The thermal behavior of the different materials was obtained using a SDT-Q600 thermal analyzer (TA Instruments) from 30°C to 900 °C. The experiments were carried out under a synthetic air atmosphere composed of oxygen and nitrogen (flux of 50 mL min^{-1}) at a heating rate of 10 °C min^{-1}. Approximately 5-10 mg of each sample was used in the analysis.

3.9.6 Ultraviolet-Visible Spectroscopy

The samples were recorded from 200 to 900 nm on a KASUAKI IL-593-BI, operating at 1 nm resolution. Quartz cuvettes with a 1 cm optical path were used, and the data were processed using UV Professional software.

UV-Vis spectroscopy was also used to investigate the stability of CQD and the hybrid nanomaterials since alterations in the absorption spectra can indicate changes in size, aggregation, and overall stability. The investigation was conducted by monitoring the visible band maxima as a function of time storage. For this purpose, dispersions were prepared in deionized water and stored in the dark at 4 °C, and the UV-Vis spectra of the samples were scanned on days 0, 4, 7, 14, 21, 28, 35, 42, 49, and 56.

3.9.7 Fluorescence Spectroscopy

The emission spectra of sepiolite, CQD, and the hybrid nanomaterials were recorded on a Fluorolog-3 FL3-122 spectrofluorometer from Horiba Jobin Yvon. For the measurements, aqueous solutions of the materials were prepared and then excited with progressive increments

of 25 nm in the range of 350 nm to 750 nm for emission spectra. The slit was maintained at 3 nm for all measurements.

Lifetimes were measured in a PicoQuant, FT300 fluorescence spectrometer. Compounds were exciting with a 450 nm picosecond pulsed diode laser (P-C-450, PicoQuant) with 80 MHz repetition rate. Signals were digitized with a Time Harp 260 PCI card (PicoQuant). Data were recorded in wizard measurement mode of EasyTau software and processed by EasyTau Analysis software using an exponential re-convolution mode.

3.9.8 Elemental analysis

Elemental analysis was used to evaluate the elemental composition of the samples, providing quantitative information. Elemental analyses were performed in an Elemental Microanalyzer CHNS Perkin-Elmer EA-2400 Series II. The CHNS analyses were based on the Pregl-Dumas technique using a furnace temperature of 1100 ºC. The results were reported as percentage by weight of each element, and the minimum sample requirement for a CHNS analysis was 5 mg.

3.9.9 N_2 adsorption-desorption isotherm

The textural properties of the materials were determined using a Micromeritics ASAP 2020 (Accelerated Surface Area and Porosimetry) analyzer, based on nitrogen adsorption–desorption measurements at −195.8 °C (77 K). Prior to the analysis, the samples were degassed at 100 °C for 3 h to remove moisture and residual gases potentially present within the porous structure. The specific surface area was calculated using the BET (Brunauer–Emmett–Teller) method.

3.10 BIOLOGICAL ASSAYS

3.10.1 Hemolysis test with sheep erythrocytes

The *in vitro* hemolytic activity of the hybrid nanomaterials and their respective counterparts was evaluated according to the International Standard Organization 10993 part 5 (ISO, 2009), following the methodology adapted fromAlmaaytah et al. (2014). For this, 10 mL of sheep blood was collected in a tube containing EDTA, authorized by the ethics and research

committee of the Federal University of Maranhão (CEUA, process nº 23115.005441/2017-62). The blood was centrifuged at 2,000 RPM for 10 minutes at 20 °C, the plasma was removed, and the erythrocytes were washed three times with phosphate-buffered saline (PBS). After, an aliquot of 100 µL of 5% v/v erythrocyte solution (in saline 0.9% w/v) was mixed with 200 µL of the sample test solutions in 96-well microplates with concentrations ranging from 1000 to 7.81 μgmL^{-1}, and incubated for 1 hour at 37 °C. The positive and negative controls received 100 µL of Triton x-100 at 1% and PBS, respectively. After the incubation time, the samples were centrifuged at 2,000 RPM for 10 minutes at 20 °C. The supernatant was removed, transferred to a microplate reader, and its absorbance measured at 450 nm.

The hemolytic activity was expressed as a function of the action of Triton x-100 and calculated by the following formula:

$$Hemolysis\ (\%) = \frac{Abs\ sample - Abs\ PBS}{Abs\ Triton\ x{-}100{-}Abs\ PBS} \times 100 \qquad \textbf{Equation 4}$$

Where Abs sample is the group of erythrocytes treated with the sample tests, Abs PBS is the group treated with only PBS, and Abs Triton x-100 is the group treated with Triton x-100.

3.10.2 Fluorescence and Phase Contrast Microscopy

U87 MG cells were cultured in Dulbecco's Modified Eagle Medium (DMEM) High Glucose (Sigma-Aldrich®) supplemented with 10% fetal bovine serum (FBS, Sigma-Aldrich®) and 1% ciprofloxacin (Sigma-Aldrich®) under controlled conditions of temperature and CO_2 percentage. After two consecutive passages, 2×10^5 cells per well were seeded into 6-well plates. Following 24 h of incubation and establishment of confluent monolayers, the culture medium was replaced with fresh medium containing the hybrid nanomaterials at a final concentration of 50.0 mg L^{-1}. The cells were further incubated for 72 h under the same culture conditions, in accordance with ATCC guidelines.

Following incubation period, the wells were washed three times with phosphate-buffered saline (PBS) 1X and maintained in the same buffer for microscopic analysis. Imaging was performed using a fluorescence microscope (Leica DMi8, Wetzlar, Germany) equipped with a 350–490 nm excitation filter and a 460–520 nm emission filter barrier (blue channel), as well as a 516–560 nm excitation filter and a 590 nm emission filter barrier (green/orange channel).

4 SEPIOLITE-CQD HYBRID NANOMATERIALS

Contents

Chapter 4 Abstract

This chapter presents the results obtained from the association of sepiolite, a fibrous clay, with carbon quantum dots, focusing on the morphology and the structural, thermal, and optical properties of the resulting hybrid nanomaterials. In addition, the effects of the different synthetic routes employed are examined. The toxicity of the materials was evaluated through hemolysis assays, and their potential for biological imaging was investigated using the U87MG cell line.

4.1 INTRODUCTION

Hybrid nanomaterials are fabricated from at least two distinct nanoparticles to improve properties and functionalities, overcome or reduce the limitations of single-component nanoparticles, to achieve multiple functionalities in a single nanoplatform (Li et al., 2023a; Ma, 2019). In this regard, hybrid nanomaterials can be endowed with new properties as a result of the synergistic effects of the counterparts at the nanoscale, surpassing the original features of the precursors(Tipa et al., 2022). These features enable them to be applied in a wide range of applications, including sensing (Buk; Pemble; Twomey, 2019; Hashemi et al., 2020; Xie et al., 2024), energy storage (Hsu et al., 2022), photocatalysis (Hazarika; Karak, 2019; Liu; Jatav; Hill, 2020; Santos et al., 2023), and diverse biomedical applications (*e.g.*, multimodal imaging, drug/gene delivery, scaffolds for tissue engineering, vascular stents, dental implants, etc.) (Park et al., 2020; Shuai et al., 2021).

Among the distinct nanomaterials available to form integrated systems, carbon dots and clays, although still quite different in terms of composition, genesis, structure, and properties, stand out as natural resources that have been used from prehistoric times to the present day. In this sense, carbon quantum dots (CQD) are a smart choice due to their attractive properties, such as tunable photoluminescence properties, high water solubility, chemical stability, low toxicity, great compatibility with other materials, and easy surface modification (Đorđević et al., 2022). CQD are zero-dimensional carbon-based nanomaterials (diameter <10 nm) with spherical or quasi-spherical morphology. They are typically formed by a carbon core, which is mainly constituted by sp^2 hybridized carbon atoms, surrounded by functional groups. The presence of functional groups (*i.e.*, hydroxyl, carboxyl, amino, carbonyl) plays a key role in optical properties, besides providing sites of interactions for surface modification with organic, polymer, and biologically active molecules (Barhoum et al., 2023). The combination of structural properties, absorption and emission features, and their functionalized surface makes them an interesting nanomaterial.

Clay minerals, although distinct from CQD in terms of composition, genesis, structure, and properties, stand out as versatile materials used from prehistoric times to the present day due to their unique structure and distinctive physicochemical properties. Among them, sepiolite (SEP) is a hydrous magnesium-rich aluminosilicate with fibrous morphology, and $Si_{12}O_{30}Mg_8(OH)_4(OH_2)_4H_2O$ is the ideal unit cell formula. Like other clays, it shows a continuous tetrahedral silica layer with a discontinuity of the octahedral sheet due to the periodic inversion of the apical oxygen atoms of the tetrahedra in every three silicate chains,

resulting in the formation of structural tunnels and channels along the fibrous structure (Ruiz-Hitzky et al., 2013; Yang; Wang, 2022) (Figure 18). The composition and morphology of SEP change depending on the origin, but its dimensions vary from 0.1 to 5 µm in length, 5–10 nm in thickness, and 10–30 nm in width, allowing it to be used as a natural nanomaterial with great availability and low cost (Besli; Orakdogen, 2021). Due to its unique structural arrangement, SEP is characterized by remarkable surface features such as high surface area and pore volume (c.a. of 300 $m^2.g^{-1}$ and 0.4 $cm^3.g^{-1}$, respectively) (Ruiz; Ruiz-García; Ruiz-Hitzky, 2023), which contribute to its excellent adsorptive capacity. Moreover, the high density of silanol groups (≡Si–OH) located at the external surface, the structure channels, and the distinct types of water molecules, offers great potential for sepiolite assembling in functional nanomaterials (Cao et al., 2022). Thanks to the presence of these silanol groups on the external surface of sepiolite, the interaction with polymers (Torres-Giner et al., 2016), biopolymers (Palem et al., 2021), metal oxides, and drugs (Rebitski et al., 2018) is facilitated, forming new hybrid materials with different interesting applications.

Figure 18 - Scheme of crystalline structure of sepiolite fibrous clay

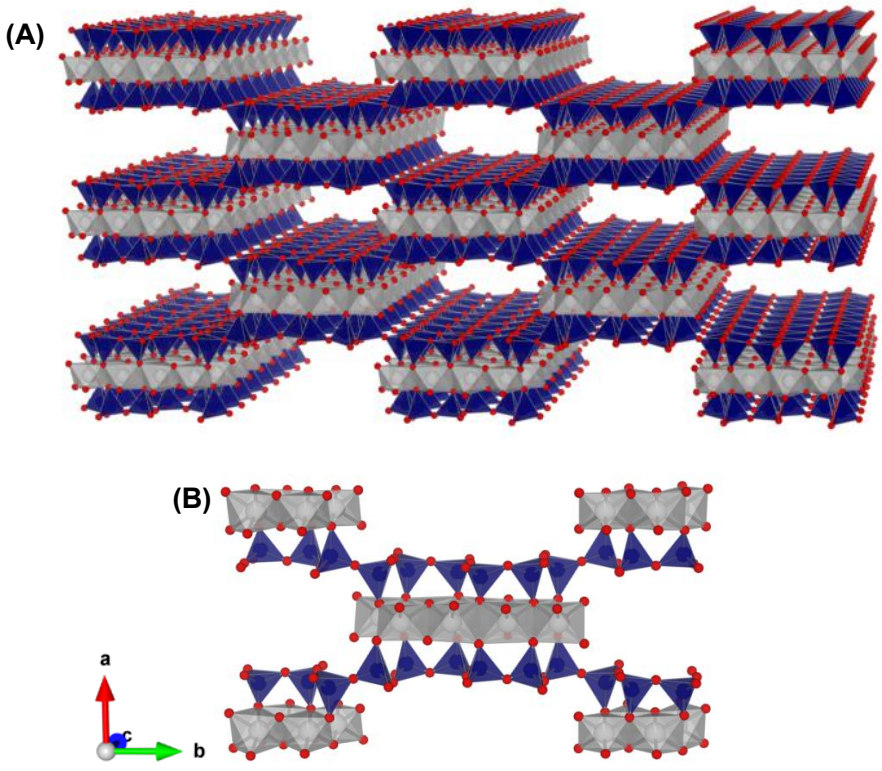

Source: Author (2025)

Despite some reports in the literature, the association of carbon dots and clay minerals often results in nanomaterials endowed with advanced functionalities. Massaro et al. (2019)

obtained a hybrid nanomaterial based on halloysite, a tubular clay, and carbon dots (HNT-CDs) using a one-step microwave-assisted pyrolysis of tartaric acid and ethylene diamine as a synthetic route. The HNT-CDs hybrid was explored as a non-viral vector for oral gene therapy and cellular imaging due to the photoluminescence properties of the HNT-CDs, making it possible to track the internalization and localization in the cells. The hybrid also demonstrates antioxidant properties, low cytotoxicity, and the ability to strongly interact with DNA. Zhai et al. (2019) used montmorillonite, a lamellar clay, to develop g-CDs@MMT as a promising alternative to traditional luminescent materials. The material exhibits high solid-state photoluminescence, photostability, thermostability, and solvent resistance. The results indicate that g-CDs@MMT can be applied for latent fingerprint detection and in the fabrication of white light-emitting diodes. Jlassi et al. (2023) described the preparation of bentonite clay modified with carbon dots for heavy metal removal. The CDs were prepared *via* the hydrothermal method using graphitic waste as the precursor, originating positively charged CDs. Further, CDs were successfully intercalated in the aluminosilicate, resulting in bentonite-carbon dots (B-CDs) with long-term stable nanohybrid and wavelength-dependent photoluminescent properties. The B-CDs designed possess a UV-light adsorptive response, removing Pb^{2+} from water with an efficiency of 95% under light conditions compared to 70% under dark conditions.

Sepiolite, on the other hand, has been combined with graphene, single-walled (Polyakov et al., 2020), and multi-walled carbon nanotubes (Fernandes; Ruiz-Hitzky, 2014; Ruiz-García et al., 2018), but there are no records in the literature for carbon quantum dots to date. In this sense, the lack of scientific reports regarding sepiolite-carbon quantum dots and their unique properties motivates us to develop SEP-CQD hybrid nanomaterials with potential for distinct applications, since it is possible to take advantage of the outstanding optical properties and excellent biocompatibility of CQD, at the same time the high adsorption capacity, large surface area, and ordered pore structure from sepiolite. Moreover, the association between SEP and CQD might help to overcome drawbacks associated with the nanoparticle aggregation of pure carbon quantum dots, which might result in photoluminescent quenching and loss of stability (Carbonaro et al., 2020).

Based on these premises, this work reports the fabrication of fluorescent sepiolite-carbon hybrid nanomaterials using different approaches without additional compatibilizers or crosslink agents. Advanced characterizations were performed to obtain a deep understanding of the structure-property relationship as it plays an important role in the development of functional hybrid nanomaterials. It is expected that the association of sepiolite and carbon quantum dots will enable the development of nanomaterials with multiple functionalities that

are compatible with several emerging technologies, such as adsorbent capacity, electrical conductivity, thermal stability, photoluminescence, bioimaging, and low toxicity. These properties can expand the possibilities of use in various areas, from electronics to medicine, opening avenues for the innovation of technologies with the potential to have a significant impact in various scientific, technological, and social areas.

4.2 MORPHOLOGICAL AND STRUCTURAL PROPERTIES

Different synthetic routes are explored in this work to combine sepiolite, a fibrous clay, and carbon quantum dots, forming hybrid nanomaterials. Initially, XRD analysis was conducted on the neat nanomaterials, and then in the hybrid nanomaterials to evaluate if any of the conditions in the synthesis process, *i.e.*, *in situ* procedure, thermal treatment, basic medium, or solvent, act modifying the structure of the clay or CQD. Figure 19A shows the diffraction patterns for CQD, exhibiting peaks at 2θ = 5.4° (d = 1.7 nm), 2θ = 27.1° (d = 0.33 nm), and 2θ = 28.3° (d = 0.31 nm). The first peak can be ascribed to the (001) plane diffraction of graphite oxide, which occurs at 2θ = 10.6° (JCPDS no 00-041-1487) (Aslam et al., 2025)in pure material. This reflection shifted to lower angles, which are related to functional groups such as hydroxyl, carbonyl, carboxylate, and amino groups formed during the CQD synthesis at tge edge of sheets, increasing the interlayer spacing and introducing disorder. The last two peaks show a slight difference in d-space from the (002) plane in graphite, which could indicate the formation of a nonideally arranged graphite-like structure (Mintz et al., 2021). Moreover, the distinct interlayer spacing might be indicative of a heterogeneous structure (Mandal et al., 2019). The peaks observed are broad and possess low intensity, indicating a partial graphitization and the presence of disordered carbon, which is consistent with other reported CQD (Bian et al., 2018; Choppadandi et al., 2021; Du et al., 2014).

For neat sepiolite, a strong diffraction plane appears at 2θ = 7.3° (110), which is characteristic of the layered structure (Tang et al., 2012). In the hybrid nanomaterials based on sepiolite, it is possible to note diffraction patterns quite similar to the clay (Figure 19A), where the main reflection plane retains its position, suggesting that the conditions in the synthesis process do not modify the structure of the clay. At the same time, the (110) diffraction plane in the hybrids becomes significantly more intense, which could be related to the content reduction of impurities associated with the sepiolite, such as dolomite and calcite (Wang et al., 2019).

For the hybrid nanomaterials, it is possible to see in the enlarged zone (Figure 19B) diffraction planes at 2θ = 26.8° related to CQD nanoparticles, confirming their presence in the

hybrids. A slight shift of the reflection planes is observed in the hybrid nanomaterials, as well as a reduction in the intensity of the peaks, which can be attributed to a dilution effect of CQD in the samples. A similar effect was described by (Chuaicham et al., 2022) for a material based on BiOBr, carbon quantum dots, and saponite (BiOBr@CQD/Clay), where the reduction of intensity of CQD was related to the low crystallinity of CQD.

Figure 19 - Diffraction patterns of SEP, SCQD-R1, SCQD-R2-1, SCQD-R2-16 hybrid nanomaterials, and CQD in the range of (A) 2θ = 4° to 70° and (B) 2θ = 22° to 32°

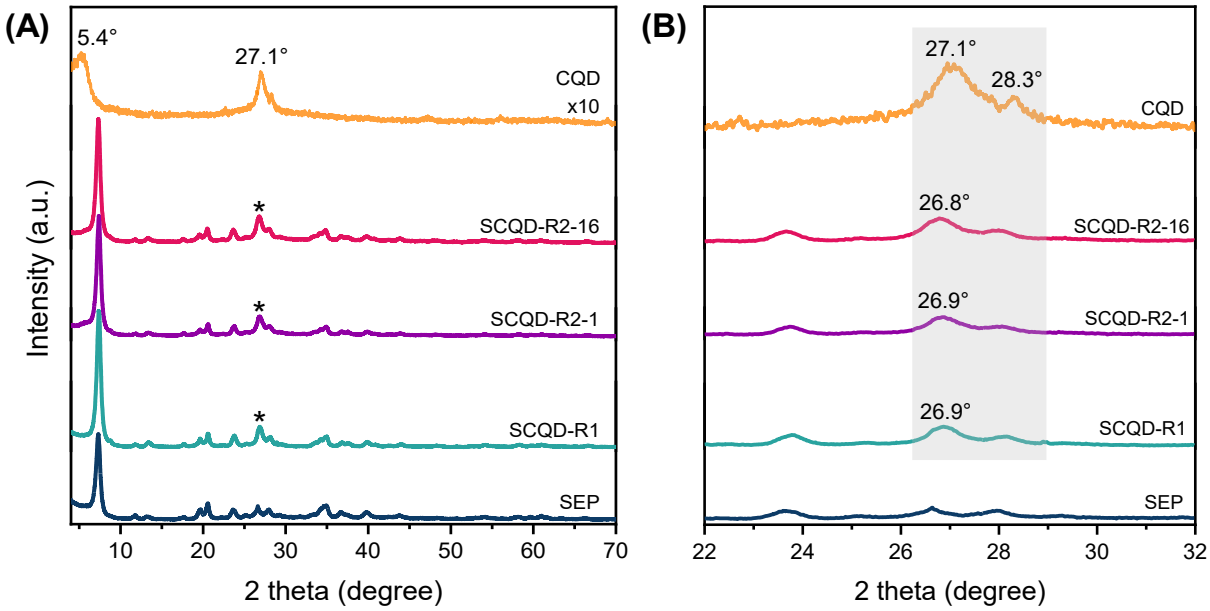

As was suggested in the discussion above, the intensity of the reflection in the diffractogram associated with CQD might be related to their amount in the hybrids. Therefore, elemental analysis was used to obtain the composition of CQD as well as to determine their amount in the hybrid nanomaterials. The percentage of CQD in each sample was calculated considering the amount of carbon in CQD. From Table 3, it is possible to observe that SCQD-R1 possesses the lowest amount of CQD, 11.08%, compared to 53.09% and 61.97% for SCQD-R2-1 and SCQD-R2-16, respectively. This result is due to the possible leaching of highly soluble CQD nanoparticles during the synthesis process. Moreover, the *in situ* synthesis seems to favor the association of the CQD on the sepiolite, where the clay might act as an effective platform for these nanoparticles. In addition, a longer time of contact between the CQD precursor and SEP before thermal treatment promotes a higher content of CQD in the final material.

Table 3 – Elemental composition in weight of CQD and the SCQD-R1, SCQD-R2-1, and SCQD-R2-16 hybrid nanomaterials

Sample	C (%)	H (%)	N (%)	Amount of CQD (%)
CQD	71.57	4.86	23.57	100
SCQD-R1	6.04	3.82	1.22	11.08
SCQD-R2-1	35.80	4.60	13.19	53.59
SCQD-R2-16	41.33	4.79	15.89	61.97

To gain information on how clays and CQD are arranged in the hybrid nanomaterials, TEM analysis was carried out. Figure 18A-B shows that the sepiolite fibers are cylindrical, elongated, and individually dispersed or form aggregations. As can be seen in Figure 20C-D, SCQD-R1, is characterized by the presence of a few CQD nanoparticles associated with the sepiolite fibers, being mostly characterized by the presence of the silicate. In contrast, the SCQD-R2-1 sample (Figure 20E-F) reveals a higher content of CQD, which is supported by the elemental analysis, showing a homogeneous coat of nanoparticles without apparent aggregation on sepiolite fibers. Similarly, the SCQD-R2-16 (Figure 20G-H) hybrid nanomaterial exhibits a high content of CQD, nevertheless, it is possible to observe nanoparticles outside the sepiolite fibers. In this case, the increase of the contact time with sepiolite may favor the dissociation of carbonaceous nanoparticles from sepiolite.

Figure 20 - TEM images of (A-C) pure sepiolite, (D-F) SCQD-R1, (G-I) SCQD-R2-1, and (J-L) SCQD-R2-16 hybrid nanomaterials

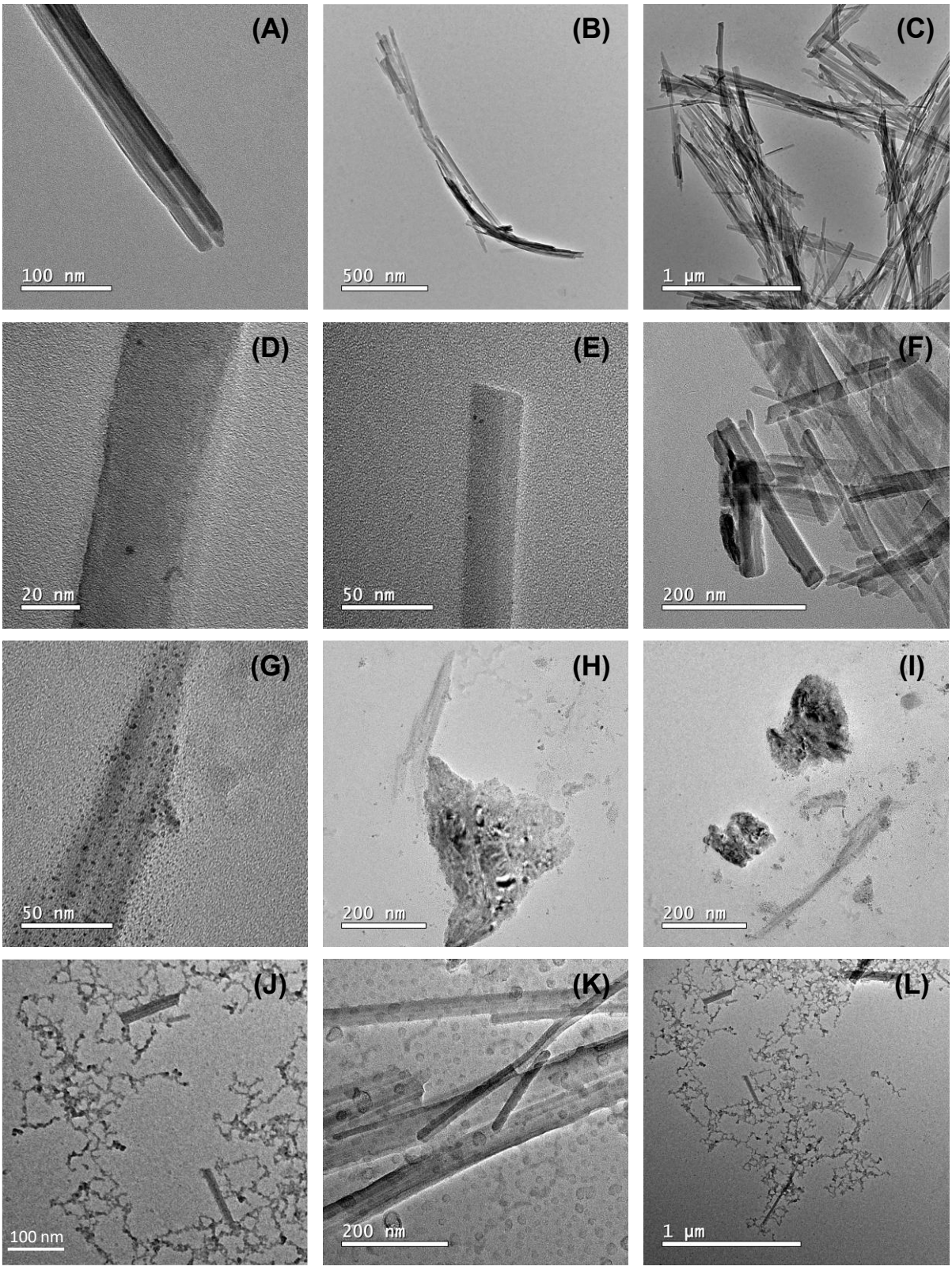

The N_2 adsorption curves are shown in Figure 21. The pure sepiolite exhibits a pattern consistent with a Type IV isotherm, exhibiting a hysteresis at high p/p^0 values that is identified

as a Type H3 hysteresis loop according to IUPAC (Thommes et al., 2015). This characteristic can be attributed to the presence of non-rigid pores formed in the interparticle spaces created by the arrangement of the particles (Gómez-Avilés et al., 2014). In comparison to the hybrid nanomaterials, neat sepiolite demonstrates significantly higher N_2 adsorbed volume, shows a much higher nitrogen adsorbed volume, which is consistent with its high surface area and porosity. Thus, the reduction observed in the hybrids can be justified by the presence of CQD nanoparticles covering the external surface of the microfibrous clay, occupying the interparticle spaces and partially blocking access to the internal pores by nitrogen gas during the BET analysis (Tang et al., 2024).

Figure 21 – N_2 isotherm for SEP, SCQD-R1, SCQD-R2-1 and SCQD-R2-16 hybrid nanomaterials

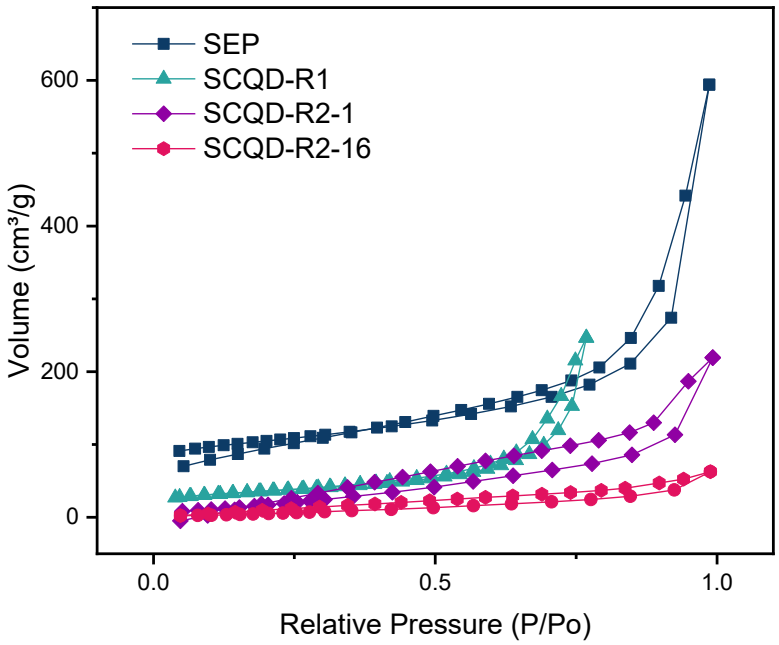

This may also justify the reduction observed in the surface area and pore diameter of the SEP-CQD hybrid nanomaterials (Table 4). In addition, it is observed that as the amount of CQD in the hybrid increases, the surface area and pore volume decreases. In SCQD-R1, for example, a content of 11.08% of CQD lead to a reduction in surface area from 342.92 m^2/g of pure sepiolite to 114.67 m^2/g, while in SCQD-R2-16 (62% CQD) it decreases drastically to 31.49 m^2/g. Vengatesan et al. (2017) synthesized a thermally reduced graphene oxide-sepiolite hybrid and reported a similar reduction in porosity, which they associated with the filling of interparticle voids and partial stacking of clay within the carbonaceous matrix during thermal treatment.

Table 4 – Textural properties of sepiolite, SCQD-R1, SCQD-R2-1, and SCQD-R2-16 hybrid nanomaterials

Sample	Surface area (m^2/g)	Pore volume (cm^3/g)	Pore diameter (nm)
SEP	342.920	0.92	10.72
SCQD-R1	114.670	0.38	13.30
SCQD-R2-1	91.192	0.34	14.88
SCQD-R2-16	31.491	0.097	12.32

Further, Raman spectra were obtained to analyze the structure of the materials. For pure sepiolite (Figure 22A), despite few scientific references, the sharp peaks observed in the range 1000-1200 cm^{-1} were associated with the vibration modes of the Si-O bond (McKeown; Post; Etz, 2002). On the other hand, CQD (Figure 20B) exhibits the characteristics of G and D bands for carbon materials, besides the D* (1102 cm^{-1}) and D' (1615 cm^{-1}) bands. The G band is related to stretching modes of carbon atoms with sp^2 hybridization (ordered carbon), while the D band is associated with structurally disordered carbon, including intrinsic carbon defects, and heteroatom doping defect that can be induced by oxygen-containing functional groups and N doping (Wang et al., 2021a). Previous works related the D* band with disordered graphitic lattice originating from sp^2-sp^3 bonds at the edges of networks (Sadezky et al., 2005), whereas the D' band can be associated with disorder due to crystal defects. As can be seen in Figure 20C, the SCQD-R1 hybrid exhibited a spectrum very similar to pure sepiolite, which can be attributed to the low amount of CQD in this hybrid. SCQD-R2-1 and SCQD-R2-16 hybrid nanomaterials have spectra similar to CQD, showing D, G, D*, and D' bands, however, additional features related to sepiolite can be observed around 1200 cm^{-1} and 1415 cm^{-1} (Figure 22D-E).

The intensity ratio of the D and G bands (I_D/I_G) is a good parameter for estimating the degree of graphitization in carbonaceous materials since it is frequently used for measuring the extension of defects by the ratio of sp^3/sp^2 carbon atoms (López-Díaz et al., 2017). The I_D/I_G decreases with the increase of ordered carbons, and with the increase in the I_D/I_G, there is an increase in disordered carbon. The intensity ratio I_D/I_G for CQD is 1.41, suggesting a highly disordered structure, which is common for carbon dots. Jlassi et al. (2023) reported an I_D/I_G of 1.36 for a CD obtained using graphite waste from hydrothermal treatment, which is close from what was observed in this work. For the results in Table 5, it is possible to note that CQD has the highest contribution of disordered carbon when compared with the hybrid nanomaterials, moreover, it seems that the presence of sepiolite in the CQD synthesis increases the contribution

of sp^2, resulting in greater structural organization. The I_D/I_G values for SCQD-R2-1 and SCQD-R2-16 are 1.26 and 1.12, respectively, suggesting that the contact time of the precursors (citric acid, urea, and DMF) and sepiolite before thermal treatment plays an important role in the degree of organization of CQD in the final hybrid nanomaterial. Similarly, Uchida et al. (2022) reported using XPS analysis that the synthesis of CD in the presence of saponite resulted in the increasing C-C bonds in the carbonaceous counterpart, indicating that the formation of *in situ* CD leads to formation of larger π-conjugated structures.

Figure 22 - Raman spectra of (A) Sepiolite, (B) CQD, (C) SCQD-R1, (D) SCQD-R2-1, and (E) SCQD-R2-16 in the range of 1000-1800 cm^{-1}

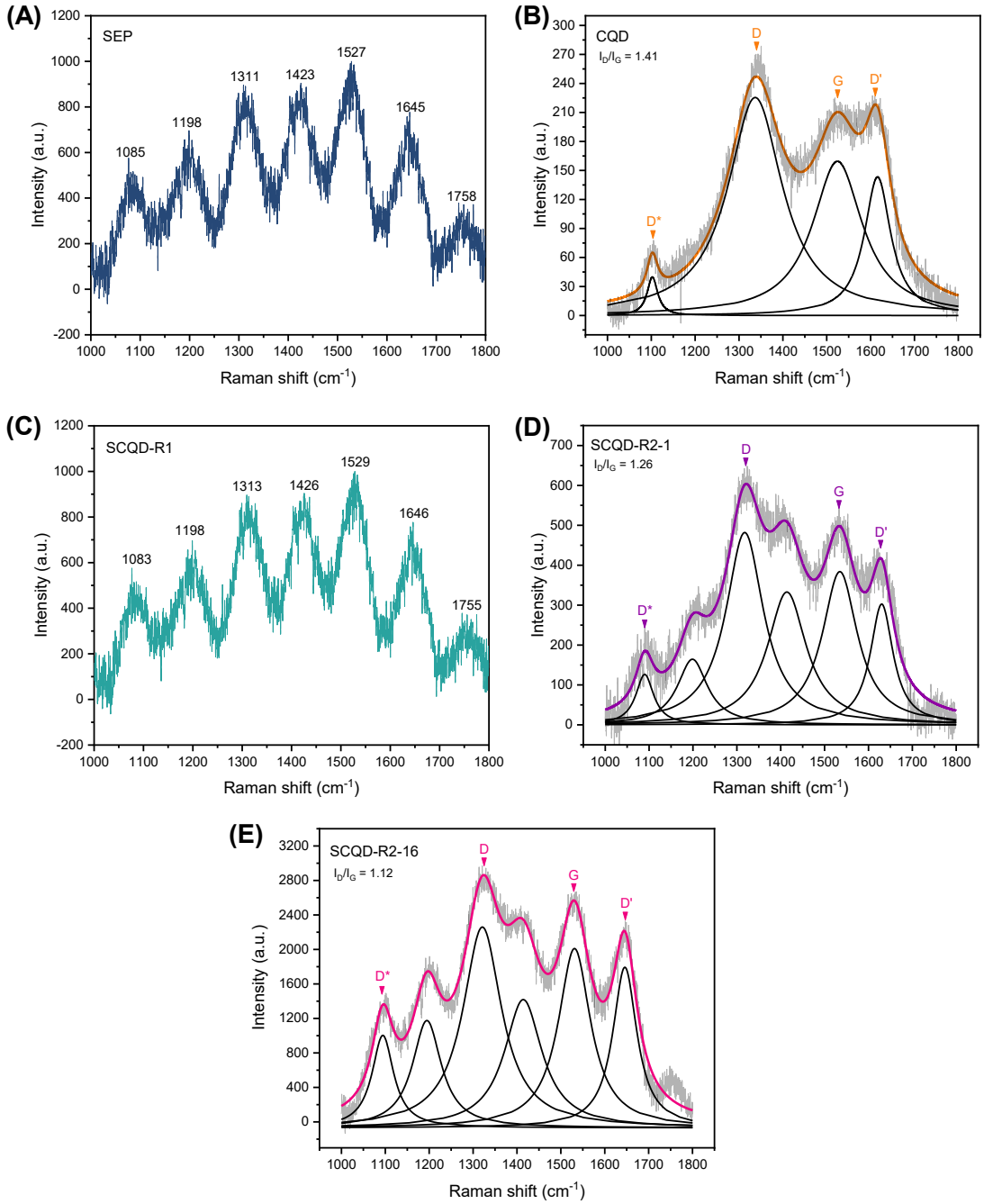

Table 5 - Raman peak properties for CQD, SCQD-R1, SCQD-R2-1, and SCQD-R2-16 hybrid nanomaterials

Sample	D*	D	G	D'	I_D/I_G
CQD	1102.49	1336.95	1524.49	1615.91	1.41
SCQD-R1	-	-	-	-	-
SCQD-R2-1	1090.01	1317.91	1534.79	1630.16	1.26
SCQD-R2-16	1094.39	1321.08	1531.08	1645.83	1.12

FT-IR can be a valuable technique to investigate the functional groups at the surface of materials and obtain information about possible interactions between clays and CQD in the hybrid nanomaterials. For materials containing sepiolite, two particular ranges of the spectra were chosen: the 4000-3000 cm^{-1} range (Figure 23A), where OH stretching vibrations can be observed, and the 1800-400 cm^{-1} region (Figure 23B), related to water deformation and lattice modes. The band at 3724 cm^{-1} is assigned to the OH stretching vibration of silanol groups (Si-OH) situated on the external surface of the pristine sepiolite, and the band at 3689 cm^{-1} corresponds to OH stretching modes in Mg_3OH units in the octahedral layer. The other bands observed in the silicate spectrum are related to two different types of water; the first one is observed at 3624 cm^{-1} and 3562 cm^{-1} and can be associated with H_2O coordinated to Mg sites at the ribbon edges, whereas the bands at 3374 cm^{-1} and 3242 cm^{-1} are due to zeolitic water in the tunnels of sepiolite (Walczyk et al., 2020). To better illustrate the distribution of functional groups, Figure 24 displays SEP structural scheme. For pure CQD, the FT-IR spectrum in the range of 4000-3000 cm^{-1} shows a broad band with maxima around 3318 cm^{-1} and 3093 cm^{-1} related to the stretching vibration of -OH and -NH groups, indicating the presence of functional groups at the CQD surface (Kundu et al., 2018). The presence of these groups is essential to the high solubility and stability of the CQD nanoparticles.

The SCQD-R1 hybrid nanomaterial shows a spectrum very similar to the sepiolite, nevertheless, it is possible to note displacements of the bands. The band associated with the silanol vibration shifts to 3735 cm^{-1}, while the feature associated with Mg_3OH units moves to 3689 cm^{-1}. The bands related to coordinated water at 3621 cm^{-1} and 3562 cm^{-1} don't appear to be too disturbed, while greater displacements can be observed in the bands of zeolitic water at 3368 cm^{-1} and 3236 cm^{-1}. Despite the similarity between the SCQD-R1 and sepiolite spectra, the displacements observed indicate perturbation of the silanol groups and zeolitic water in the clay, probably caused by the association with CQD.

Figure 23 - FT-IR spectra of pure sepiolite and SEP-CQD hybrid nanomaterials in the range of (A) 4000-3000 cm^{-1} and (B) 1800-400 cm^{-1}

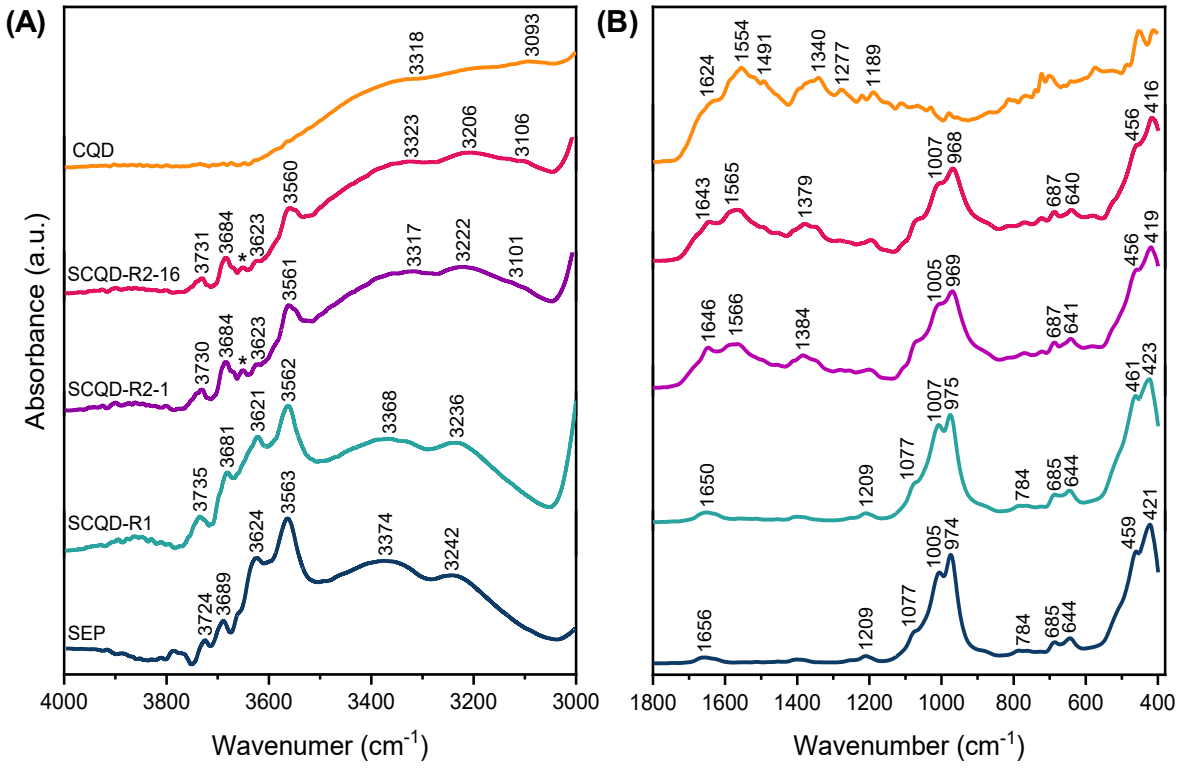

Figure 24 - Schematic illustration of sepiolite structure

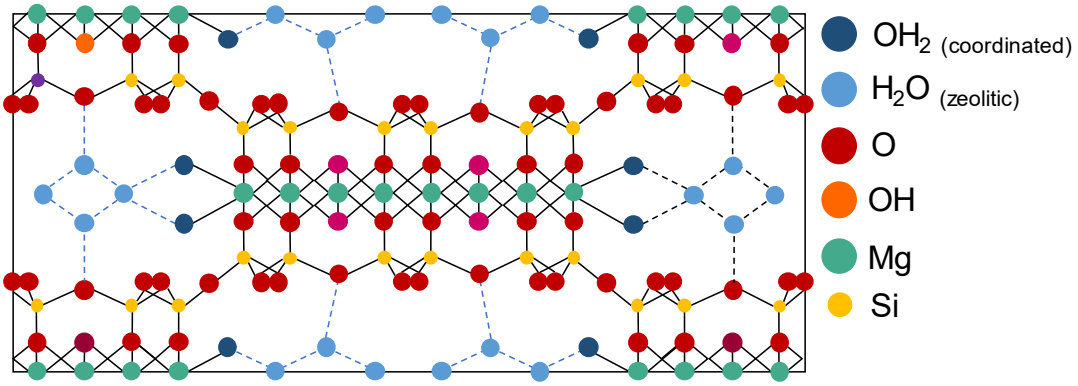

Source: Adapted from Bailey (1980)

The SCQD-R2-1 and SCQD-R2-16 hybrid nanomaterials spectra also demonstrate displacements of the band associated with the silanol group that shift from 3724 cm^{-1} in sepiolite to 3730 cm^{-1} and 3731 cm^{-1}, respectively (Figure 21A). Displacements of the bands regarding Mg_3OH units and coordinated water can be observed, however, they are less pronounced than in the SCQD-R1 hybrid. It is noteworthy that in SCQD-R2-1 and SCQD-R2-16 hybrids can be noted for the arising of a band of low intensity in 3650 cm^{-1}, besides that, the band at 3623 cm^{-1} has its intensity drastically decreased, which could indicate intense interactions of the CQD

and hydroxyls of coordinated water. The range of the spectra related to zeolitic water demonstrates the most significant displacements, where the bands at 3374 cm^{-1} and 3242 cm^{-1} for sepiolite shift to 3317 cm^{-1} and 3222 cm^{-1} in the SCQD-R2-1 sample, and 3323 cm^{-1} and 3206 cm^{-1} in SCQD-R2-16, respectively. Moreover, it is possible to observe in the spectra of the hybrids the band associated with the vibration of the N-H bond in CQD.

In the 1800-400 cm^{-1} region of the sepiolite spectrum (Figure 23B), it is possible to distinguish a band at 1656 cm^{-1} assigned to O-H bending modes in zeolitic water. The band at 1209 cm^{-1} is due to asymmetric stretching vibration of Si-O-Si, while 1005 cm^{-1} and 974 cm^{-1} are attributed to Si-O in-plane stretching vibration, and the 1077 cm^{-1} band is due to Si-O out-of-plane vibration. At 784 cm^{-1} and 459 cm^{-1} it is shown the bands associated with Si-O-Si bending stretching are shown, and the 685 cm^{-1} and 644 cm^{-1} absorptions are due to translation and bending of hydroxyls in Mg-OH, respectively. The band at 421 cm^{-1} is associated with the deformation mode of MgO_6 octahedral units (Walczyk et al., 2020).

For pure CQD, it is possible to identify bands at 1624 cm^{-1}, 1554 $cm^{-1,}$ and 1340 cm^{-1} associated with C=O and asymmetric and symmetric stretching of the COO^- group, respectively. A band at 1189 cm^{-1} associated with the bending vibration of the C-O bond in oxygen-containing groups can be observed. These results indicate the presence of functional groups on the surface of CQD. The shoulder appearing at 1491 cm^{-1} is attributed to the stretching vibration of C=C in aromatic structure, indicating the formation of the characteristic sp^2 core in CQD, whereas at 1277 cm^{-1}, it is possible to see a band related to the -C-N that could indicate the successful nitrogen doping during the synthesis (Perumal et al., 2022). In wavenumbers below 1000 cm^{-1}, it is common to observe modes attributed to O-H, C-H, and aromatic ring bending vibration (Kundu et al., 2018). In general, the spectrum of carbon quantum dots demonstrates the presence of an aromatic structure doped with nitrogen and co-functionalized by both amino groups and oxygenated groups.

As in the 4000-3000 cm^{-1} range, the SCQD-R1 hybrid has a spectrum similar to sepiolite, except for the shift of the band associated with zeolitic water from 1656 cm^{-1} in clay to 1650 cm^{-1} in the hybrid, suggesting that interactions involving O-H could take place in association with sepiolite and CQD in SCQD-R1 hybrid. For SCQD-R2-1 and SCQD-R2-16, the hybrid nanomaterials spectra with features related to sepiolite and CQD can be noted. The bands referring to C=O and the asymmetric and symmetric stretching of the COO^- group in CQD moved to 1646 cm^{-1}, 1566 $cm^{-1,}$ and 1384 cm^{-1} for SCQD-R2-1 and 1643 cm^{-1}, 1565 $cm^{-1,}$ and 1379 cm^{-1} for SCQD-R2-16, respectively.

In the FT-IR spectra of the hybrid materials, it is possible to note displacements in the band attributed to the silanol group, implying interactions through hydrogen bonds between these groups and the functional groups of the CQD. In this context, it is important to mention that the SCQD-R2 samples seem to show a smaller relative intensity of the Si-OH band when compared to the other hybrids, which can suggest a more intense perturbation of the silanol group in this sample. According to Alcântara et al. (2014), this behavior is common in sepiolite-based hybrid materials and is indicative of stronger interactions from the external surface of the silicate with other species. The bands that are characteristic of OH stretching modes in Mg_3OH did not retain their position, which could reflect that the surrounding environment of Mg_3OH units became less uniform as a result of strong interactions with CQD nanoparticles.

4.3 THERMAL ANALYSIS

Thermal analysis was recorded in the range of 30-900 °C under a synthetic air atmosphere to evaluate the thermal stability of the nanomaterials, complementing the study of the clay-carbon quantum dots hybrid nanomaterials. CQD (Figure 25A) exhibits a fourth-step degradation process. From 30 °C to 100 ºC, the material lost 11.2% of its weight. This step is associated with the T_{max} at 58.33 °C in the DTG curve and occurs due to the elimination of physically adsorbed water. The second step occurs in the range of 200-500 °C, where it can be observed a gradual weight loss of 62.6% in correspondence to the intense peak at 457.59 °C in the DTG curve, indicating the temperature where the maximum weight loss occurs. This step and the following weight loss with T_{max} at 542.7 °C are related to some complex chemical reactions, including chain scission, hydrolysis/alcoholysis of carbonaceous linkage, and branching and crosslinking reaction of the molecular chains of CQD (Yang et al., 2018). The weight loss above 650 °C associated with the peak at 803.03 °C might be associated with polyaromatic carbonaceous residues with high stability at high temperatures, justifying the subsequent slow weight loss for CQD. At 800 °C, a residue of 15.16% is observed, which is in agreement with the report by (Zhu et al., 2019) that reported a residue of approximately 20% using a CQD obtained from citric acid as a precursor in a hydrothermal synthesis.

Figure 25 - Thermogravimetric analysis and derivative thermogravimetric analysis of (A) CQD, (B) sepiolite, (C) SCQD-R1, (D) SCQD-R2-1, and (E) SCQD-R2-16 hybrid nanomaterials with a heating rate of 10°C.min^{-1} under a synthetic air atmosphere

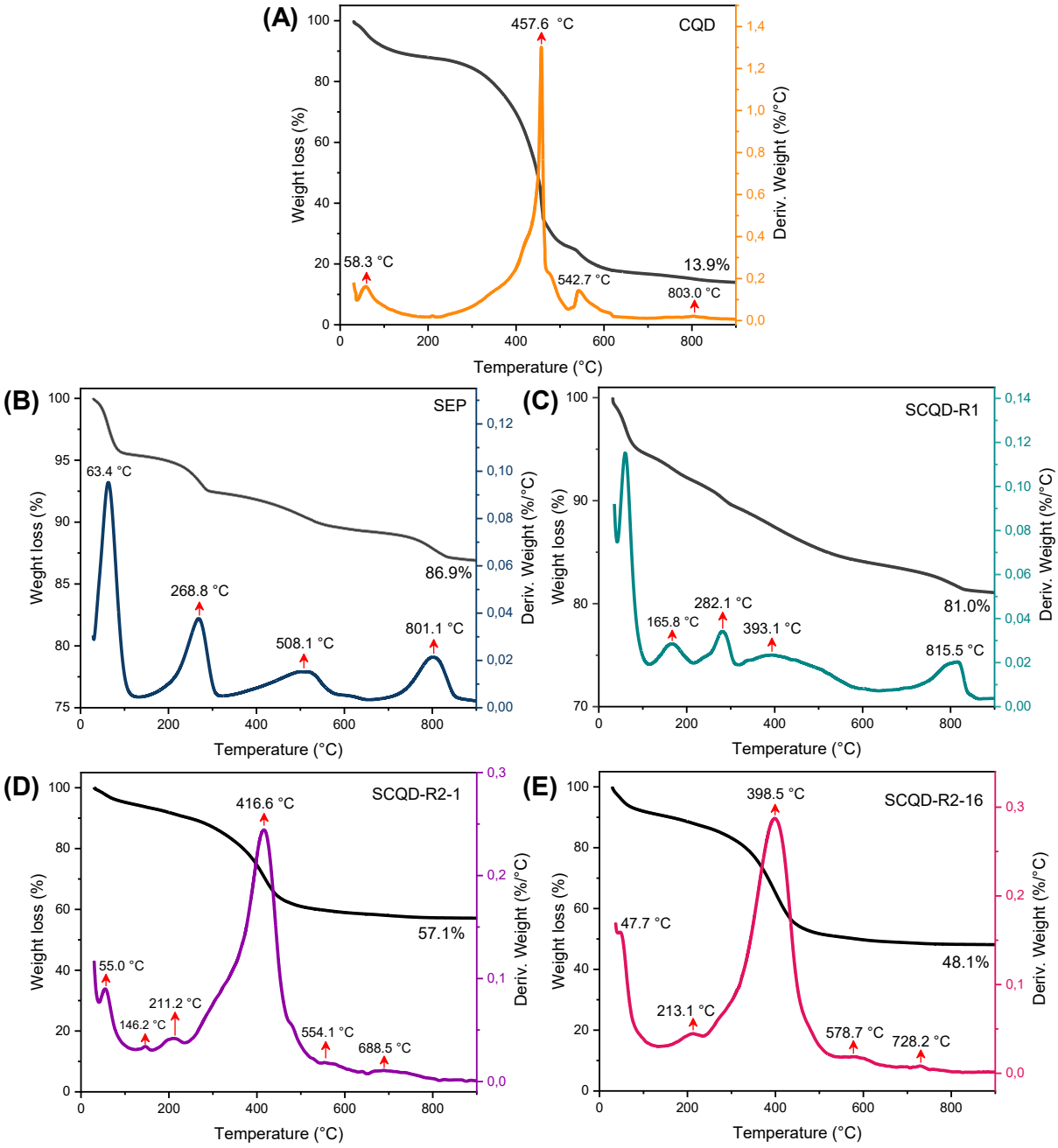

Neat sepiolite exhibited a first weight loss of approximately 4.5% that corresponds to the removal of adsorbed water, occurring between 30 °C and 130 °C with T_{max} at 63.4 °C in the DTG curve (Figure 25B). The next weight loss of 3.2% is completed before 300 °C and could be associated with the elimination of zeolitic water from the voids of the sepiolite structure. The coordinated water molecules in the sepiolite structure are released in the range of 400–650 °C, which is in correspondence with the peak at 508.1 °C in the DTG curve, resulting in a weight loss of 3.1%. These water molecules are found coordinated with magnesium atoms located in the tunnels of sepiolite (Lima et al., 2017; Sarıkaya; Önal; Pekdemir, 2020). In the

fourth step, SEP loses 2.3% of its weight in an event with T_{max} at 801.1 °C in the DTG curve, corresponding to the internal recrystallization of the dehydroxylated phase to become protoenstatite ($MgSiO_3$) (Rebitski et al., 2018). Even after thermal analysis reaching 900 °C, sepiolite degraded only 13.1% of its weight, demonstrating its outstanding thermal stability.

Different from CQD or SEP, SCQD-R1 (Figure 25C) possessed a five-step degradation process, which might suggest a more complex degradation process. From 30 °C to 114 ºC occurs the elimination of physically adsorbed water that is associated with the T_{max} at 60.1 °C in the DTG curve, resulting in a weight loss of 5.6%. The second and third steps showed a mass loss of 5.2% with T_{max} at 166.4 °C and 280.5 °C, respectively, which could be ascribed to the elimination of zeolitic water from sepiolite. The event at 393.1 °C in the DTG curve might be attributed to the degradation of functional groups at the CQD surface, which takes place from approximately 320 °C to 640 °C and generates a weight loss of 5.5%. For SCQD-R1, therefore, the association of CQD and SEP resulted in earlier onset of the step of CQD degradation. Moreover, the event associated with the elimination of coordinated water at 508.1°C in pure sepiolite cannot be seen in the DTG curve for the SCQD-R1 hybrid. The T_{max} at 813.2 °C observed in the DTG curve can indicate that the temperature of the internal recrystallization to $MgSiO_3$ became higher, which supports a gain of thermal stability. From 640 °C to 900 °C, SCQD-R1 loses 2.7% in weight, which results in a residue of 81.0%, lower than sepiolite due to the presence of CQD.

As can be observed in Figure 25D-E, the SCQD-R2-1 and SCQD-R2-16 hybrid nanomaterials show similar thermal profiles. However, the first one has a degradation process in six steps, while the second one has five. The events observed in the DTG curve at 55.0 °C and 47.7 °C for SCQD-R2-1 and SCQD-R2-16 are associated with the removal of physically adsorbed water. Considering this first event for SCQD-R1, SCQD-R2-1, and SCQD-R2-16 nanomaterials occurring at 60.1 °C, 55.0 °C, and 47.7 °C, respectively, it is possible to observe a reduction of T_{max} that can be related to the increase of CQD in hybrids. The elimination of zeolitic water in SCQD-R2-1 might be associated with two events in the DTG curve with T_{max} at 165.8 °C and 282.1 °C, similar to that observed in SCQD-R1, which could be related to a certain level of heterogeneity (distinct states) of zeolitic water. On the other hand, SCQD-R2-16 shows only one peak at 213.1 °C associated with this phenomenon, implying greater homogeneity, which could be associated with the higher content of CQD of this hybrid nanomaterial. The weight loss associated with the removal of zeolitic water in the TG curve is 3.2% for pure sepiolite, whereas for SCQD-R2-1 and SCQD-R2-16 is 4.0% and 3.6%,

respectively, suggesting that the weight loss in these samples is related to the same event occurring in sepiolite.

The most intense event observed in the DTG curve occurs at 416.6 °C and 398.5 °C, with a weight loss of 30.6% and 36.4% for SCQD-R2-1 and SCQD-R2-16, respectively, which can be related to the degradation of functional groups at the CQD surface. Additionally, the weight losses with T_{max} at 554.1 °C and 578.7 °C observed in the DTG curves are also associated with the degradation process of CQD, but in this case, the T_{max} are shifted to higher temperatures. This might suggest that the association of SEP and CQD in the SCQD-R2-1 and SCQD-R2-16 hybrids is complex, favoring or disfavoring different reactions related to the degradation of CQD. The T_{max} observed at 688.5 °C and 728.2 °C in the DTG curve are difficult to evaluate once they could be related with events regarding both CQD and SEP. Besides that, the amount of residue generated at the end of the thermal analysis, it is possible to observe an inverse trend regarding the ratio of CQD; that is, the greater the amount of CQD in the final material, the lower the amount of residue.

4.4 OPTICAL PROPERTIES

With the aim of exploring the optical properties, UV-Vis and photoluminescence spectroscopy analysis of CQD and the hybrid nanomaterials were carried out. As shown in Figure 26, an aqueous CQD dispersion exhibits three bands at 239 nm, 348 nm, and 547 nm. The first band is associated with π-π* transitions of the C=C bonds in sp^2 conjugated carbon core, whereas the second band represents n-π* transitions in C=O and C=N bonds (Li et al., 2018). The absorption band in the visible region can be ascribed to lower energy states of N-containing functional groups on the surface of CQD (Deb; Chowdhury, 2022).

The UV-Vis spectrum of a dispersion in water of sepiolite was initially measured (Appendix A), indicating the absence of absorption bands considering the range analyzed. The hybrid nanomaterials displayed a band in the visible region related to the presence of CQD, however, minor shifts of the maximum occur. For SCQD-R1, it is observed at 543 nm, and for both SCQD-R2-1 and SCQD-R2-16 at 536 nm. Moreover, the SCQD-R1 hybrid shows the rise of absorption in the range of 600-800 nm, which could indicate new molecular states. Regarding the UV region, the bands associated with CQD are not well defined for SCQD-R1, nevertheless, it is possible to see a shift to 337 nm for both SCQD-R2-1 and SCQD-R2-16 hybrid nanomaterials, which might indicate modifications involving C=O and C=N bonds. These

results indicate that the structure of CQDs is largely preserved during the synthesis in the presence of sepiolite, although slight shifts in the spectra of hybrid nanomaterials are observed, indicating electronic states alterations due to interactions between CQD surface states and the clay matrix.

Figure 26 - UV-Vis spectra of an aqueous solution of CQD (25.0 mg.L^{-1}), SCQD-R1(500.0 mg.L^{-1}), SCQD-R2-1 (80.0 mg.L^{-1}), and SCQD-R2-16 (80.0 mg.L^{-1})

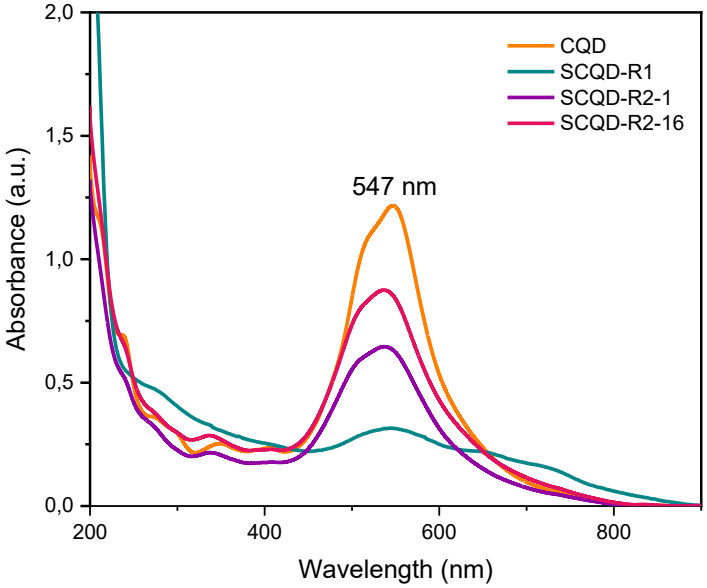

The UV-Vis spectroscopy was also applied to investigate the stability of CQD and the hybrid nanomaterials by monitoring the visible band over time as a function of storage time. From the results observed in Figure 27, after a week, the absorbance of CQD is reduced from 1.0 to 0.54, which might be associated with the loss of stability related to the aggregation of these nanoparticles. In contrast, the absorbance for SCQD-R1 slightly reduces after four days, varying from 1.0 to 0.98, remaining higher compared to other materials for approximately two weeks. After that, the absorbance in this hybrid gradually decreases, becoming lower than CQD after 30 days, approximately, and at the end of the experiment, SCQD-R1 presents the lowest stability. For SCQD-R2-1 and SCQD-R2-16 hybrid nanomaterials, the reduction in the absorbance is more pronounced in the first week, especially in the first four days, which is similar to the behavior observed for pure CQD. After a week, the absorbance for SCQD-R2-1 and SCQD-R2-16 are 0.69 and 0.74, respectively, and at the end of the study, the values are 0.61 and 0.62, indicating a slow reduction. In general, the results indicate that the higher the content of CQD, the higher the stability of the hybrid nanomaterial.

Figure 27 - Stability of CQD, SCQD-R1, SCQD-R2-1 and SCQD-R2-16 hybrid nanomaterials dispersions monitored over time using UV-Vis spectroscopy

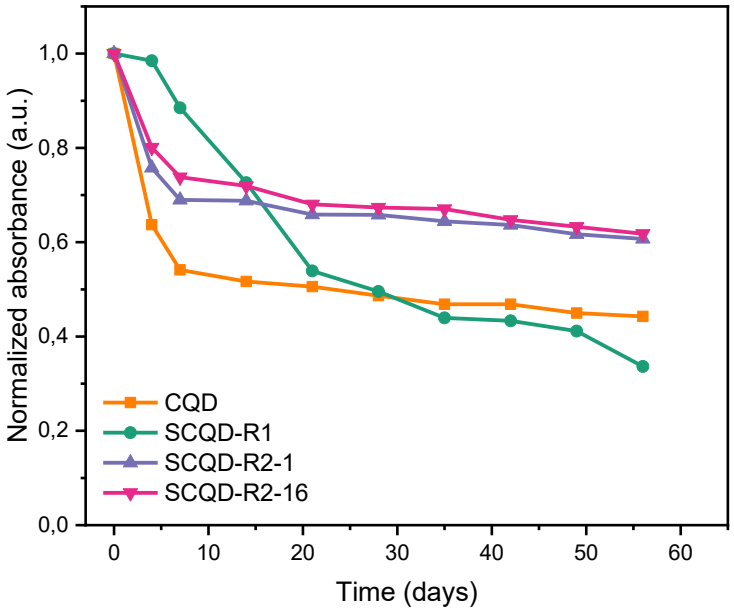

The counterparts of these hybrids may suggest their potential to be applied in different fields, especially those that use the photoluminescence property. Recently, it has been reported that sepiolite exhibits a spontaneous fluorescence (Castro-Smirnov et al., 2017; Ragu et al., 2020). Therefore, efforts were dedicated to investigating the photoluminescent properties of this clay and then evaluating the effect of interactions with other luminescent materials. The emission spectra of the sepiolite aqueous dispersion (Figure 28) exhibit a band centered at 420 nm when excited from 280 nm to 340 nm with increasing intensity, demonstrating an excitation-independent emission behavior. A second band can be observed with maximum intensity centered at 600 nm when excited at 520 nm, however, the emission appears to have an excitation-dependent behavior with the center red-shifting to wavelengths close to 650 nm. Based on these results, it can be inferred that sepiolite can be excited by different wavelengths with emission covering a wide range of the visible region.

Figure 28 – Emission spectra of aqueous suspension of pure sepiolite

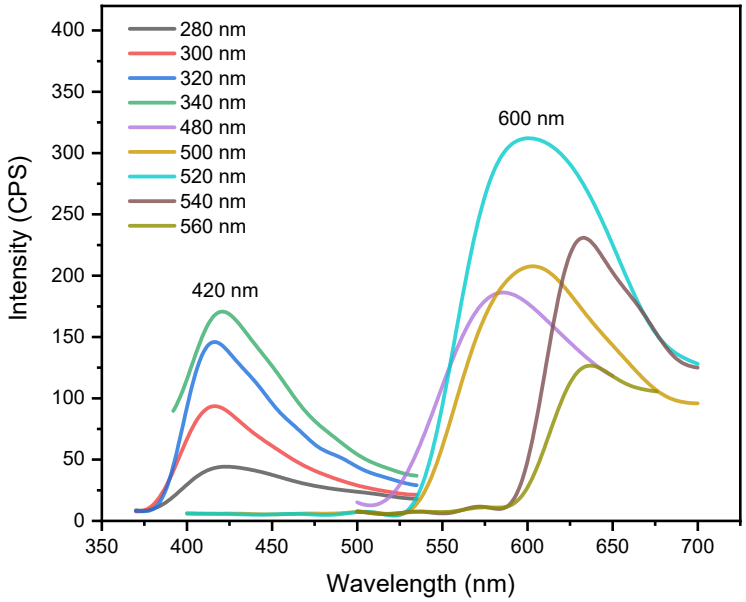

The photoluminescence spectra of CQD were evaluated at different wavelengths, as can be seen in Figure 29. By increasing the excitation wavelengths, the emission intensity of the CQD gradually increases until it reaches its maximum at 629 nm when it is excited at 550 nm and then starts to decline. The red emission remains almost unchanged with the increase in wavelength excitation, pointing out an excitation-independent behavior that could be related to a narrow size distribution and uniformity of surface state (Mintz et al., 2021). Moreover, a second emission can be observed (Figure 29B) at excitation wavelengths greater than 350 nm with an excitation-dependent behavior. The emission shifts from 450 nm to 525 nm when the excitation wavelength increases from 350 to 425 nm, and under excitation longer than 475 nm, the band can no longer be appreciable. In general, as the excitation changes, different contributions of the blue to green and red counterparts can be observed, indicating multiple fluorescence centers due to the involvement of different surface states of the CQD nanoparticles (Deb; Chowdhury, 2022; Macairan et al., 2022).

As can be observed in Figure 29B-D, the hybrid nanomaterials possess emission behavior quite similar to CQD, but some differences need to be pointed out. At first, minor shifts can be observed for all hybrids in the emission spectra, which could be associated with the interactions with the clay that act to modify the surface states of CQD. A reduction in the intensity of the red emission can be observed for all hybrids, but mainly for SCQD-R1. In that case, it can be assumed that interactions of the functional groups of CQD and sepiolite lead to non-radiative recombination, therefore decreasing the emission intensity.

Figure 29 - Emission spectra of (A, B) CQD, (C, D) SCQD-R1, (E, F) SCQD-R2-1, and (G, H) SCQD-R2-16 hybrid nanomaterials at different wavelengths

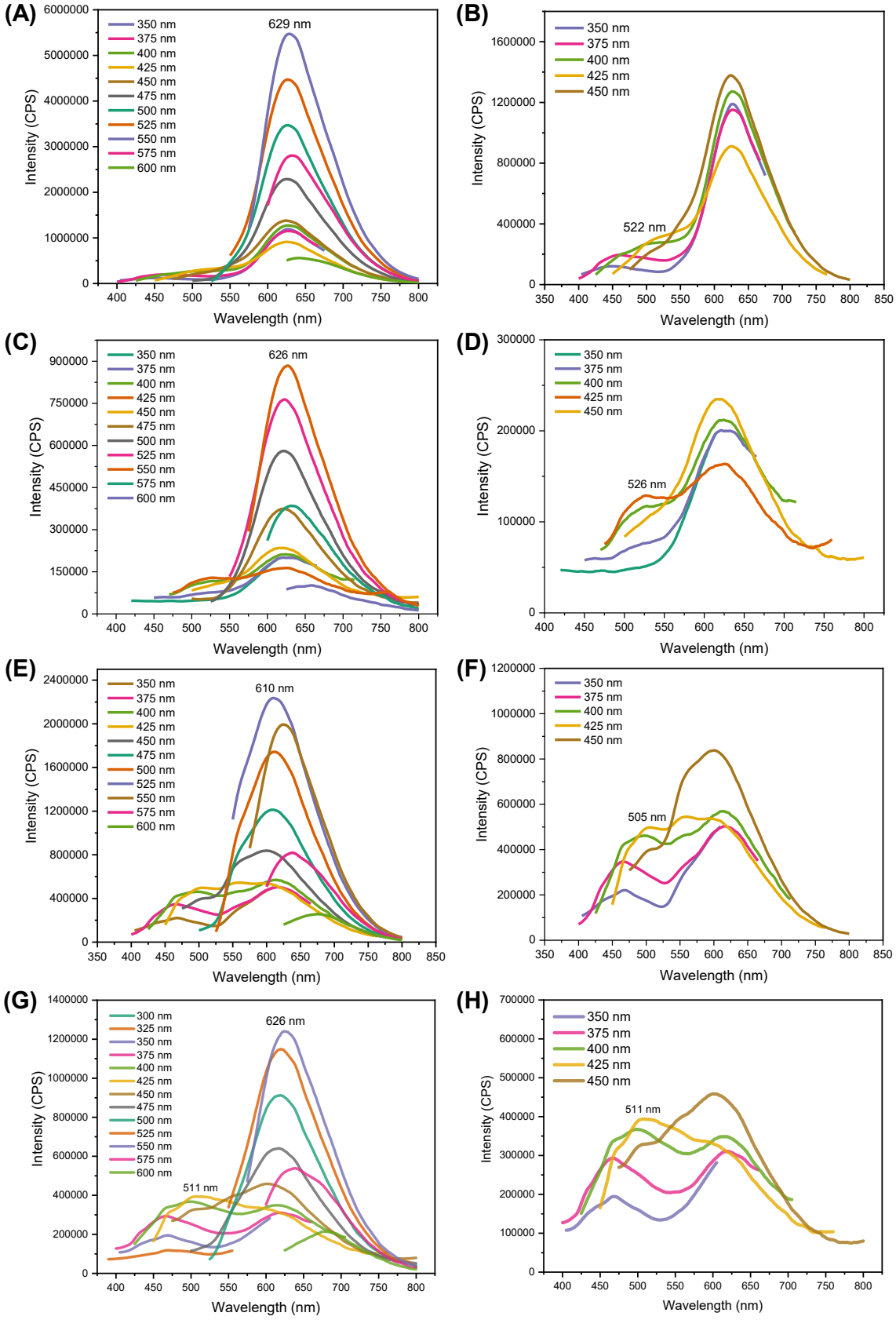

Moreover, for SCQD-R2-1 and SCQD-R2-16 hybrid nanomaterials, a higher contribution of the blue to green emission can be observed. Figure 30 exhibits the ratio between the maximum intensity emission of the red and green bands, revealing that they have higher green emission contributions compared to pure CQD. This effect is more pronounced for SCQD-R2-1 and SCQD-R2-1, which assume I_{red}/I_{green} values of 4.96 and 4.08, while CQD possesses an I_{red}/I_{green} value of 21.16. This could be related to the increase in the extension of sp^2 network, which is supported by Raman analysis, resulting in a higher degree of graphitization, detriment of the surface states upon carbonization. In detail, the blue-to-green emission mainly arises from the direct electron-hole recombination in the carbon core states of the CQD, while the surface state, related to the functional group bound to sp^2-domains at the edge of the CQD core, results in the red fluorescence. Therefore, the carbonization of functional groups on the edge/surface of CQD in favor of the growth of the sp^2 network in the CQD core is the probable cause for the increase in the short-wavelength contribution (Macairan et al., 2022; Zhang et al., 2022a).

Figure 30 – Ratio between the emission intensity in the red region (I_{red}) and the green region (I_{green}) for CQD, SCQD-R1, SCQD-R2-1, and SCQD-R2-16 hybrid nanomaterials.

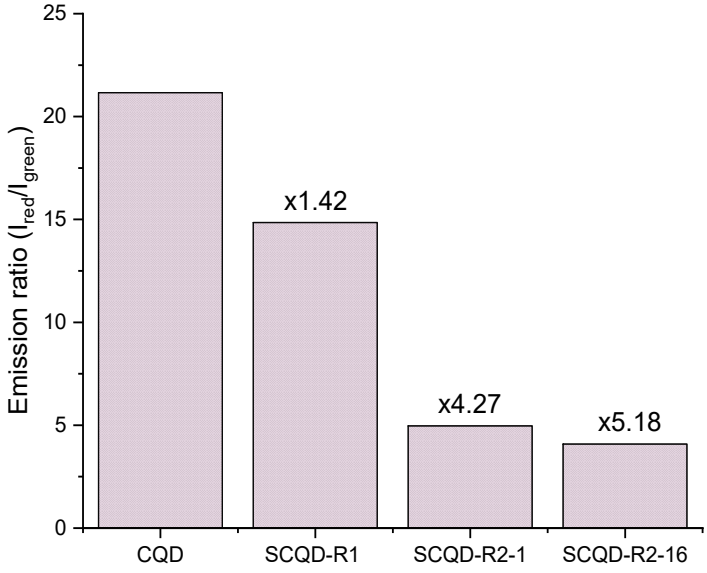

The photoluminescence excitation (PLE) spectra of CQD were recorded to unveil the excited states involved (Figure 31E). The PLE of the shorter-wavelength emission was monitored at 525 nm, revealing a transition at 430 nm. PLE of the red emission was measured at 625 nm, showing transitions at 405 nm, a shoulder around 495 nm, and 550 nm. The excited states around 400 nm can be related to n-π* transitions in the aromatic center of CQD, however,

this transition appears not to be efficient in the longer wavelength emission due to the larger Stokes shifts between the absorption and emission, indicating a nonradiative process during the transition to the lowest excited state (Zhang et al., 2022a). Nevertheless, the transition at 550 nm is effective in leading to red emission, which is related to distinct O- and N-containing groups at the edge/surface of CQD. The PLE spectra of the hybrid nanomaterials (Figure 31C-F) reveal similar profiles compared to CQD, however, a new transition is observed around 450 nm - 490 nm, which accounts for the increment of the blue to green emission. The arising of this new transition is due to the presence of sepiolite, proving that the interactions of this silicate with CQD through different routes affect the photoluminescence of CQD. It is noteworthy to mention that the red emission observed in all hybrid nanomaterials has great potential for bioimaging applications, since the red region benefits from minimum autofluorescence and light scattering by tissues, offering great imaging contrast and spatial resolution (Liu et al., 2020).

Figure 31 – PLE spectra for (A) CQD and (B) SCQD-R1, (C) SCQD-R2-1, and (D) SCQD-R2-16 hybrid nanomaterials

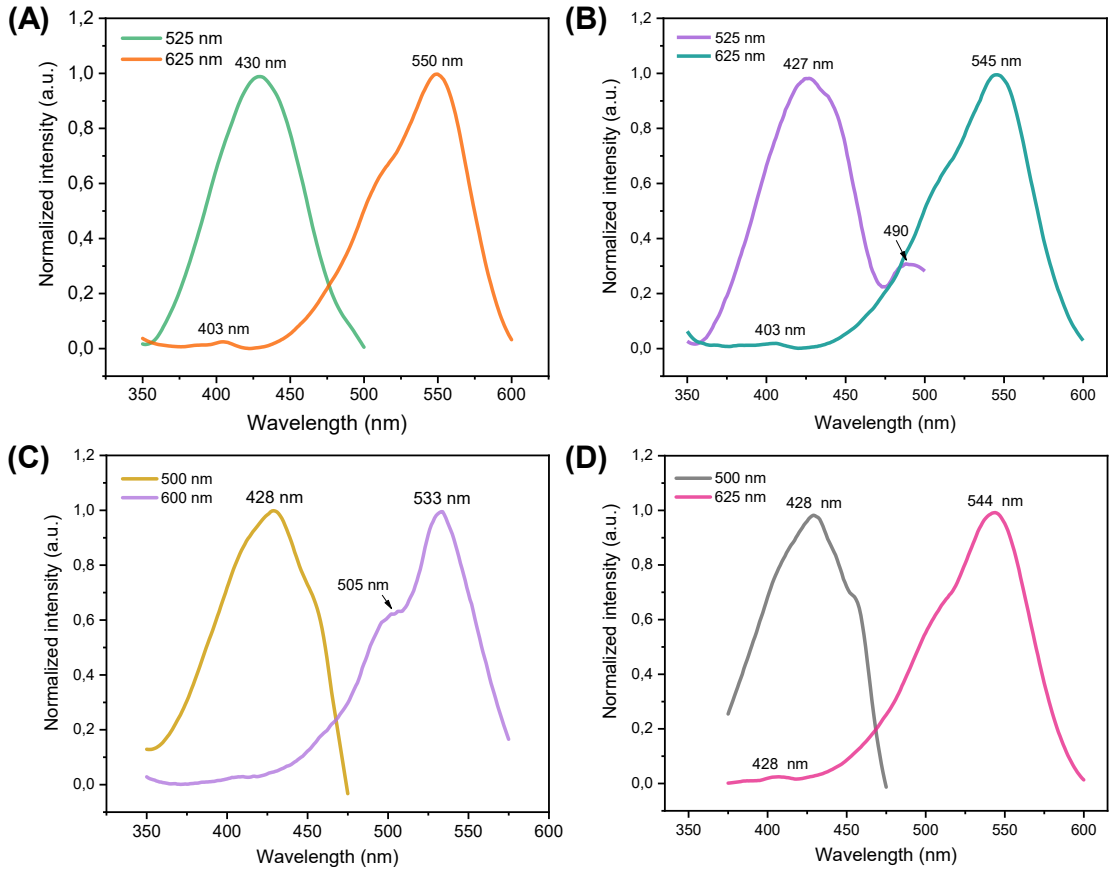

Time-resolved PL was measured for the samples under 450 nm excitation to investigate the origin of the two emissions further. All the decay profiles were fitted as bi-exponential functions on a timescale of nanoseconds (ns), confirming the presence of distinctive emissive states for green and red emissions for all samples. Table 6 summarizes the lifetimes, calculating the decay times of individual components and their respective overall contributions. The average lifetime has a faster (τ_1) and a slower (τ_2) component associated with the radiative recombination process of the core and surface states, respectively (Deb & Chowdhury, 2022; Li et al., 2018). The results indicate that the green emission has a longer average lifetime due to a greater contribution from the slower component τ_2, compared to the red emission. On the other hand, the red emission is mostly governed by the fast-lifetime component (τ_1), resulting in shorter average lifetimes. Considering CQD, the results demonstrate that as the average lifetime (τ_{AV}) decreases from 5.290 ns to 1.601 ns, the contribution of t_1 increases from 56.85% to 94.40%, suggesting that the core state plays an important role as the PL wavelength changes. The longer lifetime observed for the red emission is observed for all hybrid nanomaterials is related to the higher contribution of the slower component τ_2, indicating that the association with sepiolite results in greater involvement of functional groups in the emission.

Table 6 - Lifetimes of CQD, SCQD-R1, SCQD-R2-1 and SCQD-R2-16 hybrid nanomaterial at 450 nm excitation

Samples	**λ_{ems} (nm)**	**t_1 (ns)**	**t_2 (ns)**	**t_{AV} (ns)**
CQD	528	0.909 (56.85%)	6.141 (43.15%)	5.290
	626	0.885 (94.40%)	4.17 (5.60%)	1.601
SCQD-R1	557	1.434 (84.62%)	5.230 (15.38%)	2.947
	580	1.325 (86.23%)	4.65 (13.76%)	2.514
SCQD-R2-1	528	1.451 (56.08%)	6.125 (43.92%)	5.040
	626	0.913 (88.27%)	4.238 (11.73%)	2.182
SCQD-R2-16	528	1.422 (56.71%)	6.088 (43.29%)	4.995
	626	0.975 (87.75%)	4.11 (12.25%)	2.138

*The % values in parentheses () represent the fractional contribution of each of the lifetime components.

4.5 BIOLOGICAL ASSAY

Investigating toxicity is an important initial step when developing novel materials intended for interactions within biological systems. Hemocompatibility testing evaluates critical interactions between the materials and the different components of blood to determine if any toxic effects could originate from the exposure of these foreign materials to blood (De La Harpe et al., 2019; Sæbø et al., 2023). The highest percentage of hemolysis identified in this investigation was 4.5% for SEP at a concentration of 5000 µg/mL, indicating a slightly hemolytic activity, while CQD does not show hemolytic activity at this concentration (Figure 32).

Figure 32 - Hemolysis percentage of CQD, SEP, and the SCQD-R2-16 hybrid nanomaterial. The hemolysis percentage was evaluated at concentrations ranging from 5000 to 36.0625 µg/mL in the erythrocytes of sheep. The results correspond to averages ± of individual samples tested in triplicate. (*) $p<0.05$, compared to the positive control (Triton X-100 at 1%)

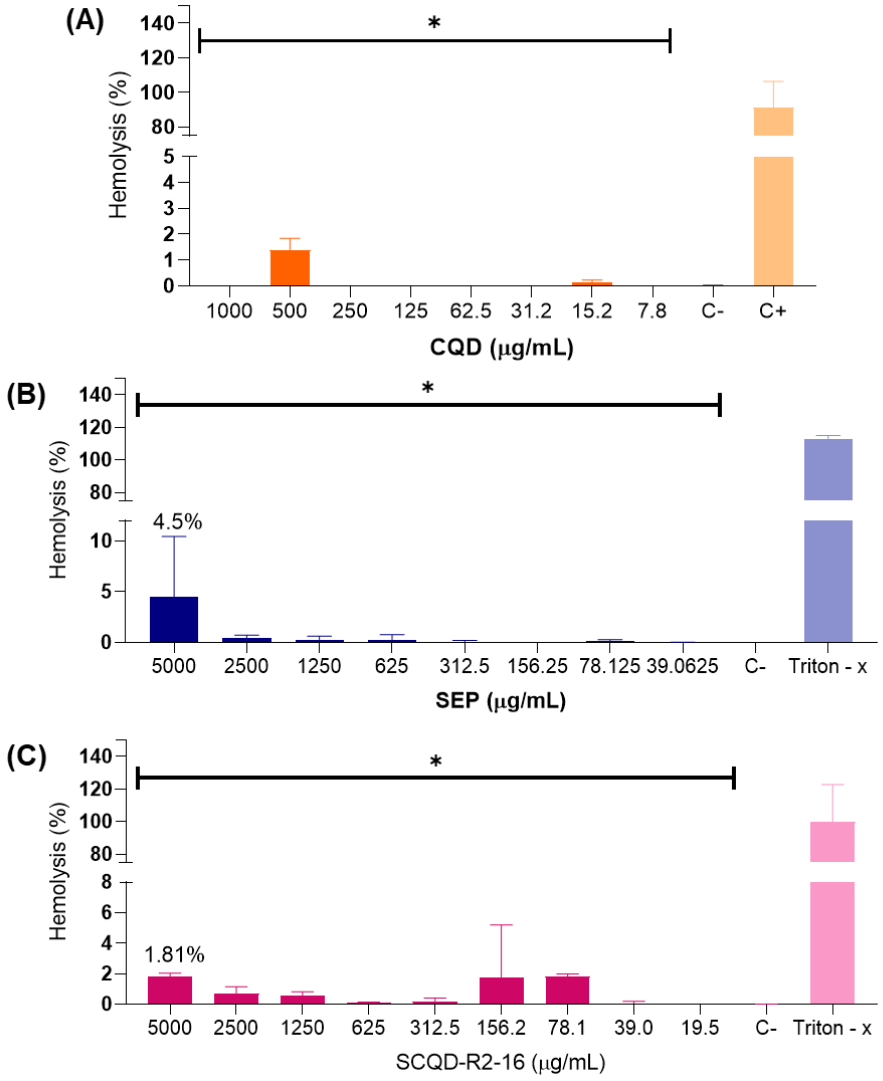

In comparison, the hybrid nanomaterial SCQD-R2-16 presented a percentage of 1.8%, indicating a reduction in hemolytic rate compared to pure sepiolite. The hemolytic activity of most nanoparticles depends on their concentration, structure, size, and shape. For silica nanoparticles, it has been reported that the toxicity is directly proportional to the amount of reactive silanol groups exposed on the surface (Yu; Malugin; Ghandehari, 2011). Considering this, the reduced toxicity observed for the SCQD-R2-16 hybrid nanomaterial can be attributed to the interactions between the silanol groups of SEP and CQDs, which likely act by passivating the active surface sites.

The non-hemolytic behavior of CQD, SEP, and SCQD-R2-16 hybrid nanomaterial was proven with a hemolysis assay, which opens up the opportunity to explore their potential applications in bioimaging. *In vitro* bioimaging was performed using U87MG cells exposed to excitation wavelengths of 408, 488, and 532 nm, corresponding to the typical DAPI, FITC, and Rhodamine channels. The images in Figure 33 demonstrate the cellular uptake of SEP, CQD, and SCQD hybrid nanomaterials, revealing well-defined intracellular fluorescence signals, consistent with their photoluminescence spectra, although no apparent differences in emission intensity were observed in 2D-cultured U87 cells. Nevertheless, the use of 2D monolayer cultures shows inherent limitations for determining subcellular localization and nanohybrids distribution.

To address these limitations, future studies should utilize 3D spheroid models and confocal laser scanning microscopy or advanced super-resolution techniques, such as Stimulated Emission Depletion (STED) or single-molecule localization microscopy techniques, including Photoactivated Localization Microscopy (PALM)/Stochastic Optical Reconstruction Microscopy (STORM) (PALM/STORM). These approaches can provide dynamic, molecule-specific, and high-resolution insights into intracellular trafficking, nanoparticle aggregation, and cytolocalization, enabling a more comprehensive understanding of hybrid nanomaterials under biological conditions. Such investigations are essential for optimizing the design of fluorescent nanoprobes and enhancing their translational potential in biomedical applications(., 2022b).

Figure 33 - Bright field and fluorescent images of U87 MG cells incubated with (A) SEP, (B) CQD, (C) SCQD-R1, (D) SCQD-R2-1 and (E) SCQD-R2-16 hybrid nanomaterials at 50.0 mgL^{-1}. Scale bar at 50 µm.

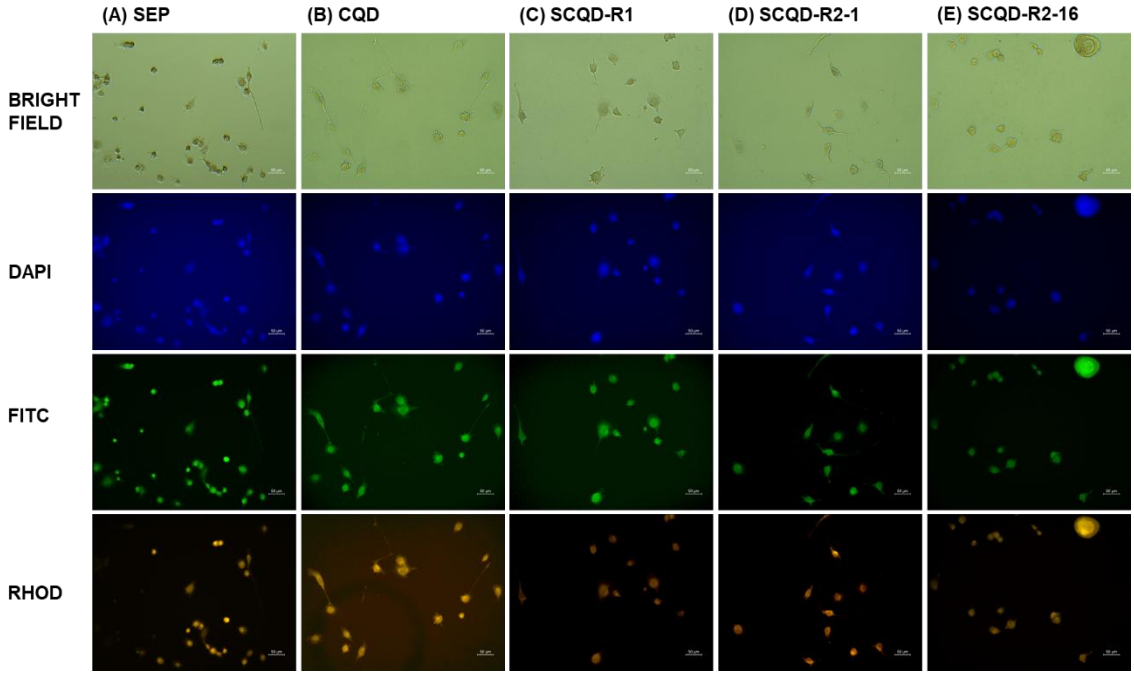

4.6 CONCLUDING REMARKS

The association of sepiolite and carbon quantum dots through different approaches demonstrates that the synthetic route is decisive in determining the structural and optical features of the resulting hybrids. When CQD was combined with pre-synthesized nanoparticles (route 1), a low content of the carbonaceous counterpart was effectively attached to the clay surface, leading to reduced photoluminescence and limited stability. In contrast, the *in situ* synthesis (route 2) enabled a much higher CQD loading with dispersed nanoparticles along the silicate fibrils as observed in TEM images. In this regard, shorter precursor-clay contact time favored stronger anchoring of CQD, while prolonged times led to partial detachment of nanoparticles. Raman analysis revealed that the presence of sepiolite in the synthetic route induced higher graphitic ordering in CQD, while FT-IR showed displacements of Si-OH and zeolitic water bands, confirming strong interfacial interactions with CQD. These structural differences impacted the optical behavior, with *in situ* hybrids exhibiting an increase in the blue–green emission and greater stability compared to free CQD. Importantly even with lower CQD content, SCQD-R1 retained sufficient luminescence to enable cellular imaging, demonstrating that limited anchoring of carbon dots on sepiolite can still impart effective fluorescent response. Furthermore, hemolysis assays confirmed that all hybrid nanomaterials

induced negligible red blood cell lysis (<5%), indicating a non-toxic response in vitro and supporting their suitability for fluorescence-based cellular studies.

5 MONTMORILLONITE-CQD HYBRID NANOMATERIALS

Contents

Chapter 5 Abstract

This chapter presents the results obtained from the association of montmorillonite, a lamellar clay with carbon quantum dots, emphasizing the morphology and the structural, thermal, and optical properties of the resulting hybrid nanomaterials. In addition, the effects of the different synthetic routes employed are examined. The toxicity of the materials was evaluated through hemolysis assay.

5.1 INTRODUCTION

The continuous evolution of human society increases the demand for innovative functional materials. In this regard, nanotechnology has made significant progress, enabling the hybridization of different classes of nanomaterials to surpass the limitations associated with single-component nanoparticle systems. Hybrid nanomaterials are defined as the combination of two or more components at the nanoscale that integrates the physical and chemical properties of the counterparts, often benefiting from the rise of synergistic effects that surpass the properties of each material alone (Azim et al., 2022; Li et al., 2023a). This approach offers the possibility of altering their morphology, structure, and composition by modifying the fabrication route, resulting in a hybrid nanomaterial with improved thermal stability, mechanical strength, electrical conductivity, and optical properties (Hayami et al., 2017; Meroni; Ardizzone, 2018).

Clay minerals are widely used to produce hybrid nanomaterials due to their outstanding properties, including high surface area, layer charge density, cation exchange, swelling capacity, chemical stability, and rheological behavior (Teixeira et al., 2025; Xie; Chen; Yang, 2023). They also had the benefit of being abundant and low-cost materials, which is particularly attractive for large-scale applications. Montmorillonite (MMT), one of the most representative members of this class, is a 2:1 dioctahedral clay mineral composed of an alumina octahedral sheet sandwiched between two silica tetrahedral sheets (TOT) (Oliveira; Alcântara; Pergher, 2017; Rebitski et al., 2018; Zhang et al., 2025). Moreover, the Si^{4+} in the silicon-oxygen tetrahedron can be replaced by cations such as Al^{3+} and Fe^{3+}, while the Al^{3+} in the octahedron is easily replaced by Fe^{2+}, Mg^{2+}, and Zn^{2+}, resulting in the formation of permanent negative charges on the MMT surface (Rebitski et al., 2019). The occurrence of isomorphic substitution also results in ion exchange capacity, swelling behavior, and surface reactivity, allowing interactions with other structural entities such as molecules, particles, and ions, through different mechanisms (Tipa et al., 2022).

Carbon quantum dots are a relatively new type of carbon nanomaterial that has attracted significant attention from the scientific community since their accidental discovery in 2004 (Xu et al., 2004). Their excellent properties include simple and low-cost synthesis, good biocompatibility, and tunable optical features (Ghosh et al., 2023; Li et al., 2022a; Siripothula et al., 2025). CQD are zero-dimensional nanoparticles (<10 nm) characterized by a sp^2 core and abundant functional groups on their surface, such as hydroxyl and carbonyl, and amine groups, which contribute to their high hydrophilicity (Sukunta et al., 2025). However, some drawbacks

of CQD are associated with nanoparticle aggregation, which leads to fluorescence quenching and loss of stability, limiting their applications (Carbonaro et al., 2020; Wang et al., 2024c). Integrating CQDs with layered hosts such as MMT offers a promising strategy to mitigate these drawbacks. The high surface area and negatively charged layers of MMT facilitate interactions with functional groups of CQD, helping to prevent the aggregation of these nanoparticles. Moreover, MMT can provide a protective microenvironment that improves CQD photostability, extending their lifetime in aqueous and biological media.

The association of carbon dots and clay minerals has been reported employing bentonite (Jlassi et al., 2023), saponite (Chuaicham et al., 2022), and halloysite (Massaro et al., 2019), however, the association of MMT and CQD is still scarce. Qu and coworkers reported the synthesis of green-emissive carbon dot@montmorillonite (g-CDs@MMT) materials that were prepared by embedding g-CDs into the structure of MMT clay. To obtain the CDs, a microwave method was employed, using citric acid and urea as precursors in the presence of water. Due to the confinement of g-CDs in the MMT clay matrix, g-CDs are uniformly dispersed in the resulting g-CDs@MMT, which efficiently prevents the aggregation-induced luminescence quenching of g-CDs (Zhai et al., 2019) . Yu and co-workers demonstrate the rapid synthesis of nitrogen and sulfur co-doped carbon dot@montmorillonite (C-dots@PGV) by adsorption onto Na^+-MMT clay. The resultant C-dots@PGV exhibited intense blue photoluminescence under UV light, good dispersibility, and enhanced stability compared to C-dot aqueous solutions(Yu; Yan, 2017) .

Despite the advances reported in the literature, studies dedicated to the fabrication of MMT–CQD hybrid materials through *in situ* synthesis are still lacking. In this context, this thesis proposes to address this gap by investigating the preparation of MMT–CQD hybrid nanomaterials *via* two routes: the physical assembly of pre-synthesized CQDs with montmorillonite, and the *in situ* formation of CQDs in the presence of the clay. Through these approaches, this work aims to understand how the synthesis pathway influences the structural organization, optical behavior, and biocompatibility of the resulting hybrid nanomaterials. The results presented in this chapter are intended to establish structure–property relationships and to provide information for applications of these materials in other fields.

5.2 MORPHOLOGICAL AND STRUCTURAL PROPERTIES

The diffraction patterns of MMT and the hybrid nanomaterials based on MMT and CQD are exhibited in Figure 34. For pristine MMT, peaks at 2θ = 7.3°, 19.8°, 28.3°, 35.0°, and 62.0°

are observed in correspondence with the reflection planes (001), (100), (005), (110), and (300), respectively. Considering the sheet thickness of MMT to be 0.96 nm (Azhar; Olad, 2014), the basal spacing of 1.21 nm (2θ = 7.3°) is observed, consistent with rich Na^+-MMT (Zhang et al., 2017a). Considering the hybrid nanomaterials, it is possible to observe diffractions associated with the presence of CQD. For MCQD-R1, the diffraction planes noted at 2θ = 26.5° and 2θ = 28.2° (in detail) are in correspondence with CQD and MMT, respectively. In the MCQD-R2-1 and MCQD-R2-16 hybrid nanomaterials, the diffraction planes observed at 2θ = 26.5° and 2θ = 26.6° are associated with CQD, while the peaks at 2θ = 27.8° and 2θ = 27.6°, respectively, are related to the presence of MMT. In general, slight displacements in this region are observed, suggesting minor structural alteration in the hybrid nanomaterials compared to their counterparts. The intensity associated with CQD in MCQD-R1 seems to be lower compared to MCQD-R2-1 and MCQD-R2-16, which may be related to its content in the hybrids.

Figure 34 - Diffraction patterns of montmorillonite, MCQD-R1, MCQD-R2-1, and MCQD-R2-16 hybrid nanomaterials, and CQD

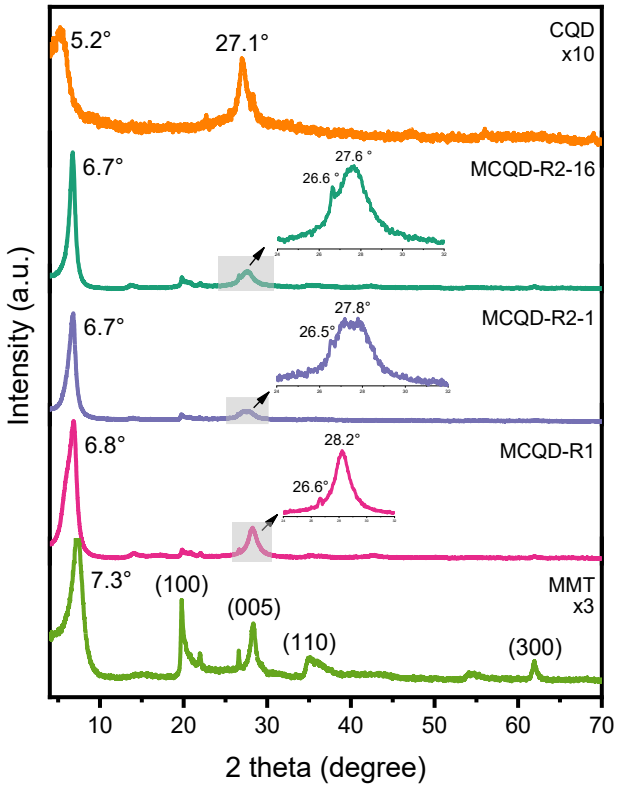

Figure 34 also shows that the hybrid nanomaterials exhibit displacements to lower angles in 2θ of the reflection plane (001) associated with MMT. Using the Bragg's Law, the increase in the interlayer spacing was calculated to be 0.34 nm for MCQD-R1 and 0.36 nm for both MCQD-R2-1 and MCQD-R2-16. These results indicate that the expansion of MMT is not

particular to a specific synthesis route, however, a higher increment is observed in the hybrid nanomaterials obtained from the *in situ* approach. In a previous work reported by the group, the average CQD diameter was determined to be approximately 4.8 nm (Cutrim et al., 2021), which is significantly larger than the basal spacing increase observed in the hybrids (0.34–0.36 nm). Therefore, the expansion of MMT cannot be ascribed to CQD intercalation. Instead, this minor shift may result from possible structural relaxation and reorientation of interlayer water molecules and/or the presence of ultrathin carbonaceous domains such as a single graphene layer (thickness = 0.34 nm) generated during synthesis as demonstrated by (Chen et al., 2014). The authors used MMT to adsorb crystal violet, followed by calcination under a N_2 atmosphere. The XRD analysis demonstrates that the interlayer of the calcinated material was 0.38 nm, close to the thickness of a single graphene layer (0.34 nm). Thus, these findings indicate that the CQDs primarily interact with montmorillonite through surface and edge-site anchoring rather than interlayer insertion.

Moreover, XRD analysis was carried out to investigate whether the increment in the interlayer space occurs before or after thermal treatment. For this, CA and U were solubilized in DMF, and then MMT was added. The mixture was kept under stirring for 1 h (R2-1) or 16 h (R2-16) and then centrifuged. The resultant samples were analyzed, and from Figure 35, it is possible to see that a time of contact of 1 hour was sufficient for the intercalation of species in MMT. The MCQD-R2-16 shows a slight displacement for lower angles (2θ = 6.48°), which could be the result of a longer contact time. However, after the thermal treatment, both hybrid nanomaterials presented the same value in 2θ = 6.70°.

Figure 35 - XRD patterns of pure montmorillonite, the synthesis mixtures before thermal treatment, and the hybrid nanomaterials (A) MCQD-R2-1 and (B) MCQD-R2-16

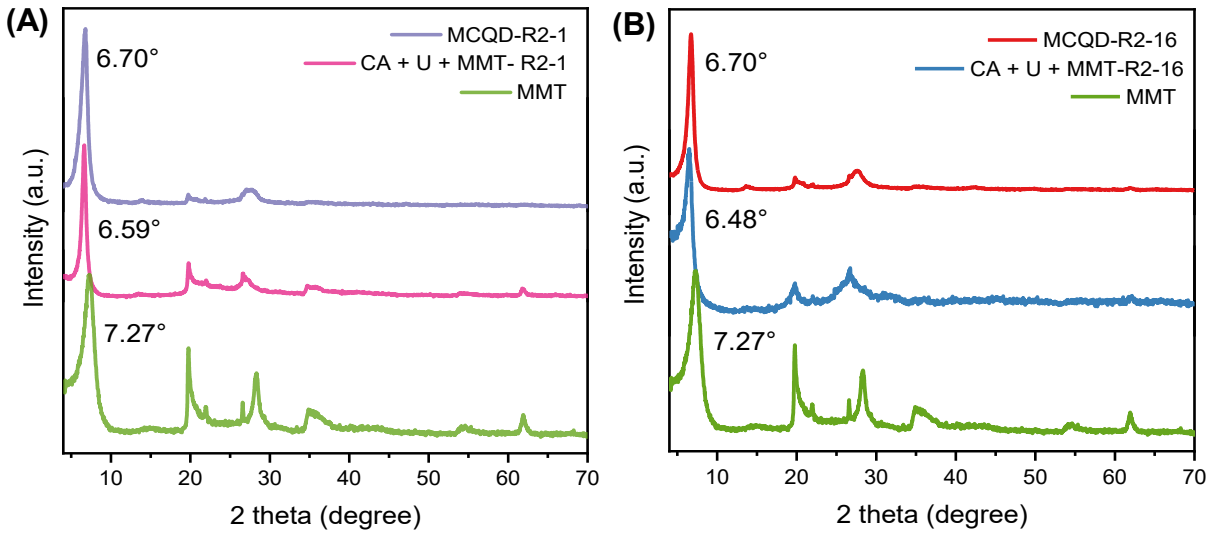

Elemental analysis was used to obtain the composition of MMT based hybrid nanomaterials as well as to determine the amount of CQD in the hybrid nanomaterials. MCQD-R1 possesses a content of 9.63% in weight (Table 7), which is similar to that observed for SCQD-R1, which can be attributed to the leaching of highly soluble CQD nanoparticles during the synthesis. Overall, the route one resulted in contents of CQD close to 10% for both clays. MCQD-R2-1 and MCQD-R2-16 have 89.32% and 34.00% of CQD, respectively, implying that a longer contact time between precursors and MMT did not allow a greater content of CQD, which is the opposite tendency observed for hybrid nanomaterials based on SEP and CQD. This counterintuitive result may be associated with the prolonged precursor–clay contact time. Extended stirring (16 h) could favor precursor aggregation or partial carbonization, leading to less efficient CQD formation and anchoring within the MMT structure.

In addition, excessive precursor adsorption on the external surface of MMT might block interlayer sites, thus reducing the effective incorporation of CQDs during the hydrothermal step. Similar behaviors have been reported in related nanocomposite systems (Li; Kaner, 2006) where extended reaction times or excessive precursor concentration resulted in decreased nanoparticle incorporation and poorer dispersion due to overgrowth or aggregation phenomena. In this study, the comparison between R2-1 and R2-16 suggests that shorter contact time facilitates more effective precursor utilization and homogeneous CQD nucleation in the presence of montmorillonite, while prolonged contact time reduces incorporation efficiency.

Table 7 - Elemental composition in weight of CQD and the MCQD-R1, MCQD-R2-1, and MCQD-R2-16 hybrid nanomaterials

Sample	C (%)	H (%)	N (%)	Amount of CQD (%)
CQD	71.57	4.86	23.57	100
MCQD-R1	4.33	3.35	1.95	9.63
MCQD-R2-1	62.93	5.45	20.94	89.32
MCQD-R2-16	22.10	3.54	8.36	34.00

To understand the possible interactions between MMT and CQD in the hybrid nanomaterials, FT-IR analysis was conducted (Figure 36). The spectrum of pure montmorillonite exhibits a band located at 3623 cm^{-1} attributed to the OH stretch of structural Al-OH bonding, while the bands centered at 3438 cm^{-1} and 1635 cm^{-1} represent the -OH stretching and bending vibrations of the interlayer water molecules. Additionally, the vibration at 1117 cm^{-1} is related to the stretching of the Si-O out-of-plane (Caccamo et al., 2020; Tyagi;

Chudasama; Jasra, 2006). The most intense bands in the MMT spectrum appear at 990 cm^{-1} and 516 cm^{-1}, representing the in-plane stretching and bending vibrations in the Si-O bond, respectively. The bands at 915 cm^{-1} and 884 cm^{-1} originate from AlAlOH and AlFeOH bending vibrations, respectively. Moreover, the band at 798 cm^{-1} corresponds to the deformation vibration of the Si-O bond of quartz and/or silica, which is present as an associated phase. The band at 615 cm^{-1} is assigned to the coupling vibrations of the Al-O group of the MMT structure, and the band at 463 cm^{-1} corresponds to the deformation of the Si-O-Si groups (Funes et al., 2020; Madejová, 2003; Wójcik-Bania; Matusik, 2021).

Figure 36 – FTIR spectra of pure montmorillonite, MCQD-R1, MCQD-R2-1, and MCQD-R2-16 hybrid nanomaterials in the range of 4000 to 400 cm^{-1}

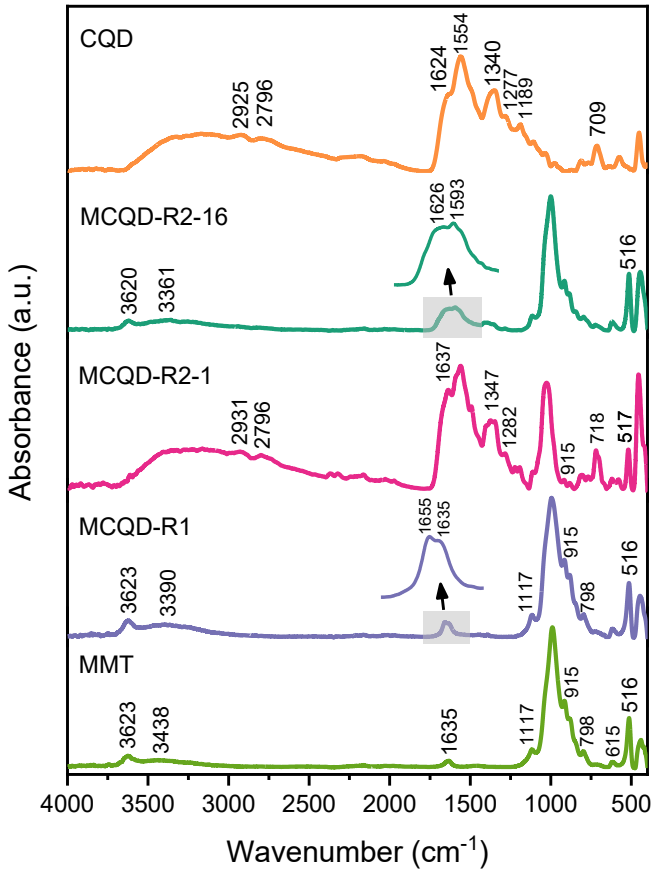

The MCQD-R1 hybrid nanomaterial possessed a spectrum similar to MMT, however, it is possible to see displacements in the bands and new features in the spectrum associated with CQD. The band related to the Al-OH stretching remains at 3623 cm^{-1}, while the band associated with the stretching of interlayer water is shifted from 3438 cm^{-1} to 3390 cm^{-1}. This displacement might suggest interactions between MMT and CQD, however, it is important to consider the contribution of hydroxyl groups from the CQD surface in this band. For pure MMT and MCQD-

R1 hybrid, it is possible to see the bending vibration -OH at 1635 cm^{-1}, nevertheless, a feature appears at 1655 cm^{-1}, as can be seen in detail, which are in correspondence with the stretching vibration of the C=O bond that appears at 1624 cm^{-1} in pure CQD. These displacements suggest strong interactions between MMT and CQD, which might have led to the increase in interlayer spacing observed in the XRD as a consequence of the perturbation introduced by the interaction of CQD groups, in particular, C=O, and the interlayer water of MMT.

The MCQD-R2-1 hybrid possesses a spectrum more similar to CQD due to a higher content of carbon quantum dots. A broad band between 3600-3000 cm^{-1} is observed, covering the range of the stretching vibrations of -NH and -OH functional groups present in the CQD surface. The bands at 2931 cm^{-1} and 2796 cm^{-1} represent the asymmetric and symmetric C-H stretching vibration, which appear at 2925 cm^{-1} and 2796 cm^{-1} in pure CQD. As the material has a similar spectrum compared to pure CQD, the band at 1637 cm^{-1} might be ascribed to the stretching vibration of C=O bonds, and a displacement for higher wavenumbers is observed, once it appears at 1624 cm^{-1} in the CQD spectrum. In addition, this band became sharper in the MCQD-R2-1 spectrum, which might be indicative of the formation of new bonds as reported by (Fang et al., 2018).

The bands associated with the asymmetric and symmetric stretching of the COO^- group for pure CQD are located at 1558 cm^{-1} and 1347 cm^{-1} in the MCQD-R2-1. The displacements described previously suggest the involvement of these groups in interactions between MMT and CQD. The band at 1490 cm^{-1}, ascribed to C=C stretching vibration in the sp^2 core of CQD, became more intense, and the vibration of the bond C-N shifted from 1277 cm^{-1} in pure CQD to 1282 cm^{-1} in the hybrid. In addition, it is possible to observe the rise of a band in 718 cm^{-1} in the MCQD-R2-1 spectrum that is ascribed to vibrations associated with the aromatic ring, suggesting possible modifications in the structure of CQD.

For MCQD-R2-16, the band ascribed to the vibrations of interlayer water is located at 3361 cm^{-1}. The bands related to the stretching vibrations of C=O bonds and with the asymmetric and symmetric stretching of the COO^- group for CQD are exhibited at 1626 cm^{-1}, 1593 $cm^{-1,}$ and 1362 cm^{-1}, respectively. It is worth mentioning that the greater shift of the bands associated with the vibrations of the carboxyl group is found for MCQD-R2-16, which suggests that a longer synthesis time might affect the interactions between MMT and CQD. The band associated with vibrations of the aromatic ring shifts from 708 cm^{-1} to 722 cm^{-1}, similar to what was observed for MCQD-R2-1. Notably, the Si-O in-plane stretching and bending vibrations observed at 990 cm^{-1} in pure MMT appear at 997 cm^{-1} in MCQD-R1, 1024 cm^{-1} in MCQD-R2-1, and 1000 cm^{-1} in MCQD-R2-16. These slight shifts suggest modifications in the local

environment, likely arising from strong interactions between CQDs and the MMT layers. Overall, FT-IR corroborates those interactions vary from weak water-mediated effects (R1) to stronger chemical bonding (R2), depending on synthesis time.

Beyond the descriptive evidence, a mechanistic understanding of the MMT–CQD interactions can be established based on the combined XRD, FTIR, and elemental data. Considering the CQD size (~ 4.8 nm) and the absence of corresponding shift in the (001) basal reflection, interlayer intercalation can be ruled out. Thus, the dominant interactions occur at the external surfaces and edge sites of montmorillonite. In Route 1 (physical mixing), the association between the components is primarily mediated by weak, water-bridged hydrogen bonding**,** consistent with the lower CQD loading and limited spectral perturbations. In contrast, Route 2 (in situ synthesis) favors the nucleation and anchoring of CQDs directly on the clay surface**,** enabling multiple bonding modes: (i) electrostatic adsorption facilitated by exchangeable cations (*e.g.*, Na^+) acting as charge compensators in the diffuse layer, which reduces repulsion between the anionic CQD surface groups and the negatively charged clay planes (Sheng et al., 2019); (ii) hydrogen bonding with surface silanols and coordinated water molecules (Wang; Wilson; Aristilde, 2024); and (iii) acid–base or ligand–surface interactions at Al–OH and Mg–OH edge sites.

5.3 THERMAL ANALYSIS

Thermal analysis was recorded in the range of 30-900°C under a synthetic air atmosphere to evaluate the thermal stability of the nanomaterials, complementing the study of the clay-carbon quantum dots hybrid nanomaterials. The thermal profile of pure CQD was presented in section 4.3. Neat montmorillonite showed a first weight loss of 7.1% occurring between 30 °C and 80 °C (Figure 37A), corresponding to the T_{max} in the DTG curve at 59.3 °C, which represents the removal of free and interlayer water (Jiang et al., 2024). The literature reports these processes to occur up to 250°C in MMT (Carazo et al., 2018). The following T_{max} are observed in the DTG curve at 651.9 °C and 860.2 °C, corresponding to the dihydroxylation process that is related to the release of water originating from -OH groups structurally bound in the lattice (Balek et al., 2006). In this step, MMT loses approximately 6.04% in weight, generating a residue of 86.84%. It is worth mentioning that the temperature intervals of dihydroxylation, as well as the amount of water released, depend on the nature of the adsorbed cations and surface hydration (Derkowski; Kuligiewicz, 2022).

For MCQD-R1, the first weight loss possesses T_{max} at 59.5 °C; however, the lowest rate of weight loss only occurs at approximately 200 °C, as can be seen in Figure 37B. This step can be attributed to the removal of free water (from both CQD and MMT) and interlayer water present in MMT. The following weight loss takes place from 200.0 °C to 440.0 °C, with T_{max} in the DTG curve at 345.1 °C, which could be associated with the removal of functional groups of CQD. The next step occurs up to 692.5 °C in the DTG curve (T_{max} at 624.0 °C) with a weight loss of 5.2% in correspondence with the dihydroxylation of the MMT, indicating that the association of CQD and the layered clay in the hybrid MCQD-R1 reduced the T_{max} associated with this event. The T_{max} at 724.7 °C in the DTG curve is associated with the weight loss of 1.8%, however, this step cannot be related directly to CQD or MMT. The hybrid nanomaterial generated a residue of 82.4%, resulting in a difference of only 4.4% from pure MMT due to the low content of CQD.

Figure 37 - TG and DTG of (A) MMT, (B) MCQD-R1, (C) MCQD-R2-1, (D) MCQD-R2-16 hybrid nanomaterials with a heating rate of 10 °C.min^{-1} under a synthetic air atmosphere

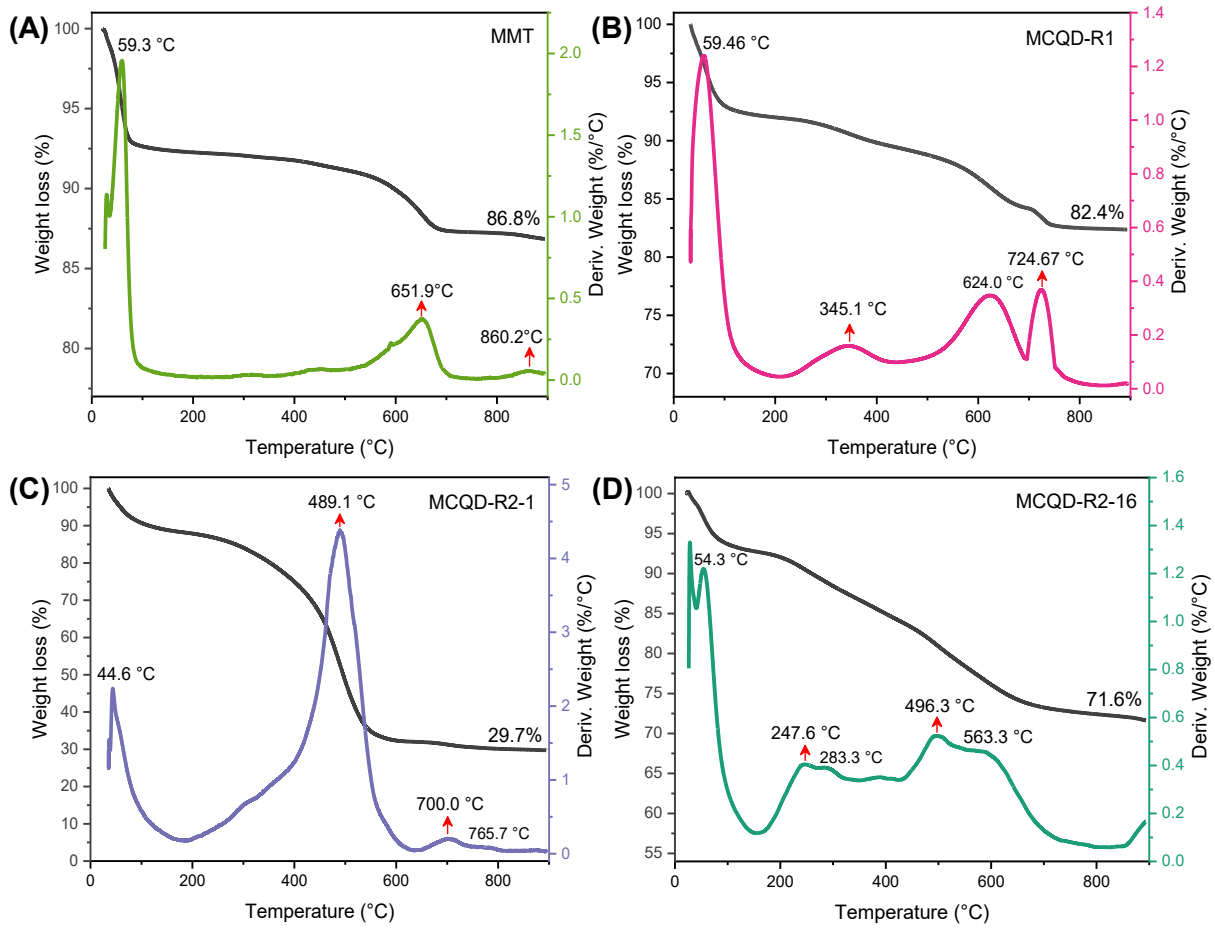

MCQD-R2-1 exhibited the thermal profile most similar to CQD among the three hybrids, probably due to its higher CQD content. The first step is observed in Figure 37C from

30 °C to 182 °C with a weight loss of 11.8%, which is related to the removal of free water from both CQD and MMT. This weight loss is related to the T_{max} at 44.6 °C and another T_{max} at approximately 300 °C, appearing as a shoulder that might be associated with the water release from the interlayer of MMT. In the following step, great weight loss occurs up to 635 °C, where the hybrid MCQD-R2-1 loses approximately 50.3% (T_{max} at 489.1 °C), which could be associated with the degradation of the CQD structure. The shift of T_{max} compared to pure CQD might suggest that the removal of functional groups takes place at a higher temperature, representing a gain of stability. The next step is related to the T_{max} at 700.0 °C in the DTG curve, indicating the dihydroxylation process of MMT. At 900 °C, a residue of 29.7% in weight was generated, the lowest considering all the hybrid nanomaterials based on clay in this work, which is related to the higher amount of the CQD in the MCQD-R2-1.

As can be observed in Figure 37D, the MCQD-R2-16 hybrid nanomaterial possesses the most complex thermal profile. From 30 °C to 155 °C occurs the first step related to removal of physiosorbed water of both MMT and CQD, resulting in the weight loss of 7.3%. The following T_{max} in the DTG curve takes place at 247.6 °C and 283.3 °C, representing the removal of interlayer water, which appears only as a T_{max} at 59.3 °C for pure MMT. These temperature differences might be associated with interactions of the functional groups of CQD and the interlayer water of MMT, which the FT-IR results can also corroborate. The T_{max} exhibited at 496.3 °C might be associated with the degradation process of CQD, and the T_{max} at 563.3 °C corresponds to the dihydroxylation of MMT. A weight loss appears to start at approximately 830 °C, however, the maximum weight loss rate probably occurs at temperatures higher than 900 °C in accordance with the second weight loss related to the dihydroxylation that takes place at 860.2 °C to pure MMT. This indicates that the interaction of CQD and the MMT lattice might have dislocated the T_{max} associated with this event to a high temperature.

5.4 OPTICAL PROPERTIES

To investigate the optical properties of the hybrid nanomaterials, UV–Vis and photoluminescence spectroscopy analyses were performed on the MCQD samples. The UV–Vis spectra show that all hybrid materials exhibit a band in the visible region, which is associated with the presence of CQDs (Figure 38). However, in the case of MCQD-R1, the intensity of this band is lower than that observed for the other materials, even when analyzed at a higher concentration, and it displays a shift from 547 nm (pure CQD) to 528 nm. This shift suggests that interactions between MMT and CQDs occur at the surface level, in agreement

with the FT-IR findings. The band at 243 nm appears to be broader than for CQD, which could be related to a contribution of MMT that exhibits a band at 243 nm (Appendix A).

MCQD-R2-1 possesses a band at 543 nm, exhibiting a slight blueshift compared to CQD, and the higher intensity of this band is a result of the high amount of CQD in this hybrid nanomaterial. Moreover, the band at 348 nm for CQD changes to 345 nm, and the band at 239 nm loses its definition, which suggests modification at the core of CQD. For MCQD-R2-16, the center of the visible band remains unaltered compared to CQD, however, in the UV region, a blue shift is observed for the band at 338 nm. These results indicate that the presence of MMT in the synthesis media results in small changes in the electronic states of the hybrid nanomaterials compared to CQD.

Figure 38 - UV-Vis spectra of CQD (25.0 mg.L^{-1}), MCQD-R1 (100.0 mg.L^{-1}), MCQD-R2-1 (50.0 mg.L^{-1}) and MCQD-R2-16 (50.0 mg.L^{-1}) hybrid nanomaterials

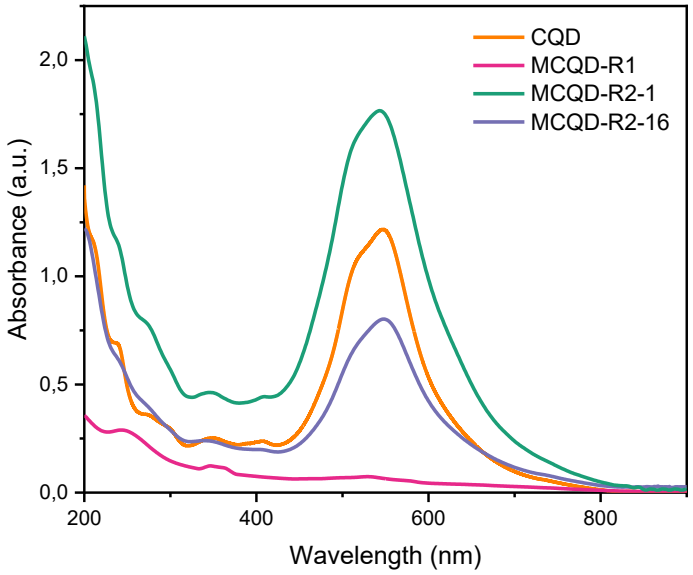

UV-Vis spectroscopy was also used to investigate the stability of MCQD hybrid nanomaterials since alterations in the absorption spectra can indicate changes in size, aggregation, and overall stability. The investigation was also conducted for CQD and discussed at section 4.4 of this thesis. From the results observed in Figure 39, MCQD-R1 exhibited the greater stability profile considering all three hybrid nanomaterials, and CQD as well, presenting an absorbance value of 0.66 after 56 days, compared to 0.44 for CQD. The reduction in the absorbance for the hybrid nanomaterials is more pronounced in the first week, especially in the first four days, behavior similar to that observed for pure CQD. MCQD-R2-1 and MCQD-R2-16 hybrids exhibited a similar profile for two weeks, reaching absorbance values of 0.69 and 0.68, respectively, which were higher than what was observed from CQD (Abs = 0.51).

After that, the absorbance of MCQD-R2-1 slowly decreased, reaching a value of 0.52 after 56 days of experiment. MCQD-R2-16, however, showed a destabilization trend after ~21 days, reaching absorbance values close to pure CQDs. This reduced stability may be related to the lower CQD content determined by elemental analysis, which suggests that prolonged precursor–clay contact time can hinder efficient CQD anchoring within the MMT layers. Additionally, stronger but less homogeneous interactions between CQD functional groups and MMT, as indicated by FT-IR shifts, may favor localized aggregation, thereby reducing colloidal stability.

Figure 39 - Stability of CQD, MCQD-R1, MCQD-R2-1, and MCQD-R2-16 hybrid nanomaterials evaluated by UV-Vis spectroscopy over time

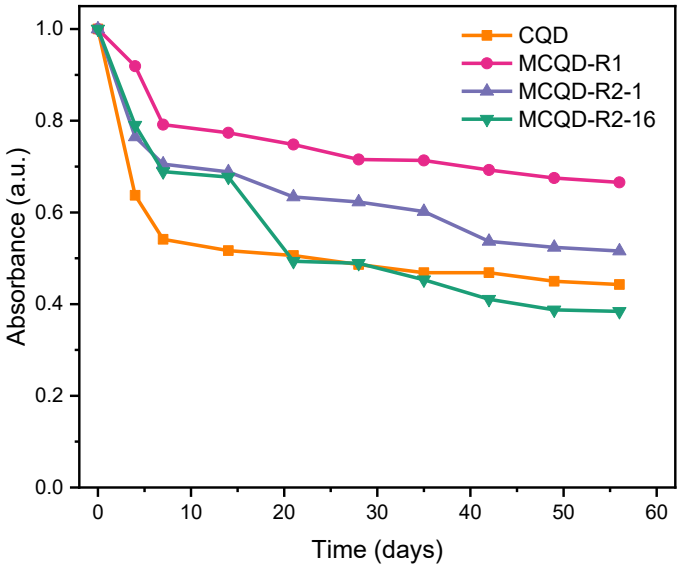

The photoluminescence spectra of CQD and the hybrids were obtained by excitation of aqueous dispersions at different wavelengths. As can be observed in Figure 40, the hybrid nanomaterials possess emission behavior similar to that observed for CQD, but some differences need to be pointed out. For MCQD-R1 hybrid nanomaterial, a minor shift is noted for the red emission, however the blue-green emissions seem to have lost their definition and intensity. MCQD-R2-1 possesses an emission profile quite similar to that observed for CQD with the emissions in blue-green region more defined (Figure 40E-F), which could be related with the higher content of CQD. The MCQD-R2-16 demonstrated the most significant alteration in the emission profile among the hybrid nanomaterials. For the blue-green emission, an excitation-dependent behavior is observed, which could be associated with modifications in the contributions of the core and surface states. Regarding the red emission, a red shift is noted for the maxima in both green and red emission, which changes from 522 nm and 629 nm in

CQD to 535 nm and 656 nm in the hybrid nanomaterial, respectively. This result might be associated to the higher nitrogen incorporation (lower C/N ratio), which could influence surface states (Kundu et al., 2018) .

Figure 40 - Emission spectra of CQD (A, B), MCQD-R1 (C, D), MCQD-R2-1 (E, F), and MCQD-R2-16 (G, H) hybrid nanomaterials as aqueous dispersion

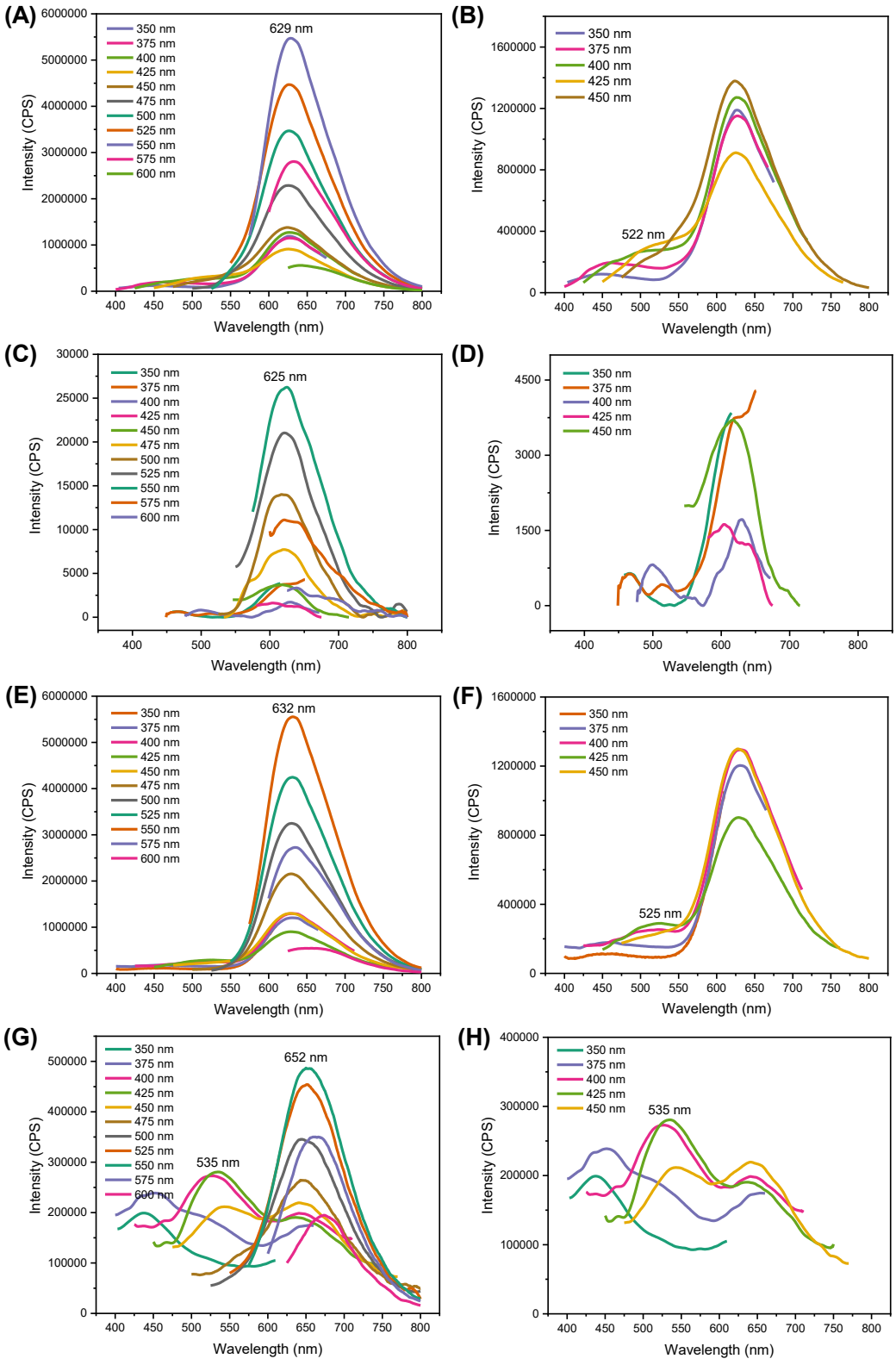

The PLE spectra were recorded to unveil the excited states involved. The PLE spectra of the hybrid nanomaterials (Figure 41A-D) reveal similar profiles compared to CQD with slight shifts in the center of the bands. For MCQD-R1, it is possible to observe a shoulder close to 434 nm, indicating possible alterations in n-π* transitions in the aromatic center of CQD. For MCQD-R2-1 a new transition is observed around 500 nm. For MCQD-R2-16, it is possible to observe an increase in the width of the PLE band, which suggests the arising of new transitions due to the presence of MMT in the hybrid.

Figure 41 - PLE spectra of CQD (A), MCQD-R1 (B), MCQD-R2-1- (C), and MCQD-R2-16 (D) hybrid nanomaterials

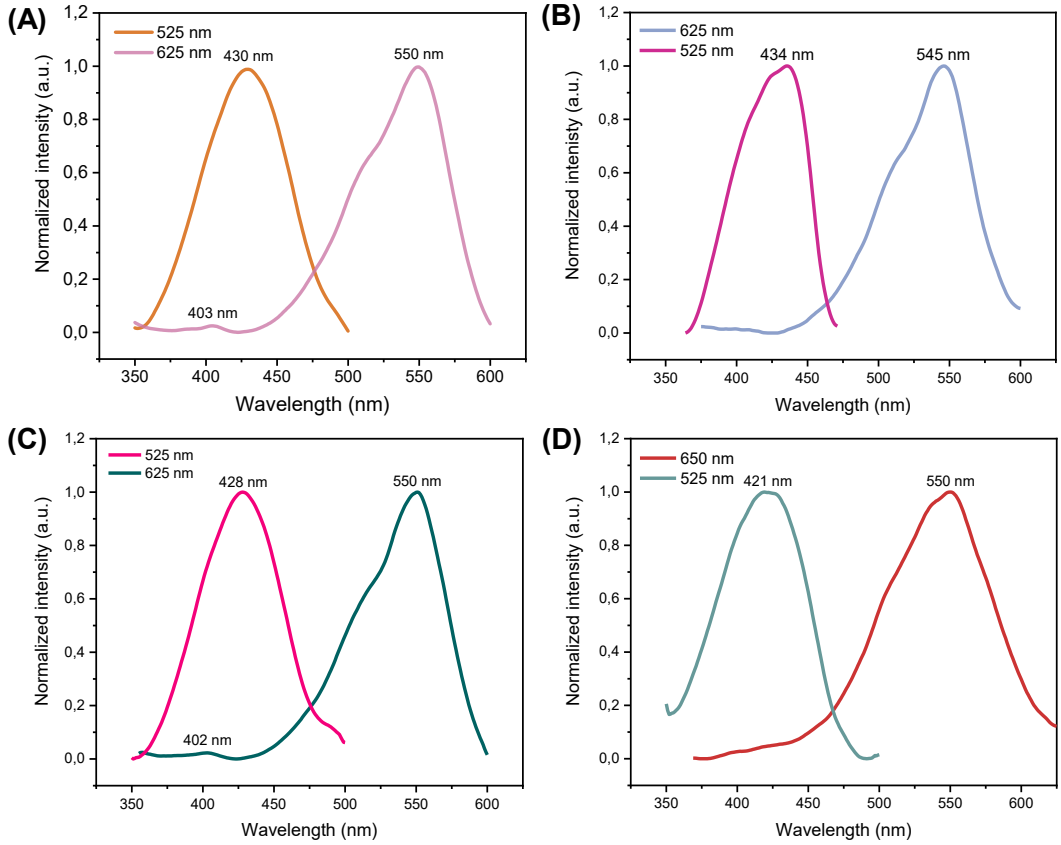

Time-resolved PL was measured for the samples under 450 nm excitation to investigate the origin of the emission. Table 8 summarizes the lifetimes, calculating the decay times of individual components and their respective overall contributions. A longer lifetime is observed for the red emission in hybrid nanomaterials compared to CQD, which is related to the increase of decay time of component τ_2, indicating that the association with MMT results in greater involvement of functional groups in the emission. The green emission of MCQD-R2-1 shows a lower contribution of the surface state, 7.33% compared to 43.15% for CQD, resulting in the

faster decay time. Considering the red emission, the contribution of the surface state cannot be appreciated, that is, the emission is uniquely governed by the component associated with the core state. In the MCQD-R2-16 exhibit the longer τ_{AV} for the red emission due to an increase in the contribution of the surface state, which increased from 5.60% in CQD to 11.93%. The association of CQD and MMT resulted in hybrid nanomaterials with longer red emission lifetimes, which could be interesting for applications that explore this property.

Table 8 - Lifetime measurements of CQD, MCQD-R1, MCQD-R2-1 and MCQD-R2-16 hybrid nanomaterial under excitation of 450 nm

Samples	λ_{em} (nm)	τ_1 (ns)	τ_2 (ns)	τ_{AV} (ns)
CQD	528	0.91 (56.85%)	6.14 (43.15%)	5.29
	626	0.88 (94.40%)	4.17 (5.60%)	1.60
MCQD-R1	530	1.57 (40.17%)	5.66 (59.82%)	5.02
MCQD-R2-1	560	1.58 (92.67%)	5.095 (7.33%)	2.29
	590	2.21 (100%)	-	2.22
MCQD-R2-16	551	1.09 (70.77%)	5.46 (29.23%)	4.04
	600	0.91 (88.07%)	4.46 (11.93%)	2.33

A comparative analysis of the two synthetic routes reveals complementary advantages and clear structure–property correlations. Route 1 preserves the crystalline integrity of montmorillonite and provides stable dispersions, but the interaction between the components is predominantly weak and water-mediated, resulting in lower CQD loading and moderate optical response. In contrast, route 2 enables direct CQD nucleation on the clay surface, strengthening interfacial coupling through electrostatic and hydrogen-bonding interactions, which leads to higher incorporation efficiency, enhanced photoluminescence, and improved colloidal stability. However, excessive precursor–clay contact time, as in MCQD-R2-16, promotes partial aggregation and limits anchoring efficiency. Overall, Route 2 offers superior control over interfacial chemistry and resulting functional properties, while Route 1 stands out for its simplicity and structural preservation.

5.5 HEMOLYSIS ASSAY

Considering the comparative analyses, the MCQD-R2-1 hybrid was selected for further evaluations. This material exhibited the most favorable balance of properties, including a higher CQD content, homogeneous dispersion along the clay fibrils, and the absence of excessive agglomeration observed in MCQD-R2-16. These structural features resulted in enhanced stability and optical performance, making MCQD-R2-1 the most representative candidate for subsequent assays. According to Figure 42, MMT presented a hemolysis rate of 1.08% even at a high concentration of 5,000 mg.L^{-1}, while MCQD-R2-1 hybrid nanomaterial exhibits a hemolytic activity of 3.99%, which is lower than the recommended value of 5% by the ISO 10993-4 standard (INTERNATIONAL ORGANIZATION FOR STANDARDIZATION, 2009). The materials tested did not trigger a hemolytic reaction, suggesting their biocompatibility and significantly enhancing their potential applications in biological systems.

Figure 42 - Hemolysis percentage of CQD, MMT, and the MCQD-R2-1 hybrid nanomaterial. The hemolysis percentage was evaluated at concentrations ranging from 5000 to 36.0625 µg/mL in the erythrocytes of sheep. The results correspond to averages ± of individual samples tested in triplicate. (*) $p<0.05$, compared to the positive control (Triton X-100 at 1%).

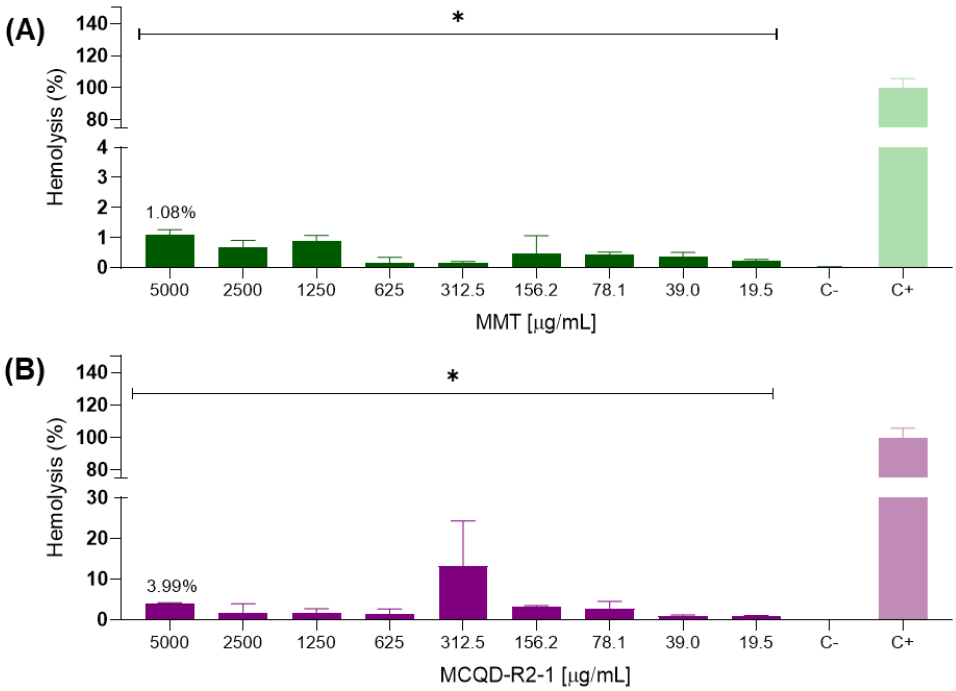

5.6 CONCLUDING REMARKS

Based on the structural, optical, and hemocompatibility results obtained in this study, it can be concluded that the combination of montmorillonite and carbon quantum dots through

distinct synthesis approaches leads to the formation of hybrid nanomaterials with preserved crystalline integrity of both components. XRD and FT-IR analyses revealed that while Route 1 primarily promotes interactions mediated by interlayer water molecules, the *in situ* synthesis (Route 2) induces stronger chemical interactions involving the carbonyl and carboxylate groups of CQDs, with slight variations depending on the contact time with the clay. Elemental analysis confirmed that Route 2 incorporated a higher amount of CQD, likely due to the CQDs nucleating in close proximity to clay surfaces/edges, favoring multipoint anchoring (electrostatics + H-bonds + edge acid–base). Thermal analysis demonstrated that the hybrids exhibit modified degradation profiles and, in some cases, enhanced thermal stability compared to pristine CQDs, highlighting the influence of montmorillonite on the thermal behavior of the composites.

Optical characterization indicated that the hybrids retain the independent emission features of CQDs, with subtle spectral shifts and variations in lifetime decay related to the interactions in the hybrids and nitrogen incorporation, particularly in MCQD-R2-16. Stability tests showed that the presence of MMT mitigates CQD aggregation over time, especially in MCQD-R1 and MCQD-R2-1, enhancing their potential for long-term applications. Moreover, hemolysis assays confirmed that the selected hybrid, MCQD-R2-1, possesses a hemolysis ratio below 5%, confirming its hemocompatibility. It is worth highlighting that, despite its relatively low CQD loading, MCQD-R1 exhibited exceptional colloidal stability, which demonstrates the ability of MMT to prevent nanoparticle aggregation even under less favorable incorporation conditions.

6 DRUG-CLAY-CQD HYBRID NANOMATERIALS

Contents

Chapter 6 Abstract

This chapter describes the association of montmorillonite or sepiolite with 5-fluorouracil, followed by their integration with carbon quantum dots to form hybrid nanoplatforms, focusing on their structural and compositional evaluation by XRD, FT-IR, elemental analysis, and EDS to elucidate loading mechanisms and drug–carrier interactions.

6.1 INTRODUCTION

Clay minerals have been extensively used since ancient times for both cosmetic and therapeutic purposes (Massaro et al., 2018). For instance, clay is used as an active ingredient in oral treatments for diarrhea, as gastrointestinal protectors, and as antacids (Carretero; Pozo, 2009; López-Galindo et al., 2011). Their antacid effect arises from the ability of the clay surface to adsorb protons from gastric acid while releasing non-toxic ions such as Mg^{2+} and Al^{3+}. As gastrointestinal protectors, clay minerals can increase thickness of the mucosal barrier, adhere to gastric and intestinal membranes, and consequently reduce irritation and gastric secretion. Their antidiarrheal action, on the other hand, is linked to their capacity to reduce liquid content in the colon and possibly adsorb enteropathogens (Yang et al., 2016).

In addition, clay minerals are also widely applied as pharmaceutical excipients in different pharmaceutical dosage forms intended for oral (Bravo et al., 2023; Wu et al., 2025) and topical administration (Swain et al., 2022; Zhang et al., 2022d). More recently, they have attracted attention as efficient carriers for bioactive molecules (Borrego-Sánchez et al., 2018). Among the different clay minerals used in pharmaceutical formulations, MMT stands out as one of the most widely employed. Structurally, it is a 2:1 phyllosilicate consisting of an octahedral sheet of aluminum sandwiched between two tetrahedral sheets of silicon coordinated with oxygen atoms. This arrangement creates an interlayer space between the triple-sheet layers, which accounts for nearly 90% of its accessible surface area and is available for interaction with water and other molecules, thereby endowing MMT with a remarkable adsorption capacity (Borrego-Sánchez et al., 2018). Furthermore, the interlayer space can accommodate and stabilize bioactive compounds, improving their photostability, thermal stability, and dispersion, essential requirements for enhancing the performance of molecules in biological systems (Rebitski et al., 2018).

Although less commonly employed than MMT in the biomedical area, fibrous clays such as SEP also offer great potential for pharmaceutical applications. This mineral is characterized by a 2:1 ribbon structure composed of external tetrahedral silicon sheets and a central octahedral sheet containing magnesium. Unlike layered clays, SEP displays a periodic discontinuity in these T:O:T layers, which gives rise to an architecture of alternating blocks and tunnels, along with structural channels exposed on the external surface. This unique morphology results in a remarkably high specific surface area (approximately 320 $m^2\ g^{-1}$) and an abundance of silanol groups (≡Si−OH) located at the edges of the external blocks. The presence of these silanol groups on the outer surface endows SEP with remarkable versatility

for functionalization, allowing interactions with a broad range of organic species, including drugs and polymer matrices, through hydrogen bonding or covalent attachment. This unique surface chemistry makes SEP an excellent platform for the design and development of diverse hybrid materials. A comparison of the different features of layered and fibrous clay is summarized in Table 9.

Table 9 - Main differences between layered and fibrous clays

Layered Clays	Fibrous Clays
1-nanodimensional particle	2-nanodimensional particle
High charge density	Low charge density
High CEC	Low CEC
Low density of silanol groups	High density of silanol groups
High internal surface area	Low internal surface area
Particles in layer stacks	Particles in bundles
Swelling clay	Non-swelling and non-exfoliable clay

Source: Nomicisio et al. (2023)

These differences influence the ability of clay minerals to bind active compounds, however some mechanisms can be generalized, and include: i) intercalation within clays interlaminar space through cation exchange reaction; ii) adsorption on the layer surfaces of clays via electrostatic interactions; iii) binding of biomolecules at active sites among other interactions such as iv) hydrogen bonding, Van der Waals interactions, ligand exchange, and cation/water bridging (Peña-Parás; Sánchez-Fernández; Vidaltamayo, 2018; Tipa et al., 2022).

The interactions between clay and drugs can enhance the bioavailability of poorly soluble drugs and improve their permeability, promoting greater drug absorption across physiological barriers (Nomicisio et al., 2023). Owing to these features, clays are considered as promising nanocarriers for the loading of diverse classes of drugs, including antibiotics, anticancer (Hemmatpour et al., 2023), antioxidant, and anti-inflammatory. A hybrid system based on oxaprozin, a poorly water-soluble anti-inflammatory drug, cyclodextrins, and clays was investigated using sepiolite, attapulgite and bentonite, with SEP being selected for its greater drug adsorption capacity. The study demonstrated that the dissolution efficiency of oxaprozin increased when incorporated into the clay, a result attributed to drug–clay complexation or to the extremely fine dispersion of the drug within the clay structure (Mura et

al., 2016). These findings highlight the potential of SEP-based hybrids as an effective strategy to enhance the therapeutic performance of poorly soluble drugs. Vitamin A, an important molecule in several physiological functions, is easily oxidized. In the study developed for Calabrese et al. (2016), this molecule was immobilized in two different clays, MMT K-10, SEP and MCM-41 by impregnation. The kinetics of the release exhibited dependence on the structural features of the support material and the pH. For MMT K-10 and MCM-41, Vitamin A starts to degrade after two hours of release. On the contrary, for SEP no oxidation of Vitamin A occurs, which demonstrates their ability to prevent oxidation (Calabrese et al., 2016).

Beyond the interactions established between clays and drugs, the incorporation of CDs into clay–drug systems introduce additional interaction pathways, resulting into new functionalities. CDs possess a high density of surface functional groups, such as hydroxyl, carboxyl and amino moieties, which can simultaneously interact with both the clay and the drug molecules via hydrogen bonding, electrostatic interactions or covalent coupling, leading to the formation of more complex and multifunctional systems. Recent studies have demonstrated that the integration of CDs with clay minerals enhances drug loading capacity, modulates release profiles and improves colloidal stability. In addition, the presence of CDs can endow the hybrids with photoluminescent properties, enabling simultaneous drug delivery and bioimaging (Mehdi et al., 2018; Prashanth et al., 2022). Therefore, the incorporation of CDs into clay–drug hybrid nanomaterials not only strengthen drug–carrier interactions but also enables the development of multifunctional nanocarriers capable of combining delivery, protection, imaging and improved biocompatibility in a single platform.

6.2 RESULTS AND DISCUSSION

The features of the neat host matrices, SEP and MMT, have been previously studied, and in this chapter, the characterizations of the hybrid nanomaterials SEP-5FU and MMT-5FU are explored. For the loading of 5FU onto SEP, any alteration in the pH values of the drug solution occurred as reported by Akyuz, Akyuz, and Akalin (2014). Figure 43 shows the diffraction patterns of SEP, 5FU, and the SEP-5FU hybrid nanomaterials obtained using different initial concentrations of 5FU. Characteristic reflections assigned to the (110) plane of SEP are observed in all samples, indicating that the structure of the materials was maintained. Pure 5FU exhibits an intense, sharp peak at $2\theta = 28.5°$ due to its crystalline nature, however this diffraction plane cannot be noted in the diffractogram for hybrid nanomaterials. This does not imply the unsuccessful loading of the drug onto SEP, since interaction with this clay might

occur at the surface level, in this case, other characterization techniques are more adequate to evaluate the clay-drug interactions.

Figure 43 - XRD diffraction patterns of SEP, SEP-5FU hybrid nanomaterials with different ratios of the drug, and 5-Fluorouracil

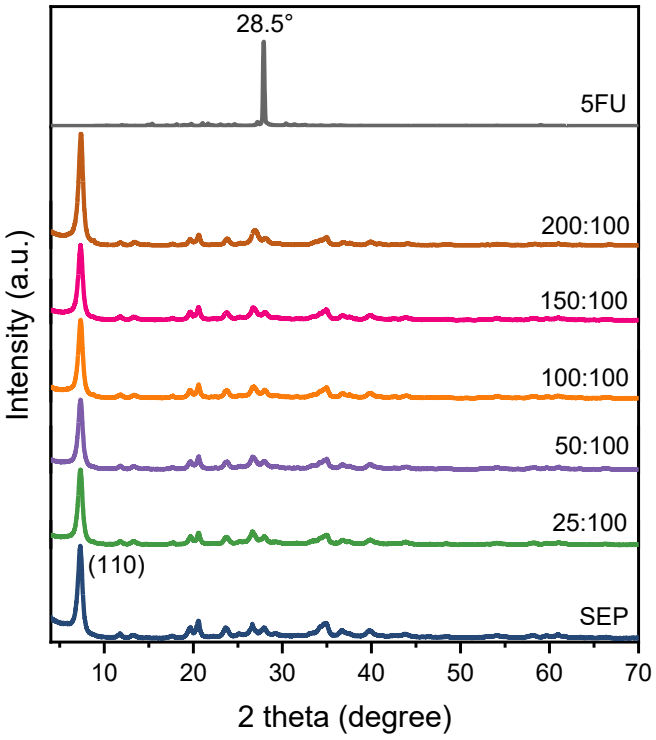

Considering layered clays, such as MMT, the pH of the drug solution plays a crucial role in the intercalation mechanism. The alkaline environment, especially pH values higher than 9, favors 5FU intercalation as reported by other works (Çiftçi et al., 2020; Gârea et al., 2015; Lin; Jian; Lee, 2000) Besides that, high drug loading capacities in high pH values can be associated with the formation of more stable structures and greater susceptibility to interactions due to ionization of 5-FU molecules in alkaline environments. However, a decrease in loading capacity is observed at pH values higher than 10, which can be explained by the inhibition of the adsorption of 5FU molecules as a result of the competitive effect with OH^- ions (Çiftçi et al., 2020; Luo et al., 2016). Taking this into consideration, in this study, pH = 10 was chosen, allowing different deprotonated 5-FU forms (5-FU^- and 5-FU^{2-}) to coexist, as can be seen in Figure 44.

Figure 44 - (A) The 5-FU species distribution and (B) its respective forms (neutral, ionized, and deprotonated) as a function of pH. Data obtained using MarvinSketch software version 22.22

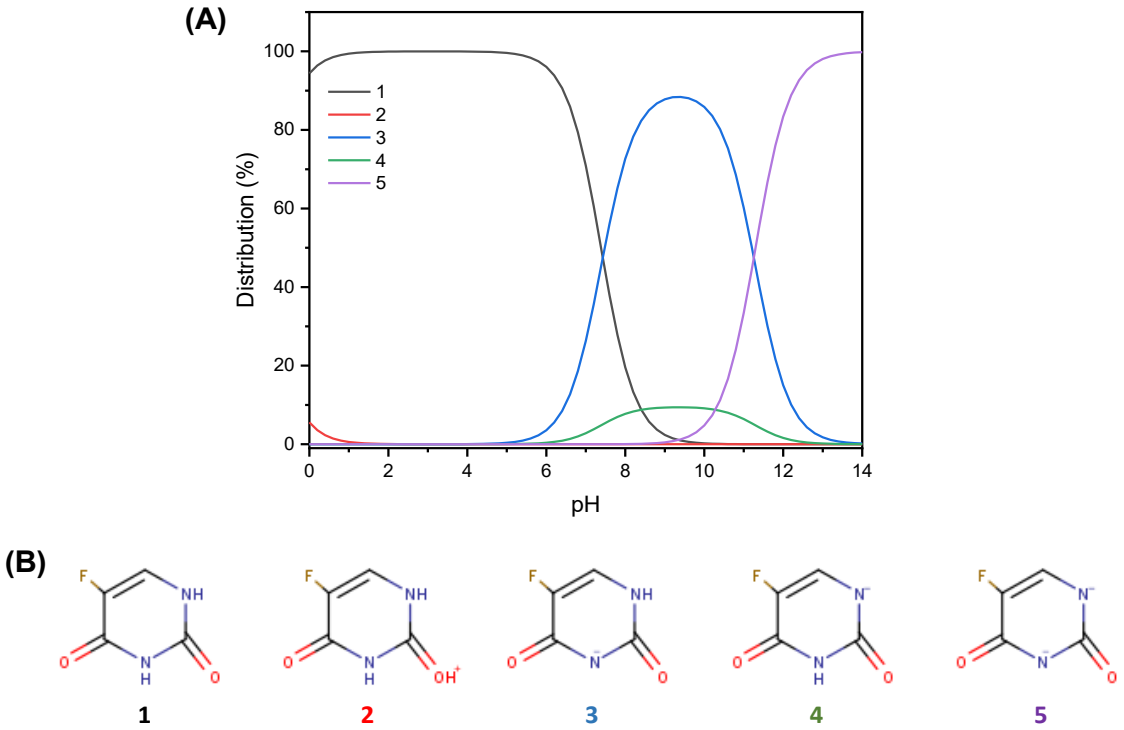

Source: Author (2025)

The XRD patterns of the pristine MMT and MMT-5FU hybrid nanomaterials are exhibited in Figure 45. Pristine MMT showed a typical XRD pattern with the basal spacing of 1.21 nm (2θ = 7.27°), and after 5FU loading, a shift in the position of the reflection plane (001) towards lower angles in 2θ is observed in all hybrid materials, indicating the successful intercalation of 5FU (Kevadiya et al., 2012). The increase in the basal spacing values varies from 1.25 to 1.27 nm (Table 10), and the basal spacing does not seem to increase gradually with the increase in the amount of drug. Besides that, it is not possible to observe the arising of any characteristic peak that could be associated with 5FU, which could indicate that the majority of the drug associated with MMT is intercalated. This result might indicate that the intercalation mechanism of 5FU into MMT occurs by the replacement of sodium ions in the interlayer space by 5FU molecules. However, Lin, Jian and Lee (2000) reported the existence of two other mechanisms of interaction of MMT and 5-FU were: i) 5-FU adsorbs onto the free surface of MMT, and ii) 5-FU replaces clay OH groups to form ionic bonds with Al^{3+} and Mg^{2+} in the MMT.

The thickness of a single layer of MMT is reported to be 0.96 nm, thus, in the prepared MMT-5FU hybrid nanomaterials, the basal spacing increased by around 0.30 nm after 5FU intercalation. Considering that the dimensions of 5-FU are (0.30 nm x 0.53 nm x 0.49 nm)

(Wang et al., 2005), it is likely that the drug is conformed as a monolayer in the MMT interlayer space, adopting a planar arrangement, justifying the value of 0.30 nm for the increase of MMT basal spacing. The intercalation is a strong indication that MMT acts as an efficient carrier, accommodating the drug within its crystalline network without compromising the structural stability of the clay.

Figure 45 - XRD patterns of pure montmorillonite and MMT-5-FU hybrid materials with different initial concentrations of 5-FU

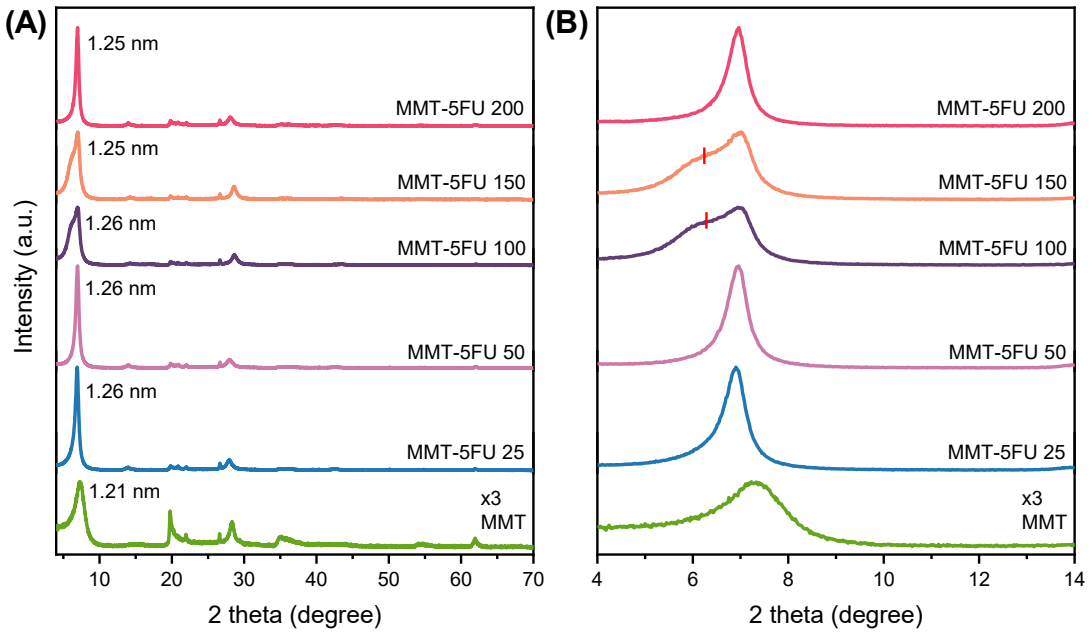

Table 10 - Basal spacing for pure montmorillonite and MMT-5-FU hybrid nanomaterials calculated using Bragg's Law

Material	Basal spacing (nm)	Increase (nm)
MMT	1.21	-
MMT-5FU 25:100	1.27	0.31
MMT-5FU 50:100	1.26	0.30
MMT-5FU 100:100	1.27	0.31
MMT-5FU 150:100	1.25	0.29
MMT-5FU 200:100	1.26	0.30

For MMT-5FU 100 and MMT-5FU 150, it is possible to observe that an additional peak close to 2θ = 6.3°, representing an increase in the interlayer space of 0.44 nm, which is not in good agreement with the other dimensions of 5FU. This might indicate that the drug accommodates in the interlayer space in a tilted way (partially perpendicular to the layer),

forming a second phase in the MMT-5FU 100 and MMT-5FU 150 hybrid nanomaterials that coexist with the planar orientation discussed before in the hybrid nanomaterials. The possible arrangement of 5FU in the hybrid nanomaterials is presented in Figure 46. It is important to mention that the tilt orientation starts to occur in the hybrid nanomaterial that possesses the same amount of MMT in the reaction media (100 mg) or higher (150 mg), despite the fact that this behavior was not observed for MMT-5FU 200.

Figure 46 – Schematic illustration of the pure MMT intercalated with Na^+ ions (turquoise spheres), and MMT intercalated with 5-FU molecules (MMT-5FU hybrid nanomaterial) in different orientations (planar and tilt)

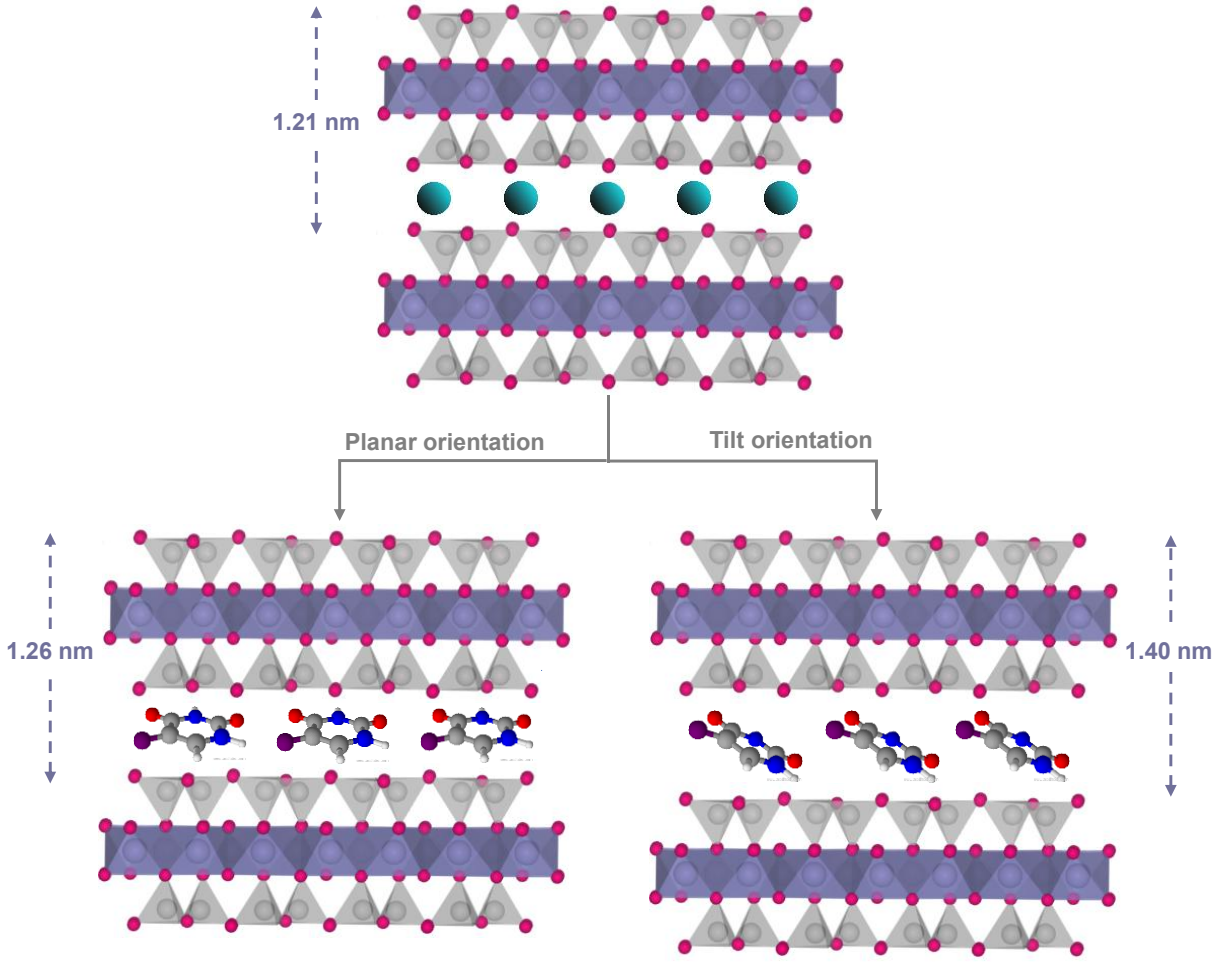

The amount of drug in the SEP-5FU and MMT-5FU hybrid nanomaterials was calculated using elemental analysis, and the composition of 5FU (C = 36.88%; H = 2.18%; N = 21.43%) was taken as a reference for calculation. The drug loading content and entrapment efficiency for SEP-based materials are presented in Table 11. SEP-5FU 25:100 exhibited DLC of 3.70%, and in spite of the low rate of retained drug, it represented the highest EE due to the lower amount of initial drug. As the initial concentration of 5FU increases, the DLE also rises, reaching the highest value of 5.88% in SEP-5FU 100:100 hybrid nanomaterial. Above this

concentration, a slight decrease in DLE is observed, however, the value remains around 5.5% for the hybrid nanomaterials. This may indicate a saturation of active sites of SEP for the adsorption of new 5FU molecules, even with an increase in the initial drug concentration from 50.0 $mg.L^{-1}$ to 200.0 mgL^{-1}, which also resulted in progressively lower EE. The SEP-5FU 50:100 was the selected hybrid nanomaterial for the following experiments, considering its good DLC without the necessity of a high amount of 5FU.

Table 11 – Drug loading content and entrapment efficiency in SEP-5FU hybrid nanomaterials evaluated using elemental analysis

Material	Drug loading content (%)	Entrapment efficiency (%)
SEP-5FU 25:100	3.70	19.15
SEP-5FU 50:100	5.34	15.98
SEP-5FU 100:100	5.88	11.44
SEP-5FU 150:100	5.56	9.13
SEP-5FU 200:100	5.61	8.19

For MMT-5FU hybrid nanomaterials (Table 12), an overall tendency is not observed for DLC and EE. MMT-5FU 25:100 possesses a DLC of 3.47% and an EE of 17.35%, the highest value for this group of material, which is similar to that observed for SEP-5FU 25:100. In opposition, the increase of the initial 5FU concentration leads to a general decrease in the DLC except for MMT-5FU 150:100 material, which shows a DLC of 4.96%. The previous XRD discussion revealed that MMT-5FU 150 has different intercalation phases of 5FU, which could result in a higher content of 5FU in the material, which also resulted in the second-high value of EE = 8.27%. Even though MMT-5FU 100 presented a similar structure, this was not reflected in a higher amount of drug in the material. Considering the good DLC and EE, and the distinct structural arrangements, the MMT-5FU 25:100 and MMT-5FU 150:100 hybrid nanomaterials were selected for the following experiments.

Table 12 - Drug loading content and entrapment efficiency in MMT-5FU hybrid nanomaterials evaluated using elemental analysis

Material	Drug loading content (%)	Entrapment efficiency (%)
MMT-5FU 25:100	3.47	17.35

MMT-5FU 50:100	1.73	5.21
MMT-5FU 100:100	2.18	4.37
MMT-5FU 150:100	4.96	8.27
MMT-5FU 200:100	2.96	4.43

The loading of 5-FU into MMT was also investigated using an energy-dispersive X-ray spectrometer coupled with SEM. The analysis aims to determine the Si/Na ratio in the MMT-5FU hybrids and compare it to the value obtained for pure MMT. The hypothesis suggests that during the intercalation process, sodium ions are exchanged for 5FU molecules, resulting in a decrease in sodium content and an increase in the Si/Na ratio. For this evaluation, different points of each sample were analyzed, as demonstrated in Figure 47. For pure MMT, the Si/Na ratio was calculated to be 24.85 ± 2.90, while for MMT-5FU 25 was 39.46 ± 6.50, demonstrating an increase in the ratio due to the interaction of 5FU (Figure 47B). The DLC behavior follows the same tendency observed for Si/Na, including the increase in value for MMT-5FU 150 that presents a Si/Na of 34.23 ± 3.51, corroborating the XRD and CHN results. These results suggest that the decrease in sodium content was due to the intercalation of 5FU, and that the preferred mechanism of association between MMT and 5FU occurs through intercalation.

Figure 47 – (A) Representation of different points in EDS measurements for pure MMT and (B) graph with drug loading content (%) and Si/Na ratio in MMT-5FU hybrid nanomaterials as a function of 5FU initial amount

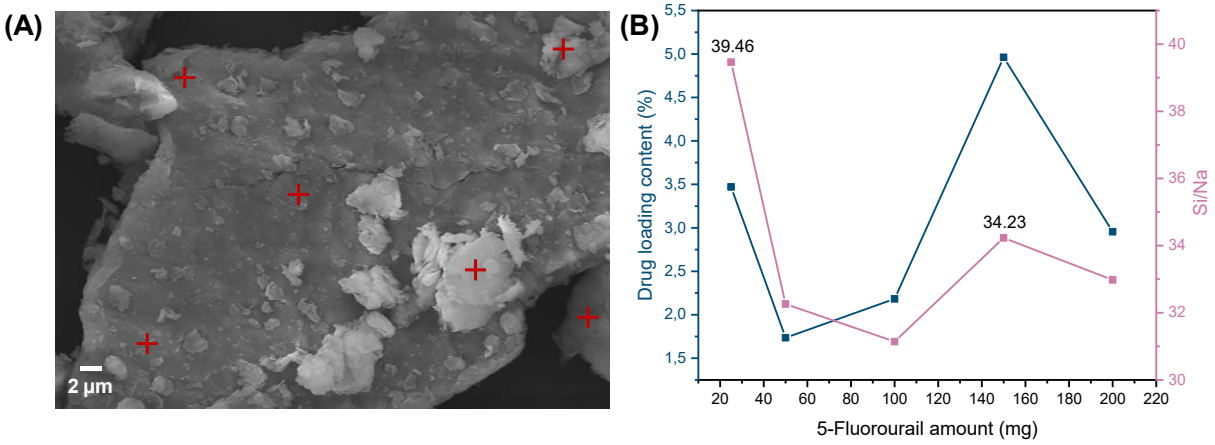

FT-IR analyses were performed to understand the interactions between the clay minerals and 5-FU molecules. In the spectra of the hybrid nanomaterials, it is noted a profile quite similar to pure SEP (Figure 48A), however, in detail (Figure 48B) it is possible to see contributions associated with the drug. The band that appears at 1661 cm^{-1}, assigned to O-H bending modes

in zeolitic water, shift to approximately 1654 cm^{-1} in the hybrid nanomaterials. In addition, a feature at 1252 cm^{-1} is observed in the spectra of hybrid nanomaterials related to the starching vibration of C-F bond that is observed at 1243 cm^{-1} in 5-FU. A band at 689 cm^{-1} is observed in the hybrid nanomaterials in association with the out of plane bending vibration N-H bond (Rastogi et al., 2000; Rastogi; Palafox, 2011). Although the characteristic bands of 5FU were observed at low intensity in hybrids and subtle displacements were observed, indicating interactions between the C-F and N-H groups of 5-FU.

Figure 48 – FT-IR spectra of SEP and SEP-5FU hybrid nanomaterials with different ratio of drug in the range of (A) 4000 cm^{-1} to 400 cm^{-1} and 1800 cm^{-1} to 400 cm^{-1}

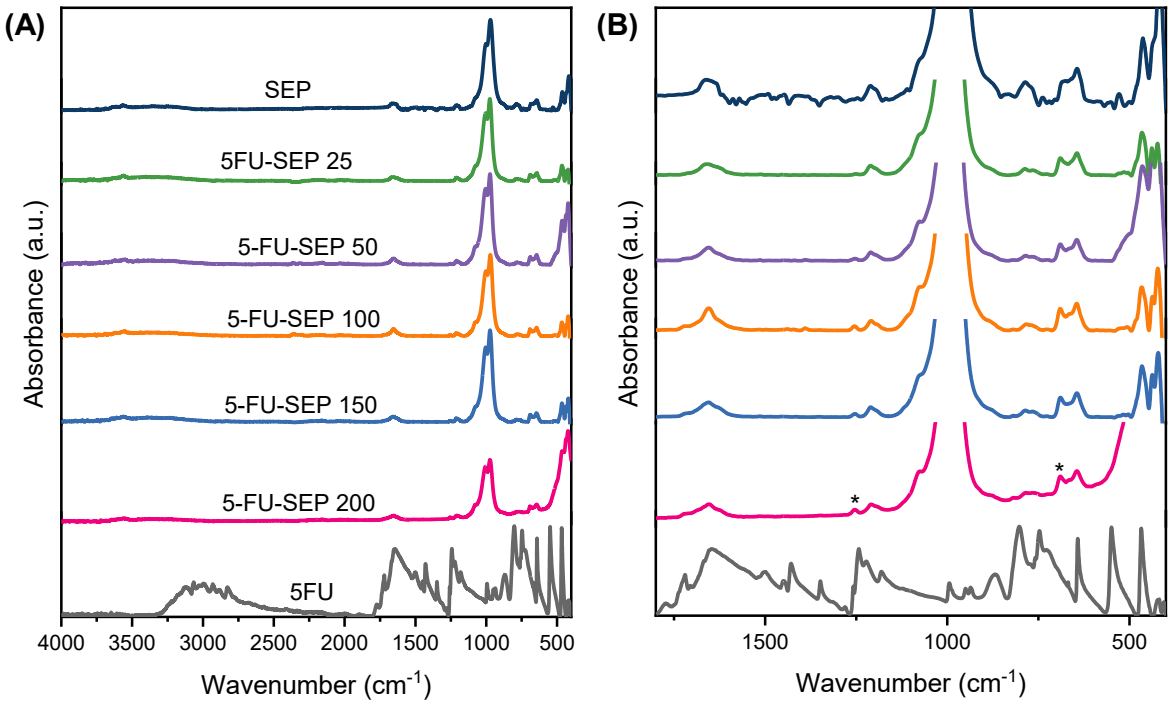

Similarly, MMT-5FU hybrid nanomaterials (Figure 49A) possessed a profile quite similar to pure MMT. However, in detail (Figure 49B) it is possible to see the presence of a new feature around 777 cm^{-1} in all hybrids, which is ascribed to the out of plane bending vibration of C=O bond. The arising of this band is also reported by Golubeva et al. (2020). Moreover, the presence of this band may suggest that interactions involving this group takes place in the intercalation of 5-FU in the interlayer space of MMT. The intercalation process is likely governed by a combination of electrostatic interactions between partially protonated 5-FU species and the negatively charged clay layers, together with hydrogen bonding involving carbonyl and imide groups. The relative contribution of these interactions depends on the pH-dependent speciation of 5-FU. From a functional point of view, the stabilization of the drug

inside the lamellas protects against rapid degradation in aqueous medium, besides allowing a controlled release due to diffusion through the layers of clay.

Figure 49 - FT-IR spectra of MMT and MMT-5FU hybrid nanomaterials with different ratio of drug in the range of (A) 4000 cm^{-1} to 400 cm^{-1} and 1800 cm^{-1} to 400 cm^{-1}

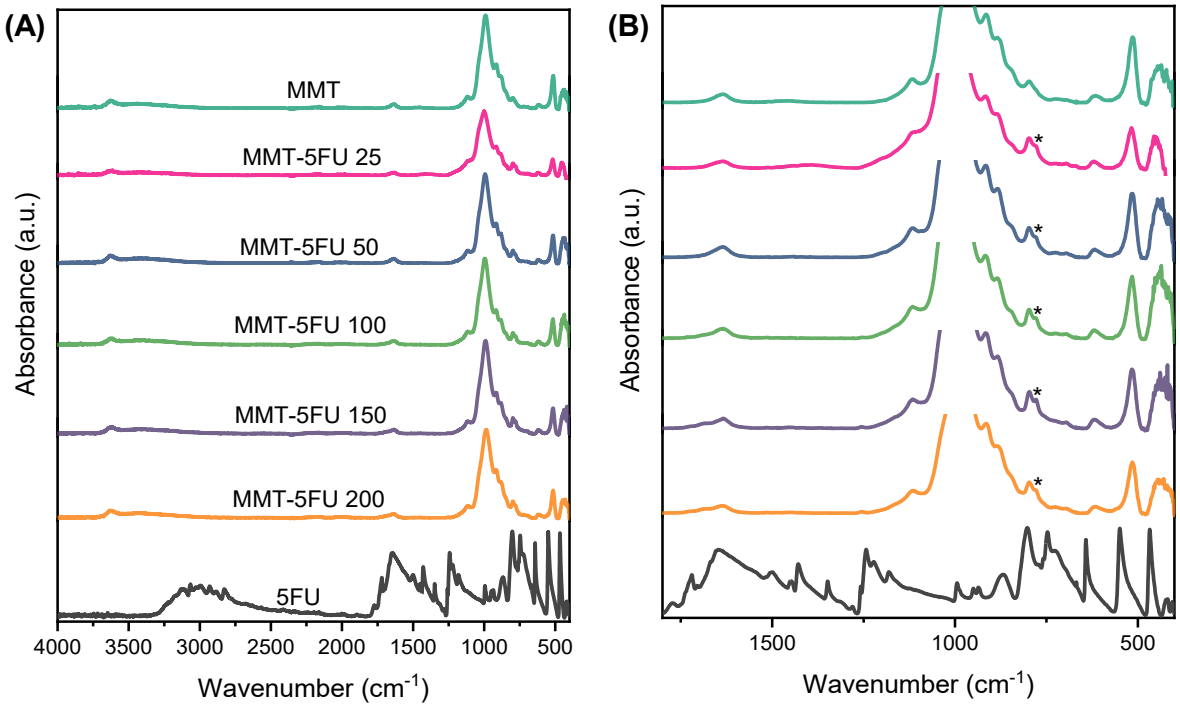

One relevant aspect to consider is the feasibility of incorporating CQDs into the clay–5FU systems to create a hybrid platform with enhanced properties. The introduction of CQDs could provide additional functionalities, particularly the photoluminescent behavior observed for the SEP–CQD hybrids in Chapter 5, which may enable monitoring of cellular internalization and drug distribution in biological tissues through fluorescent bioimaging. To maximize these functionalities, the hybrids containing the highest CQD content were selected for association with the clay–5FU systems. Therefore, SCQD-R2-16 and MCQD-R2-1 were chosen as precursors for the preparation of the SCQD-R2-16-5FU and MCQD-R2-1-5FU hybrid nanomaterials.

In the Figure 50A is presented the diffractogram of the SCQD-R2-16-5FU as well as neat 5FU, CQD, SEP and SCQD-R2-16 hybrid nanomaterial. As discussed previously, the presence of CQD in SCQD-R2-16 using XRD was confirmed by the presence of the peak at 2θ = 26.8°. In the case of SCQD-R2-16-5FU, this peak is also noted, as ascribed in Figure 50A. However, any additional peak related to 5-FU was observed, indicating that it is necessary additional characterization to identify the presence of the drug. In Figure 50B, the diffractograms of MMT, MCQD-R2-1, and the MCQD-R2-1-5FU hybrid nanomaterial are

shown. A shift of the (001) reflection plane toward lower angles is observed from 2θ = 7.3° (d_{001} = 1.21 nm) in pure MMT for 2θ = 6.7° (d_{001} = 1.32 nm) in MCQD-R2-1, and 2θ = 6.0° (d_{001} = 1.47 nm) for MCQD-R2-1-5FU. As discussed in Chapter 6, the increase in the interlayer spacing during the *in situ* CQD synthesis results from anchoring at surface and edge sites, and this expanded the structure was subsequently used to obtain MCQD-R2-1-5FU, which exhibited an additional increase of 0.50 nm in the interlayer space. This value is consistent with the dimensions of 5-FU, suggesting that the drug intercalates in a vertical orientation, representing a larger expansion compared with MMT-5FU materials. Therefore, these results indicate that the interlayer expansion induced by the *in situ* synthesis in MCQD-R2-1 facilitates the stabilization of 5-FU within the MMT galleries in a vertical arrangement, confirming the successful intercalation of the drug.

Figure 50 - XRD diffractogram of (A) 5-FU, CQD, SEP, SCQD-R2-16, and SCQD-R2-16-5FU hybrid nanomaterials and (B) 5-FU, CQD, MMT, MCQD-R2-1, and MCQD-R2-1-5FU hybrid nanomaterials

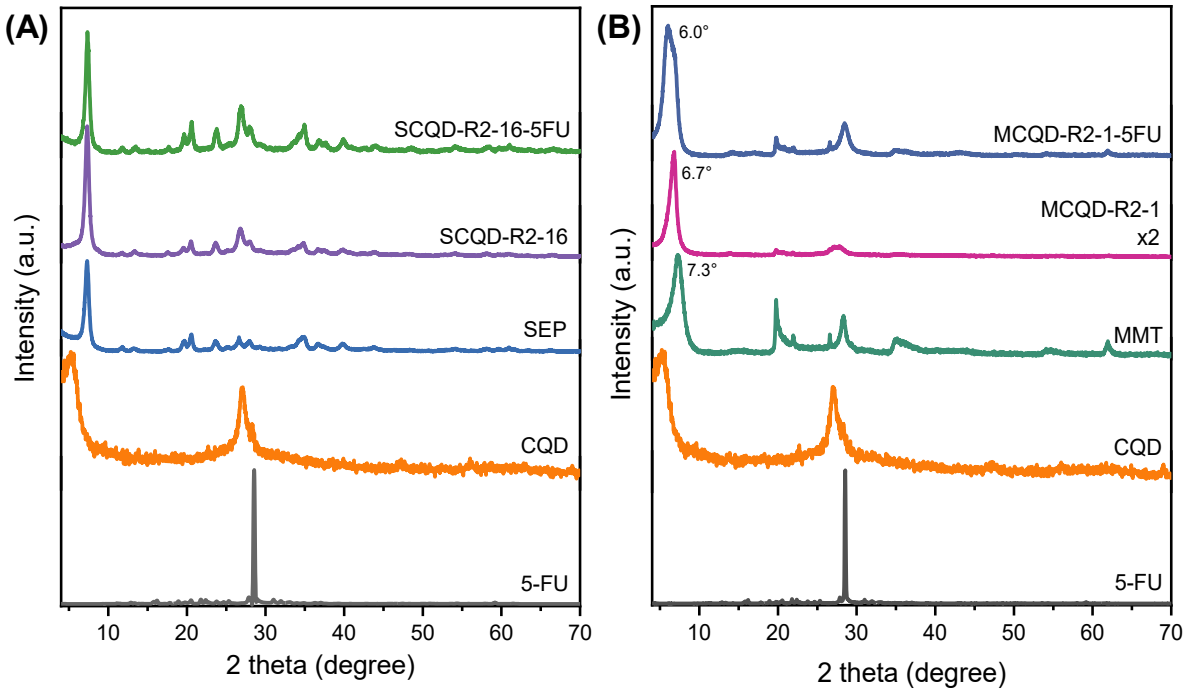

To elucidate the interactions occurring in the clay–CQD and 5-FU systems, FT-IR analyses were performed. Figure 51 shows the spectra of 5-FU, CQD, SEP, SCQD-R2-16, and the SCQD-R2-16-5FU hybrid nanomaterial. The bands associated with the in-plane Si–O stretching vibration appear at 974 and 1005 cm^{-1} for pure SEP, while in SCQD-R2-16-5FU these bands are observed at 974 and 1002 cm^{-1}. For SCQD-R2-16, similar modification was observed, being attributed to the alterations of surrounding environment of the clay. Regarding the CQDs, the characteristic band at 1340 cm^{-1}, attributed to the asymmetric and symmetric

stretching of the COO^- groups, shifts to 1386 cm^{-1} in SCQD-R2-16-5FU, indicating that the interactions previously identified in SCQD-R2-16 (shift to 1379 cm^{-1}) are preserved in the hybrid. Additionally, the bands associated with –OH and –NH groups appear less intense in SCQD-R2-16-5FU compared to SCQD-R2-16, which may reflect a reduction in CQD content. This decrease could be related to the washing step in the synthetic procedure, leading to the removal of non-conjugated CQD nanoparticles, as also suggested by TEM observations. The presence of 5-FU in the hybrid is confirmed by the band at 1651 cm^{-1}, corresponding to the C=O stretching vibration (1644 cm^{-1} in pure 5-FU), and with the signal at 462 cm^{-1} related to in plane bending vibration (469 cm^{-1} in pure 5-FU). Additional characterizations will be carried out for the MCQD-R2-1-5FU hybrid material to further elucidate the interaction mechanisms and quantify the amount of drug incorporated into the systems.

Figure 51 – FT-IR spectra of 5FU, CQD, SEP, SCQD-R2-16, and SCQD-R2-16-5FU hybrid nanomaterials in the range of 4000-400 cm^{-1}

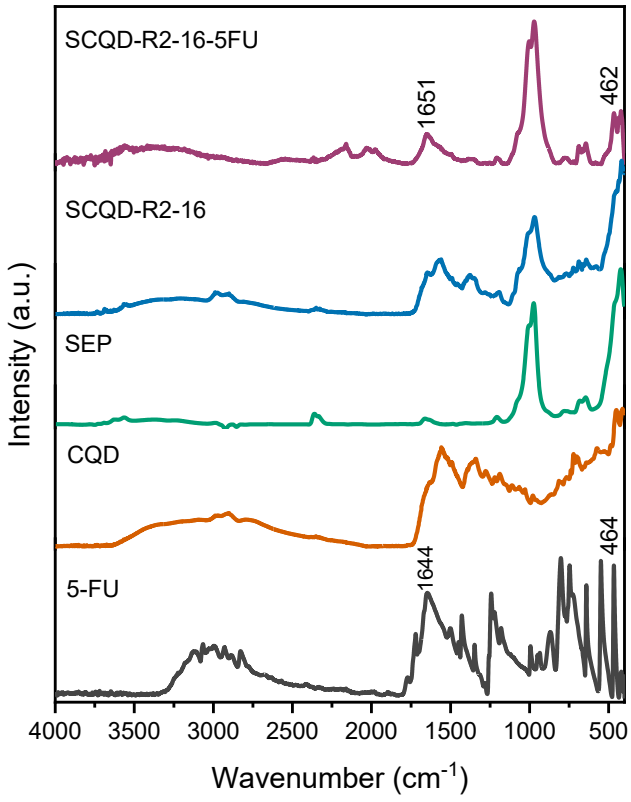

6.3 CONCLUDING REMARKS

The results presented in this chapter demonstrate that both sepiolite (SEP) and montmorillonite (MMT) are effective hosts for the incorporation of 5-fluorouracil (5-FU). For SEP-based systems, XRD confirmed the preservation of the fibrous structure after drug

association, while elemental analysis revealed drug loading contents up to 5.88% for SEP-5FU 100:100, followed by a plateau at higher initial concentrations, indicating saturation of surface silanol sites. FT-IR analyses evidenced subtle band shifts related to C–F and N–H vibrations, supporting surface adsorption as the dominant interaction mechanism.

In contrast, the results obtained for MMT clearly indicate the intercalation of 5-FU within the clay interlayer space. XRD showed a systematic expansion of the basal spacing from 1.21 nm (pure MMT) to 1.25–1.27 nm in MMT-5FU hybrids, consistent with a planar monolayer arrangement of 5-FU. For selected compositions (MMT-5FU 100 and 150), an additional reflection corresponding to an expansion of ~0.44 nm suggested the coexistence of a tilted drug configuration. Elemental analysis and EDS corroborated these findings, with the Si/Na ratio increasing from 24.85 ± 2.90 (MMT) to 39.46 ± 6.50 for MMT-5FU 25, confirming cation exchange as a major intercalation pathway.

The incorporation of CQDs further modified the structural organization of the hybrids. In MCQD-R2-1-5FU, the basal spacing increased to 1.47 nm, corresponding to an interlayer expansion of ~0.50 nm, indicative of vertical 5-FU intercalation facilitated by the pre-expanded galleries generated during in situ CQD synthesis. FT-IR spectra confirmed the simultaneous presence of clay, CQD, and drug, evidencing preserved CQD–clay interactions and successful drug incorporation. Overall, the findings reveal that differences in clay architecture, together with CQD integration, might influence drug accommodation and the resulting loading efficiency. However, further studies, including quantitative drug loading in CQD-containing systems, release kinetics, and spectroscopic and thermal analyses, are required to elucidate the interaction mechanisms and to correlate structural features with functional properties as nanocarriers. At this stage, the role of CQDs is mainly structural and optical, and further studies are required to confirm their effectiveness as real-time imaging probes in drug delivery.

7 ZIF-8/CQD hybrid nanomaterials

Contents

Chapter 7 Abstract

This chapter aims to make a brief review of MOF, addressing their concept and main characteristics, highlighting the subclass of ZIF and one of its members, ZIF-8. Additionally, the methods of association with CQDs are also reviewed. This chapter is also intended to discuss the results obtained from the hybrid nanomaterial CQD@ZIF-8 in relation to its morphology, structure, and optical properties.

7.1 INTRODUCTION

Metal–organic frameworks are crystalline porous materials formed through the coordination between metal ions and organic ligands, giving rise to periodic networks with well-defined pores (Rasheed et al., 2020; Zeggai et al., 2025). Their modular nature allows precise control over pore size, topology, and chemical composition. As a result, MOFs exhibit exceptionally high surface areas (up to 7000 $m^2.g^{-1}$) and permanent porosity, distinguishing them from conventional porous materials such as activated carbons and zeolites (Qian et al., 2020; Yusuf; Malek; Kailasa, 2022). Among the various subclasses of MOFs, zeolitic imidazolate frameworks have attracted considerable attention due to their structural similarity with aluminosilicate zeolites. In these materials, the coordination between transition metal ions and imidazolate linkers gives rise to framework topologies similar to those of zeolites, while preserving the compositional and structural diversity of MOFs (Zhang et al., 2021; Zhang et al., 2023a).

CDs are zero-dimensional nanomaterials with sizes typically below 10 nm and a structure that can be described as core–shell structure, in which the core may be amorphous, composed of mixed sp^2 and sp^3 hybridized carbon, or partially graphitic with a predominance of sp^2 domains (Bazazi et al., 2024; Li; Gong, 2022). Their surfaces are functionalized with oxygen- and nitrogen-containing groups such as hydroxyl, carboxyl, and amino moieties introduced during synthesis. These surface functionalities play a key role in determining the physicochemical behavior of CDs, including solubility, surface charge, and interactions with the surrounding environment (Sukunta et al., 2025). The optical properties of CDs are strongly influenced by particle size through quantum confinement effects, as well as by surface chemistry (Ozyurt et al., 2023). Consequently, control over morphology, size distribution, and surface chemistry enables the preparation of CDs with desirable properties, including high quantum yield, tunable emission, photostability, and low toxicity (Elugoke et al., 2024; Ghosh et al., 2023).

Despite these optical characteristics, CDs tend to aggregate at high concentrations, leading to the aggregation-induced quenching (AIQ) effect that can severely weaken their fluorescence and limit practical applications(Li et al., 2024b). While CDs remain homogeneously dispersed at low concentrations, increasing concentration promotes particle aggregation and enhances non-radiative pathways (Yang et al., 2022). One possible mechanism associated with the AIQ effect is related to the predominantly planar aromatic structures of CD chromophores. In the aggregated state, strong π-π stacking interactions between adjacent carbon

cores lead to energy level splitting into quasi-continuous bands, which favors non-radiative transitions and ultimately results in fluorescence quenching (Hu; Li; Gong, 2024; Kang et al., 2022). Therefore, preventing the accumulation of CDs is a key challenge for maintaining their optical performance. In this context, combining CDs with porous host materials has emerged as an effective strategy to overcome AIQ (Zhang et al., 2020).

This association can be achieved through pore confinement or through surface interactions with host materials, which restrict particle mobility and reduce interparticle interactions among CDs (Li et al., 2021). Even when confinement within pores is not possible due to dimensional incompatibilities, interactions between CDs and the host matrix can promote a more homogeneous distribution (Yang et al., 2022; Zhang et al., 2023b). Among available host materials, MOFs are particularly attractive due to their high specific surface area, tunable structure and pore diameters, and modified surface (Jia; Gu; Li, 2022; Yin et al., 2021). Their ordered architecture allows CDs to be located either within internal pores or at specific sites of the framework, depending on the synthesis strategy. In consequence, the formation of hybrid materials provides an effective alternative for preserving the optical properties of CDs while suppressing AIQ (Zheng; Cui; Qian, 2023).

The formation of MOF–CD hybrid materials leads to functional behavior that cannot be achieved by the individual components (Zhang et al., 2023b). From a functional perspective, the integration of CDs within MOF frameworks provides an effective pathway for the development of multifunctional hybrid nanomaterials, allowing their properties to surpass those of the counterpart materials. As a result, MOF–CD hybrids can exhibit enhanced or even new functionalities compared with the individual components (Li et al., 2024b). For example, MOFs typically exhibit low electrical conductivity, which can be improved through association with CDs that modulate charge transport via interfacial interactions (Zhang et al., 2023b).

Several synthetic approaches have been developed to integrate CDs into MOF structures. In ship-in-a-bottle strategies (or *in situ* CDs), CDs precursors are introduced into pre-formed MOFs and subsequently transformed into CDs within the confined pores. This approach limits particle growth and promotes uniform size distribution (Li et al., 2021). In bottle-around-ship methods (or *in situ* MOF), pre-synthesized CDs are used as nucleation centers around which the MOF framework grows, leading to encapsulation during crystallization. In situ encapsulation involves the simultaneous formation of both carbon dots and the MOF from their respective precursors, while impregnation methods rely on diffusion and adsorption of CDs into existing pores or onto external surfaces. Each method results in

different spatial distributions and interfacial interactions between CDs and the MOF host (Lone; Rohit, 2025; Zhang et al., 2023b)

ZIF-8, a zeolitic imidazolate framework composed of Zn^{2+} centers coordinated by 2-methylimidazolate ligands, was selected as the host material in this study for the preparation of ZIF-8/CQD hybrid nanomaterials. The high porosity of ZIF-8 can facilitate the dispersion of CQDs and contribute to the suppression of aggregation-induced quenching. In addition, the chemical stability of ZIF-8 provides a stable environment that supports the preservation of CQD optical properties. In this work, a bottle-around-ship approach was employed, in which CQDs were synthesized from citric acid and urea under solvothermal conditions in the presence of ZIF-8 precursors. Under these conditions, ZIF-8 nanocrystals retained their crystalline structure and rhombic dodecahedral morphology, while the generated CQDs became associated with the ZIF-8 framework. The resulting hybrid nanomaterial exhibits dual-emission behavior under different excitation wavelengths and shows low toxicity. Preliminary results further indicate improved stability of the ZIF-8/CQD hybrid compared with the individual components, suggesting its potential for use in a range of applications.

7.2 METAL-ORGANIC FRAMEWORKS

Metal–organic frameworks are a class of porous materials constructed through the self-assembly of ordered metal ions or clusters, commonly referred to as secondary building units (SBU), which are connected by organic ligands (linkers), resulting in complex architectures that can extend from one-dimensional to three-dimensional (Benny et al., 2024; Shatery; Omer, 2022). Some representative SBUs and organic linkers are illustrated in Figure 52. The organic linkers are most frequently carboxylic acid or nitrogen-containing molecules, which can be classified according to the number of available coordination sites they provide: ditopic (two sites), tritopic (three sites), or polytropic (more than three sites) (Alshammari; Jiang; Cordova, 2016; De Villenoisy et al., 2023). Compared with conventional porous materials such as zeolites and carbons, one distinctive feature of MOFs is the high degree of tunability arising from their modular construction, which allows, in principle, an almost unlimited combination of inorganic and organic building units. This level of structural control enables precise tailoring of framework composition, topology, and pore environment to achieve targeted functionalities (Jiao et al., 2019).

Figure 52 - Representative SBU and organic linkers

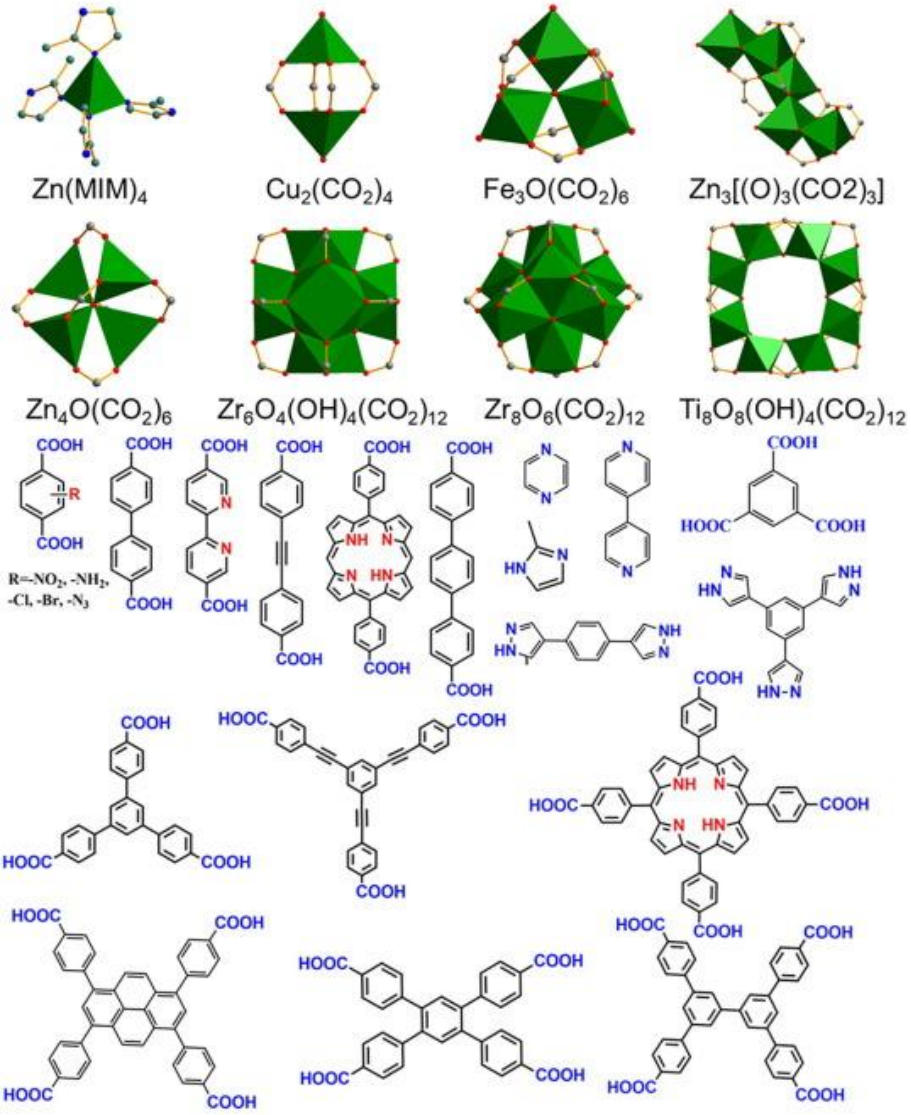

Source: Jiao et al. (2019)

Despite their relatively recent development, the background of MOF chemistry is based on over a century of early studies on transition-metal coordination complexes (Kirlikovali et al., 2023). In 1965, Tomic reported the MOF kind of structures (coordination polymers) formed from carboxylic linkers and Zn, Ni, Al, and Fe. In this study, they investigated the role of the metal ion in thermal stability and the coordination sites on the linkers (Tomic, 1965). Later, in 1989, Hoskins and Robson proposed innovative materials by linking tetrahedral or octahedral centers with rod-like connecting units with more rigid coordination networks with large porous channels. The structures had potential for application in ion exchange, however, these structures were not stable to remove solvent guest molecules from the pores (Hoskins; Robson, 1989).

The term 'metal-organic framework' was first introduced in 1995 by Yaghi and Li, who described the hydrothermal synthesis of a crystalline structure resembling zeolites through the

polymeric coordination of copper with 4,4'-bipyridine and nitrate ions (Yaghi; Li, 1995). Another work from the Yaghi group published in 1999 has contributed to establishing this class of materials as a prominent area of research. MOF-5, the object of this study, is composed of octahedral $Zn_4O(\text{-}COO)_6$ SBUs joined by ditopic BDC (1,4-benzenedicarboxylate) linkers to give a 3D framework structure with alternating interconnected pores of 15.1 Å and 11.0 Å in diameter and a pore aperture of 8.0 Å. MOF-5 allowed for gas sorption measurements, revealing a porosity of 61% and a BET surface area of 2320 m^2/g. An important feature of this material is that the pores have no walls. This provides an unprecedented openness of the structure that allows guest molecules with great mobility without clogging the pores (Li et al., 1999).

Initially, MOFs were named according to the discovery order, such as MOF-5, MOF-9, MOF-253, etc. Later, they were named after the place of their discovery, for example, the University of Oslo (UiO-66, UiO-67, UiO-68, etc.), Hong Kong University of Science and Technology (HKUST-1, etc.), Materials Institute Lavoisier (MIL-53, MIL-101, etc.), Instituto de Tecnología Química Metal-organic framework (ITQMOF), Leiden Institute of Chemistry (LIC-1), Seoul National University (SNU), Jilin University China (JUC), Cambridge University KRICT (CUK-1), Washington State University (WSU-5) and Pohang University of Science and Technology (POST), etc (Fatima et al., 2023; Li et al., 2024a). This wide class of MOFs was also consolidated by the study of (Furukawa et al., 2013) that reported the development of over 20,000 different MOFs studied in the past two decades, with the number continuing to grow each year.

The synthesis of MOFs can be influenced by diverse factors, including the nature of metal center, that can coordinate in different geometry (octahedral, tetrahedral, square planar, etc.) during the synthesis process. In contrast, the organic linker is already prepared before the synthetic process, including cyanide, pyridyl, carboxylate, azolates, sulfonates, phosphonates, and hydroxyl. Therefore, the pore size and shape of MOFs are defined by the preferred coordination geometry and the organic linkers as well as by their connectivity (Wuttke et al., 2017). As a representative example (Deng et al., 2012), reported the expansion of the well-known structure IRMOF-74, M_2(2,5-DOT) where M is Zn^{2+}, Mg^{2+} and DOT is dioxidoterephthalate, from the original DOT link of one phenylene ring to create a series of links with two, three, four, five, six, seven, nine, and eleven phenylene rings, resulting in an isoreticular series termed IRMOF-74-I to XI. The systematic elongation of the ligand structure resulted in MOFs with pore apertures ranging from 14 Å to 98 Å, which allowed the incorporation of large molecules such as vitamin B_{12}, metal organic polyhedron-18, myoglobin, and green fluorescent protein in the pores of IRMOF-74-IV, V, VII, and IX, respectively.

These entities are primarily linked through coordination bonds, along with some weaker interactions like Van der Waals forces and hydrogen bonds. These additional interactions provide greater flexibility to the porous crystalline structures (Alshammari; Jiang; Cordova, 2016; Katoch; Goyal; Gautam, 2019). In addition, these interactions force not only stabilize MOF structure but also play a major role in the accommodation of various guest molecules (De Villenoisy et al., 2023; Gangu; Jonnalagadda, 2021). Several methods such as hydrothermal or solvothermal synthesis, mechanochemical, slow diffusion, ultrasonic, microwave, and electrochemical have been employed in the production of highly ordered MOF (Joseph et al., 2021; Kaushal et al., 2021).

MOFs have generated considerable interest as advanced porous materials due to their design flexibility and outstanding properties, including high surface area, reaching values of 7800 m^2/g, tunable and high porosity and thermal stability (degradation temperature between 450 ºC – 500 ºC) (Fatima et al., 2023; Hönicke et al., 2018; Jiang et al., 2022). These materials can exhibit up to 90% free volume, pore sizes typically ranging from 3 Å to 98 Å, covering the full pore size gap between microporous zeolites and mesoporous silicas (Jiao et al., 2019; Katoch; Goyal; Gautam, 2019). Moreover, the permanent porosity of MOFs enables the adsorption of guest molecules, thereby facilitating extensive host–guest interactions. As a result, MOFs are considered promising candidates for a wide range of applications, including gas adsorption and separation (Duong et al., 2020), catalysis (Daturi et al., 2024), drug delivery (Schnabel; Ettlinger; Bunzen, 2020), and sensing (Ma et al., 2025).

7.2.1 Zeolitic Imidazolate Frameworks

Zeolitic imidazolate frameworks (ZIFs) are a subclass of MOFs that integrate the structural characteristics of both zeolites and MOFs. They are constructed according to the principles of reticular chemistry, in which the tetrahedral framework of zeolites, composed of silicon (Si) or aluminum (Al) atoms bridged by oxygen, is replaced by tetrahedrally coordinated metal cations such as Co^{2+}, Zn^{2+}, or Cu^{2+} (Noh; Lee; Kim, 2018). These metal centers are interconnected by imidazolate or derivative linkers, resulting in hybrid frameworks that exhibit zeolite-like topologies (Feng et al., 2021).

In these structures, the metal ions coordinate through the nitrogen atoms of ditopic imidazolate ligands, forming neutral three-dimensional networks with tunable nanoscale pores The resulting M–IM–M connections (where M denotes the tetrahedrally coordinated metal ion and IM represents the imidazolate ligand) exhibit an angle of approximately 145°, closely

resembling the Si(Al)–O–Si(Al) angle in conventional zeolite frameworks (Figure 53) (Zhang et al., 2020; Zheng et al., 2023).

Figure 53 - (a) Bridging angle (145°) of Si−O−Si in zeolites. (b) The M−Im−M in ZIFs, which is a requisite for synthesizing zeolite-type structures, as presented in ZIF

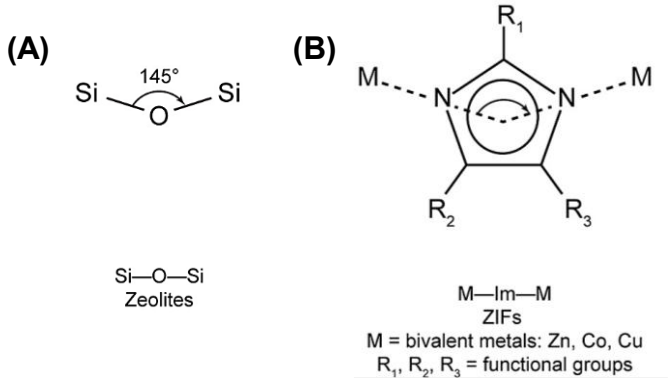

Source: Adapted from Zheng et al. (2023)

The structure of ZIFs largely depends on the choice of the imidazole ligand incorporated into the framework. A wide variety of imidazole ligands can be selected based on their functional groups and molecular size, which lead to markedly different framework architectures. In 2006, Park and co-workers synthesized ZIFs 1–12 with diverse structures by incorporating different ligands and metal atoms (Table 13). For example, they obtained $Zn(MeIM)_2$ with a sodalite (SOD) topology, $Zn(IM)_2$ with a merlinoite structure, and $Zn(PhIM)_2$ with a rhombic dodecahedron (RHOD) topology. Furthermore, distinct framework topologies can be achieved even for the same structural composition (*i.e.,* identical metal and linker) by modifying the synthetic parameters or introducing structure-directing agents. In the same study, for instance, the authors reported body-centered tetragonal (BCT) and deformed ferrite (DFT) zeolite topologies for $Zn(IM)_2$ (Park et al., 2006).

Structural diversity can also be introduced by incorporating two or three different ligands into the framework in varying ratios. For example, the gmelinite (GME) zeolite topology has only been obtained for ZIFs containing two types of imidazole ligands. (Banerjee et al., 2009) synthesized ZIF-78 to ZIF-82 using a combination of 2-nitroimidazole and five different functionalized imidazoles, all of which exhibit the GME topology (Figure 54). Moreover, the pore aperture and cage size can be significantly increased by combining small and bulky imidazole ligands within the same framework.

Table 13 – Composition, and topology of ZIF series of compounds

ZIF	Metal source	Composition	Topology
ZIF-1	Zn(II)	$Zn(IM)_2$	CRB
ZIF-2	Zn(II)	$Zn(IM)_2$	CRB
ZIF-3	Zn(II)	$Zn(IM)_2$	DFT
ZIF-4	Zn(II)	$Zn(IM)_2$	CAG
ZIF-5	Zn(II), In(III)	$In_2Zn_3(IM)_{12}$	GAR
ZIF-6	Zn(II)	$Zn(IM)_2$	GIS
ZIF-7	Zn(II)	$Zn(PhIM)_2$	SOD
ZIF-8	Zn(II)	$Zn(MeIM)_2$	SOD
ZIF-9	Co(II)	$Co(PhIM)_2$	SOD
ZIF-10	Zn(II)	$Zn(IM)_2$	MER
ZIF-11	Zn(II)	$Zn(PhIM)_2$	RHO
ZIF-12	Co(II)	$Co(PhIM)_2$	RHO

Source: Adapted from Park et al. (2006)

Figure 54 – Structure of ZIFs and their respective topology

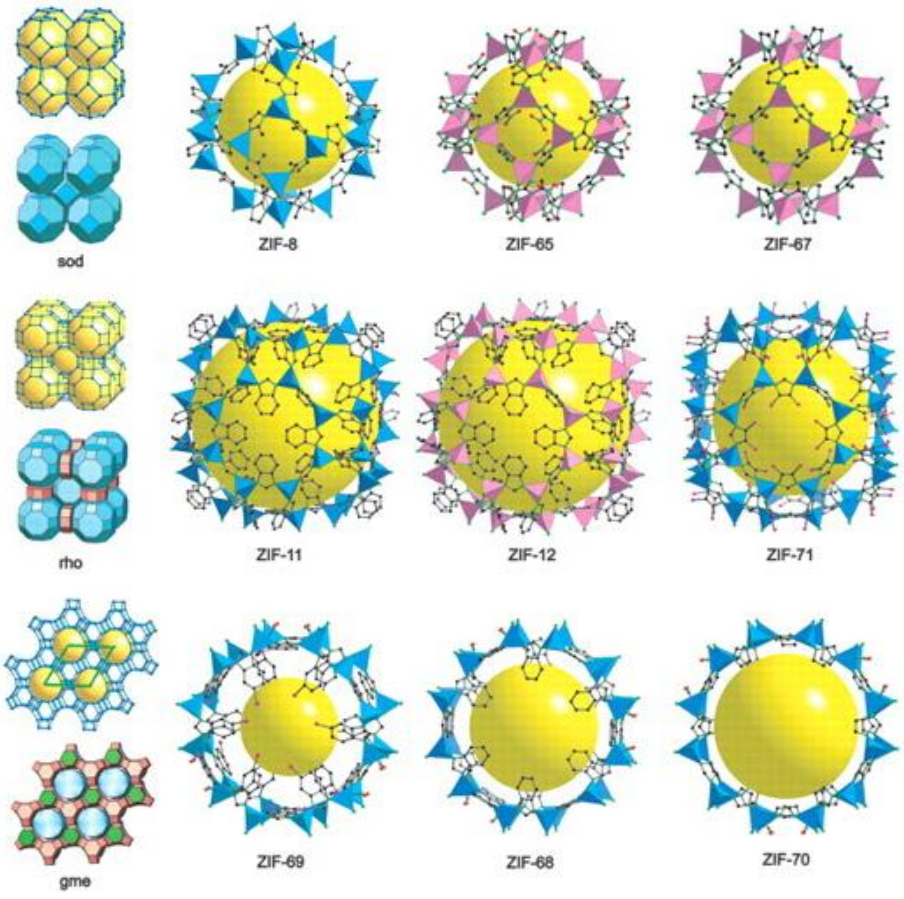

Source: Adapted from Banerjee et al. (2008)

The great interest in ZIFs arises from their outstanding physicochemical properties, including high crystallinity, permanent porosity, rich structural diversity with tunable pore sizes and adjustable functional groups, high specific surface area, and exceptional chemical/thermal stability, which result from strong nitrogen–metal bonds (Noh; Lee; Kim, 2018; Sun et al., 2022). These characteristics make ZIFs highly attractive for practical applications, leading to their extensive use as porous materials in fields such as energy storage (Ikhioya et al., 2024; Karim et al., 2024; Yetiman et al., 2022), separation (Deng; Dai; Deng, 2020; Kachhadiya; Murthy, 2021; Zhang et al., 2022c), catalysis (Kang et al., 2023; Wang et al., 2021b, 2023b), and adsorption (Ismail; Onaizi; Vohra, 2023; Li et al., 2020; Nazir et al., 2022) .

7.2.1.1 Zeolitic Imidazolate Framework-8

As one of the most representative members of the ZIFs, Zeolitic Imidazolate Framework-8 (ZIF-8) is produced when 2-methylimidazole coordinates Zn^{2+}, resulting in a sodalite topology. ZIF-8 features a space group of interconnected six-membered ring windows with an accessible diameter and pore width of 3.4 Å and 11.6 Å, respectively (Bergaoui et al., 2021; Nazir et al., 2025). They possess exceptional surface area (>1600 $m^2.g^{-1}$), and remarkable thermal stability (up to 400 °C), besides the particular stability in water and even mild NaOH aqueous solution, which is rarely seen in MOFs (Noh; Lee; Kim, 2018; Wang et al., 2024a). It was fabricated for the first time by Chen group (Huang et al., 2006), and later, a systematic study was performed by Yaghi's research group and officially named ZIF-8 (Park et al., 2006).

Figure 55 – Crystal structure of ZIF-8: Zn (polyhedral), N (sphere), and C (line)

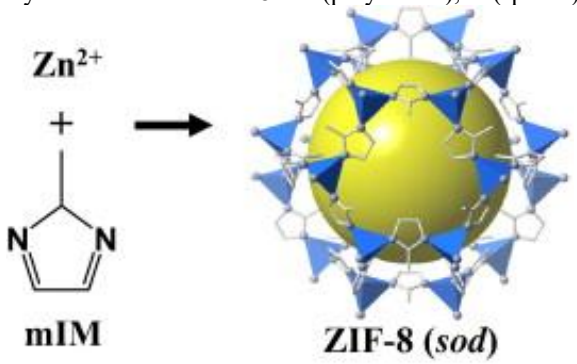

Source: (Lee et al., 2015)

ZIF-8 is typically synthesized at room temperature using solvents such as ethanol, methanol, DMF, or diethylformamide, with zinc nitrate serving as the Zn^{2+} source (Kukkar et al., 2021). This procedure generally yields highly crystalline materials with a cubic topology. Although the synthesis route is easy, a detailed understanding of the nucleation and growth

mechanisms is essential to control the physicochemical properties of the final product. The rates of both nucleation and crystal growth are influenced by various synthesis parameters, which in turn affect particle size, morphology, surface area, and porosity.

A mechanistic pathway for ZIF-8 nucleation has been proposed by (Öztürk; Filez; Weckhuysen, 2017) involving three principal steps: (i) coordination of 2-methylimidazole ligands to Zn^{2+} centers; (ii) deprotonation of the coordinated ligands; and (iii) polymerization of the resulting deprotonated $Zn(mim)_4$ units. The deprotonation step is particularly critical, as it enables the formation of Zn–N–Zn bridges that initiate the nucleation process. Complementarily, (Liu et al., 2021) proposed an initial prenucleation stage, in which the reaction medium undergoes phase separation to form solute-rich domains. These domains subsequently condense into dense, metastable amorphous aggregates of $Zn(mim)_4$ units, which act as precursors for the crystallization of ZIF-8.

The morphological evolution of ZIF-8 crystals during growth is illustrated in Figure 56, ZIF-8 crystals may adopt either a cubic morphology, where all six facets are [100]-oriented, or a rhombic dodecahedral morphology, characterized by 12 equivalent rhomboid facets oriented along [110]. The rhombic dodecahedral form represents the most thermodynamically stable morphology. During crystal growth, intermediate truncated polyhedral can be observed, indicating the progressive transformation from cubic to rhombic dodecahedral shapes. For instance, a truncated rhombic dodecahedron presents 12 hexagonal [110] facets and six square [100] facets (Troyano et al., 2019).

Figure 56 - Schematic of the morphological evolution of ZIF-8 crystals, from cubic to truncated dodecahedra (TRD) to rhombic dodecahedra (RD) (top). FESEM images of colloidal ZIF-8 crystals of cubic, TRD or RD morphology (middle and bottom). Scale bars: 250 nm (middle) and 1 mm (bottom).

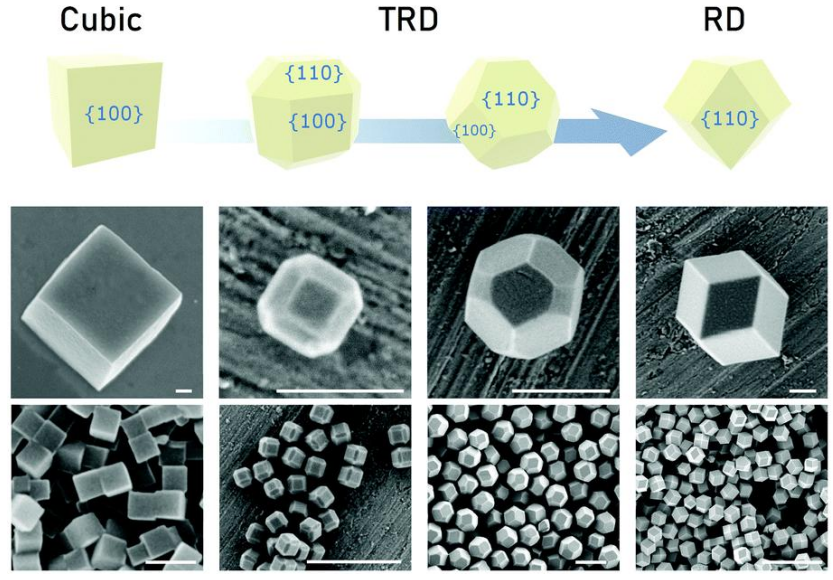

Source: Troyano et al. (2019)

7.3 MOF/C-DOTS HYBRID NANOMATERIALS

7.3.1 General strategies for fabrication of MOF/carbon dots hybrid nanomaterials

Various CD/MOF materials with different properties have been synthesized using distinct construction strategies. According to previous reports, four main routes are well-stablished: *in situ* CD synthesis, *in situ* MOF synthesis, in *situ* CD/MOF synthesis, and impregnation method. The differences among these strategies are not only in the synthesis steps, but also in the ways CDs are combined with the MOF, which gives the resulting hybrid nanomaterial different characteristics and properties. The next section describes these approaches and the main features of each one.

7.3.1.1 *In situ* CD synthesis

The *in situ* CD synthetic process, also known as "ship in a bottle" approach, involves mixing the initial CD precursors with a pre-synthesized MOF, followed by applying the chosen method to generate the CDs. This strategy can limit the growth of the CD nanoparticles but prevents their aggregation by immobilizing them in the MOF pores (Zhang et al., 2023).

(Yi et al., 2024) described the successful fabrication of a bifunctional MOF-encapsulated cobalt-doped CD (Co-CD/PMOF) using the "ship in a bottle" strategy. The porphyrinic MOF was prepared mixing $ZrCl_4$ (17 mg), Fe-TCPPCl (24 mg) and DMF as solvent, following by heating at 120 °C for 24 h. For the preparation of Co-CD/PMOF, the resultant PMOF composed of Zr/Fe nodes was dispersed in deionized water, and then CA, $CoCl_2$ and ethylenediamine (EDA) were added to the mixture and transferred to an autoclave and heated at 180 °C for 10h. During this synthesis, the Co-CDs were doped *in situ* within the pore channel of PMOF, and their uniform size distribution with an average of diameter of 11 nm was observed by TEM images. In contrast, Co-CD/PMOF showed a typical rod-shaped structure with ~1 μm width and ~4 μm length but it was noted CD agglomeration into large particles. XPS analysis evidenced the presence of abundant Co-N_4 active sites provided by doped Co-CDs, and the synergistic effect between fully exposed Fe-N_4 and Co-N_4 active centers, which results in excellent peroxidase-mimic catalytic activity of the resultant material Co-CD/PMOF.

In the study conducted by (Gu et al., 2017), MOFs with different pore sizes were employed as host templates for the synthesis of CDs. Initially, the MOFs were loaded with

glucose, an inexpensive carbon source that can be carbonized at low temperatures. Due to the small molecular size of glucose, it can infiltrate the MOF pores from the liquid phase, forming a glucose–MOF hybrid that is subsequently heated at 200 °C under a nitrogen atmosphere for 2 h. Since the MOF framework remains stable at this temperature, the CDs generated by calcination are confined within the MOF pores, resulting in CD@MOF. The CD size could be controlled by selecting the appropriate MOF template, namely HKUST-1, ZIF-8, or MIL-101, with pore sizes of approximately 1.35 nm, 1.9 nm, and 3.4 nm, respectively (Figure 57). To characterize the morphology of the resulting CDs, the CD@MOF samples were digested by KOH solution, dissolving the MOF and resulting in a suspension of CD nanoparticles. The TEM images revealed average CD sizes of 1.5 nm, 2.0 nm, and 3.2 nm for CD@HKUST-1, CD@ZIF-8, and CD@MIL-101, respectively, which correspond closely to the pore sizes of the MOF templates. When glucose powder was calcined under the same conditions without an MOF template, the resulting CDs exhibited an average diameter of approximately 4.5 nm and an irregular size distribution. These findings demonstrate that porous MOFs serve as effective templates for the controlled synthesis of uniform, nanometer-sized CDs. Using a similar approach, (Lin et al., 2018) and (Gholizadeh; Shahsavari; Gholami, 2021) employed glucose as a precursor, followed by calcination under a nitrogen atmosphere, to obtain MIL-53(Fe)/CQDs and CDs/MIL-88B(Fe)/Bi_2S_3, respectively.

Figure 57 – TEM images of CDs prepared with the templates HKUST-1 (a), ZIF-8 (b), and MIL-101 (c). d–f) Size distributions of the CDs obtained with the templates HKUST-1 (d), ZIF-8 (e), and MIL-101 (f). g) Comparison between the size of CDs templated by MOFs and the corresponding simulated MOF pore size

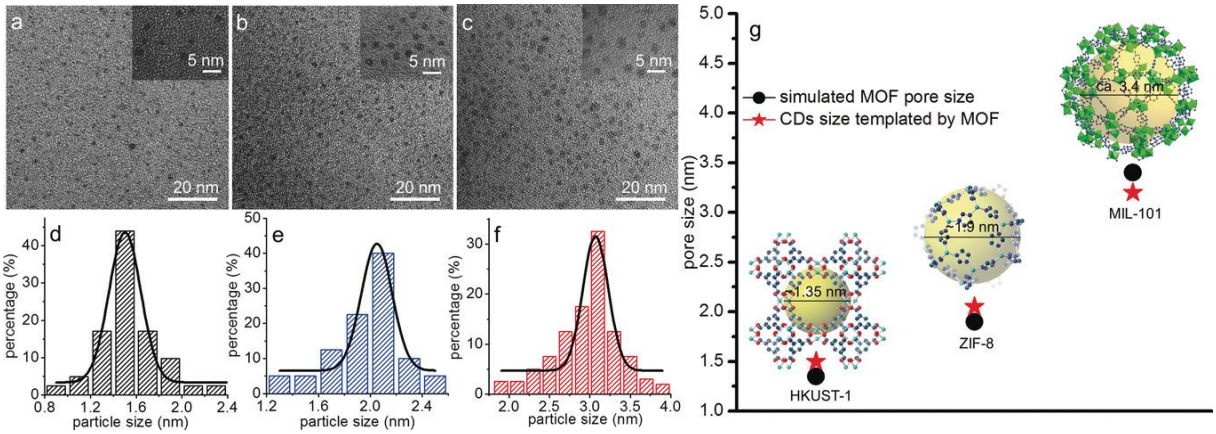

Source: Gu et al. (2017)

Meng et al. (2019) describe the preparation of a ternary hybrid material in which CdS and CDs are formed inside the pores of MIL-101 using the “ship in a bottle” strategy. MIL-101, using $Cr(NO_3)_3 \cdot 9H_2O$ and terephthalic acid is dispersed in n-hexane while aqueous

solutions containing $Cd(Ac)_2$, Na_2S and glucose are added dropwise. According to the authors, the hydrophilic nature of the MIL-101 pores favors the incorporation of aqueous precursors into the internal cavities, enabling encapsulation inside the pores rather than deposition on the external surface or remaining in solution. After precursor filtration, the solid heated at 200 °C under a nitrogen atmosphere, promoting the *in situ* carbonization of glucose and leading to the formation of CD. Subsequently, a hydrothermal treatment at 180 °C enables the reaction between Cd^{2+} and S^{2-} species already present inside the framework, resulting in the formation of CdS. The HRTEM images show that CdS have particle sizes of approximately 3 nm and exhibit clear lattice fringes with an interplanar spacing of 0.336 nm, corresponding to the (002) crystallographic plane of hexagonal CdS. In addition, CDs with a narrow size distribution around 3 nm are also observed, displaying no visible lattice fringes, suggesting their amorphous structure. In addition, TG analysis estimates a CD content of approximately 5.2% in weight.

7.3.1.2 *In situ* MOF synthesis

The *in situ* MOF synthesis, also known as “bottle around ship” approach, consists of preparation of CDs first and then assembling with MOF precursors around them. This strategy allows the encapsulation of CDs within the MOF matrix, which reduces their agglomeration. More importantly, since CD can be pre-synthesized, their size and structure can be adjusted considering a specific application (Zhang et al., 2023b).

In 2016, Xu et al. synthesized CDs@ZIF-8**,** in which CDs prepared by a rapid thermal method were directly introduced into a zinc nitrate and 2-methylimidazole reaction medium, enabling their incorporation into the ZIF-8 framework during *in situ* crystallization (Xu et al., 2016). For comparison, a control material denoted as CDs+ZIF-8 was prepared by physically mixing preformed ZIF-8 with CDs, in which the carbon nanoparticles are only weakly associated with the MOF surface. XRD patterns of CDs@ZIF-8 show diffraction planes that are consistent with those of pristine ZIF-8, indicating that the presence of CDs does not alter the crystalline structure of the framework. FT-IR spectra contain the characteristic vibrational bands of ZIF-8 together with signals associated with the CDs, supporting the coexistence of both components without evidence of new bond formation. TEM images show that CDs@ZIF-8 retains the rhombic dodecahedral morphology of ZIF-8 with particle sizes around 40 nm, while the CDs are not directly observed, which was attributed to their size. Dynamic light scattering (DLS) analysis shows that CDs@ZIF-8 suspensions present aggregation with an increased hydrodynamic diameter of 550 nm, which is attributed to reactions between

Zn(Hmin) moieties at particle surfaces during drying, leading to Zn–min–Zn linkages between nanoparticles. PL measurements indicate that CDs@ZIF-8 preserves the emission profile of free CDs, with a maximum near 480 nm, and maintains fluorescence after repeated washing, in contrast to CDs+ZIF-8, confirming stable incorporation of CDs within the ZIF-8 matrix. Lin et al. (2014) reported branched poly(ethyleimine)-capped CQDs (BPEI-CQDs) into ZIF-8 using the *in situ* strategy at room temperature.

Peng et al. (2024) reported the synthesis of a hybrid fluorescent material based on CDs combined with a zirconium metal–organic framework, denoted as CDs@MOF-808, followed by post-synthetic modification with Eu^{3+} ions. In this approach, CD were synthesized independently and subsequently introduced into the solvothermal synthesis of MOF-808. XRD analysis shows that the diffraction patterns of CDs@MOF-808 shows negligible changes with the addition of CDs, indicating that the incorporation did not significantly affect the characteristic reflection planes of MOF-808. FT-IR spectroscopy further support hybrid formation through the enhancement of absorption bands at 1661 cm^{-1} and 1553 cm^{-1}, attributed to C=O and C=N vibrations associated with surface functional groups of the CDs, while the characteristic vibrational features of the MOF ligands remain unchanged, indicating that CD incorporation occurs without altering the coordination between zirconium centers and the trimesate ligands. The specific surface area measured by BET decrease from 1984.1 $m^2\ g^{-1}$ for pristine MOF-808 to 653.9 $m^2\ g^{-1}$ for Eu/CDs@MOF-808, accompanied by a reduction in average pore size from 3.64 to 2.96 nm, indicating a reduction in the porous network available. Optical characterization shows dual-emission behavior under 290 nm excitation, with a blue emission band at 440 nm arising from the CDs and a red emission band at 614 nm attributed to Eu^{3+} via ligand-to-metal energy transfer. The incorporation of Eu^{3+} introduces a stable reference emission, enabling ratiometric fluorescence while maintaining the framework structure.

In the study developed by (Dai et al., 2024), a hybrid material referred to as ZIF-Cu/C-dots was synthesized by integrating copper-doped carbon dots (Cu/C-dots) into ZIF-8. The hybrid material was produced by dispersing Cu/C-dots in a 2-methylimidazole solution followed by the rapid addition of zinc acetate. According to authors, during this process, Cu/C-dots participated directly in framework formation through competitive coordination with Zn^{2+} ions. The presence of oxygen-containing surface groups on Cu/C-dots favored Zn–O interactions, accelerating nucleation compared to the synthesis of pure ZIF-8. XPS results revealed shifts in Zn2p and O1s binding energies, suggesting coordination between Zn^{2+} and oxygenated groups from Cu/C-dots. SEM analysis showed that pristine ZIF-8 exhibits a regular 12-hedral morphology with smooth surfaces and an average particle size of approximately 695

nm. After incorporation of Cu/C-dots, the resulting ZIF-Cu/C-dots displayed increased surface roughness and larger particle sizes, which scaled with Cu/C-dot content (Figure 58). At high loadings, particle growth became irregular, suggesting disruption of controlled ZIF crystallization. In this study, the hybrid material exhibited pH-responsive release behavior, antioxidant enzyme-mimicking activity, and antibacterial effects associated with Zn^{2+} release, contributing to improved wound healing in diabetic models.

Figure 58 - (A) Schematic illustration of the formation of ZIF-Cu/C-dots and their (B) particle size statistics. (C) SEM images of ZIF and ZIF-Cu/C-dots-1-5. (D) EDS element mapping of ZIF and ZIF-Cu/C-dots

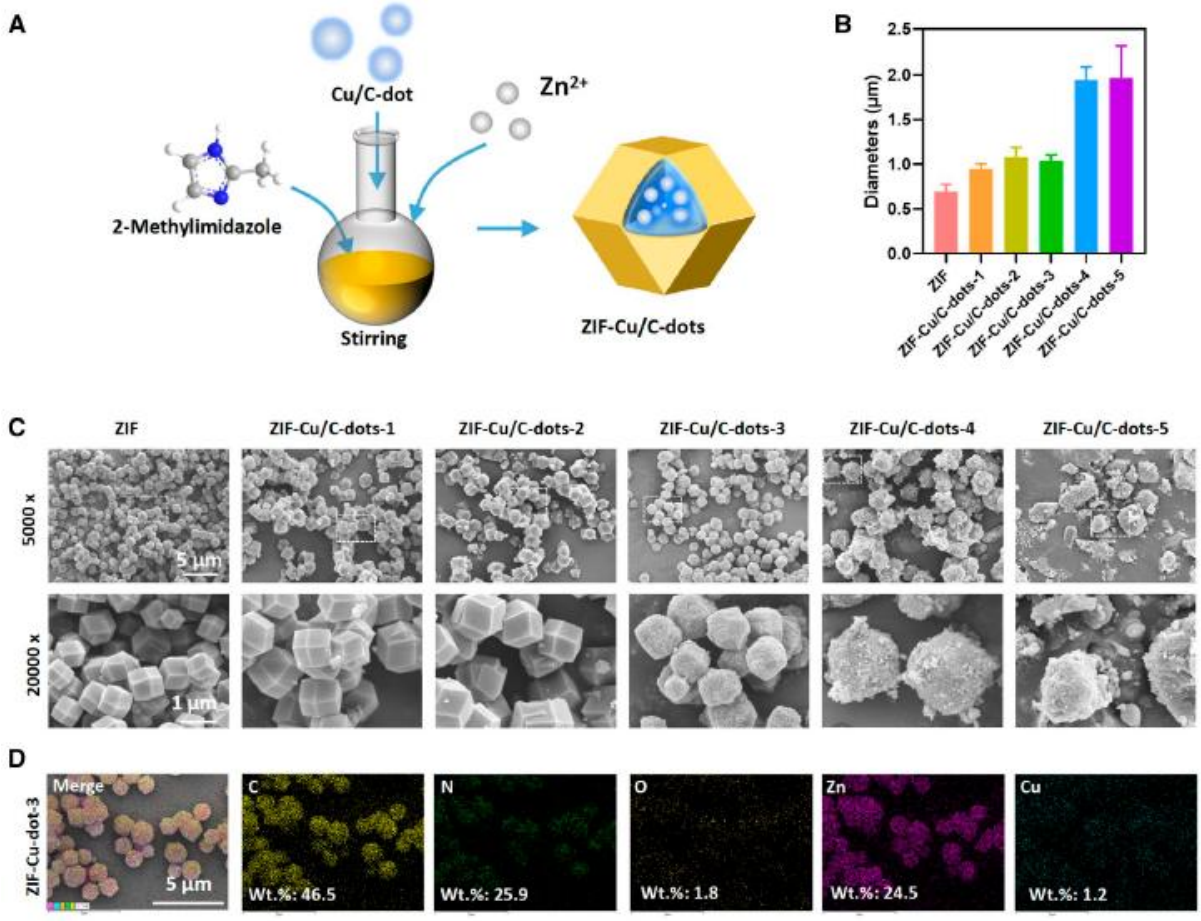

Source: Adapted from Dai et al. (2024)

The “bottle around ship” or *in situ* method presents the advantage of ease of synthesis, which makes it applicable to the preparation of most CD@MOF hybrid materials, enabling the incorporation of pre-synthesized CDs into MOFs while minimizing surface agglomeration. However, a drawback of this strategy is that the fluorescence of the CDs may be partially quenched by metal ions used as MOF precursors during the synthesis, leading to a decrease in fluorescence intensity. Therefore, the successful application of this method depends on the careful selection of compatible MOFs and CDs, as well as control over synthesis conditions to

ensure compatibility between framework growth and optical performance (Li et al., 2021; Zhang et al., 2023).

7.3.1.3 *In situ* CD/MOF synthesis

In this method, MOF and CD are synthesized simultaneously by mixing their precursors together and reacting by specific conditions to generate CD@MOF. The one-step synthetic approach offers advantages in terms of integration, scalability, and reduced consumption of time, solvents, and energy, making it a more efficient and environmentally friendly methodology (Lone; Rohit, 2025). However, its success requires precise control of the synthesis conditions to preserve both the fluorescence of the CDs and the crystallinity of the MOF framework. In this context, key aspects must be considered, including the compatibility of the synthesis conditions for both CDs and MOFs, the absence of interference of CD formation with MOF crystallization, the avoidance of fluorescence quenching by MOF precursors, and the potential formation of CDs outside the MOF cavities (Li et al., 2021).

In a pioneering contribution, Shatery & Omer (2022) reported for the first time the *in situ* synthesis of blue-emissive carbon dots (bCDs) encapsulated within a chromium-based MOF (MIL-101(Cr)), using 2-aminoterephthalic acid both as the organic linker for the MOF and as the carbon precursor for the CDs. This dual role enabled the one-pot hydrothermal formation of the hybrid nanomaterial bCD@Cr-MOF, where the porous MOF architecture acted as a host matrix to entrap and stabilize the luminescent nanoparticles during crystal growth. Moreover, the confinement of bCDs in the MOF framework improved the stability of the bCD@Cr-MOF, preventing aggregation and extending its shelf life to at least four weeks without loss of fluorescence intensity. Morphological and structural analyses confirmed the simultaneous formation and integration of 5–10 nm spherical bCDs inside 120–150 nm rod-like MOF crystals. Importantly, the association of bCDs with the MOF generated clear synergistic effects: while free bCDs typically undergo strong photoluminescence quenching in the presence of various biomolecules and metal ions, their encapsulation minimized this effect, resulting in selective and stable quenching only in the presence of uric acid. This property was successfully applied to bioanalytical assays for the selective and reliable detection of uric acid.

Wang et al. (2025) describe the synthesis of multicolor CDs@ZIF-8 through a controlled *in situ* solvothermal carbonization process (Figure 59). In the first step, the precursors of ZIF-8 were mixed with o-phenylenediamine (OPD), the carbon source, promoting the formation of ZIF-8 crystals while OPD molecules became trapped within the growing

porous structure. The p-OPD@ZIF-8 was subsequently treated under solvothermal conditions in DMF at 200–240 °C for periods between 3 and 12 hours. Within this temperature range, the confined OPD molecules underwent gradual carbonization, producing CDs of increasing size (2.8-6.7 nm). At the same time, the emission wavelength of CDs shifted from blue to red (424-650 nm), mainly owing to the quantum size effect of CDs dominating the photoluminescent properties of CDS@ZIF-8.The proposed mechanism of CD formation emphasizes the cooperative effects of spatial confinement, chemical bonding, and electronic stabilization. The ZIF-8 network acts as a nanoreactor that limits particle growth and suppresses the aggregation-induced quenching. The study also suggests that chemical bonds such as C–N and C–O form at the CD–ZIF interface, increasing the rigidity of the hybrid framework and reducing vibrational energy loss. This explanation is consistent with improved thermal and photostability. An additional factor proposed by the authors is the partial diffusion of Zn^{2+} ions from the ZIF-8 lattice into the carbon network, which creates electronic trap states that regulate radiative recombination.

Figure 59 - Schematic diagram of multicolor CDs@ZIF-8 with high stability prepared by an in situ solvothermal method

Source: Wang et al. (2025)

Yao, Xu and Xia (2018) reported the encapsulation of CDs within a UiO-type zirconium MOF via a solvent free strategy. In this approach, $ZrOCl_2 \cdot 8H_2O$, 2,5-dihydroxyterephthalic acid, and tetraethylammonium bromide (TEAB) are ground together and then crystallizes in an autoclave 180 °C for 24 hours. During this process, UiO-66$(OH)_2$ crystallizes while CDs form in situ and become confined within its pores. The PXRD patterns validated the successful

preparation of UiO-66-$(OH)_2$, and CDs with spherical morphology in 3-8 nm sizes were discovered in high-resolution TEM (HRTEM). In addition, compared to UiO-66$(OH)_2$, the surface area of CDs@UiO-66-$(OH)_2$ decreased, indicating that CDs was successfully encapsulated in UiO-66$(OH)_2$. Optically, the material exhibits blue emission at 464 nm that is independent of excitation wavelength, demonstrating uniformity in size distribution and emissive sites produced by porous confinement, resulting in the application of fluorescence sensors for temperature, pH and Fe^{3+} ions.

7.3.1.4 Impregnation method

In the impregnation method, also known as physical mixing strategy, both CD and MOF are pre-synthesized and mixed directly to form CD/MOF hybrid nanomaterials. Due to size and affinity, the CD can access to the pores of MOF and interact with its surface to form hybrid nanomaterials (Li et al., 2022). Nevertheless, weak interaction may lead to leaching of CD nanoparticles and result in limited encapsulation efficiency (Lone; Rohit, 2025) .

Si et al. (2020) employed a simple impregnation strategy to obtain a core-shell CQD@ZIF-8 material. A solution of CQD synthesized with glucose as the carbon source (Figure 60) was added dropwise to a methanolic suspension of ZIF-8, followed by sonication and stirring for 24 h at room temperature to achieve adsorption equilibrium. FT-IR spectroscopy showed bands corresponding to the functional groups of both CQD and ZIF-8, suggesting the successful loading of CQD onto ZIF-8 nanoparticles. Specifically, this might be indicated by the bands at 3520 cm^{-1} and 1628 cm^{-1} associated with the stretching vibration of hydroxyl groups and C=C, respectively, in the CQD structure. Moreover, Field Emission Scanning Microscopy (FESEM) images were used to demonstrate the rhombic dodecahedron morphology of ZIF-8, while TEM images revealed that the CQD with 3-5 nm were decorating the ZIF-8 surface, further supporting the core-shell structure.

Figure 60 - Schematic Illustration of the synthesis of CQDs@ZIF-8. The insert exhibits the absorption and excitation-dependent fluorescence spectra of the CQD solution. Optical photograph: CQDs solution under UV light (365 nm) illumination

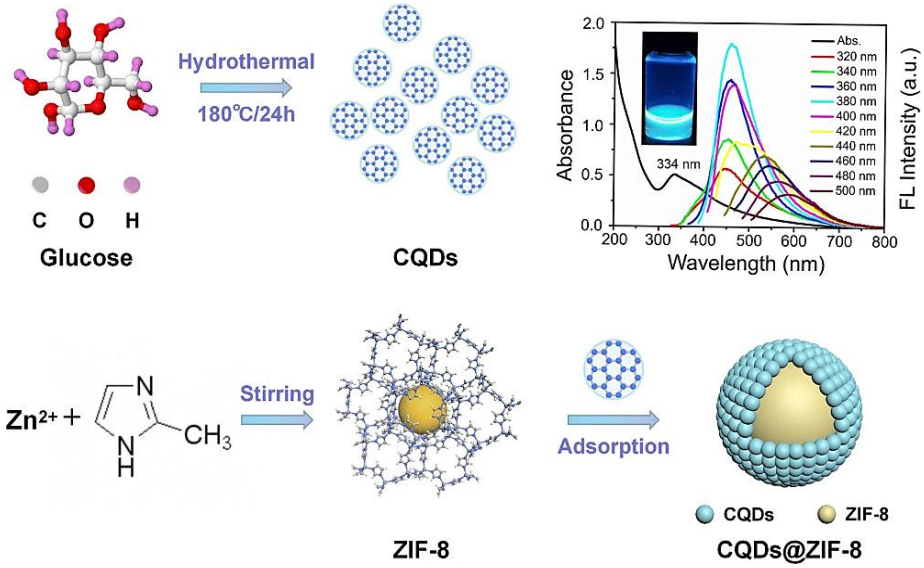

Source: Si et al. (2020)

Yanget al. (2019) obtained amine-CQD@UiO-66 nanomaterials with a similar methodology. Initially, blue fluorescent amine-CQD was prepared using citric acid and ethylenediamine in deionized water, and UiO-66 nanocrystals were obtained by mixing DMF solutions of $ZrCl_4$, 1,4-benzenedicarboxylic acid (H_2BDC), polyvinylpyrrolidone (PVP), and acetic acid (HAc). The final material was synthesized by the immersion of UiO-66 in the presence of amine-CQD for 12 h at room temperature. The XRD patterns of the resulting amine-CQD@UiO-66 agreed well with those of the pristine UiO-66 nanoparticles, indicating their structure was not disturbed during the post-synthetic loading treatment. Regarding PL, amine-CQD showed a maximum emission at 440 nm, and the amine-CQD@UiO-66 showed a slight redshift to 444.5 nm. After storage for 10 days, no obvious PL quenching was observed, implying good stability in the fluorescence properties of the final material. The work discussed above might be an example of the advantages of using this strategy to obtain CD@MOF materials. As the synthetic process of MOF and CD does not interfere with each other, CD@MOF materials can benefit from retained crystallinity and fluorescence. Moreover, it is important to take the size of the CD into consideration. If the size of CDs is larger than the pore diameters of the MOFs, CDs cannot go through the cavities of MOFs, restraining the formation of CD@MOF composites (Hammad et al., 2024).

Another zirconium metal-organic framework was used by Chen and coauthors (2019) to incorporate graphene quantum dots into the mesopores of the PCN-222 (porous coordination framework) to obtain GQD-PCN-222 *via* direct impregnation (Figure 61). Free PCN-222

microcrystals were synthesized using $ZnCl_2$, TCPP (tetrakis(4-carboxyphenyl)porphyrin), and benzoic acid in the presence of DMF. Meanwhile, GQD, with an average size of 3.1 nm was synthesized in aqueous solutions using a direct current microplasma electrochemical reactor operated at ambient conditions. For the synthesis of GQD-PCN-222, initially, it was mixed 7.53 mL of the GQD solution was mixed with 9.72 mL of a 0.1 M HCl aqueous solution in a scintillation vial. Following this, 25 mg of activated PCN-222 was added to the mixture, and the suspension was kept at room temperature for 7 days to obtain the final material. As revealed in the nitrogen-desorption isotherm and BET calculations, PCN-222 possesses mesoporous characteristics and a surface area of 2420 m^2/g. After the incorporation of GQD into the PCN-222, the BET surface area decreases to 1010 m^2/g. A remarkable reduction in pore size in the mesoporous region from 3.2 to 2.7 nm also were noted, but such reduction does not occur in the microporous region; this observation indicated that the graphene quantum dots are presented in the mesoporous channels of the framework in GQD-PCN-222 rather than adsorbed on the external surface of MOF crystals (Chen et al., 2019).

Figure 61 - Incorporation of Graphene Quantum Dots via direct impregnation

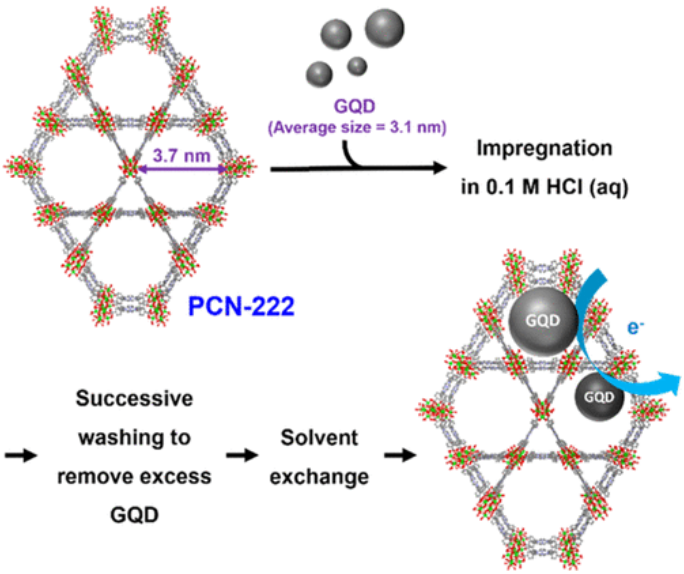

Source: Chen et al. (2019)

As the characteristics of both CDs and MOFs can be pre-adjusted, the prepared CD-MOF with the physical mixing method can be more easily targeted for application. With this methodology, the distribution of CD involves diverse forms like adsorbing on the MOF surface and/or occupying the pore space of the framework.

7.4 RESULTS AND DISCUSSION

The XRD pattern of ZIF-8 shows reflections at 2θ = 7.30°, 10.37°, 12.70°, 14,71°, 16.44°, and 18.01°, which correspond to the (011), (002), (211), (022), (031), and (222) diffraction planes, respectively (JCPDS Card No: JCPDS 00–062-1030), which are in good agreement with previous reported findings (W. D. C. Santos et al., 2023). For the synthesis of ZIF-8/CQD hybrid nanomaterials, 200 mg and 400 mg of CQD were used in the *in situ* synthesis. As observed in Figure 62A, the diffractogram of the sample ZIF-8/CQD 400 shows the absence of the main reflection plane of ZIF-8, indicating that the crystallization of the zeolitic imidazolate is significantly hindered. This behavior can be attributed to the high concentration of CQDs in the reaction medium, which may interfere with nucleation and crystal growth. On the contrary, the diffraction pattern of ZIF-8/CQD 200 (Figure 62B) is consistent with pure ZIF-8, confirming the successful formation of ZIF-8 crystalline phase in the presence of a lower amount of CQD. Nevertheless, no diffraction peaks of CQD were observed, which could be related to the low content of CQD (dilution effect) and low crystallization (Si et al., 2020). Moreover, the sharp and intense diffraction peaks observed for both pristine ZIF-8 and the ZIF-8/CQD 200 hybrid nanomaterial indicate a high degree of crystallinity, suggesting that the incorporation of CQDs at this concentration does not compromise the structural integrity of the ZIF-8 framework.

Figure 62 – Diffraction patterns of (A) ZIF-8 and ZIF-8/CQD 400, and (B) ZIF-8 and ZIF-8/CQD 200 hybrid nanomaterials

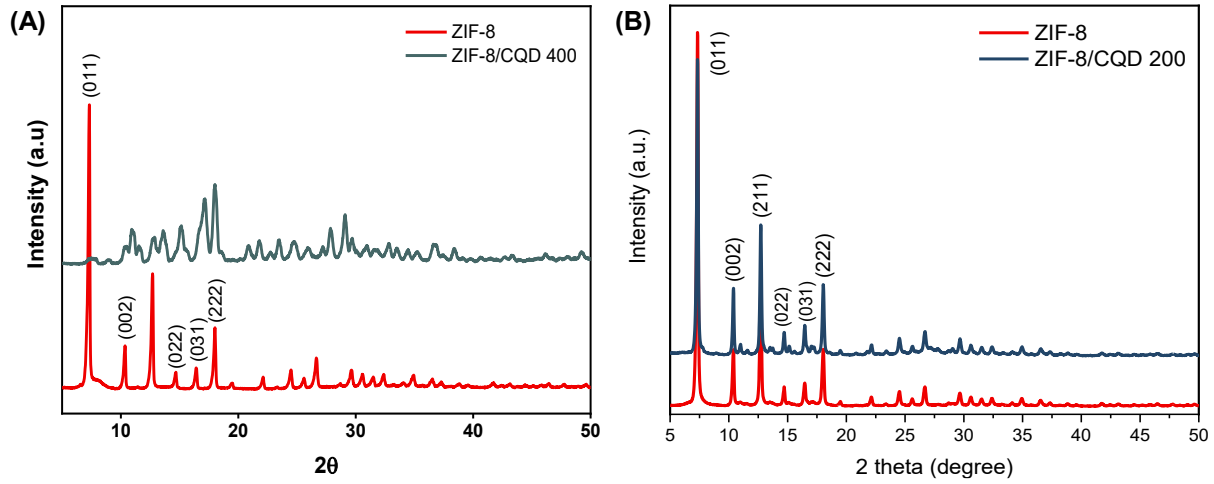

FT-IR measurements were used to gain valuable information regarding the incorporation CQD into ZIF-8 (Figure 63). The ZIF-8 spectrum showed bands at 2978 cm^{-1} and 2906 cm^{-1} corresponding to the stretching vibration of the C-H bond of imidazole and methyl

group in 2-MI, respectively. At 1673 cm^{-1} and 1583 cm^{-1} it is observed the bands associated with the stretching vibration of C=C and C=N in the imidazole ring, respectively (Tuncel & Ökte, 2021). The band at 1425 cm^{-1} is related to the elongation of the imidazole ring, whereas the band at 1146 cm^{-1} is ascribed to C-N stretching vibration. The out-of-plane bending vibrations of the imidazole ring are in correspondence with bands at 1311 cm^{-1}, 996 cm^{-1}, and 757 cm^{-1}. Similarly, the band at 691 cm^{-1} occurs due to the out of plane bending vibration of the imidazole ring (Gao et al., 2023). In addition, the intense band exhibited at 422 cm^{-1} is attributed to Zn-N stretching vibrations, which suggests the coordination between the metal ion and the organic ligands (Tuncel; Ökte, 2021).

Figure 63 - FT-IR spectra of ZIF-8, ZIF-8/CQD hybrid nanomaterial, and CQD recorded in ATR mode in the range of 4000-400 cm^{-1}

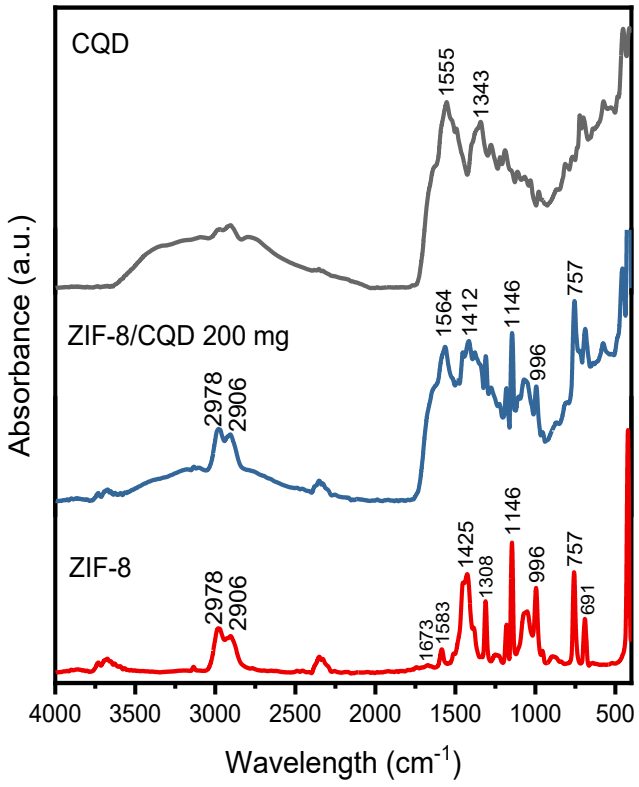

After the incorporation of CQD, the FT-IR spectrum of ZIF-8/CQD 200 showed features of both ZIF-8 and CQD. It is possible to identify a wide band at 3500-3200 cm^{-1} associated with -OH and -NH_2 stretching vibration of CQD in the ZIF-8/CQD 200 spectrum. In addition, the bands associated with vibrations of C-H bond of imidazole ring and methyl group at 2978 cm^{-1} and 2906 cm^{-1} are preserved. The antisymmetric and symmetric stretching vibration of COO^- group appears at 1555 cm^{-1} and 1343 cm^{-1} in CQD, respectively, shifting to 1564 cm^{-1} and 1378 cm^{-1} indicating possible interactions involving this group. Moreover, in the hybrid nanomaterial

bands at 1146 cm-1, 996 cm^{-1}, and 757 cm^{-1} related with the starching of C-N bond and the bending modes of imidazole ring. Furthermore, the band attributed to the Zn-N bond is evidenced in the spectrum of the hybrid. These results indicated the preservation of both CQD and ZIF-8 features, and the main alterations observed are suggestive of interactions involving the oxygen-containing groups of CQD in the ZIF-8/CQD 200 hybrid nanomaterial.

Figure 64 shows the TG/DTG profiles of ZIF-8 and the ZIF-8/CQD 200 hybrid nanomaterial evaluated under a synthetic air atmosphere. Pristine ZIF-8 exhibits high thermal stability up to 300 °C, with a weight loss of only 5.45%, which can be attributed to the removal of guest molecules occluded within the pores and/or adsorbed on the ZIF-8 surface *(e.g.,* H_2O and CO_2). In addition, the presence of residual methanol from the synthesis process cannot be discarded. Above this temperature, a gradual mass loss is observed up to 614 °C, accompanied by two DTG maxima (T_{max}) at 449.4 °C and 532.15 °C (James; Lin, 2016). The first T_{max} corresponds to the thermal instability of the ZIF-8 nanocrystals, indicating the beginning of framework decomposition. After reaching this decomposition temperature, the weight-loss with a T_{max} at 532.15 °C is associated with the collapse of the ZIF-8 structure and partial carbonization under extreme thermal stress. Beyond this stage, no significant mass loss is detected, resulting in a final residue of 31.55% at 900 °C, which can be ascribed to the formation of ZnO (Missaoui; Kahri; Demirci, 2022).

Figure 64 – TG and DTG curves for (A) ZIF-8 and (B) ZIF-8/CQD 200 hybrid nanomaterial up to 900 °C under a synthetic air atmosphere

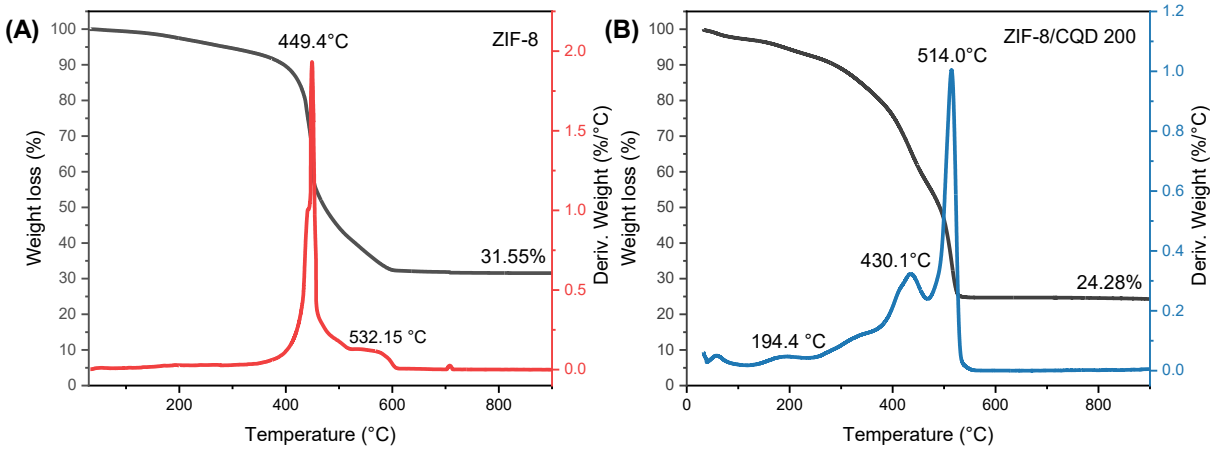

For ZIF-8/CQD 200 hybrid nanomaterial, the TG curve shows a weight loss of 11.03% with T_{max} at 58.75 °C and 194.4 °C, in correspondence with removal of physorbed water molecules at the surface of CQD nanoparticles and within the pores/surface of ZIF-8. Above this temperature, is observed a gradual and intense loss of approximately 64.26% in weight up

to 560 °C. The T_{max} at 430.1° observed is related with the removal of functional groups of CQD surface, and the most intense DTG peak at 514 °C is in corresponded with decomposition of ZIF-8 structure. It is worth mentioning that the T_{max} associated with structural collapse is shifted to 449.4 °C in pure ZIF-8 to 514.0 °C in ZIF-8/CQD 200 material, indicating that the association between ZIF-8 and CQD not only permits the formation of a crystalline structure as observed in XRD, but improves their thermic stability. At the end of analysis, the remaining mass fraction was 24.28%, indicating a reduction compared to pure ZIF-8, which could be attributed to the presence of CQD that possesses a lower thermal stability profile. Using thermogravimetric analyses, the CQD content in ZIF-8/CQD 200 hybrid was calculated to be 41.18% in weight, indicating that the *in situ* approach was efficient for incorporating CQDs during MOF formation.

The morphology of ZIF-8 and ZIF-8/CQD 200 hybrid nanomaterial was investigated by SEM images. Figure 65 shows the formation of rhombic dodecahedron-shaped crystals of ZIF-8 with uniform size distribution. Moreover, ZIF-8/CQD 200 hybrid nanomaterial maintains the polyhedral structure, however the distribution appears to be more heterogeneous with large particles compared to ZIF-8, which can be attributed to the incorporation of CQD in the structure. The size distribution of the materials confirmed this interpretation. For ZIF-8 (Figure 65E), the mean diameter the particles were 111.29 ± 16.82 nm compared to 132.46 ± 31.05 nm for ZIF-8/CQD 200, indicating that the presence of CQD in the ZIF-8 synthesis led to an increase in the diameter of the particles. This effect was also observed in the work of Li et al., (2025) that found values of particles sizes of approximately 122 nm for ZIF-8 and 150 nm for ZIF-8@CDs, which they attributed to the strong binding between ZIF-8 and CDs.

Figure 65 - SEM of ZIF-8 at magnification of (A) 25,000 and of (B) 50,000, and ZIF-8/CQD 200 hybrid nanohybrids at magnification of (C) 25,000 and of (D) 50,000

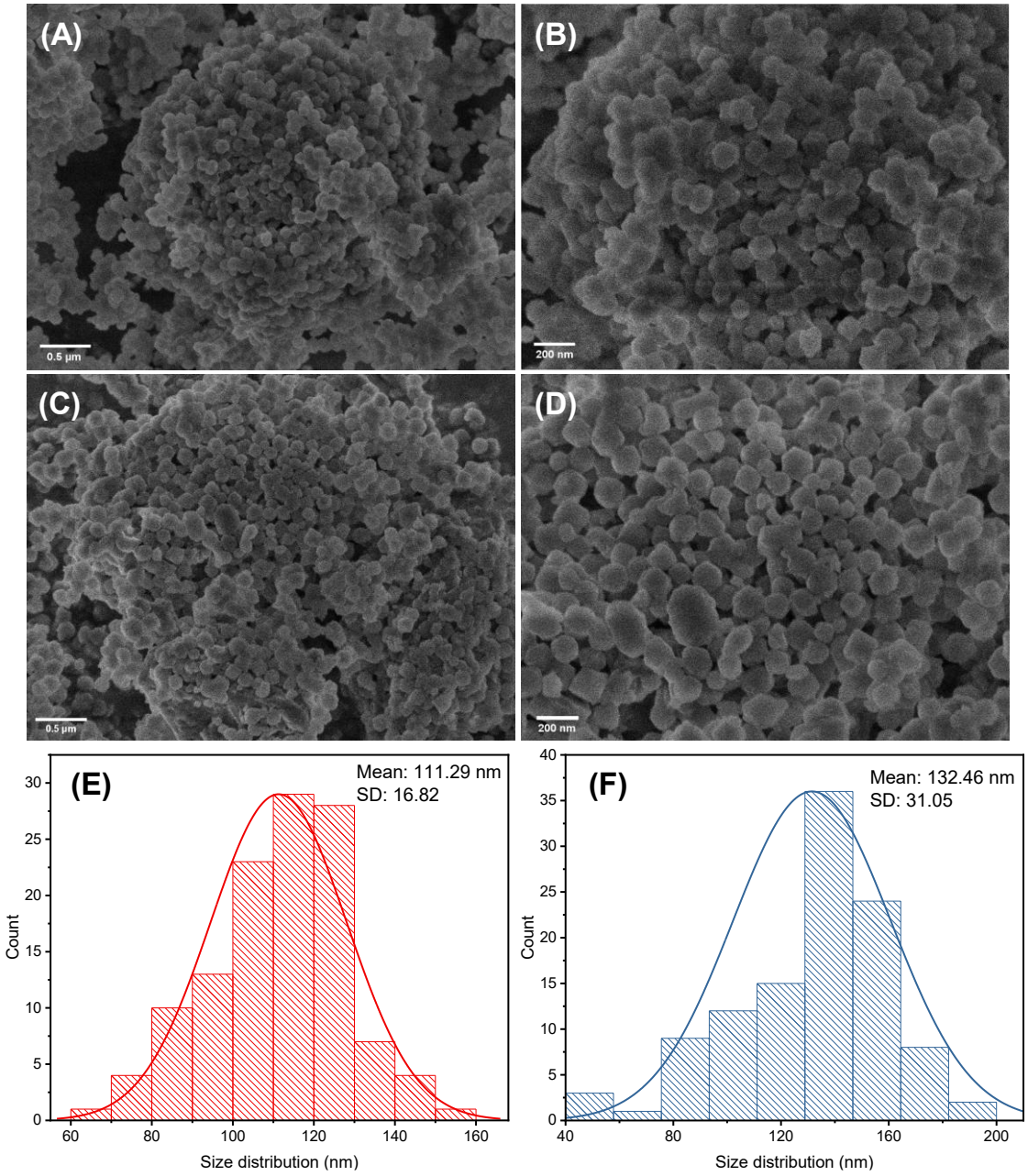

N_2 adsorption-desorption isotherms were used to evaluate the textural properties of the synthesized materials at -196 °C (Figure 66). ZIF-8 presents a type I isotherm according to the IUPAC classification, which is characteristic of microporous materials and agrees with other previous reports (Li et al., 2022). ZIF8/CQD 200 also exhibits type I isotherm, suggesting that the structure of ZIF-8 remains unaltered after the introduction of CQD which confirms the results discussed from XRD data. Moreover, the isotherm curves show a secondary rise at

higher pressure (when $P/P_0 = 0.75$), indicating the existence of mesopores in the structure of the materials.

From the isotherm data, it was also possible to determine the specific surface, the volume and pore diameters of ZIF-8 and ZIF8/CQD 200 material. The data displayed in Table 15, demonstrated that the specific surface is and pore volume decrease from 758.33 m^2/g and 0.58 cm^3/g in pure ZIF-8 to 264 m^2/g and 0.20 cm^3/g in ZIF8/CQD 200, respectively, confirming the attachment of CQD into the surface of ZIF-8, that acting blocking their pore channels and limiting the access of nitrogen used in the measurements(Santos et al., 2024) . In opposition, the pore diameter of the samples remains almost unchanged, indicating the CQD was not able to enter in the pores structure of ZIF-8. According to the set of results obtained, it can be inferred that incorporation of CQDs into the ZIF-8 structure may occur through two main pathways: (i) physical encapsulation within the microporous framework during nucleation, or (ii) surface adsorption and coordination with unsaturated Zn sites, being necessary complementary techniques, such as XPS or confocal fluorescence mapping in order to distinguish between these mechanisms. This possible incorporation may influence the optical behavior and stability of the hybrid nanomaterial, as discussed in the following section.

Figure 66 – Nitrogen adsorption-desorption of ZIF-8 and ZIF8/CQD 200 hybrid nanomaterial at 77 K

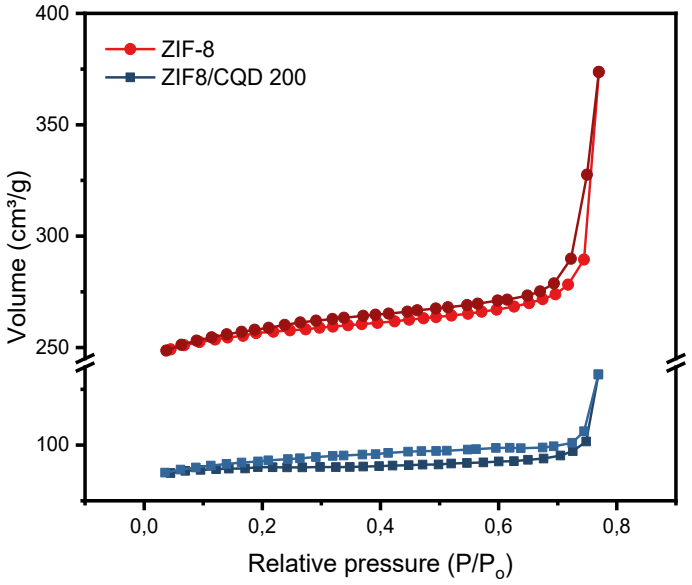

Table 14 - Textural properties of ZIF-8 and ZIF8/CQD 200 hybrid nanomaterials

Sample	Surface area (m^2/g)	Pore volume (cm^3/g)	Pore diameter (nm)
ZIF-8	753.33	0.58	3.07
ZIF8/CQD 200	264.91	0.20	3.08

7.4.1 Optical properties

Absorption spectroscopy was performed to gain insight about the incorporation of CQD into ZIF-8. Figure 67 shows the UV-Vis spectra of ZIF-8, CQD, and ZIF-8/CQD 200 dispersions in methanol. For CQD, the absorption profile in methanol is similar to that observed in water (Chapter 4), however their behavior is thoroughly discussed by Zaini et al. (2023) . Two main absorption bands are observed in the UV region, corresponding to π–π* (272 nm) and n–π* (400 nm) electronic transitions. The n–π* transition involves the excitation of an electron from a non-bonding (n) orbital to an anti-bonding (π*) orbital. This transition occurs at lower energy levels and is therefore associated with the absorption of longer wavelengths (~300–400 nm).

Figure 67 - UV-Visible spectra of CQD (100 mgL^{-1}), ZIF-8 (100 mgL^{-1}) and ZIF8/CQD 200 (100 mgL^{-1}) dispersed in methanol

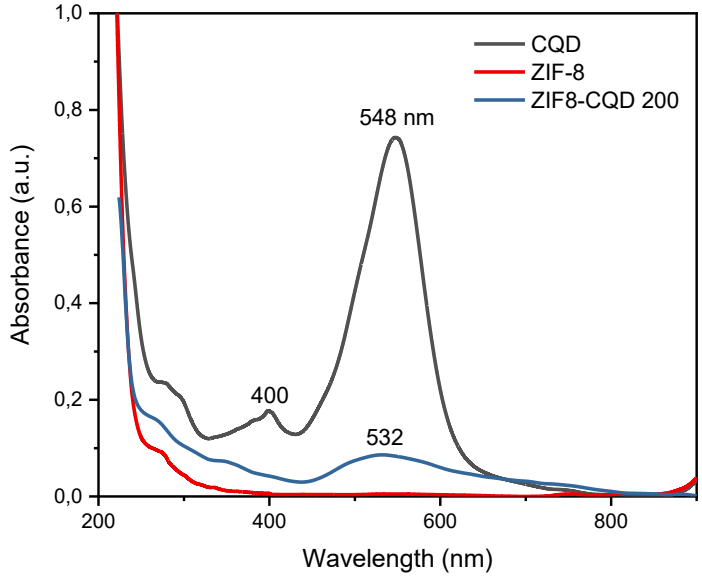

In CQDs dispersed in methanol, the n–π* transition is primarily attributed to the presence of oxygen-containing surface functional groups, such as carboxyl and hydroxyl groups. These moieties act as electron acceptors, enabling the formation of excited states through n–π* transitions. Upon energy absorption, an electron from an n orbital is promoted to a π* orbital, resulting in light absorption. Conversely, the π–π* transition involves the excitation of an electron from a bonding π orbital to an anti-bonding π* orbital. This process occurs at higher energy levels and corresponds to absorption in the shorter wavelength UV region (~200–300 nm). The π–π* transition is mainly associated with the presence of sp^2-hybridized carbon atoms in the carbon core of the nanoparticles, and their delocalized π electrons participate in

these transitions. Beside these two features, the band in the visible region of the spectrum can be ascribed to lower-energy states of N-related functional groups on the surface of CDs (Carbonaro et al., 2019). Regarding ZIF-8, it is possible to observe a slight absorbance around 270 nm that could be attributed to intraligand (M-MeIM) charge transfer (Li et al., 2019). In the spectrum of ZIF-8/CQD 200, features corresponding to both the CQD and ZIF-8 can be observed, however the intensity of their bands appears to be reduced, which can be related with the low amount of CQD in the final material. Moreover, the UV band related with oxygen containing groups is dislocated from 400 nm in CQD to 342 nm in the hybrid nanomaterial, whereas the visible band at 548 nm at CQD is shifted to 532 nm, which potentially suggests electronic interactions or altered environments upon coordination or integration of the CQD within the ZIF-8 structure (Azizi et al., 2025).

UV-Vis spectroscopy was also employed to evaluate the stability of CQD and the ZIF-8/CQD 200 hybrid nanomaterial in solution by monitoring the intensity of the visible band as a function of storage time. Considering the results exhibited in Figure 68, ZIF-8/CQD 200 material demonstrated superior stability compared to pure CQD over 56 days. In detail, a pronounced decrease in absorbance was observed after the first week from 1.0 to 0.75, a behavior that can be generalized for the materials based on CQD in this study. After this, it is noted a slow decrease in the absorbance, reaching an absorbance value of 0.62 after 56 days of assay, while pure CQD showed a decrease to 0.44 over the same period. Moreover, the spectral profiles recorded over the assay period (Appendix B) did not show significant shift in the band maxima, indicating the absence of major structural or electronic alterations in the materials.

Figure 68 – Stability of CQD and ZIF-8/CQD 200 hybrid nanomaterial evaluated by UV-Vis spectroscopy over time

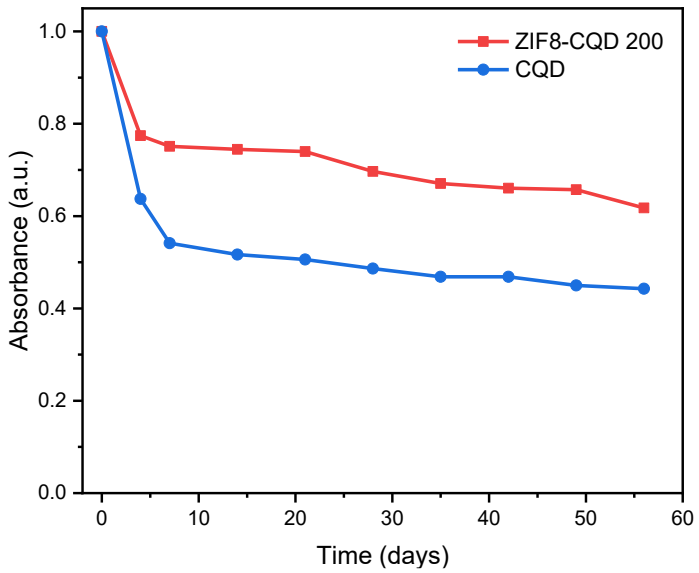

Figure 69 shows the emission spectra of CQD and the ZIF-8/CQD 200 hybrid nanomaterial dispersed in methanol, obtained under excitation wavelengths ranging from 350 to 590 nm with 20 nm increments. For CQD, a progressive increase in emission intensity is observed with increasing excitation wavelength, reaching a maximum upon excitation at 530 nm, with the emission centered at 618 nm. CQDs dispersed in methanol exhibit excitation-independent emission behavior similar to that observed in aqueous dispersions, however, the emission maximum is centered at 629 nm in water, while a blue shift is observed in methanol. In this case, the higher polarity of the solvent (water compared to methanol) induces a red shift in the PL spectrum (Lee et al., 2019). This behavior is attributed to a solvatochromic effect, reflecting the solvent-dependent stabilization of the emissive states. Zaini et al. (2023) discussed that the solvent molecules help stabilize and reduce the energy level of the excited state by reorienting (a process known as solvent relaxation) around the excited CQDs fluorophore. Therefore, there is a reduced energy gap, which results in a redshift of the fluorescence emission. The energy level of the excited state of the excited state is proportionally reduced when the solvent polarity is increased, whereas decreasing the polarity of solvents reduces the solvent effect on the excited-state energy level.

When CQDs are associated with ZIF-8, the emission profile is considerably modified, with the emergence of two distinct emission bands. A blue emission, appearing at approximately 450 nm, has been reported to originate from the organic 2-methylimidazolate linkers coordinated to Zn^{2+} ions (Wang et al., 2018), leading to ZIF-8/CQD hybrid systems with dual-emission features (Yang et al., 2022). However, in the hybrid nanomaterial analyzed here, the second emission band exhibits a maximum intensity at 523 nm upon excitation at 410 nm. This wavelength is different from those typically reported for pristine ZIF-8, indicating that this emission can be attributed to the CQDs. Nevertheless, the contribution of the 2-methylimidazolate ligands to this emission band cannot be completely disregarded. The enhanced intensity observed for this band compared to pure CQDs may arise from interactions between the sp^2-hybridized C=C conjugated domains of the CQDs and the 2-methylimidazole ligands within the ZIF-8 framework, which may promote additional radiative recombination pathways.

Figure 69 - Photoluminescence emission (PL) (A, B) and excitation (PLE) (C, D) spectra of CQD and ZIF-8/CQD 200 hybrid nanomaterial dispersions in methanol under different excitation wavelength

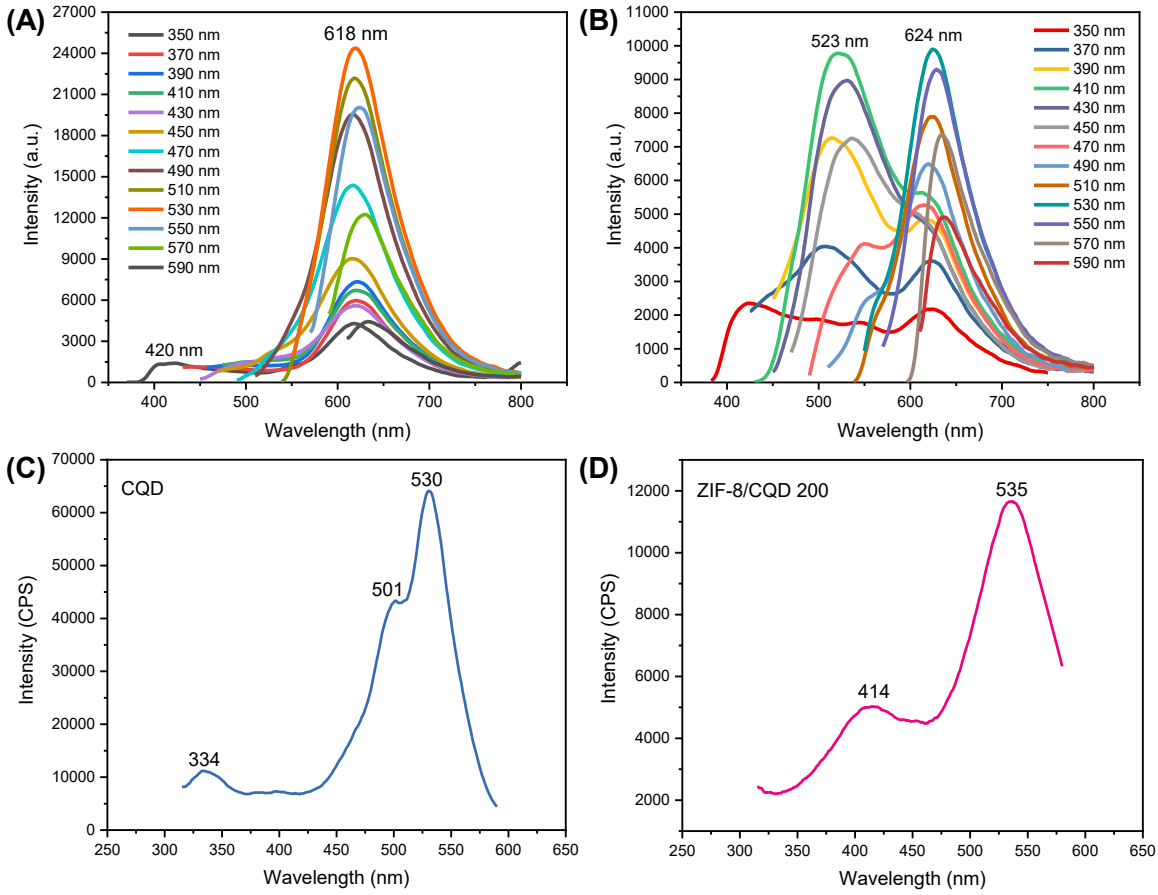

Moreover, the emission band centered at 618 nm for pure CQDs exhibits a slight red shift to 624 nm in the ZIF-8/CQD 200 material, while maintaining the same optimal excitation wavelength. This red shift can be attributed to the ability of ZIF-8, acting as a host matrix, to modify the microenvironment surrounding the CQDs, leading to changes in their electronic energy level structure and, consequently, in the fluorescence emission wavelength. In addition, charge transfer after CQDs is associated with ZIF-8, altering the charge distribution within the CQDs and further contributing to the observed shift in the emission wavelength (Li et al., 2024b).

The photoluminescence excitation spectra of both CQDs and the ZIF-8/CQD 200 hybrid nanomaterial were analyzed to elucidate the excited states involved in their emission processes. For the CQDs, the excitation band observed at 334 nm (Figure 69C) can be attributed to electronic transitions associated with oxygen-containing surface groups, such as carboxyl and hydroxyl functionalities. The excitation bands appearing at 501 nm and 530 nm are attributed to the visible emission centered at 618 nm, which is associated with functionalized surface of CQD functionalization. These results indicate that the visible emission of CQDs in methanol

originates from multiple emissive states. In contrast, the ZIF-8/CQD 200 hybrid material (Figure 69D) exhibits a more intense excitation band centered at 414 nm that can also be associated with transitions involving oxygen-containing groups. However, the observed shift relative to pure CQDs likely reflects interactions between the CQDs and the 2-methylimidazole ligands within the ZIF-8 framework. This excitation transition can be related to the emission band observed at 523 nm in the ZIF-8/CQD 200 hybrid nanomaterial.

7.4.2 Hemolysis assay

The hemolysis assay is one of the indicators to study the biocompatibility of nanoparticles. As observed in Figure 70, erythrocytes exposed to Triton X-100 in the positive control group ruptured, leading to a high rate of hemolysis. In this study, the hemolysis rate of ZIF-8 and ZIF-8/CQD 200 was evaluated at concentrations of 19.5 $\mu g.mL^{-1}$ to 5000 $\mu g.mL^{-1}$. ZIF-8 demonstrated a hemolysis rate of 0.45% at higher concentration, suggesting good biocompatibility.

Figure 70 - Hemolysis percentage of ZIF-8, and ZIF-8/CQD 200 hybrid nanomaterial. The hemolysis percentage was evaluated at concentrations ranging from 5000 to 19.5 µg/mL in the erythrocytes of sheep. The results correspond to averages ± of individual samples tested in triplicate. (*) $p<0.05$, compared to the positive control (Triton X-100 at 1%).

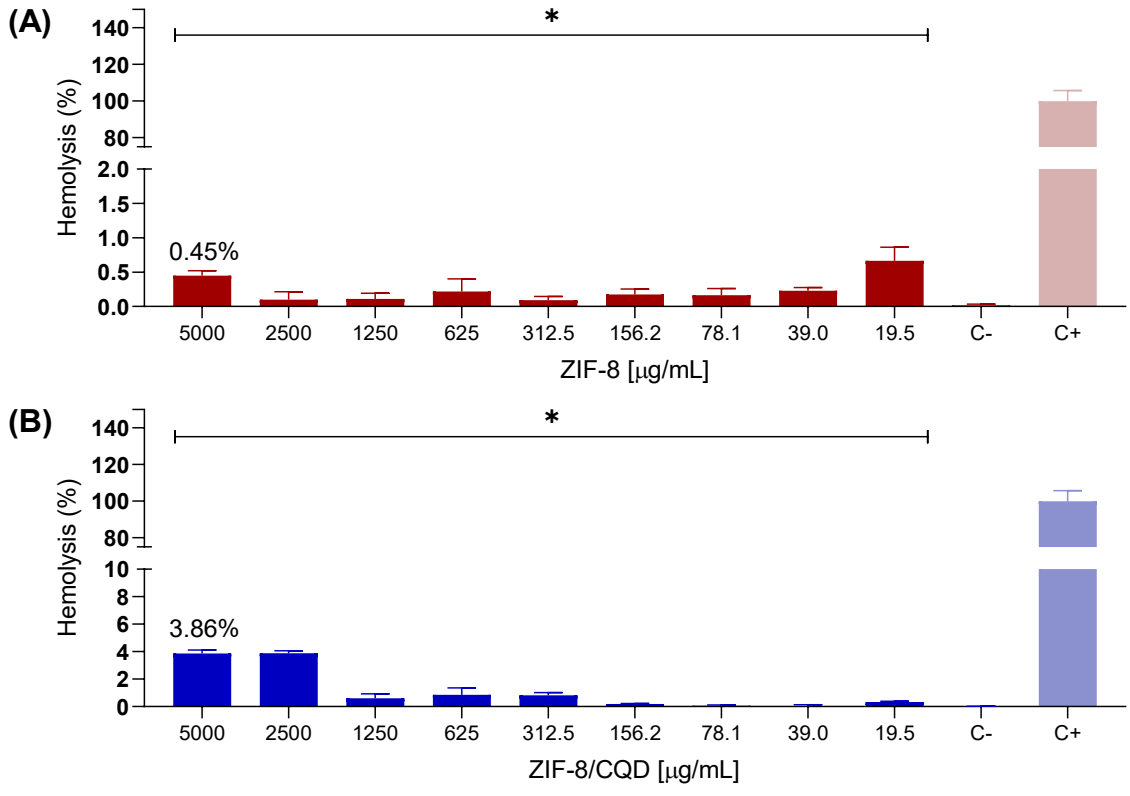

For ZIF-8/CQD 200 hybrid nanomaterial, an increase in the hemolysis rate is observed, reaching 3.86% at the concentration of 5000 mg.mL^{-1} (Figure 70B). Despite the increase in the percentage, the hemolysis remains below the recommended value of 5% (as mentioned in Chapter 4), which opens up the possibility of applying these materials in the biomedical field. In the study developed by (Zhou et al., 2024), CDs, ZIF-8 and CD@ZIF-8 was tested from 10 to 200 mg.mL^{-1}, and in all cases the hemolysis rate was less than 3%, indicating their low toxicity. It should be mentioned that the contact with the extracellular media leads to disassembly of ZIF-8 structure and the release of Zn ions (Lin et al., 2021). This effect may lead to interactions between Zn^{2+} and CQDs, which reduces the availability of the functional groups that contribute to their good biocompatibility (Tian et al., 2020).

7.5 CONCLUDING REMARKS

The ZIF-8/CQD hybrid nanomaterial was successfully obtained by an *in situ* MOF approach, and the results demonstrated that CQD initial amount strongly affects the framework formation. XRD analysis showed that the use of 200 mg of CQDs allowed the preservation of the ZIF-8 crystalline structure, whereas a higher CQD content (400 mg) suppressed the crystallization. FT-IR spectrum revealed that ZIF-8/CQD 200 retained the characteristic Zn–N vibration at 422 cm^{-1} and imidazolate bands, while additional features related to CQD surface groups were observed. Shifts in the COO^- stretching vibrations suggest interactions between oxygen-containing groups of CQDs and the ZIF-8 framework without disrupting metal–ligand coordination.

Thermogravimetric analysis revealed an increase in the main decomposition temperature from 449 °C for pristine ZIF-8 to 514 °C for ZIF-8/CQD 200, indicating enhanced thermal stability. The CQD content in the hybrid was estimated to be 41.18 wt%, confirming efficient incorporation during synthesis. SEM images showed that the rhombic dodecahedral morphology of ZIF-8 was preserved, although with a broader particle size distribution. BET measurements revealed a reduction in surface area from 753 to 265 m^2 g^{-1}, indicating surface-associated CQDs rather than pore confinement. Optical analyses demonstrated dual-emission behavior and improved dispersion stability over 56 days of assay. Hemolysis assays showed a maximum hemolysis of 3.86% at 5000 μg mL^{-1}, remaining below the 5% recommended, supporting the biocompatibility of the hybrid material.

8 GENERAL CONCLUSIONS

This thesis explored carbon quantum dots integrated with three porous supports (montmorillonite, sepiolite, and ZIF-8) in order to investigate how the host matrix influences the properties of CQD-based nanohybrids. The results demonstrate that the nature of support plays a key role in modulating the properties of the final materials, with these effects being governed predominantly by interfacial interactions rather than by physical confinement. In sepiolite-based systems, CQDs interact primarily with surface silanol groups and zeolitic water, leading not only to modifications in surface-related emissive states but also to significant changes in their structural organization. Raman analysis indicates an increase in graphitic ordering, demonstrating that the presence of sepiolite can modulate the carbon domains in CQDs.

In contrast, montmorillonite-based hybrids exhibit slightly structural modifications, observed by the increase in basal spacing in all hybrid nanomaterials. In addition, these systems show a significant red-shift in the maximum emission (e.g., from 629 nm to 656 nm), indicating that the clay environment strongly influences the emissive states of CQDs. For ZIF-8-based hybrids, the results provide strong evidence of surface-associated CQDs rather than pore incorporation. The ZIF-8/CQD hybrids show a reduction in specific surface area (from 753 m^2/g to 264 m^2/g) and pore volume (from 0.58 to 0.20 cm^3/g), while the average pore diameter remains unchanged. This is consistent with CQDs coating the external surface rather than entering the pores. In these systems, modifications in photoluminescence behavior, including shifts in emission and changes in emission profiles, as well as improved dispersion stability, are attributed to interfacial interactions and possible charge transfer processes. In addition, the hybrid materials exhibit dual-emission behavior, suggesting the existence of multiple emissive states, which opens possibilities for their application in ratiometric sensing platforms.

Overall, the results indicate that the support contributes directly to the modulation of CQD properties via interfacial interactions, rather than acting as a host. While sepiolite predominantly influences the structural organization and graphitic ordering of CQDs, MMT and ZIF-8 mainly modulate their photoluminescence and stability in solution. The pore structure of the support alone did not determine the final properties of the hybrids, instead their optical properties were mainly influenced by surface chemistry. These results show that controlling interfacial interactions, such as surface charge and bonding, is an effective way to tune the properties of CQD-based nanohybrids. This work helps to better understand how these materials can be designed by focusing on the role of interfacial interactions.

The properties of the hybrid nanomaterials suggest potential for future applications. The preservation and tunability of photoluminescence, together with the emergence of dual-emission behavior in hybrids, indicating suitability for optical sensing applications, particularly in ratiometric platforms, and cellular imaging. Furthermore, the demonstrated compatibility of CQDs with both clay-based and MOF-based support, allows their integration into more complex systems such as drug-loaded hybrids, highlights the potential for the development of multifunctional platforms combining imaging and therapeutic functionalities.

REFERENCES

AKYUZ, Sevim; AKYUZ, Tanil; AKALIN, Elif. Investigation of adsorption of 5-fluorouracil and 5-bromouracil onto sepiolite and loughlinite: An IR spectroscopic study. **Asian Journal of Chemistry**, v. 26, n. 15, p. 4875–4878, 2014.

ALAFEEF, Maha *et al.* Carbon Dots: From Synthesis to Unraveling the Fluorescence Mechanism. **Small**, v. 20, n. 4, 15 jan. 2024.

ALAMIER, Waleed M. *et al.* Synthesis of high-performance Fe3O4/Graphene/Bentonite clay nanocomposite for sustainable ciprofloxacin adsorption. **Inorganic Chemistry Communications**, v. 174, p. 113991, 1 abr. 2025.

ALCÂNTARA, Ana C. S. *et al.* Polysaccharide-fibrous clay bionanocomposites. **Applied Clay Science**, v. 96, p. 2–8, 2014.

ALCÂNTARA, Ana C. S. *et al.* Magnetite-sepiolite nanoarchitectonics for improving zein-based bionanocomposite foams. **Dalton Transactions**, v. 52, n. 45, p. 16951–16962, 2023.

ALCÂNTARA, Ana C. S.; DARDER, Margarita. Building Up Functional Bionanocomposites from the Assembly of Clays and Biopolymers. **Chemical Record**, v. 18, n. 7, p. 696–712, 2018.

ALMAAYTAH, Ammar *et al.* Antimicrobial and Antibiofilm Activity of Mauriporin, a Multifunctional Scorpion Venom Peptide. **International Journal of Peptide Research and Therapeutics**, v. 20, n. 4, p. 397–408, 2014.

ALSHAMMARI, Ahmad; JIANG, Zheng; CORDOVA, Kyle E. Metal Organic Frameworks as Emerging Photocatalysts. *In*: **Semiconductor Photocatalysis - Materials, Mechanisms and Applications**. 1. ed. *[S.l.: S.n.]*. p. 676.

ÁLVAREZ, Antonio *et al.* Current Industrial Applications of Palygorskite and Sepiolite. *In*: *[S.l.: S.n.]*. p. 281–298.

ARNOLD, Dean E. *et al.* The first direct evidence for the production of Maya Blue: rediscovery of a technology. **Antiquity**, v. 82, n. 315, p. 151–164, 2008.

ASLAM, Ruby *et al.* Effect of temperature, and immersion time on the inhibition performance of Q235 steel using spent coffee grounds derived carbon quantum dots: Electrochemical, spectroscopic and surface studies. **Biomass and Bioenergy**, v. 200, 1 set. 2025.

AWAD, Mahmoud E. *et al.* Kaolinite in pharmaceutics and biomedicine. **International Journal of Pharmaceutics**, v. 533, n. 1, p. 34–48, nov. 2017.

AZHAR, Fahimeh Farshi; OLAD, Ali. A study on sustained release formulations for oral delivery of 5-fluorouracil based on alginate-chitosan/montmorillonite nanocomposite systems. **Applied Clay Science**, v. 101, n. November, p. 288–296, 2014.

AZIM, Muhamad *et al.* **Recent progress in emerging hybrid nanomaterials towards the energy storage and heat transfer applications: A review**. **Journal of Molecular Liquids**Elsevier B.V., , 15 ago. 2022.

AZIZI, Jahanghir *et al.* Green synthesis of zeolitic imidazolate frameworks/marshmallow extract-derived carbon quantum dots for improved antibacterial properties. **Surfaces and Interfaces**, v. 72, p. 107215, set. 2025.

BALEK, V. *et al.* Emanation thermal analysis study of Na-montmorillonite and montmorillonite saturated with various cations. **Journal of Thermal Analysis and Calorimetry**, v. 83, n. 3, p. 617–623, 2006.

BALKANLOO, Peyman Gozali *et al.* Clay mineral/polymer composite: characteristics, synthesis, and application in Li-ion batteries: A review. **Applied Clay Science**, v. 228, p. 106632, out. 2022.

BANERJEE, Rahul *et al.* High-Throughput Synthesis of Zeolitic Imidazolate Frameworks and Application to CO_2 Capture. **Science**, v. 319, n. 5865, p. 939–943, 15 fev. 2008.

BANERJEE, Rahul *et al.* Control of Pore Size and Functionality in Isoreticular Zeolitic Imidazolate Frameworks and their Carbon Dioxide Selective Capture Properties. **Journal of the American Chemical Society**, v. 131, n. 11, p. 3875–3877, 25 mar. 2009.

BANGER, Anjali *et al.* Synthetic Methods and Applications of Carbon Nanodots. **Catalysts**, v. 13, n. 5, p. 858, 9 maio 2023.

BARHOUM, Ahmed *et al.* A review on carbon dots as innovative materials for advancing biomedical applications: synthesis, opportunities, and challenges. **Journal of Materials Science**, v. 58, n. 34, p. 13531–13579, 2023.

BARTKOWSKI, Michał *et al.* CARBON DOTS: Bioimaging and Anticancer Drug Delivery. **Chemistry – A European Journal**, v. 30, n. 19, 2 abr. 2024.

BAZAZI, Sina *et al.* Metal-organic framework (MOF)/C-dots and covalent organic framework (COF)/C-dots hybrid nanocomposites: Fabrications and applications in sensing, medical, environmental, and energy sectors. **Advances in Colloid and Interface Science**, v. 328, p. 103178, jun. 2024.

BEHI, Mohammadreza *et al.* Carbon dots: a novel platform for biomedical applications. **Nanoscale Advances**, v. 4, n. 2, p. 353–376, 2022.

BELGHAZDIS, Mohammed; HACHEM, El-Kaber. Clay and Clay Minerals: A Detailed Review. **International Journal of Recent Technology and Applied Science**, v. 4, n. 2, p. 54–75, 29 set. 2022.

BENNY, Alan *et al.* Metal organic frameworks in biomedicine: Innovations in drug delivery. **Results in Chemistry**, v. 7, p. 101414, jan. 2024.

BERGAOUI, Manel *et al.* A review of the features and applications of ZIF-8 and its derivatives for separating CO2 and isomers of C3- and C4- hydrocarbons. **Journal of Natural Gas Science and Engineering**, v. 96, n. September, p. 104289, 2021.

BESLI, Nur Sena Okten; ORAKDOGEN, Nermin. Sepiolite-embedded binary nanocomposites of (alkyl)methacrylate-based responsive polymers: Role of silanol groups of fibrillar nanoclay on functional and thermomechanical properties. **Reactive and Functional Polymers**, v. 161, n. February, p. 104844, 2021.

BIAN, Wei *et al.* Boron and nitrogen co-doped carbon dots as a sensitive fluorescent probe for the detection of curcumin. **Luminescence**, v. 33, n. 1, p. 174–180, 2018.

BORREGO-SÁNCHEZ, Ana *et al.* Biopharmaceutical improvement of praziquantel by interaction with montmorillonite and sepiolite. **Applied Clay Science**, v. 160, p. 173–179, 1 ago. 2018.

BRAVO, Isaac *et al.* Cellulose/pectin-based materials incorporating Laponite-indole derivative hybrid for oral administration and controlled delivery of the neuroprotective drug. **International Journal of Biological Macromolecules**, v. 234, p. 123765, abr. 2023.

BUK, Vuslat; PEMBLE, Martyn E.; TWOMEY, Karen. Fabrication and evaluation of a carbon quantum dot/gold nanoparticle nanohybrid material integrated onto planar micro gold electrodes for potential bioelectrochemical sensing applications. **Electrochimica Acta**, v. 293, p. 307–317, 2019.

CACCAMO, Maria Teresa *et al.* Self-assembly processes in hydrated montmorillonite by FTIR investigations. **Materials**, v. 13, n. 5, 2020.

CALABRESE, Ilaria *et al.* Porous materials as delivery and protective agents for Vitamin A. **RSC Advances**, v. 6, n. 71, p. 66495–66504, 2016.

CAO, Lihua *et al.* Fibrous Clays in Dermopharmaceutical and Cosmetic Applications: Traditional and Emerging Perspectives. **International Journal of Pharmaceutics**, v. 625, n. July, p. 122097, 2022.

CARAZO, Esperanza *et al.* Kinetic and thermodynamic assessment on isoniazid/montmorillonite adsorption. **Applied Clay Science**, v. 165, n. June, p. 82–90, 2018.

CARBONARO, Carlo Maria *et al.* On the Emission Properties of Carbon Dots: Reviewing Data and Discussing Models. **C**, v. 5, n. 4, p. 60, 2 out. 2019.

CARBONARO, Carlo Maria *et al.* How porosity affects the emission of fluorescent carbon dot-silica porous composites. **Microporous and Mesoporous Materials**, v. 305, n. March, 2020.

CARRETERO, M. Isabel; POZO, Manuel. Clay and non-clay minerals in the pharmaceutical industry. **Applied Clay Science**, v. 46, n. 1, p. 73–80, set. 2009.

CASTRO-SMIRNOV, Fidel Antonio *et al.* Cellular uptake pathways of sepiolite nanofibers and DNA transfection improvement. **Scientific Reports**, v. 7, n. 1, p. 1–10, 2017.

CHAE, Hee K. *et al.* A route to high surface area, porosity and inclusion of large molecules in crystals. **Nature**, v. 427, p. 523–527, 2004.

CHEN, Qingze *et al.* From used montmorillonite to carbon monolayer-montmorillonite nanocomposites. **Applied Clay Science**, v. 100, n. C, p. 112–117, 2014.

CHEN, Wen L.; GRABOWSKI, Robert C.; GOEL, Saurav. Clay Swelling: Role of Cations in Stabilizing/Destabilizing Mechanisms. **ACS Omega**, v. 7, n. 4, p. 3185–3191, 1 fev. 2022.

CHEN, Yu Chuan *et al.* Impregnation of Graphene Quantum Dots into a Metal-Organic Framework to Render Increased Electrical Conductivity and Activity for Electrochemical Sensing. **ACS Applied Materials and Interfaces**, v. 11, n. 38, p. 35319–35326, 2019.

CHOPPADANDI, Mounika *et al.* Structural features regulated photoluminescence intensity and cell internalization of carbon and graphene quantum dots for bioimaging. **Materials Science and Engineering C**, v. 129, n. July, p. 112366, 2021.

CHUAICHAM, Chitiphon *et al.* Efficient photocatalytic degradation of emerging ciprofloxacin under visible light irradiation using BiOBr/carbon quantum dot/saponite composite. **Environmental Research**, v. 212, n. PE, p. 113635, 2022.

ÇIFTÇI, Hakan *et al.* Development and evaluation of mesoporous montmorillonite/magnetite nanocomposites loaded with 5-Fluorouracil. **Microporous and Mesoporous Materials**, v. 303, n. April, 2020.

CINÀ, Giuseppe *et al.* Development of alginate film filled with halloysite-carbon dots for active food packaging. **International Journal of Biological Macromolecules**, v. 277, p. 134375, out. 2024.

CUI, Lin *et al.* Carbon Dots: Synthesis, Properties and Applications. **Nanomaterials**, v. 11, n. 12, p. 3419, 16 dez. 2021.

CUTRIM, Elaine S. M. *et al.* Preparation, characterization and in vitro anticancer performance of nanoconjugate based on carbon quantum dots and 5-Fluorouracil. **Materials Science and Engineering C**, v. 120, n. December 2020, 2021.

DAI, Sheng *et al.* MOF-encapsulated copper-doped carbon dots nanozymes with excellent biological activity promote diabetes wound healing. **Regenerative Biomaterials**, v. 11, 2 jan. 2024.

DASHUAI, Yan *et al.* Smart self-healing coating based on the highly dispersed silica/carbon nanotube nanomaterial for corrosion protection of steel. **Progress in Organic Coatings**, v. 164, p. 106694, 2022.

DATURI, Marco *et al.* Room Temperature Reduction of Nitrogen Oxide on Iron Metal–Organic Frameworks. **Advanced Materials**, v. 36, n. 31, 28 ago. 2024.

DAWSON, Jonathan I.; OREFFO, Richard O. C. Clay: New Opportunities for Tissue Regeneration and Biomaterial Design. **Advanced Materials**, v. 25, n. 30, p. 4069–4086, 14 ago. 2013.

DE VILLENOISY, Thibault *et al.* Principles of Design and Synthesis of Metal Derivatives from MOFs. **Advanced Materials**, v. 35, n. 24, 12 jun. 2023.

DEB, Ankita; CHOWDHURY, Devasish. Unraveling the origin of photoluminescence in dual emissive biogenic carbon dot. **Materials Today Communications**, v. 31, n. May, p. 103777, 2022.

DEHMANI, Younes *et al.* A critical review of natural clay minerals: Structural characterization, textural properties, and adsorption mechanisms for sustainable wastewater treatment. **Materials Today Advances**, v. 29, p. 100682, mar. 2026.

DENG, Hexiang *et al.* Large-Pore Apertures in a Series of Metal-Organic Frameworks. **Science**, v. 336, n. May, p. 170–171, 2012.

DENG, Jing; DAI, Zhongde; DENG, Liyuan. Effects of the Morphology of the ZIF on the CO_2 Separation Performance of MMMs. **Industrial & Engineering Chemistry Research**, v. 59, n. 32, p. 14458–14466, 12 ago. 2020.

DERKOWSKI, Arkadiusz; KULIGIEWICZ, Artur. Thermal Analysis and Thermal Reactions of Smectites: a Review of Methodology, Mechanisms, and Kinetics. **Clays and Clay Minerals**, v. 70, n. 6, p. 946–972, 2022.

DIAB, Amira S. *et al.* Clay nanostructures in geotechnical engineering: A critical review of mechanisms, performance, and sustainable soil stabilization. **Materials Today Sustainability**, v. 33, p. 101284, mar. 2026.

DOMÉNECH, Antonio *et al.* Maya Blue as a nanostructured polyfunctional hybrid organic–inorganic material: the need to change paradigms. **New Journal of Chemistry**, v. 33, n. 12, p. 2371–2379, 2009.

ĐORĐEVIĆ, Luka *et al.* A multifunctional chemical toolbox to engineer carbon dots for biomedical and energy applications. **Nature Nanotechnology**, v. 17, n. 2, p. 112–130, 2022.

DU, Fengyi *et al.* Nitrogen-doped carbon dots with heterogeneous multi-layered structures. **RSC Advances**, v. 4, n. 71, p. 37536–37541, 2014.

DUONG, Thien D. *et al.* Observation of binding of carbon dioxide to nitro-decorated metal–organic frameworks. **Chemical Science**, v. 11, n. 20, p. 5339–5346, 2020.

ELUGOKE, Saheed E. *et al.* Carbon Quantum Dots: Basics, Properties, and Fundamentals. *In*: *[S.l.: S.n.]*. p. 3–42.

FAN, Wenjuan *et al.* Facile synthesis of ZnCdS quantum dots via a novel photoetching MOF strategy for boosting photocatalytic hydrogen evolution. **Separation and Purification Technology**, v. 330, 1 fev. 2024.

FANG, Yanfen *et al.* Complex Formation via Hydrogen bonding between Rhodamine B and Montmorillonite in Aqueous Solution. **Scientific Reports**, v. 8, n. 1, p. 1–10, 2018.

FATIMA, Syeda Fiza *et al.* Recent advances in Metal-Organic Frameworks as nanocarriers for triggered release of anticancer drugs: Brief history, biomedical applications, challenges and future perspective. **Colloids and Surfaces B: Biointerfaces**, v. 225, n. March, p. 113266, 2023.

FENG, Simin *et al.* Zeolitic imidazolate framework-8 (ZIF-8) for drug delivery: A critical review. **Frontiers of Chemical Science and Engineering**, v. 15, n. 2, p. 221–237, 2021.

FERNANDES, Francisco M.; RUIZ-HITZKY, Eduardo. Assembling nanotubes and nanofibres: Cooperativeness in sepiolite-carbon nanotube materials. **Carbon**, v. 72, p. 296–303, 2014.

FRANCO, Francisco *et al.* Reversed Mg-Based Smectites: A New Approach for CO2 Adsorption. **Nanomaterials**, v. 14, n. 18, p. 1532, 21 set. 2024.

FUNES, Israel G. A. *et al.* Facile modification of montmorillonite by intercalation and grafting: The study of the binding mechanisms of a quaternary alkylammonium surfactant. **Applied Clay Science**, v. 195, n. January, p. 105738, 2020.

FURUKAWA, Hiroyasu *et al.* The chemistry and applications of metal-organic frameworks. **Science**, v. 341, n. 6149, 2013.

GANGU, Kranthi Kumar; JONNALAGADDA, Sreekantha B. A Review on Metal-Organic Frameworks as Congenial Heterogeneous Catalysts for Potential Organic Transformations. **Frontiers in Chemistry**, v. 9, 17 dez. 2021.

GAO, Dong *et al.* Photoluminescence-tunable carbon dots from synergy effect of sulfur doping and water engineering. **Chemical Engineering Journal**, v. 388, 15 maio 2020.

GAO, Lan-Xing *et al.* Photonic Crystals Based on ZIF-8 Nanoparticles with Embedded Carbon Dots for Optical Information Encryption. **ACS Applied Nano Materials**, v. 6, n. 16, p. 15054–15062, 25 ago. 2023.

GAO, Wenting *et al.* Multifunctional honeysuckle extract/attapulgite/chitosan composite films containing natural carbon dots for intelligent food packaging. **International Journal of Biological Macromolecules**, v. 280, p. 136042, nov. 2024.

GÂREA, S. A. *et al.* Porous clay heterostructures: A new inorganic host for 5-fluorouracil encapsulation. **International Journal of Pharmaceutics**, v. 491, n. 1–2, p. 299–309, 10 jul. 2015.

GE, Guili *et al.* Green Synthesis of Nitrogen–Doped Carbon Dots from Fresh Tea Leaves for Selective Fe3+ Ions Detection and Cellular Imaging. **Nanomaterials**, v. 12, n. 6, p. 986, 17 mar. 2022.

GETTENS, Rutherford J. Maya Blue: An Unsolved Problem in Ancient Pigments. **American Antiquity**, v. 27, n. 4, p. 557–564, 1962.

GHOLIZADEH, S. K.; SHAHSAVARI, S.; GHOLAMI, M. R. Green synthesis of ternary carbon dots (CDs)/MIL-88B (Fe)/Bi2S3 nanocomposite via MOF templating as a reusable heterogeneous nanocatalyst and nano-photocatalyst. **Materials Research Bulletin**, v. 138, p. 111204, jun. 2021.

GHOSH, Trisita *et al.* Nitrogen and sulphur doped carbon dot: An excellent biocompatible candidate for in-vitro cancer cell imaging and beyond. **Environmental Research**, v. 217, 15 jan. 2023.

GODA, Emad S. *et al.* Halloysite nanotubes based electrochemical sensors: A review. **Microchemical Journal**, v. 147, p. 1083–1096, jun. 2019.

GOLUBEVA, Olga Yu *et al.* Peculiarities of the 5-fluorouracil adsorption on porous aluminosilicates with different morphologies. **Applied Clay Science**, v. 184, p. 105401, jan. 2020.

GÓMEZ-AVILÉS, Almudena *et al.* Zeolite–sepiolite nanoheterostructures. **Journal of Nanostructure in Chemistry**, v. 4, n. 1, 2014.

GU, Zhi-Gang *et al.* MOF-Templated Synthesis of Ultrasmall Photoluminescent Carbon-Nanodot Arrays for Optical Applications. **Angewandte Chemie**, v. 129, n. 24, p. 6957–6962, 6 jun. 2017.

HAMMAD, Sherin F. *et al.* Metal organic framework-derived carbon nanomaterials and MOF hybrids for chemical sensing. **Trends in Analytical Chemistry**, v. 170, n. November 2023, p. 117425, 2024.

HASHEMI, Seyyed Alireza *et al.* Coupled graphene oxide with hybrid metallic nanoparticles as potential electrochemical biosensors for precise detection of ascorbic acid within blood. **Analytica Chimica Acta**, v. 1107, p. 183–192, 2020.

HAYAMI, Ryohei *et al.* Preparation and properties of organic-inorganic hybrid materials using titanium phosphonate cluster. **Polymer Journal**, v. 49, n. 9, p. 665–669, 1 set. 2017.

HAZARIKA, Deepshikha; KARAK, Niranjan. Nanocomposite of waterborne hyperbranched polyester and clay@carbon dot as a robust photocatalyst for environmental remediation. **Applied Surface Science**, v. 498, n. August, p. 143832, 2019.

HEMMATPOUR, Hamoon *et al.* Temperature-responsive and biocompatible nanocarriers based on clay nanotubes for controlled anti-cancer drug release. **Nanoscale**, v. 15, n. 5, p. 2402–2416, 2023.

HÖNICKE, Ines M. *et al.* Balancing Mechanical Stability and Ultrahigh Porosity in Crystalline Framework Materials. **Angewandte Chemie International Edition**, v. 57, n. 42, p. 13780–13783, 15 out. 2018.

HOSKINS, Bernard F.; ROBSON, Richard. Infinite Polymeric Frameworks Consisting of Three Dimensionally Linked Rod-like Segments. **J. Am. Chem. Soc.**, v. 111, p. 5962–5964, 1989.

HOSSAIN, Syed Imdadul *et al.* A Review on Montmorillonite-Based Nanoantimicrobials: State of the Art. **Nanomaterials**, v. 13, n. 5, p. 848, 24 fev. 2023.

HOU, Xiaotong *et al.* **Strategies for induced defects in metal-organic frameworks for enhancing adsorption and catalytic performance**. **Dalton Transactions**Royal Society of Chemistry, , 29 abr. 2022.

HSU, Hao Lin *et al.* Environmental-friendly three-dimensional carbon nanotubes grown by soil clay and graphene oxide nanosheets for energy storage. **Materials Today Chemistry**, v. 23, p. 100644, 1 mar. 2022.

HU, Huajiang; LI, Jiurong; GONG, Xiao. Hour-Level Persistent Multicolor Phosphorescence Enabled by Carbon Dot-Based Nanocomposites Through a Multi-Confinement-Based Approach. **Small**, v. 20, n. 23, 21 jun. 2024.

HUANG, Xiao-Chun *et al.* Ligand-Directed Strategy for Zeolite-Type Metal–Organic Frameworks: Zinc(ii) Imidazolates with Unusual Zeolitic Topologies. **Angewandte Chemie**, v. 45, p. 1557–1559, 2006.

HUANG, Xiaoying *et al.* Novel strategy for engineering the metal-Oxide@MOF Core@Shell architecture and its applications in cataluminescence sensing. **ACS Applied Materials and Interfaces**, v. 13, n. 2, p. 3471–3480, 20 jan. 2021.

HUANG, Zhujun; REN, Lili. Large Scale Synthesis of Carbon Dots and Their Applications: A Review. **Molecules**, v. 30, n. 4, p. 774, 7 fev. 2025.

IKHIOYA, Imosobomeh L. *et al.* Electrochemical engineering of ZIF-7 electrode using ion beam technology for better supercapacitor performance. **Journal of Energy Storage**, v. 90, p. 111833, jun. 2024.

INNOCENZI, Plinio; STAGI, Luigi. Carbon dots as oxidant-antioxidant nanomaterials, understanding the structure-properties relationship. A critical review. **Nano Today**, v. 50, p. 101837, jun. 2023.

INTERNATIONAL ORGANIZATION FOR STANDARDIZATION. "Biological evaluation of medical devices". Part 5: Tests for cytotoxicity: in vitro methods", 3st ed, ISO 10993-5. *In*: *[S.l.: S.n.]*.

ISLAM, Md. Rashidul; NAIDU, Ravi; BISWAS, Bhabananda. Kaolin clay-based diets for managing livestock's health and methane emission problem. **Applied Clay Science**, v. 276, p. 107891, nov. 2025.

ISMAIL, Usman M.; ONAIZI, Sagheer A.; VOHRA, Muhammad S. Aqueous Pb(II) Removal Using ZIF-60: Adsorption Studies, Response Surface Methodology and Machine Learning Predictions. **Nanomaterials**, v. 13, n. 8, p. 1402, 18 abr. 2023.

JAMES, Joshua B.; LIN, Y. S. Kinetics of ZIF-8 Thermal Decomposition in Inert, Oxidizing, and Reducing Environments. **The Journal of Physical Chemistry C**, v. 120, n. 26, p. 14015–14026, 7 jul. 2016.

JIA, Lei *et al.* A stick-like intelligent multicolor nano-sensor for the detection of tetracycline: The integration of nano-clay and carbon dots. **Journal of Hazardous Materials**, v. 413, p. 125296, jul. 2021.

JIA, Tao; GU, Yifan; LI, Fengting. Progress and potential of metal-organic frameworks (MOFs) for gas storage and separation: A review. **Journal of Environmental Chemical Engineering**, v. 10, n. 5, p. 108300, out. 2022.

JIANG, Chuanhai *et al.* Recent advances in metal–organic frameworks for gas adsorption/separation. **Nanoscale Advances**, v. 4, n. 9, p. 2077–2089, 2022.

JIANG, Kai *et al.* Preparation of Multicolor Photoluminescent Carbon Dots by Tuning Surface States. **Nanomaterials**, v. 9, n. 4, p. 529, 3 abr. 2019.

JIANG, Zhangsong *et al.* Synergistic preparation and properties of ceramic foams from wolframite tailings and high-borosilicate waste glass. **Construction and Building Materials**, v. 457, p. 139367, dez. 2024.

JIAO, Long *et al.* Metal–organic frameworks: Structures and functional applications. **Materials Today**, v. 27, p. 43–68, jul. 2019.

JIN, Yingmin *et al.* An Eu3+-functionalized metal–organic framework (Eu@Zn-MOF) for the highly sensitive detection of rotenone in serum. **New Journal of Chemistry**, v. 46, n. 40, p. 19168–19173, 2022.

JLASSI, Khouloud *et al.* A carbon dot-based clay nanocomposite for efficient heavy metal removal. **Nanoscale Advances**, v. 5, n. 16, p. 4224–4232, 3 jul. 2023.

JOSEPH, Jessy *et al.* Iron-based metal-organic framework: Synthesis, structure and current technologies for water reclamation with deep insight into framework integrity. **Chemosphere**, v. 284, n. June, 2021.

KACHHADIYA, Dipeshkumar D.; MURTHY, Z. V. P. Preparation and characterization of ZIF-8 and ZIF-67 incorporated poly(vinylidene fluoride) membranes for pervaporative separation of methanol/water mixtures. **Materials Today Chemistry**, v. 22, p. 100591, dez. 2021.

KANG, Chunyuan *et al.* Aggregation and luminescence in carbonized polymer dots. **Aggregate**, v. 3, n. 2, 20 abr. 2022.

KANG, Naixin *et al.* Fast Au-Ni@ZIF-8-catalyzed ammonia borane hydrolysis boosted by dramatic volcano-type synergy and plasmonic acceleration. **Applied Catalysis B: Environmental**, v. 320, p. 121957, jan. 2023.

KAR, Dilip Kumar *et al.* Carbon Dots and Their Polymeric Nanocomposites: Insight into Their Synthesis, Photoluminescence Mechanisms, and Recent Trends in Sensing Applications. **ACS Omega**, v. 9, n. 10, p. 11050–11080, 12 mar. 2024.

KARIM, Md Rezaul *et al.* Fabrication of high-performance supercapacitor of surface-engineered ZIF-8 for energy storage applications. **Journal of Energy Storage**, v. 93, p. 112199, jul. 2024.

KATOCH, Abhishek; GOYAL, Navdeep; GAUTAM, Sanjeev. Applications and advances in coordination cages: Metal-Organic Frameworks. **Vacuum**, v. 167, p. 287–300, set. 2019.

KAUSHAL, Sandeep *et al.* First transition series metal–organic frameworks: synthesis, properties and applications. **Materials Advances**, v. 2, n. 22, p. 7308–7335, 2021.

KEVADIYA, Bhavesh D. *et al.* Layered inorganic nanocomposites: A promising carrier for 5-fluorouracil (5-FU). **European Journal of Pharmaceutics and Biopharmaceutics**, v. 81, n. 1, p. 91–101, maio 2012.

KHAN, Waheed Ullah *et al.* Solvent-free synthesis of nitrogen doped carbon dots with dual emission and their biological and sensing applications. **Materials Today Nano**, v. 18, p. 100205, jun. 2022.

KIM, Dong Jin *et al.* Graphene Quantum Dots from Carbonized Coffee Bean Wastes for Biomedical Applications. **Nanomaterials**, v. 11, n. 6, p. 1423, 28 maio 2021.

KIRLIKOVALI, Kent O. *et al.* Back to the Basics: Developing Advanced Metal-Organic Frameworks Using Fundamental Chemistry Concepts. **ACS Nanoscience Au**, v. 3, n. 1, p. 37–45, 2023.

KOHAY, Hagay *et al.* PEG-PE/clay composite carriers for doxorubicin: Effect of composite structure on release, cell interaction and cytotoxicity. **Acta Biomaterialia**, v. 55, p. 443–454, jun. 2017.

KUKKAR, Preeti *et al.* Recent advances in the synthesis techniques for zeolitic imidazolate frameworks and their sensing applications. **Coordination Chemistry Reviews**, v. 446, p. 214109, nov. 2021.

KUNDU, Aniruddha *et al.* Facile approach to synthesize highly fluorescent multicolor emissive carbon dots via surface functionalization for cellular imaging. **Journal of Colloid and Interface Science**, v. 513, p. 505–514, 2018.

LAZORENKO, Georgy; KASPRZHITSKII, Anton. Kaolin-group and sepiolite–palygorskite-group clay minerals as next-generation platforms for polymer nanocomposites. **Advanced Industrial and Engineering Polymer Research**, nov. 2025.

LEE, Hye Jin *et al.* The effect of solvent polarity on emission properties of carbon dots and their uses in colorimetric sensors for water and humidity. **Materials Research Bulletin**, v. 119, p. 110564, nov. 2019.

LEE, Yu-Ri *et al.* ZIF-8: A comparison of synthesis methods. **Chemical Engineering Journal**, v. 271, p. 276–280, jul. 2015.

LI, Bingzhi *et al.* Rational design, synthesis, and applications of carbon dots@metal–organic frameworks (CD@MOF) based sensors. **TrAC Trends in Analytical Chemistry**, v. 135, p. 116163, fev. 2021.

LI, Chenhao *et al.* Single Solid-State Emissive Carbon Quantum Dots for Multicolor, Bright and Efficient Electroluminescent Light-Emitting Diodes. **Angewandte Chemie International Edition**, v. 64, n. 7, 10 fev. 2025.

LI, Dan; KANER, Richard B. Shape and Aggregation Control of Nanoparticles: Not Shaken, Not Stirred. **Journal of the American Chemical Society**, v. 128, n. 3, p. 968–975, 1 jan. 2006.

LI, Dongxiao *et al.* Advances and Applications of Metal-Organic Frameworks (MOFs) in Emerging Technologies: A Comprehensive Review. **Global Challenges**, v. 8, n. 2, p. 1–32, 2024a.

LI, Hailian *et al.* Design and synthesis of an exceptionally stable and highly porous metal-organic framework. **Nature**, v. 402, n. November, p. 276–279, 1999.

LI, Haitao *et al.* Water-Soluble Fluorescent Carbon Quantum Dots and Photocatalyst Design. **Angewandte Chemie International Edition**, v. 49, n. 26, p. 4430–4434, 14 jun. 2010.

LI, Hao *et al.* Preparation and Adsorption Performance Study of Graphene Quantum Dots@ZIF-8 Composites for Highly Efficient Removal of Volatile Organic Compounds. **Nanomaterials**, v. 12, n. 22, p. 4008, 14 nov. 2022a.

LI, Jianing *et al.* Hybrid Nanomaterials for Cancer Immunotherapy. **Advanced Science**, v. 10, n. 6, 2023a.

LI, Jiurong *et al.* Metal–Organic Framework-Assisted Rational Design of Multicolor Solid-State Fluorescent Carbon Nanodots and Its Application for LEDs. **Laser & Photonics Reviews**, v. 18, n. 3, 18 mar. 2024b.

LI, Jiurong; GONG, Xiao. The Emerging Development of Multicolor Carbon Dots. **Small**, v. 18, n. 51, 3 dez. 2022.

LI, Junqi *et al.* Synthesis and adsorption performance of La@ZIF-8 composite metal–organic frameworks. **RSC Advances**, v. 10, n. 6, p. 3380–3390, 2020.

LI, Ping *et al.* Metal-organic frameworks with photocatalytic bactericidal activity for integrated air cleaning. **Nature Communications**, v. 10, n. 1, p. 2177, 16 maio 2019.

LI, Wei *et al.* Enhanced Biological Photosynthetic Efficiency Using Light-Harvesting Engineering with Dual-Emissive Carbon Dots. **Advanced Functional Materials**, v. 28, n. 44, 31 out. 2018.

LI, Wei *et al.* **Fluorescent Nanoparticles for Super-Resolution Imaging**. **Chemical Reviews**American Chemical Society, , 10 ago. 2022b.

LI, Yan *et al.* Formation and Band Gap Tuning Mechanism of Multicolor Emissive Carbon Dots from *m* -Hydroxybenzaldehyde. **Advanced Science**, v. 10, n. 18, 21 jun. 2023b.

LI, Yuan *et al.* Recent Advances in the Application and Mechanism of Carbon Dots/Metal-Organic Frameworks Hybrids in Photocatalysis and the Detection of Environmental Pollutants. **Chemistry - An Asian Journal**, v. 17, n. 13, 2022c.

LIANG, Yan-Mei *et al.* Waste tobacco leaves derived carbon dots for tetracycline detection: Improving quantitative accuracy with the aid of chemometric model. **Analytica Chimica Acta**, v. 1191, p. 339269, jan. 2022.

LIMA, Juliana A. De *et al.* Applied Clay Science A new approch to sepiolite dispersion by treatment with ionic liquids. **Applied Clay Science**, v. 143, n. March, p. 234–240, 2017.

LIN, F. H.; JIAN, C. H.; LEE, Y. H. A study of purified montmorillonite intercalated with 5-fluorouracil as drug carrier. **Second Smith and Nephew International Symposium - Tissue Engineering 2000: Advances in Tissue Engineering, Biomaterials and Cell Signalling**, v. 23, p. 70, 2000.

LIN, Jiansheng *et al.* Effects of ZIF-8 MOFs on structure and function of blood components. **RSC Advances**, v. 11, n. 35, p. 21414–21425, 2021.

LIN, Rongbin *et al.* Facile generation of carbon quantum dots in MIL-53(Fe) particles as localized electron acceptors for enhancing their photocatalytic Cr(<scp>vi</scp>) reduction. **Inorganic Chemistry Frontiers**, v. 5, n. 12, p. 3170–3177, 2018.

LIU, Haipeng; YE, Tao; MAO, Chengde. Fluorescent Carbon Nanoparticles Derived from Candle Soot. **Angewandte Chemie International Edition**, v. 46, n. 34, p. 6473–6475, 27 ago. 2007.

LIU, Junjun *et al.* Deep Red Emissive Carbonized Polymer Dots with Unprecedented Narrow Full Width at Half Maximum. **Advanced Materials**, v. 32, n. 17, p. 1–9, 2020.

LIU, Junjun; LI, Rui; YANG, Bai. Carbon Dots: A New Type of Carbon-Based Nanomaterial with Wide Applications. **ACS Central Science**, v. 6, n. 12, p. 2179–2195, 23 dez. 2020.

LIU, Junying; JATAV, Sanjay; HILL, Eric H. Few-Layer In2S3in Laponite Interlayers: A Colloidal Route Toward Heterostructured Nanohybrids with Enhanced Photocatalysis. **Chemistry of Materials**, v. 32, n. 23, p. 10015–10024, 2020.

LIU, Ruili *et al.* An Aqueous Route to Multicolor Photoluminescent Carbon Dots Using Silica Spheres as Carriers. **Angewandte Chemie International Edition**, v. 48, n. 25, p. 4598–4601, 8 jun. 2009.

LIU, Xiangwen *et al.* Three-step nucleation of metal–organic framework nanocrystals. **Proceedings of the National Academy of Sciences**, v. 118, n. 10, 9 mar. 2021.

LONE, Imtiyaz Ahmad; ROHIT, Jigneshkumar V. Carbon dots encapsulated metal-organic frameworks: An emerging optical sensors for monitoring of environmental pollutants. **Inorganic Chemistry Communications**, v. 180, p. 114918, out. 2025.

LÓPEZ-DÍAZ, David *et al.* Evolution of the Raman Spectrum with the Chemical Composition of Graphene Oxide. **Journal of Physical Chemistry C**, v. 121, n. 37, p. 20489–20497, 2017.

LÓPEZ-GALINDO, Alberto *et al.* Pharmaceutical and Cosmetic Uses of Fibrous Clays. *In*: *[S.l.: S.n.]*. p. 299–324.

LUO, Honglin *et al.* Layered nanohydroxyapatite as a novel nanocarrier for controlled delivery of 5-fluorouracil. **International Journal of Pharmaceutics**, v. 513, n. 1–2, p. 17–25, 20 nov. 2016.

MA, Dongling. Hybrid Nanoparticles: An Introduction. *In*: **Noble Metal-Metal Oxide Hybrid Nanoparticles: Fundamentals and Applications**. *[S.l.: S.n.]*. p. 3–6.

MA, Rong *et al.* Preparation of Graphene Quantum Dots Decorated Montmorillonite to Reinforce Fire Retardancy of Polystyrene. **Industrial & Engineering Chemistry Research**, v. 62, n. 34, p. 13510–13518, 30 ago. 2023.

MA, Wei *et al.* Metal-Organic Framework (MOF)-Based Sensors for Mercury (Hg) Detection: Design Strategies and Recent Progress. **Chemistry – A European Journal**, v. 31, n. 7, 3 fev. 2025.

MACAIRAN, Jun Ray *et al.* Elucidating the mechanism of dual-fluorescence in carbon dots. **Journal of Colloid and Interface Science**, v. 606, p. 67–76, 2022.

MADEJOVÁ, J. FTIR techniques in clay mineral studies. **Vibrational Spectroscopy**, v. 31, n. 1, p. 1–10, 2003.

MADEJOVÁ, J.; GATES, W. P.; PETIT, S. IR Spectra of Clay Minerals. *In*: *[S.l.: S.n.]*. p. 107–149.

MANDAL, Saptarshi *et al.* Bovine Serum Albumin Amplified Reactive Oxygen Species Generation from Anthrarufin-Derived Carbon Dot and Concomitant Nanoassembly for Combination Antibiotic-Photodynamic Therapy Application. **ACS Applied Materials and Interfaces**, v. 11, n. 36, p. 33273–33284, 2019.

MANSURIYA, Bhargav D.; ALTINTAS, Zeynep. Carbon Dots: Classification, Properties, Synthesis, Characterization, and Applications in Health Care—An Updated Review (2018–2021). **Nanomaterials**, v. 11, n. 10, p. 2525, 27 set. 2021.

MAS, Nuria *et al.* Laser-driven direct synthesis of carbon nanodots and application as sensitizers for visible-light photocatalysis. **Carbon**, v. 156, p. 453–462, jan. 2020.

MASSARO, Marina *et al.* **The use of some clay minerals as natural resources for drug carrier applications**. **Journal of Functional Biomaterials**MDPI AG, , 19 out. 2018.

MASSARO, Marina *et al.* Halloysite nanotubes-carbon dots hybrids multifunctional nanocarrier with positive cell target ability as a potential non-viral vector for oral gene therapy. **Journal of Colloid and Interface Science**, v. 552, p. 236–246, 2019.

MASSARO, Marina *et al.* Comparison of Synthetic Pathways for Obtaining Fluorescent Nanomaterials Based on Halloysite and Carbon Dots for Potential Biological Sensing. **International Journal of Molecular Sciences**, v. 25, n. 10, p. 5370, 14 maio 2024.

MASSARO, Marina; NOTO, Renato; RIELA, Serena. Past, Present and Future Perspectives on Halloysite Clay Minerals. **Molecules**, v. 25, n. 20, p. 4863, 21 out. 2020.

MCKEOWN, David A.; POST, Jeffrey E.; ETZ, Edgar S. Vibrational analysis of palygorskite and sepiolite. **Clays and Clay Minerals**, v. 50, n. 5, p. 667–680, 2002.

MEHDI, Yamina Ait *et al.* Preparation of multifunctional PEG-graft-Halloysite Nanotubes for Controlled Drug Release, Tumor Cell Targeting, and Bio-imaging. **Colloids and Surfaces B: Biointerfaces**, v. 170, p. 322–329, out. 2018.

MENG, Xiang-Bin *et al.* Metal-organic framework as nanoreactors to co-incorporate carbon nanodots and CdS quantum dots into the pores for improved H2 evolution without noble-metal cocatalyst. **Applied Catalysis B: Environmental**, v. 244, p. 340–346, maio 2019.

MERONI, Daniela; ARDIZZONE, Silvia. **Preparation and application of hybrid nanomaterials**. **Nanomaterials**MDPI AG, , 1 nov. 2018.

MINTZ, Keenan J. *et al.* A deep investigation into the structure of carbon dots. **Carbon**, v. 173, p. 433–447, 1 mar. 2021.

MISSAOUI, Nadhem; KAHRI, Hamza; DEMIRCI, Umit B. Rapid room-temperature synthesis and characterizations of high-surface-area nanoparticles of zeolitic imidazolate framework-8 (ZIF-8) for CO2 and CH4 adsorption. **Journal of Materials Science**, v. 57, n. 34, p. 16245–16257, 30 set. 2022.

MORAES, Jemima Daniela Dias *et al.* Clay minerals: Properties and applications to dermocosmetic products and perspectives of natural raw materials for therapeutic purposes—A review. **International Journal of Pharmaceutics**, v. 534, n. 1–2, p. 213–219, dez. 2017a.

MORAES, Jemima Daniela Dias *et al.* Clay minerals: Properties and applications to dermocosmetic products and perspectives of natural raw materials for therapeutic purposes—A review. **International Journal of Pharmaceutics**, v. 534, n. 1–2, p. 213–219, dez. 2017b.

MORBIATO, Laura *et al.* Structure Matters: Tailored Graphitization of Carbon Dots Enhances Photocatalytic Performance. **ACS Nano**, v. 19, n. 4, p. 4887–4900, 4 fev. 2025.

MOUSA, Mohamed *et al.* Clay nanoparticles for regenerative medicine and biomaterial design: A review of clay bioactivity. **Biomaterials**, v. 159, p. 204–214, 2018.

MURA, Paola *et al.* Hybrid systems based on “drug – in cyclodextrin – in nanoclays” for improving oxaprozin dissolution properties. **International Journal of Pharmaceutics**, v. 509, n. 1–2, p. 8–15, jul. 2016.

MURRAY, Haydn H. Chapter 2 Structure and Composition of the Clay Minerals and their Physical and Chemical Properties. *In*: *[S.l.: S.n.]*. p. 7–31.

NATH, Debarshi *et al.* Nanoclay-based active food packaging systems: A review. **Food Packaging and Shelf Life**, v. 31, p. 100803, mar. 2022.

NAWAZ, Sumra *et al.* Phyllosilicate derived catalysts for efficient conversion of lignocellulosic derived biomass to biodiesel: A review. **Bioresource Technology**, v. 343, p. 126068, jan. 2022.

NAZIR, Muhammad Altaf *et al.* Heterointerface engineering of water stable ZIF-8@ZIF-67: Adsorption of rhodamine B from water. **Surfaces and Interfaces**, v. 34, p. 102324, nov. 2022.

NAZIR, Muhammad Altaf *et al.* Zeolitic imidazolate frameworks (ZIF-8 & ZIF-67): Synthesis and application for wastewater treatment. **Separation and Purification Technology**, v. 356, p. 129828, abr. 2025.

NIETO, Steven *et al.* Flocculation of Clay-Based Tailings: Differences of Kaolin and Sodium Montmorillonite in Salt Medium. **Materials**, v. 15, n. 3, p. 1156, 2 fev. 2022.

NOH, Kyungkyou; LEE, Jisu; KIM, Jaheon. Compositions and Structures of Zeolitic Imidazolate Frameworks. **Israel Journal of Chemistry**, v. 58, n. 9–10, p. 1075–1088, 18 out. 2018.

NOMICISIO, Cristian *et al.* Natural and Synthetic Clay Minerals in the Pharmaceutical and Biomedical Fields. **Pharmaceutics**, v. 15, n. 5, 2023.

NONES, Janaína *et al.* Effects of bentonite on different cell types: A brief review. **Applied Clay Science**, v. 105–106, p. 225–230, mar. 2015.

OLIVEIRA, Artur S.; ALCÂNTARA, Ana C. S.; PERGHER, Sibele B. C. Bionanocomposite systems based on montmorillonite and biopolymers for the controlled release of olanzapine. **Materials Science and Engineering C**, v. 75, p. 1250–1258, 2017.

ÖZTÜRK, Zafer; FILEZ, Matthias; WECKHUYSEN, Bert M. Decoding Nucleation and Growth of Zeolitic Imidazolate Framework Thin Films with Atomic Force Microscopy and Vibrational Spectroscopy. **Chemistry – A European Journal**, v. 23, n. 45, p. 10915–10924, 10 ago. 2017.

OZYURT, Derya *et al.* Properties, synthesis, and applications of carbon dots: A review. **Carbon Trends**, v. 12, p. 100276, set. 2023.

PALEM, Ramasubba Reddy *et al.* Physicochemical characterization, drug release, and biocompatibility evaluation of carboxymethyl cellulose-based hydrogels reinforced with sepiolite nanoclay. **International Journal of Biological Macromolecules**, v. 178, p. 464–476, 2021.

PARK, Kyo Sung *et al.* Exceptional chemical and thermal stability of zeolitic imidazolate frameworks. **Proceedings of the National Academy of Sciences of the United States of America**, v. 103, n. 27, p. 10186–10191, 2006.

PARK, Wooram *et al.* Advanced hybrid nanomaterials for biomedical applications. **Progress in Materials Science**, v. 114, n. March, p. 100686, 2020.

PEIXOTO, Diana *et al.* Emerging role of nanoclays in cancer research, diagnosis, and therapy. **Coordination Chemistry Reviews**, v. 440, p. 213956, 2021.

PEÑA-PARÁS, Laura; SÁNCHEZ-FERNÁNDEZ, José Antonio; VIDALTAMAYO, Román. Nanoclays for Biomedical Applications. *In*: **Handbook of Ecomaterials**. Cham: Springer International Publishing, 2018. p. 1–19.

PENG, Liping *et al.* A novel dual-function fluorescence sensor Eu/CDs@MOF-808 for the sensitive detection of adenosine triphosphate and uric acid. **Chemical Engineering Journal**, v. 500, p. 156811, nov. 2024.

PENG, Zhili *et al.* Carbon dots: Biomacromolecule interaction, bioimaging and nanomedicine. **Coordination Chemistry Reviews**, v. 343, p. 256–277, jul. 2017.

PENG, Zhili *et al.* Facile Synthesis of "Boron-Doped" Carbon Dots and Their Application in Visible-Light-Driven Photocatalytic Degradation of Organic Dyes. **Nanomaterials**, v. 10, n. 8, p. 1560, 8 ago. 2020.

PERUMAL, Suguna *et al.* Simultaneous removal of heavy metal ions using carbon dots-doped hydrogel particles. **Chemosphere**, v. 286, n. P2, p. 131760, 2022.

PIRHAJI, Jamileh Zare *et al.* Synthesis and characterization of halloysite/graphene quantum dots magnetic nanocomposite as a new adsorbent for Pb(II) removal from water. **Journal of Molecular Liquids**, v. 300, p. 112345, fev. 2020.

POLYAKOV, Maxim *et al.* A hybrid nanomaterial based on single walled carbon nanotubes cross-linked via axially substituted silicon (IV) phthalocyanine for chemiresistive sensors. **Molecules**, v. 25, n. 9, p. 1–17, 2020.

PRASHANTH, M. K. *et al.* Multifunctional carbon dot anchored halloysite nanotube: Nanovehicle for cisplatin drug release, cytotoxicity on breast cancer cells and DNA binding studies. **Chemical Data Collections**, v. 38, p. 100827, abr. 2022.

QIAN, Qihui *et al.* MOF-Based Membranes for Gas Separations. **Chemical Reviews**, v. 120, n. 16, p. 8161–8266, 26 ago. 2020.

QU, Songnan *et al.* Toward Efficient Orange Emissive Carbon Nanodots through Conjugated sp2-Domain Controlling and Surface Charges Engineering. **Advanced Materials**, v. 28, n. 18, p. 3516–3521, 2016.

RAGU, Sandrine *et al.* Responses of human cells to sepiolite interaction. **Applied Clay Science**, v. 194, n. May, p. 105655, 2020.

RAHMANI, Erfan *et al.* Preparation of a pH-responsive chitosan-montmorillonite-nitrogen-doped carbon quantum dots nanocarrier for attenuating doxorubicin limitations in cancer therapy. **Engineering in Life Sciences**, v. 22, n. 10, p. 634–649, 2022.

RASAL, Akash S. *et al.* Carbon quantum dots: Classification-structure-property-application relationship for biomedical and environment remediation. **Coordination Chemistry Reviews**, v. 533, p. 216510, jun. 2025.

RASHEED, Tahir *et al.* Metal-Organic Framework-Based Engineered Materials—Fundamentals and Applications. **Molecules**, v. 25, n. 7, p. 1598, 31 mar. 2020.

RASTOGI, V. K. *et al.* Fourier transform Raman spectrum andab initio and density functional computations of the vibrational spectrum, molecular geometry, atomic charges and some molecular properties of the anticarcinogenic drug 5-fluorouracil. **Journal of Raman Spectroscopy**, v. 31, n. 7, p. 595–603, jul. 2000.

RASTOGI, V. K.; PALAFOX, M. Alcolea. Vibrational spectra, tautomerism and thermodynamics of anticarcinogenic drug: 5-Fluorouracil. **Spectrochimica Acta Part A: Molecular and Biomolecular Spectroscopy**, v. 79, n. 5, p. 970–977, set. 2011.

REBITSKI, Ediana P. *et al.* Functional Carboxymethylcellulose/Zein Bionanocomposite Films Based on Neomycin Supported on Sepiolite or Montmorillonite Clays ˆ. 2018.

REBITSKI, Ediana P. *et al.* Bionanocomposites based on cationic and anionic layered clays as controlled release devices of amoxicillin. **Applied Clay Science**, v. 173, n. February, p. 35–45, 2019.

RUIZ, Ana I.; RUIZ-GARCÍA, Cristina; RUIZ-HITZKY, Eduardo. From old to new inorganic materials for advanced applications: The paradigmatic example of the sepiolite clay mineral. **Applied Clay Science**, v. 235, n. January, p. 106874, 2023.

RUIZ-GARCÍA, Cristina *et al.* Sepiolite-carbon nanocomposites doped with Pd as improving catalysts for hydrodechlorination processes. **Applied Clay Science**, v. 161, n. April, p. 132–138, 2018.

RUIZ-HITZKY, Eduardo *et al.* Fibrous clays based bionanocomposites. **Progress in Polymer Science**, v. 38, n. 10–11, p. 1392–1414, 2013.

SAADAT, Saeida; RAWTANI, Deepak; RAO, Piyush K. Antibacterial activity of chitosan film containing Syzygium aromaticum (clove) oil encapsulated halloysite nanotubes against foodborne pathogenic bacterial strains. **Materials Today Communications**, v. 32, p. 104132, ago. 2022.

SADEZKY, A. *et al.* Raman microspectroscopy of soot and related carbonaceous materials: Spectral analysis and structural information. **Carbon**, v. 43, n. 8, p. 1731–1742, 2005.

SANTOS, Josefa Dina; *et al.* Exploring the potential of a ZIF-8@MCM-41-based heterostructured material for battery-type electrodes for supercapatteries. **New Journal of Chemistry**, v. 48, n. 37, p. 16311–16322, 2024.

SANTOS, Wemerson D. C. *et al.* Photocatalytic degradation of ciprofloxacin using semiconductor derived from heterostructured ZIF-8-based materials. **Microporous and Mesoporous Materials**, v. 359, n. June, 2023.

SARIKAYA, Yüksel; ÖNAL, Müşerref; PEKDEMIR, Abdullah Devrim. Thermal degradation kinetics of sepiolite. **Clay Minerals**, v. 55, n. 1, p. 96–100, 2020.

SCHEJN, Aleksandra *et al.* Controlling ZIF-8 nano- and microcrystal formation and reactivity through zinc salt variations. **CrystEngComm**, v. 16, n. 21, p. 4493–4500, 2014.

SCHNABEL, Jennifer; ETTLINGER, Romy; BUNZEN, Hana. Zn-MOF-74 as pH-Responsive Drug-Delivery System of Arsenic Trioxide. **ChemNanoMat**, v. 6, n. 8, p. 1229–1236, 16 ago. 2020.

SEN, Shreeja; BOSE, Anindya. Carbon dots: A review of innovations, applications, challenges, and future prospects. **Inorganic Chemistry Communications**, v. 173, p. 113852, mar. 2025.

SHABBIR, Hasan; CSAPÓ, Edit; WOJNICKI, Marek. Carbon Quantum Dots: The Role of Surface Functional Groups and Proposed Mechanisms for Metal Ion Sensing. **Inorganics**, v. 11, n. 6, p. 262, 20 jun. 2023.

SHATERY, Omer Baqi Ahmed; OMER, Khalid M. Selectivity Enhancement for Uric Acid Detection via *In Situ* Preparation of Blue Emissive Carbon Dots Entrapped in Chromium Metal–Organic Frameworks. **ACS Omega**, v. 7, n. 19, p. 16576–16583, 17 maio 2022.

SHENG, Xue *et al.* Metal cation saturation on montmorillonites facilitates the adsorption of DNA via cation bridging. **Chemosphere**, v. 235, p. 670–678, nov. 2019.

SHUAI, C. *et al.* A self-assembled montmorillonite-carbon nanotube hybrid nanoreinforcement for poly-L-lactic acid bone scaffold. **Materials Today Advances**, v. 11, p. 100158, 2021.

SI, Yunhui *et al.* Fabrication of a novel core–shell CQDs@ZIF-8 composite with enhanced photocatalytic activity. **Journal of Materials Science**, v. 55, n. 27, p. 13049–13061, 2020.

SIRIPOTHULA, Rambabu *et al.* Facile synthesis of heteroatom-doped carbon dots: Structural insights, Solvatochromism and selective sensing of picric acid. **Inorganic Chemistry Communications**, v. 181, p. 115259, nov. 2025.

SIVA, V. *et al.* Nanoscale Zn-MOF enwrapped polymer nanocomposite as electrode material for enhanced energy storage system. **Inorganic Chemistry Communications**, v. 154, 1 ago. 2023.

SUKUNTA, Jirasak *et al.* Green synthesis of carboxymethyl cellulose-derived carbon quantum dots using microplasma technology. **Applied Surface Science Advances**, v. 29, p. 100830, set. 2025.

SUL, Yoonjung; EZATI, Parya; RHIM, Jong-Whan. Preparation of chitosan/gelatin-based functional films integrated with carbon dots from banana peel for active packaging application. **International Journal of Biological Macromolecules**, v. 246, p. 125600, ago. 2023.

SUN, Ya-Ping *et al.* Quantum-Sized Carbon Dots for Bright and Colorful Photoluminescence. **Journal of the American Chemical Society**, v. 128, n. 24, p. 7756–7757, 1 jun. 2006.

SUN, Yubing *et al.* Recent advances in the application of zeolitic imidazolate frameworks (ZIFs) in environmental remediation: a review. **Environmental Science: Nano**, v. 9, n. 11, p. 4069–4092, 2022.

SUPAJARUWONG, Siriboon *et al.* Scaling-up of carbon dots hydrothermal synthesis from sugars in a continuous flow microreactor system for biomedical application as *in vitro* antimicrobial drug nanocarrier. **Science and Technology of Advanced Materials**, v. 24, n. 1, 31 dez. 2023.

SWAIN, Rakesh *et al.* Bentonite clay incorporated topical film formulation for delivery of trimetazidine: Control of ocular pressure and in vitro-in vivo correlation. **Journal of Drug Delivery Science and Technology**, v. 67, p. 102956, jan. 2022.

TANG, Qingguo *et al.* Study on pore distribution and formation rule of sepiolite mineral nanomaterials. **Journal of Nanomaterials**, v. 2012, 2012.

TANG, Yue *et al.* Modified Sepiolite Nanoclays in Advanced Composites for Engineering Applications. **ACS Applied Nano Materials**, v. 7, n. 16, p. 19221–19232, 2024.

TAO, Songyuan *et al.* Crosslink-Enhanced Emission Effect on Luminescence in Polymers: Advances and Perspectives. **Angewandte Chemie**, v. 132, n. 25, p. 9910–9924, 15 jun. 2020.

TAO, Songyuan *et al.* Confined-domain crosslink-enhanced emission effect in carbonized polymer dots. **Light: Science & Applications**, v. 11, n. 1, p. 56, 10 mar. 2022.

TAVAN, Mansoureh *et al.* Carbon quantum dots: Multifunctional fluorescent nanomaterials for sustainable advances in biomedicine and agriculture. **Industrial Crops and Products**, v. 231, p. 121207, set. 2025.

TEIXEIRA, Mayara M. *et al.* Ag_3PO_4/clay-based heterostructures as sustainable devices for efficient water disinfection and contaminant removal via cooperative processes of adsorption and visible light-driven degradation. **Journal of Water Process Engineering**, v. 75, 1 jun. 2025.

THOMMES, Matthias *et al.* Physisorption of gases, with special reference to the evaluation of surface area and pore size distribution (IUPAC Technical Report). **Pure and Applied Chemistry**, v. 87, n. 9–10, p. 1051–1069, 2015.

TIAN, P. *et al.* Graphene quantum dots from chemistry to applications. **Materials Today Chemistry**, v. 10, p. 221–258, dez. 2018.

TIAN, Xiumei *et al.* Carbon Quantum Dots: In vitro and in vivo Studies on Biocompatibility and Biointeractions for Optical Imaging. **International Journal of Nanomedicine**, v. Volume 15, p. 6519–6529, ago. 2020.

TIPA, Cezar *et al.* Clay-Based Nanocomposite Hydrogels for Biomedical Applications: A Review. **Nanomaterials**, v. 12, n. 19, 2022.

TOMIC, E. A. Thermal stability of coordination polymers. **Journal of Applied Polymer Science**, v. 9, n. 11, p. 3745–3752, 1965.

TORRES-GINER, S. *et al.* Melt grafting of sepiolite nanoclay onto poly(3-hydroxybutyrate-co-4-hydroxybutyrate) by reactive extrusion with multi-functional epoxy-based styrene-acrylic oligomer. **European Polymer Journal**, v. 84, p. 693–707, 2016.

TROYANO, Javier *et al.* Colloidal metal–organic framework particles: the pioneering case of ZIF-8. **Chemical Society Reviews**, v. 48, n. 23, p. 5534–5546, 2019.

TUNCEL, D.; ÖKTE, A. N. Improved Adsorption Capacity and Photoactivity of ZnO-ZIF-8 Nanocomposites. **Catalysis Today**, v. 361, p. 191–197, fev. 2021.

TYAGI, Beena; CHUDASAMA, Chintan D.; JASRA, Raksh V. Determination of structural modification in acid activated montmorillonite clay by FT-IR spectroscopy. **Spectrochimica Acta - Part A: Molecular and Biomolecular Spectroscopy**, v. 64, n. 2, p. 273–278, 2006.

UCHIDA, Junya *et al.* One-step solvent-free synthesis of carbon dot-based layered composites exhibiting color-tunable photoluminescence. **RSC Advances**, v. 12, n. 14, p. 8283–8289, 2022.

UDDIN, Md. Nur *et al.* Research and applications of nanoclays: A review. **SPE Polymers**, v. 5, n. 4, p. 507–535, 4 out. 2024.

VENGATESAN, M. R. *et al.* Facile synthesis of thermally reduced graphene oxide-sepiolite nanohybrid via intercalation and thermal reduction method. **Applied Clay Science**, v. 135, p. 510–515, 2017.

WALCZYK, A. *et al.* New insight into the phase transformation of sepiolite upon alkali activation: Impact on composition, structure, texture, and catalytic/sorptive properties. **Applied Clay Science**, v. 195, n. March, 2020.

WANG, Dongdong *et al.* Tunable Zeolitic Imidazolate Framework-8 Nanoparticles for Biomedical Applications. **Small Methods**, v. 8, n. 3, 23 mar. 2024a.

WANG, Fei *et al.* A facile fabrication of sepiolite mineral nanofibers with excellent adsorption performance for Cd2+ ions. **RSC Advances**, v. 9, n. 69, p. 40184–40189, 2019.

WANG, Jiaxing; WILSON, Rebecca S.; ARISTILDE, Ludmilla. Electrostatic coupling and water bridging in adsorption hierarchy of biomolecules at water–clay interfaces. **Proceedings of the National Academy of Sciences**, v. 121, n. 7, 13 fev. 2024.

WANG, Jingyi *et al.* Facile fabrication of Fe3O4-Biochar hybrid nanomaterials as catalysts for Photo-Fenton degradation of tetracycline. **Optical Materials**, v. 143, p. 114156, 2023a.

WANG, Junli *et al.* N, B-Codoping Induces High-Efficiency Solid-State Fluorescence and Dual Emission of Yellow/Orange Carbon Dots. **ACS Sustainable Chemistry and Engineering**, v. 9, n. 5, p. 2224–2236, 2021a.

WANG, Pengsheng *et al.* Clay-Based Materials for Heavy Metals Adsorption: Mechanisms, Advancements, and Future Prospects in Environmental Remediation. **Crystals**, v. 14, n. 12, p. 1046, 30 nov. 2024b.

WANG, Yuegang *et al.* A Review on the Synthesis of Carbon Dots and Their Applications in Environmental Analysis. **Crystals**, v. 15, n. 5, p. 384, 22 abr. 2025a.

WANG, Yufei *et al.* Carbon nanodots in ZIF-8: synthesis, tunable luminescence and temperature sensing. **Inorganic Chemistry Frontiers**, v. 5, n. 11, p. 2739–2745, 2018.

WANG, Zelin *et al.* Engineering the structure of ZIF-derived catalysts by revealing the critical role of temperature for enhanced oxygen reduction reaction. **Journal of Materials Chemistry A**, v. 9, n. 34, p. 18515–18525, 2021b.

WANG, Zhi *et al.* Revealing the in-situ growth mechanism of carbon dots confined in ZIF-8 as multicolor fluorescent material with high photothermal stability. **Journal of Colloid and Interface Science**, v. 688, p. 172–182, jun. 2025b.

WANG, Zhiying *et al.* Fabrication of fluorescence sensor based on semi-covalent dummy molecularly imprinted silica on silane-modified carbon quantum dot for highly selective and

sensitive detection of bisphenol A in spirits. **Colloids and Surfaces A: Physicochemical and Engineering Aspects**, v. 696, p. 134292, set. 2024c.

WANG, Zhongliang *et al.* Synthesis and properties of Mg2Al layered double hydroxides containing 5-fluorouracil. **Journal of Solid State Chemistry**, v. 178, n. 3, p. 736–741, 2005.

WANG, Zhufeng *et al.* Selective catalytic reduction of NO by CO over MOF-based CuOx@ZIF-67 catalysts and reaction mechanism. **Fuel**, v. 348, p. 128565, set. 2023b.

WÓJCIK-BANIA, Monika; MATUSIK, Jakub. The effect of surfactant-modified montmorillonite on the cross-linking efficiency of polysiloxanes. **Materials**, v. 14, n. 10, p. 7–9, 2021.

WU, Ting *et al.* Dodecyl glycoside intercalated organo-montmorillonite as the excipient for the development of alginate/organo-montmorillonite composite hydrogel beads based oral formulations for hydrophobic drug delivery. **Colloids and Surfaces A: Physicochemical and Engineering Aspects**, v. 709, p. 136154, mar. 2025.

WUTTKE, Stefan *et al.* Positioning metal-organic framework nanoparticles within the context of drug delivery – A comparison with mesoporous silica nanoparticles and dendrimers. **Biomaterials**, v. 123, p. 172–183, 2017.

WYPYCH, Fernando;; DE FREITAS, Rilton Alves. Clay minerals: Classification, structure, and properties. *In*: *[S.l.: S.n.]*. p. 3–35.

XIA, Chunlei *et al.* Evolution and Synthesis of Carbon Dots: From Carbon Dots to Carbonized Polymer Dots. **Advanced Science**, v. 6, n. 23, 30 dez. 2019.

XIE, Haojie *et al.* Synthesis of a COF-on-MOF hybrid nanomaterial for enhanced colorimetric biosensing. **Talanta**, v. 274, n. April, p. 126071, 2024.

XIE, Weimin; CHEN, Ying; YANG, Huaming. **Layered Clay Minerals in Cancer Therapy: Recent Progress and Prospects**. **Small**John Wiley and Sons Inc, , 23 ago. 2023.

XU, Bailu *et al.* Aptamer carbon nanodot sandwich used for fluorescent detection of protein. **The Analyst**, v. 137, n. 23, p. 5483, 2012.

XU, Longhua *et al.* One-pot synthesis of nanoscale carbon dots-embedded metal–organic frameworks at room temperature for enhanced chemical sensing. **Journal of Materials Chemistry A**, v. 4, n. 41, p. 15880–15887, 2016.

XU, Xiaoyou *et al.* Electrophoretic analysis and purification of fluorescent single-walled carbon nanotube fragments. **Journal of the American Chemical Society**, v. 126, n. 40, p. 12736–12737, 2004.

XUE, Shanshan *et al.* The Formation Process and Mechanism of Carbon Dots Prepared from Aromatic Compounds as Precursors: A Review. **Small**, v. 19, n. 31, 17 ago. 2023.

YAGHI, O. M.; LI, Hailian. Hydrothermal Synthesis of a Metal-Organic Framework Containing Large Rectangular Channels. **J. Am. Chem. Soc.**, v. 117, p. 10401–10402, 1995.

YAN, Fanyong *et al.* Conjugate area-controlled synthesis of multiple-color carbon dots and application in sensors and optoelectronic devices. **Sensors and Actuators B: Chemical**, v. 329, p. 129263, fev. 2021.

YANG, Fan *et al.* Controllable and eco-friendly synthesis of P-riched carbon quantum dots and its application for copper (II) ion sensing. **Applied Surface Science**, v. 448, p. 589–598, 2018.

YANG, Fangfang; WANG, Aiqin. Recent researches on antimicrobial nanocomposite and hybrid materials based on sepiolite and palygorskite. **Applied Clay Science**, v. 219, n. November 2021, p. 106454, 2022.

YANG, Jae Hun *et al.* Drug–clay nanohybrids as sustained delivery systems. **Applied Clay Science**, v. 130, p. 20–32, 1 set. 2016.

YANG, Jie *et al.* Carbon dots-embedded zinc-based metal-organic framework as a dual-emitting platform for metal cation detection. **Microporous and Mesoporous Materials**, v. 331, p. 111630, jan. 2022.

YANG, Ji-min *et al.* Fabrication of a carbon quantum dots-immobilized zirconium-based metal- organic framework composite fl uorescence sensor for highly sensitive detection of 4-nitrophenol. **Microporous and Mesoporous Materials**, v. 274, n. July 2018, p. 149–154, 2019.

YAO, Chuanxu; XU, Yan; XIA, Zhiguo. A carbon dot-encapsulated UiO-type metal organic framework as a multifunctional fluorescent sensor for temperature, metal ion and pH detection. **Journal of Materials Chemistry C**, v. 6, n. 16, p. 4396–4399, 2018.

YENDLURI, Raghuvara *et al.* Paclitaxel Encapsulated in Halloysite Clay Nanotubes for Intestinal and Intracellular Delivery. **Journal of Pharmaceutical Sciences**, v. 106, n. 10, p. 3131–3139, out. 2017.

YETIMAN, Sevda *et al.* Rational Integration of ZIF-8 and $BiPO_4$ for Energy Storage and Environmental Applications. **ACS Omega**, v. 7, n. 49, p. 44878–44891, 13 dez. 2022.

YI, Hao *et al.* Photoluminescence Mechanism of Carbon Dots: Triggering Multiple Color Emissions through Controlling the Degree of Protonation. **Molecules**, v. 27, n. 19, p. 6517, 2 out. 2022.

YI, Zhihao *et al.* Bifunctional MOF-Encapsulated Cobalt-Doped Carbon Dots Nanozyme-Powered Chemiluminescence/Fluorescence Dual-Mode Detection of Aflatoxin B1. **ACS Applied Materials & Interfaces**, v. 16, n. 13, p. 16494–16504, 3 abr. 2024.

YIN, Yongqi *et al.* Nanoarchitecturing Carbon Nanodot Arrays on Zeolitic Imidazolate Framework - Derived Cobalt – Nitrogen - Doped Carbon Nanoflakes toward Oxygen Reduction Electrocatalysts. **ACS Nano**, v. 15, n. 8, p. 13240–13248, 24 ago. 2021.

YU, Tian; MALUGIN, Alexander; GHANDEHARI, Hamidreza. Impact of Silica Nanoparticle Design on Cellular Toxicity and Hemolytic Activity. **ACS Nano**, v. 5, n. 7, p. 5717–5728, 26 jul. 2011.

YU, Yanlin; YAN, Lei. Rapid synthesis of C-dots@PGV nanocomposites powders for development of latent fingermarks. **Bulletin of the Chemical Society of Japan**, v. 90, n. 11, p. 1217–1223, 2017.

YUAN, Ting *et al.* Carbon Quantum Dots with Near-Unity Quantum Yield Bandgap Emission for Electroluminescent Light-Emitting Diodes. **Angewandte Chemie**, v. 135, n. 20, 8 maio 2023.

YUSUF, Vadia Foziya; MALEK, Naved I.; KAILASA, Suresh Kumar. Review on Metal–Organic Framework Classification, Synthetic Approaches, and Influencing Factors: Applications in Energy, Drug Delivery, and Wastewater Treatment. **ACS Omega**, v. 7, n. 49, p. 44507–44531, 13 dez. 2022.

ZAINI, Muhammad Safwan *et al.* Solvent-Dependent Photoluminescence Emission and Colloidal Stability of Carbon Quantum dots from Watermelon Peels. **Journal of Fluorescence**, v. 35, n. 1, p. 245–256, 1 dez. 2023a.

ZAINI, Muhammad Safwan *et al.* Solvent-Dependent Photoluminescence Emission and Colloidal Stability of Carbon Quantum dots from Watermelon Peels. **Journal of Fluorescence**, v. 35, n. 1, p. 245–256, 1 dez. 2023b.

ZEGGAI, Fatima zohra *et al.* Investigation of Metal-Organic Frameworks (MOFs): Synthesis, Properties, and Applications - An In-Depth Review. **Chemical Physics Impact**, v. 10, p. 100864, jun. 2025.

ZHAI, Yuechen *et al.* Synthesis of green emissive carbon dots@montmorillonite composites and their application for fabrication of light-emitting diodes and latent fingerprints markers. **Journal of Colloid and Interface Science**, v. 554, p. 344–352, 15 out. 2019.

ZHANG, Bohan *et al.* Assignment of Core and Surface States in Multicolor-Emissive Carbon Dots. **Small**, v. 19, n. 31, 2022a.

ZHANG, Hongyue *et al.* Carbon Dots in Porous Materials: Host–Guest Synergy for Enhanced Performance. **Angewandte Chemie**, v. 132, n. 44, p. 19558–19570, 26 out. 2020.

ZHANG, Jie; TAN, Yan; SONG, Wen-Jun. Zeolitic imidazolate frameworks for use in electrochemical and optical chemical sensing and biosensing: a review. **Microchimica Acta**, v. 187, n. 4, p. 234, 16 abr. 2020.

ZHANG, Jing *et al.* Hectorite: Synthesis, modification, assembly and applications. **Applied Clay Science**, v. 177, p. 114–138, set. 2019a.

ZHANG, Jing *et al.* Manganese-based MOF interconnected carbon nanotubes as a high-performance cathode for rechargeable aqueous zinc-ion batteries. **Journal of Energy Storage**, v. 76, 15 jan. 2024.

ZHANG, Kangjie *et al.* Structural design of metal catalysts based on ZIFs: From nanoscale to atomic level. **Nano Select**, v. 2, n. 10, p. 1902–1925, 30 out. 2021.

ZHANG, Likang *et al.* A review on carbon quantum dots: Synthesis, photoluminescence mechanisms and applications. **Luminescence**, v. 37, n. 10, p. 1612–1638, 16 out. 2022b.

ZHANG, Miaoran *et al.* Red/orange dual-emissive carbon dots for pH sensing and cell imaging. **Nano Research**, v. 12, n. 4, p. 815–821, 1 abr. 2019b.

ZHANG, Na; TONG, Man; YUAN, Songhu. Redox transformation of structural iron in nontronite induced by quinones under anoxic conditions. **Science of The Total Environment**, v. 801, p. 149637, dez. 2021.

ZHANG, Siqi *et al.* Rheological behaviors of Na-montmorillonite considering particle interactions: A molecular dynamics study. **Journal of Rock Mechanics and Geotechnical Engineering**, v. 17, n. 7, p. 4657–4671, jul. 2025.

ZHANG, Xian *et al.* Correlation of montmorillonite exfoliation with interlayer cations in the preparation of two-dimensional nanosheets. **RSC Advances**, v. 7, n. 66, p. 41471–41478, 2017a.

ZHANG, Xiaoke *et al.* Metal-organic-framework derived Zn-V-based oxide with charge storage mechanism as high-performance anode material to enhance lithium and sodium storage. **Journal of Colloid and Interface Science**, v. 652, p. 1394–1404, dez. 2023a.

ZHANG, Yanqiu *et al.* The fabrication strategies and enhanced performances of metal-organic frameworks and carbon dots composites: State of the art review. **Chinese Chemical Letters**, v. 34, n. 3, p. 107478, mar. 2023b.

ZHANG, Yating *et al.* A hybrid ZIF-8/ZIF-62 glass membrane for gas separation. **Chemical Communications**, v. 58, n. 68, p. 9548–9551, 2022c.

ZHANG, Yi *et al.* Intercalated 2D nanoclay for emerging drug delivery in cancer therapy. **Nano Research**, v. 10, n. 8, p. 2633–2643, 5 ago. 2017b.

ZHANG, Zhaolun *et al.* Fibrous palygorskite clays as versatile nanocarriers for skin delivery of tea tree oils in efficient acne therapy. **International Journal of Pharmaceutics**, v. 623, p. 121903, jul. 2022d.

ZHAO, Linduo *et al.* Biological Redox Cycling of Iron in Nontronite and Its Potential Application in Nitrate Removal. **Environmental Science & Technology**, v. 49, n. 9, p. 5493–5501, 5 maio 2015.

ZHENG, Chengyu *et al.* Crosslink-Enhanced Emission-Dominated Design Strategy for Constructing Self-Protective Carbonized Polymer Dots With Near-Infrared Room-Temperature Phosphorescence. **Angewandte Chemie International Edition**, v. 63, n. 44, 24 out. 2024.

ZHENG, He-Qi; CUI, Yuanjing; QIAN, Guodong. Guest Encapsulation in Metal–Organic Frameworks for Photonics. **Accounts of Materials Research**, v. 4, n. 11, p. 982–994, 24 nov. 2023.

ZHENG, Zhiling *et al.* Structural Chemistry of Zeolitic Imidazolate Frameworks. **Inorganic Chemistry**, v. 62, n. 51, p. 20861–20873, 25 dez. 2023.

ZHOU, Shuwen *et al.* Carbon dots encapsulated zeolitic imidazolate framework-8 as an enhanced multi-antioxidant for efficient cytoprotection to HK-2 cells. **Journal of Colloid and Interface Science**, v. 676, p. 726–738, dez. 2024.

ZHOU, Wenxuan *et al.* **MOF derived metal oxide composites and their applications in energy storage**. **Coordination Chemistry Reviews**Elsevier B.V., , 15 fev. 2023.

ZHU, Ruifeng *et al.* Nitrogen-doped carbon dots-V2O5 nanobelts sensing platform for sensitive detection of ascorbic acid and alkaline phosphatase activity. **Analytica Chimica Acta**, v. 1089, p. 131–143, 2019.

ZHUANG, Guanzheng *et al.* Application of Nanofibrous Clay Minerals in Water-Based Drilling Fluids: Principles, Methods, and Challenges. **Minerals**, v. 14, n. 8, p. 842, 21 ago. 2024.

APPENDIX A – UV-Visible spectra of clay minerals

Figure A – UV-Vis spectra of (A) sepiolite and (B) montmorillonite dispersions in water (20 mg.L^{-1})

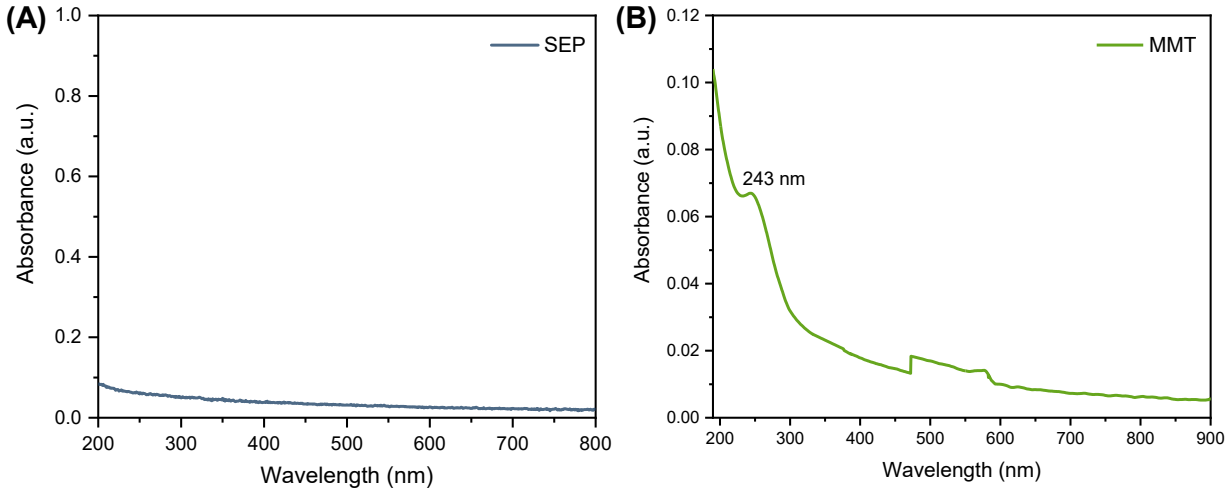

APPENDIX B – UV-Visible spectra of ZIF-8/CQD over the stability assay period

Figure B – Spectra of CQD and ZIF-8/CQD 200 hybrid nanomaterial in solution over the period of stability assay

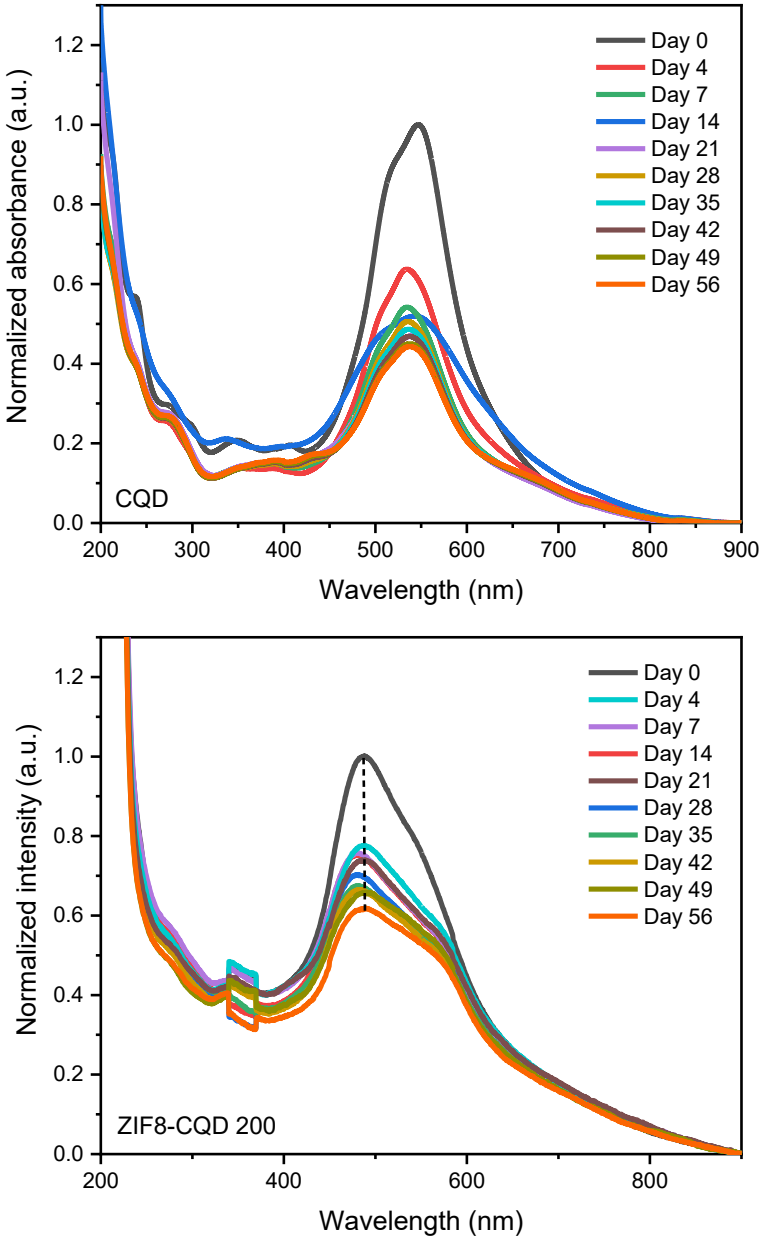

APPENDIX C – Cell viability of SEP-5FU hybrid nanomaterial using A549 cells (human cancer cells)

Figure C - MTT assay of SEP-5FU hybrid nanomaterials at concentrations ranging of 1000 to 1.93 μg.mL^{-1} using A549 cells (humam cancer cells). The IC_{50} was calculated to be 475.9 ± 245.9 μg.mL^{-1} for pure 5-FU and 0,8428 ± 0.584292 μg.mL^{-1}